THE UNIVERSITY of ADELAIDE

Integrating Concentrating Solar Thermal Energy into the Bayer Alumina Process

30th April 2023

Authors:

UA: Woei Lean Saw, Leok Lee, Philip Ingenhoven, Alfonso Chinnici, Xincheng Zhang, Muhammad Rafique, Yining Tang, Daniel Ang Jin Tung, Tse Chuen Tsai, Zimeng He, Eyad Al Smadi, Zhao Feng Tian, Tim Lau, Zhiwei Sun, Rey Chin, Philip van Eyk, Bassam Dally, Graham Nathan

CSIRO: Daniel Potter, Andrew Beath

UNSW: Evatt Hawkes

Project website: www.adelaide.edu.au/cet/solar-alumina/

make history.

Disclaimer and Acknowledgement

The views expressed herein are not necessarily the views of the Australian Government. The Australian Government does not accept responsibility for any information or advice contained within this document.

This project received funding from the Australian Renewable Energy Agency (ARENA) as part of ARENA's Research and Development Program.

Valuable inputs from the Technical Steering Committee, comprising members from CSIRO, UNSW, ITP Thermal, Alcoa of Australia and Hatch, are acknowledged.

Executive Summary

The project has evaluated the potential pathways to progressively integrate three complementary concentrating solar thermal (CST) energy technologies into the current energy-intensive Bayer Process, which produces calcined alumina from bauxite with natural gas as the energy source. These are the use of steam, heated with commercially available molten-salt technology, the generation of solar syngas by reforming natural gas with concentrated solar radiation, which was available at technology readiness level (TRL) 5/6 at the start of the project, and the production of high temperature hot air, which was at TRL 3 at the temperatures of interest at the start of the project. These three platforms are potentially complementary, since they are different stages of development and are implementable in different ways.

The main findings are as follows:

- **Solar thermal steam:**
  - The assessment of commercially-ready steam production via established molten salt storage technology has found this technology has potential to be comparably economically viable with the other alternative, such mechanical vapour recompression (MVR), that was assessed for net zero, based on the criteria adopted in the project. In order for this system to reach a solar share in the range of 29 to 45%, around 7 and 14 hours of full-load thermal energy storage will be required. The economics generally improve with decreasing storage size, due to the large added capital cost of a large thermal energy storage system. This also implies that these solar thermal systems need to be hybridised for alumina production, since it is uneconomic to achieve continuous production with thermal storage alone. Net-zero operation with a combustion back-up could potentially be achieved with alternative fuels, such as hydrogen or bio-gas;
  - The viability of solar steam via molten salt technology is strongly dependent on the quality of the solar resource. A resource of outstanding quality is available at potential green-field sites such as Learmonth, although the quality around Perth is lower.
  - All of the large-scale system configurations were found to yield positive internal rate of returns (IRR). Using the average of the cost estimates provided by suppliers, which represent a conservative estimate for today's costs, the IRR values were found to range from 3.5 to 7%, while the low-cost estimates of suppliers, which represent the lowest available cost opportunities, IRR was found to range from 6 to 13.5%. Values of LCOH are estimated to be in the range of AUD22 to 30/GJ based on the average costs and in the range of AUD14 to 24/GJ based on the low-cost estimates.
  - The viability of solar steam is expected to increase rapidly as the costs of CST technologies continue to fall, as discussed in more detail in the Program 1 final report, and at sites with a better solar resource. (https://www.adelaide.edu.au/cet/solar-alumina/publications).

- **Solar thermal syngas:**
  - The conversion of methane into syngas with concentrated solar thermal energy has good potential to be economically attractive. This process allows for the harnessing of both the sensible (thermal) energy and the chemical energy of the syngas. This approach is particularly advantageous when the hot syngas is introduced directly to the calciner, eliminating the need for cooling before use.
  - It is likely to be more viable to operate the syngas reactor off-sun (i.e. indirectly heated) than on-sun (i.e. in the receiver). This is partly because the storage of heat is both cheaper

and easier to manage than the storage of syngas, and partly because it facilitates more stable operation of the reactor. On this basis, a preliminary design for a new configuration of reactor was developed; Particular attention was also given to the emerging thermal storage technology of solid particles as they offer a cost-effective solution at the temperatures required to drive a steam reformer. Additionally, a thermal storage enables high utilisation of the captured solar energy by allowing any latent and sensible heat to directed to the industrial process.

- Net-zero operation with syngas in the context of an alumina plant would be achieved most plausibly with the use of bio-gas as the source of the methane, rather than natural gas. This is because CCU/S is not presently considered to be a priority for the alumina industry, and CO_2 is an inevitable product from the combustion of syngas. On the other hand, biogas is a low-carbon fuel because it is produced from biological sources. Nevertheless, access to sufficient resources of biogas to meet the needs of alumina calciners would be challenging in Western Australia. Another potential option is to conduct the methane reforming off-site at locations with good solar resource and sequestration sites. This would offer the potential to use natural gas as the feedstock and require transporting the hydrogen to the plant via a pipeline.

- **High temperature process heat from Solar thermal energy:**
  - There is strong potential for solar thermal energy to provide stored heat to high temperature industrial reactors, such as alumina calciners, at prices that are attractive with other sources of net-zero energy on the proviso that ongoing investment is provided to develop and upscale the technology and that the solar resource is sufficiently good. In particular, we estimate that stored heat could be provided to a plant at costs of around AUD15.6/GJ (USD12/GJ), including the cost of transporting heat from the tower to the plant, where an allowance is made for 40% reduction in CapEx (incorporating benefits of design for manufacture) and 40% for further advances in efficiency that are expected to be achievable by incorporating additional advances in technology already under development and the advantages of processing in steam.
  - The cost of heat integration (that is the supply of heat to the plant) are significant for scales of order $50MW_{th}$, but fall to only some 5% where the thermal scale becomes sufficiently large (around $450MW_{th}$).
  - The levelised cost of heat with air as the heat transfer media, as is suitable for direct retrofit, was estimated to be AUD37.4/GJ(USD28.8/GJ) based on current manufacturing costs in Australia. A reduction in these costs to below AUD26/GJ (USD20/GJ), based on the scenario of a 20% improvement in performance and a 20% reduction in CapEx, seems readily achievable given the wide range of other CST technologies that are under development that are applicable to air heating.
  - The amount of heat that can be provided to a retrofit without a redesign of the plant and using air as the heat transfer fluid, is limited to some 50% owing to the constraints of providing sufficient energy to drive the high temperature reaction and the need to match the velocities through the plant. However, this could be higher for a re-designed process, such as one designed to operate in steam.

- **Potential advantages of operating a calciner in a steam-rich atmosphere:**
  - We have also identified strong potential benefit from modifying the operation of an alumina calciner to operate in a stream-rich atmosphere. This mode of operation is made possible

in net-zero operation because the combustion of a fossil-fuel with air is replaced with an alternative energy source. The use of steam could be particularly attractive for solar thermal energy because steam also has strong radiation absorptivity, as evidenced by the development of a steam-based receiver commercially. Nevertheless, operation in steam is also potentially applicable to electrification or the combustion of hydrogen with oxygen. Importantly, we have provided the first evidence that calcination in steam offers potential to achieve an alumina product with a higher surface area, with slot-shaped pores, than smelter-grade-alumina (SGA) for the same loss on ignition. In addition, this can be achieved with a lower temperature, which offers the potential for a lower energy consumption of the calciner. This benefit is attributed to the role of steam in influencing the phase of the calcined alumina and inhibiting its transformation to alpha, which is undesirable for SGA. Further work is required to understand how such SGA will influence the aluminium smelting process.

  - Calcination in steam also opens the possibility for further benefits by unlocking the potential to recover the steam that is released during calcination process and returning it to the Bayer process. Not only would this recovery of steam reduce water consumption, but it would also achieve an overall energy-saving of some 20%, which would significantly offset the higher costs of a net-zero energy source. Nevertheless, further technology development is required to achieve this, since the steam would need to be pressurised and the fine particles carried in suspension with the steam would need to be removed or otherwise managed. Further work is therefore needed to fully unlock this potential.

- **Further development of the Solar Expanding Vortex Receiver (SEVR) for air heating:**

  - **Selection of this receiver:** The SEVR was selected for development because it was judged to be the technology with greatest potential for retrofit into an existing calciner within minimum risk to the plant, which requires reheating return air from the plant at some 600°C and reheating it to temperatures of above some 1100°C. The receiver was developed from TRL-3 to TRL-4 (based on its application as an air heater) with the work summarised below.

  - **Cold flow experiments and numerical models** were undertaken for both single-phase and two-phase flows to advance understanding and increase upscaling capability. The use of iso-thermal assessments is complementary to hot-testing, owing to the greater ease of measurement access and more complete nature of the data. The experiments included both flow-field measurements of velocity and particle number density and performance measurements of particle egress from small-scale receivers. These were used to provide validation data for CFD models, which were then used for optimisation of the receiver design and facilitate upscaling. Various methods to mitigate particle egress from the receiver were developed, using a combination of optimisation of geometric parameters and flow control, leading to the development and submission of a provisional patent application.

  - **Lab scale demonstration of SEVR**: A high temperature air receiver has been developed and demonstrated that achieves for the first time, to our knowledge, the unique advantages of being able to reheat already warm air (or steam) that has been returned to the receiver from the low temperature (but still relatively hot) thermal storage system to temperatures of >1000°C with estimated efficiencies of greater than 80%. This system uses particles achieve high radiation adsorption through an open aperture and to transfer the heat to the air. The open aperture has the advantage over a transparent window of being mechanically

robust but is also more vulnerable to particle egress and the ingress of cold air. Significant progress has been achieved in mitigating particle egress from the receiver, although further work is required to fully prevent any egress.

Table of Contents

Table of Figures

1. Introduction

Alumina is Australia's biggest value-added mineral export, with an annual production of approximately 18 million tonnes (Australian Government, 2021, David Thurtell, 2021). In 2020, more than $7 billion in revenue for Australia was contributed by its exports, rendering Australia the second largest global exporter (David Thurtell, 2021). The process is energy intensive, requiring heat at both low temperatures (~7 GJ/tonne-alumina), notably in the digestion stage of the Bayer process to extract aluminium-rich minerals from the ore, and at high temperatures (~3 GJ/tonne-alumina) for calcination (i.e. thermal decomposition), currently fuelled with natural gas. Approximately 14 million tonnes of CO_2 is released annually from the alumina refineries, corresponding to 24% of Australia's Scope 1 manufacturing carbon emissions, most of which is derived from the combustion of natural gas to drive the process (The Australian Aluminium Council, 2021). There is therefore good potential for alternative sources of renewable energy, including concentrating solar thermal (CST), to displace the use of natural gas for process heat in Australia as the price of natural gas continues to rise (Lovegrove et al., 2015). Furthermore, this opportunity was identified as being particularly significant for the Bayer refining process used to produce alumina, which is also Australia's largest user of natural gas in the minerals processing sector (Lovegrove et al., 2015).

1.1. The Bayer alumina refining process

The process for production of alumina was invented and patented by Karl Josef Bayer in 1888, whose name it bears. The principles of the process have scarcely changed over the years, although its efficiency and effectiveness continue to improve. The Bayer process coverts bauxite into alumina, which is the feedstock for the subsequent stage of aluminium production that is performed in an electric arc furnace. While the latter stage is more energy intensive than the former, only about 8% of Australia's alumina is converted into aluminium within Australia, with 92% exported as alumina (Armitage, 2013). Hence alumina is a bigger energy consumer in Australia. The key stages of the Bayer process, which are illustrated in Figure 1, are as follows:

- **Grinding:** The raw bauxite is ground to a find powder with a diameter of ~ 100 μm (depending on the raw material and the downstream process).
- **Digestion:** Depending on the composition of the bauxite, the digestion can be undertaken at temperatures of either 180-200 °C or 220-260 °C. In this step the bauxite is dissolved in hot caustic liquor of sodium hydroxide, NaOH, under pressure. This converts the aluminium oxide in the ore to soluble sodium aluminate, $NaAlO_2$, as shown in Eq. 1 and Eq. 2:

Gibbsite: $Al(OH)_{3(s)} + NaOH_{(l)} \rightarrow 2\ NaAl(OH)_{4(l)}$ **Eq. 1**

Boehmite and Diaspore: $AlO(OH)_{(s)} + NaOH_{(l)} + H_2O_{(l)} \rightarrow NaAl(OH)_{4(l)}$ **Eq. 2**

- **Clarification:** The impurities are then removed in several stages. The liquor is first cooled, following which flocculants are added to remove some of the impurities by gravity separation. Further impurities are then removed by filtration. The residue is termed "red mud", while the product stream of sodium aluminate solution is transferred to the precipitation step.
- **Precipitation:** The solution is further cooled to form a supersaturated solution where crystals grown by agglomeration, which is alumina tri-hydrate, $Al(OH)_3$

- **Calcination:** The alumina tri-hydrate is then heated to temperatures of ~1000°C, to thermally decompose it to aluminium oxide, a highly endothermic reaction that releases water vapour as per the following equation:

$$2\ Al(OH)_{3(s)} \rightarrow Al_2O_{3(s)} + 3\ H_2O_{(g)}$$

The calcination was traditionally performed in rotary kilns, although these have mostly been replaced by either fluidised bed or "flash" calciners. For the latter process, which is employed by the industry partner, the material is processed as a powder of diameter ~100μm and conveyed in high temperature air at velocities of ~20m/s, at which conditions the powder remains in suspension. The calcination process is complex, with several phases of alumina being possible, and the final product requiring a high degree of conversion (see Section 5.2.1 for more details). The quality of the fuel is also important, so that natural gas is mostly the fuel of choice since it yields the lowest impact on product quality.

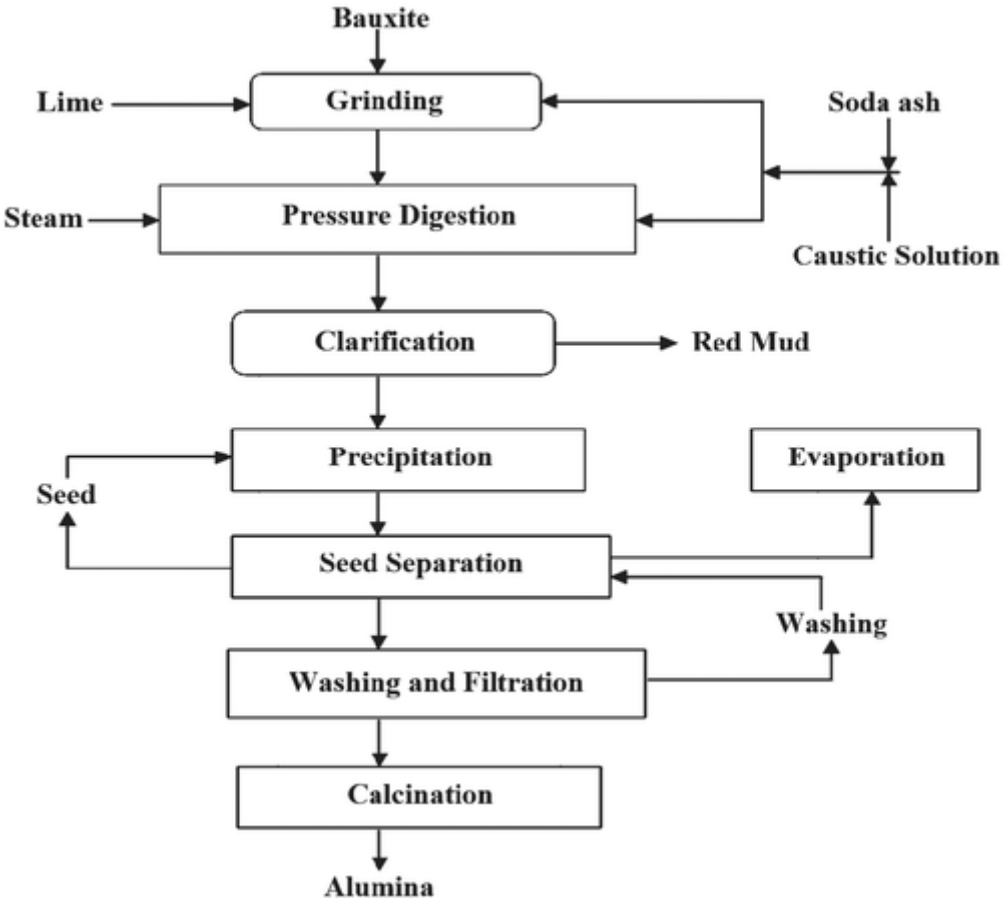

Figure 1: Block flow diagram of the Bayer process (Process Flow sheets, 2012).

1.2. Drivers for introducing CST into alumina production

Of the range of thermochemical industrial processes being undertaken in Australia, alumina is an ideal target for application of both low temperature and high temperature process heat with CST, for the following reasons.

1. The Bayer process is the largest user of natural gas at approximately 160PJ pa and the dominant contributor to Australia's greenhouse gas emissions from the mining and minerals processing sector. In particular:

- it is Australia's largest consumer of low temperature process heat, consuming 80PJ pa at <280°C (Lovegrove et al., 2015). These temperatures are also well suited to commercially available CST solar trough, linear Fresnel and tower technologies (Lovegrove et al., 2015).
- it is also Australia's largest consumer of high temperature process heat, i.e. >800°C, where it also consumes >80PJ pa (Lovegrove et al., 2015).

2. While the temperature of the calcination step within the Bayer refining (~1000°C) is well above the temperatures that can be supplied with commercially available CST technology, it is nevertheless comparable with a number of technologies under development at pilot scale, making it technically realistic for processing with CST. Furthermore:

- the temperature of about 1000°C is at the low-end of the range of the major high temperature industrial processes, being comparable with the calcination reactions for nickel, magnesium and lime, but significantly below the 1500°C employed in blast-furnaces and cement kilns (Eglinton et al., 2013). Its temperature is also readily achievable with commercially available solar tower concentrators, which have been demonstrated at smaller scale to achieve up to approximately 1300°C (Z'Graggen et al., 2006);
- it is a relatively high value opportunity for CST because the sensitivity of the alumina product to contamination from the fuel has driven the alumina sector to preferentially select natural gas as the preferred fuel over coal, whose ash would contaminate the product despite being a lower cost. Furthermore, the recent increases in the price of natural gas are making alternatives even more viable and also make the cost of fuel a major contributor to the economics of alumina production. These points provide a strong incentive to consider the introduction of alternative energy sources, such as CST.

3. Since the start of the present project, a growing number of both national and international commitments has driven many companies, including those of the present project, to sign up to commitments to transition their high temperature process to net-zero CO_2 emissions by 2050. Furthermore, the introduction of new markets with a premium for low-carbon products is incentivising companies to seek to be early movers in accessing these markets. Since CST is a renewable energy source, this makes it an important potential contributor to meet this need:

1.3. Direct irradiation of particles to heat air for the calcination process

The project advances two alternative potential approaches to employ CST for alumina calcination, both of which involve heating particles in a suspension of gas, together with two potential locations of the solar receiver. The first of the general approaches is the direct heating of the alumina particles with concentrated solar radiation, while the latter heats the alumina indirectly with hot air which, in turn, is heated with the solar resource. The direct approach requires transporting the alumina particles to a solar tower for heating within the solar receiver itself, building on the concepts pioneered by Professor Aldo Steinfeld at ETH Zurich (Z'Graggen et al. 2006), the German Aerospace (DLR) and others (Siegel et al. 2010). However, the receiver can either be mounted on top of the tower (the 'beam up' configuration), or below the tower, in which case an additional mirror is placed on top of the tower to focus the radiation below it (the 'beam-down' configuration). Each of these has potential advantages and disadvantages. On the one hand, it is much easier to process material on the ground, while on the other, it is more optically efficient to mount

the receiver on top of the tower. Insufficient information is available to determine which of these potential options is preferred apriori, making it necessary to model both options.

The indirect approach uses inert particles suspended in air within the solar receiver, since the particles are much stronger radiation adsorber than the air, following which the particles are separated from air, which is then transported to the plant. (As above, the receiver can potentially also be either mounted on the tower or on the ground below the receiver). This indirect process was developed using the University of Adelaide's patented windowless Solar Expanding Vortex Reactor (SEVR), building on Professor Steinfeld's previous work on the windowed Solar Vortex Receiver, which we also employed to evaluate the direct approach. The vortex receiver is well suited to achieving the requisite temperatures, having previously been demonstrated at lab scale to heat particles in suspension to temperatures of >1300°C. The SEVR is employs as an air heater to harness the direct heat transfer to particles. This is known to be the most efficient form of heat transfer in solar receivers, because it avoids the exergetic losses associated with heating a fluid through tubes, thereby achieving a higher rate of heat transfer.

The SEVR was chosen as the reference solar thermal technology for evaluation for the indirect calcination approach for the following reasons:

1. **It is well suited to re-heating hot air to temperatures > 1000°C:** Not only can the SEVR be configured to heat air to temperatures greater > 1000°C, it is also well suited to re-heat already hot air, which is challenging to do efficiently with devices such as volumetric air receivers (Ho and Iverson, 2014).
2. **It is robust and readily scalable:** The SEVR can be configured to be built with refractory-lined steel in a manner that is closely compatible with a wide range of high temperature reactors, providing confidence that a mechanically robust device is realistic. In this way it avoids the thermal stresses that are inherent in tubular receiver concepts (Ho and Iverson, 2014).
3. **It offers significant potential for further improvement:** Significant improvements have been made in the mitigation of the egress of both particles and hot air from the receiver with a novel buffer. Although the current configurations showed that the buffer can significantly prevent ambient air ingress and both heated air and particle egress from the main chamber, it has not fully eliminated particle egress. It is also not yet known whether complete elimination of particle egress is necessary. In addition, the aerodynamic studies have identify significant opportunities for further improvements.
4. **It enables the techno-economic performance to be estimated for a range of relevant scenarios:** The use of a sensitivity study allows the economic viability to be estimated based on both for configurations of solar air heater that have already been demonstrated at various scales and for performance that would be possible with further developments of high temperature air receivers, either using the SEVR or with other types of receivers under development elsewhere.

The SEVR heats particles in suspension, so that the heat absorbed by the particles is transferred by convection. The SEVR can also be configured to achieve a longer residence time of particles relative to the transporting fluid. The system proposed for this option thus employs the SEVR to heat air, which is then transported to the calciner, while also allowing thermal storage to be incorporated. The proposed option for heating air is retrofittable to the existing calcination process without major modification to the existing plant. This is one important component that will be necessary to mitigate particle egress from the SEVR, which contains an open aperture to achieve efficient adsorption of solar energy. An additional tool to mitigate particle egress will be an aerodynamic shield, details of which will be developed under the proposal. In this way, hot air will be able to be sent to the calcination plant.

a) Developing sub-models of the single-phase flow field

No previous experimental investigations have been performed of the windowless configuration of SEVR, with all previous experimental work being performed for the simpler case of a windowed reactor. The flow through the windowless configuration is more complex, not only because there is greater potential to induce external air flow into the chamber, but also because of the effect of wind. That is, the development of a reliable reactor requires not only new measurements of the flow-field without a window within an ambient environment, but also for the cases with cross flows of various relative speeds and direction. Furthermore, reliable windowless operation also requires development of a passive control intervention technique (i.e., buffer chamber) to optimise the system efficiency by reducing hot air and particle egress and cold air ingress from the secondary aperture. This, in turn, requires new data for various configurations of buffer chamber, with which to assess their effectiveness in mitigating transport through the aperture.

b) Developing sub-models of the two-phase flow field

Computational Fluid Dynamics (CFD) uses numerical analysis to simulate fluid flows, allowing detailed study of solid and gas behaviour in a virtual environment. Despite extensive international research, new experimental data, and development in CFD models are required to reliably predict the transport of particles and heat transfer between suspended particles and the transporting gas phase as a function of particle size in the presence of radiative heating and convective cooling is needed. This is due to high degree of uncertainty in current models in relation to the transport of mass and energy in suspended particle flows at the mass loadings. and physical scale of flash calciners.

c) Developing sub-model of particle thermo-physical-chemical properties

The introduction of indirect heat from a concentrated solar thermal plant to an alumina calciner can potentially be undertaken in a range of alternative configurations and result in a range of alternative gaseous atmospheres in which the calcination will occur, thereby influencing reaction temperatures, rates and/or product quality. The introduction of hot air to displace some of the combustion gases will reduce the concentration of combustion gases, including H_2O and CO_2, which would lower the partial pressure of steam in the reactor. On the other hand, it is also possible to use steam as the heat transfer media from the solar field, which would increase the partial pressure of steam in the reactor. Heat can potentially be supplemented with combustion gases, so that a wide range of atmospheres is possible. It is therefore necessary to investigate the influence of the partial pressure of steam on the calcination of alumina.

1.4. Objectives

For the reasons above, the objectives of the project are:

1. To develop and evaluate at least two alternative configurations of SEVR and select at least one with significant potential for large-scale, alumina calcination from TRL-3 (completed) to TRL-5 (completed). The configurations to be considered for more detailed evaluation will be:
   1.1. a single-cavity, single-aperture tower-mounted SEVR;
   1.2. a beam-down configuration of the SEVR, and

Each of the above will be evaluated in windowless operation.

2. To develop the experimentally validated tools needed to reliably design a pilot-scale SEVR to meet the high temperature process heat demand for alumina calcination process, and to reasonably estimate performance at industrial scale;
3. To develop the experimentally validated process models needed to reliably estimate plant performance of an SEVR at industrial scale;
4. To identify the preferred plant layout for integrating CST into an alumina flash calcination plant of up to 10,000 tonnes per day of alumina,
5. To develop a plan for scale-up and testing facility on-sun and for further development toward commercialisation.

1.5. List of publications generated from this project

1. Ingenhoven, P., Lee, L., Saw, W., Rafique, M. M., Potter, D., Nathan, G. J. (2023). Techno-economic assessment from a transient simulation of a concentrated solar thermal plant to deliver high-temperature industrial process heat. Renewable and Sustainable Energy Reviews, 185, 1-17
2. Nathan, G. J., Lee, L., Ingenhoven, P., Tian, Z., Sun, Z., Chinnici, A., Jafarian, M., Ashman, P., Potter, D., Saw, W. (2023). Pathways to the use of concentrated solar heat for high temperature industrial processes. Solar Compass, 5, 100036
3. Smadi, E., Saw, W., Chinnici, A., Dally, B., Nathan, G.J. (2023). Effect of heating rate on the kinetics of gibbsite calcination. Chemical Engineering Science, 268, 118444.
4. Tang, Y., Sun, Z., Tian, Z., Lau, T., Chinnici, A., Saw, W., Nathan, G.J. (2022). Experimental and numerical investigation on the geometric parameters of an open-to-atmosphere vortex-based solar particle receiver. Solar Energy, 243, 315-326.
5. Rafique, M. M., Nathan, G., Saw, W. (2022). Thermal response of multilayered refractory-lined solar receivers to transient operation. Solar Energy, 243, 70-80.
6. Rafique, M. M., Nathan, G., Saw, W. (2022). Modelled annual thermal performance of a 50MW_{th} refractory-lined particle-laden solar receiver operating above 1000°C. Renewable Energy, 197, 1081-1093.
7. Chinnici, A., Davis, D., Lau, T. C. W., Ang, D., Troiano, M., Saw, W. L., Tian, Z.F., Solimene, R., Salatino, P., Nathan, G. J. (2022). Measured global thermal performance of a directly irradiated suspension-flow solar particle receiver with an open aperture. Solar Energy, 231, 185-193.
8. Ang, D., Chinnici, A., Tian, Z. F., Saw, W. L., Nathan, G. J. (2022). Influence of particle loading, Froude and Stokes number on the global thermal performance of a vortex-based solar particle receiver. Renewable Energy, 184, 201-214.
9. Tang, Y., Sun, Z., Tian, Z.F, Lau, T.C.W., Chinnici, A., Saw, W.L., Nathan, G.J., (2022) Direct measurements and prediction of the particle egress from a vortex-based solar cavity receiver with an open aperture, Solar Energy, 105-117
10. Profaiser, A., Saw, W., Nathan, G. J., Ingenhoven, P. (2022). Bottom-Up Estimates of the Cost of Supplying High-Temperature Industrial Process Heat from Intermittent Renewable Electricity and Thermal Energy Storage in Australia. Processes, 10(6), 1070
11. Long, S., Lau, T. C. W., Chinnici, A., Nathan, G. J. (2021). The flow-field within a vortex-based solar cavity receiver with an open aperture. Experimental Thermal and Fluid Science, 123, 110314.
12. Davis D, Troiano M, Chinnici A, Saw WL, Lau T, Solimene R, Salatino P, Nathan GJ., (2020) Particle residence time distributions in a vortex-based solar particle receiver-reactor: An experimental, numerical and theoretical study, Chemical Engineering Science, 115421.

13. Davis D, Troiano M, Chinnici A, Saw WL, Lau T, Solimene R, Salatino P, Nathan GJ., (2019) Particle residence time distributions in a vortex-based solar particle receiver-reactor: The influence of receiver tilt angle, Solar Energy, 126-138.
14. Zhang, X., Nathan, G. J., Tian, Z. F., & Chin, R. C. (2021). The influence of the coefficient of restitution on flow regimes within horizontal particle-laden pipe flows. Physics of Fluids, 33(12), 123318-1-123318-19.
15. Zhang, X., Zonta, F., Tian, Z. F., Nathan, G. J., Chin, R. C., & Soldati, A. (2021). Dynamics of semi- and neutrally-buoyant particles in thermally stratified turbulent channel flow. International Journal of Multiphase Flow, 139, 103595-1-103595-12.
16. Zhang, X., Nathan, G. J., Tian, Z. F., & Chin, R. C. (2021). Flow regimes within horizontal particle-laden pipe flows. International Journal of Multiphase Flow, 143, 1-12.

References

2021. *Supporting a low emissions future in alumina refining* [Online]. Available: https://www.minister.industry.gov.au/ministers/taylor/media-releases/supporting-low-emissions-future-alumina-refining [Accessed].

AUSTRALIAN GOVERNMENT. 2021. *Resources and energy quarterly: September 2021* [Online]. Available: https://www.industry.gov.au/publications/resources-and-energy-quarterly-september-2021 [Accessed].

DAVID THURTELL. 2021. *Resources and Energy Quarterly September 2021* [Online]. Available: https://www.industry.gov.au/sites/default/files/2022-08/resources-and-energy-quarterly-september-2021.pdf [Accessed].

HO, C. K. & IVERSON, B. D. 2014. Review of high-temperature central receiver designs for concentrating solar power. *Renewable and Sustainable Energy Reviews,* 29**,** 835-846.

LOVEGROVE, K., EDWARDS, S., JACOBSON, N., JORDAN, J., PETERSEIM, J., RUTOWITZ, J., SADDLER, H., WATT, M. & WYDER, J. 2015. RENEWABLE ENERGY OPTIONS FOR AUSTRALIAN INDUSTRIAL GAS USERS. Australian Renewable Energy Agency.

PROCESS FLOW SHEETS. 2012. *Aluminum production process-Bayer & Hall-Héroult* [Online]. Available: http://processflowsheets.blogspot.com/2012/05/aluminum-production-process-bayer-hall.html [Accessed].

SIEGEL, N. P., HO, C. K., KHALSA, S. S., & KOLB, G. J. Development and Evaluation of a Prototype Solid Particle Receiver: On-Sun Testing and Model Validation. *Journal of Solar Energy Engineering-Transactions of the ASME* 2010;132:2.

THE AUSTRALIAN ALUMINIUM COUNCIL. *Sustainability* [Online]. Available: https://aluminium.org.au/sustainability/ [Accessed].

Z'GRAGGEN, A., HAUETER, P., TROMMER, D., ROMERO, M., DE JESUS, J. C., & STEINFELD, A., Hydrogen production by steam-gasification of petroleum coke using concentrated solar power—II Reactor design, testing, and modeling. *Int. J. Hydrogen Energy*, 2006, 31, 797–811.

2. Development of Solar Expanding Vortex Receiver (SEVR)

2.1. Flow and scalar fields for single-phase and two-phase flow fields under iso-thermal conditions

2.1.1. Developing sub-models of the single-phase flow field

The project selected a high temperature gas (air or steam) as the preferred heat transfer media, which to transfer thermal energy from the solar energy to the plant, on the basis that these are the media that are already used in commercial alumina processes. On these bases, technology assessments also identified the need for a high temperature solar receiver suitable for heating either air or steam to temperatures of order 1000°C, since no suitable ones were available at pilot-scale at the start of the project. This technology is referred to as the Solar Expanding Vortex Receiver (SEVR). In the meantime, a commercial supplier of a solar steam receiver has been identified, with whom a partnership has been established.

Windowless configurations of the SEVR at 50-150MW_{th} scale have been developed and evaluated in this project. Since insufficient measured data of the flow in and around these devices was available before the project, we have performed these for both single-phase and two-phase environments. These data are needed for model development and validation, together with optimisation, all of which are needed for the scale-up processes. These processes were performed with a wide range of experimental and numerical methods, spanning those that evaluate the overall performance of the reactor, both alone and coupled to the system, through to detailed measurements of the flow-field, internal and external, using laser diagnostics and numerical models using Computational Fluid Dynamics (CFD), techno-economic models of the technologies integrated within an alumina process were also performed.

2.1.1.1. Methodology

A laboratory-scale Solar Expanding-Vortex Receiver/Rector (SEVR) was designed, commissioned and built at the University of Adelaide. The device features two tangential particle/fluid inlets (positioned at the opposite end to the aperture) to generate a vortex flow within the device, a conical/cylindrical body with a windowed opening and one radial outlet section as shown in Figure 2. The device was made of acrylic to allow optical access and, hence, laser-based diagnostic (Particle Image Velocimetry, PIV) to be performed. The device is flanged and consists of four different sections to enable systematic investigation of the influence of the dominant geometrical parameters on the vortex structure. The window covering the aperture can be removed to allow windowless cases to be investigated. Also, the device has been built in such a way that different sealing gas configurations can be easily implemented at the top of the aperture and their performance tested.

The PIV experiments were performed using water as working fluid under isothermal conditions as shown in Figure 3. The entire model was fully submerged in a rectangular water tank to reduce optical distortion. Water was pumped into the tangential inlets from a long round pipe to approach fully developed flow conditions at the receiver inlet. The inlet jet Reynolds number was varied in the range 10500-25000 by varying the total inlet fluid flow rate. The water discharged from the outlets was recirculated back into the water tank, resulting in a closed system. The flow was seeded with hollow glass spheres with a mean

diameter of 10μm and a specific gravity of 1.05. The calculated inlet Stokes number was sufficiently low to enable particles to faithfully follow the fluid flow.

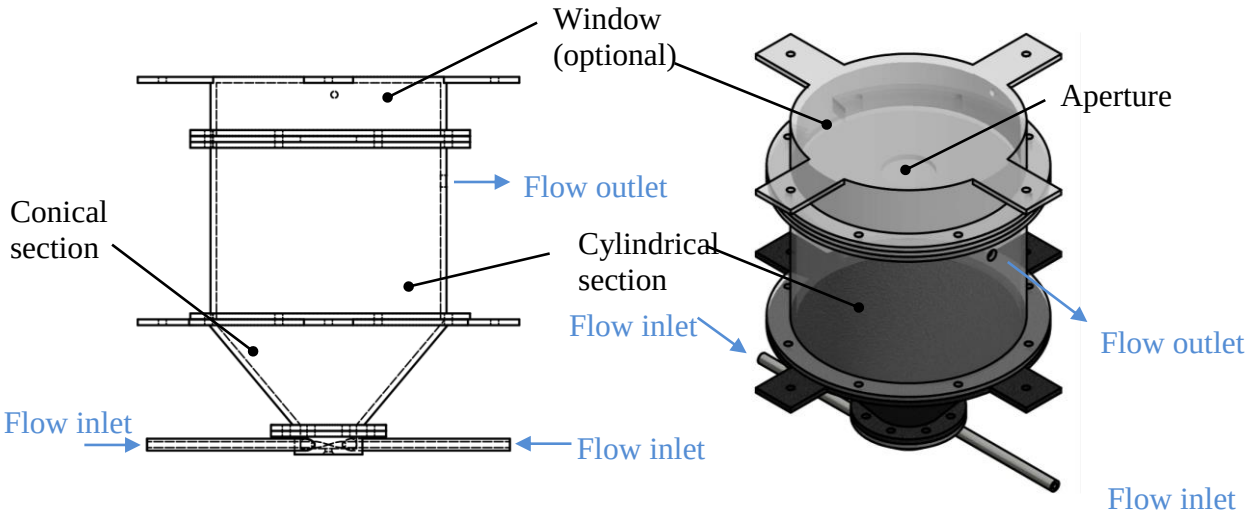

Figure 2: Schematic diagram and isometric view of laboratory-scale Solar Expanding Vortex Reactor (SEVR) model.

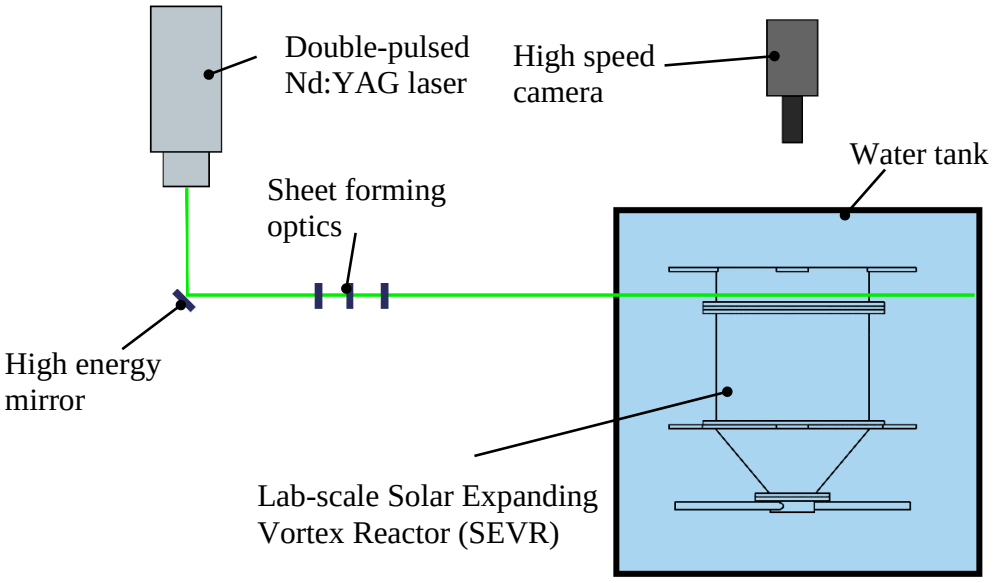

Figure 3: Schematic diagram of the Particle Image Velocimetry (PIV) experimental arrangement.

2.1.1.2. Results

Flow structure within the device for one configuration

Figure 4 presents the axial and tangential velocity profiles within the cavity for one particular configuration. It can be seen that the SEVR generates a well-established vortex structure, which approaches a forced vortex near to the injection plane and a combined one in the main body of the cavity. The device also features a reversed flow in the vortex core region and a low-swirl, low-intensity vortex near the aperture plane. This suggests that the device is able to minimise the flow through the aperture through a modification of the vortex structure along the receiver length.

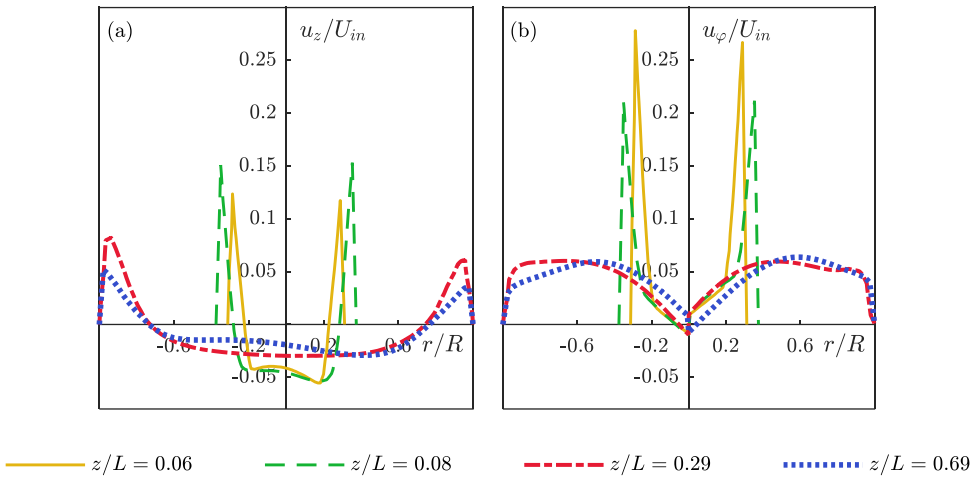

Figure 4: Axial (a) and tangential (b) velocity profiles within one SEVR configuration.

2.1.1.2.1. Influence of Reynolds inlet jet number

Figure 5 presents the influence of the Reynolds jet number (*Re* = 10000-16000) on the vortex structure within the device (tangential velocity profiles), for a fixed inlet flow rate, and by varying the inlet jet diameter (5, 6, 7.5mm). It can be seen that the main features of the vortex structure are preserved by varying the inlet jet diameter (and *Re*). This suggests that the established flow field within the device is flexible to any variation of the input conditions.

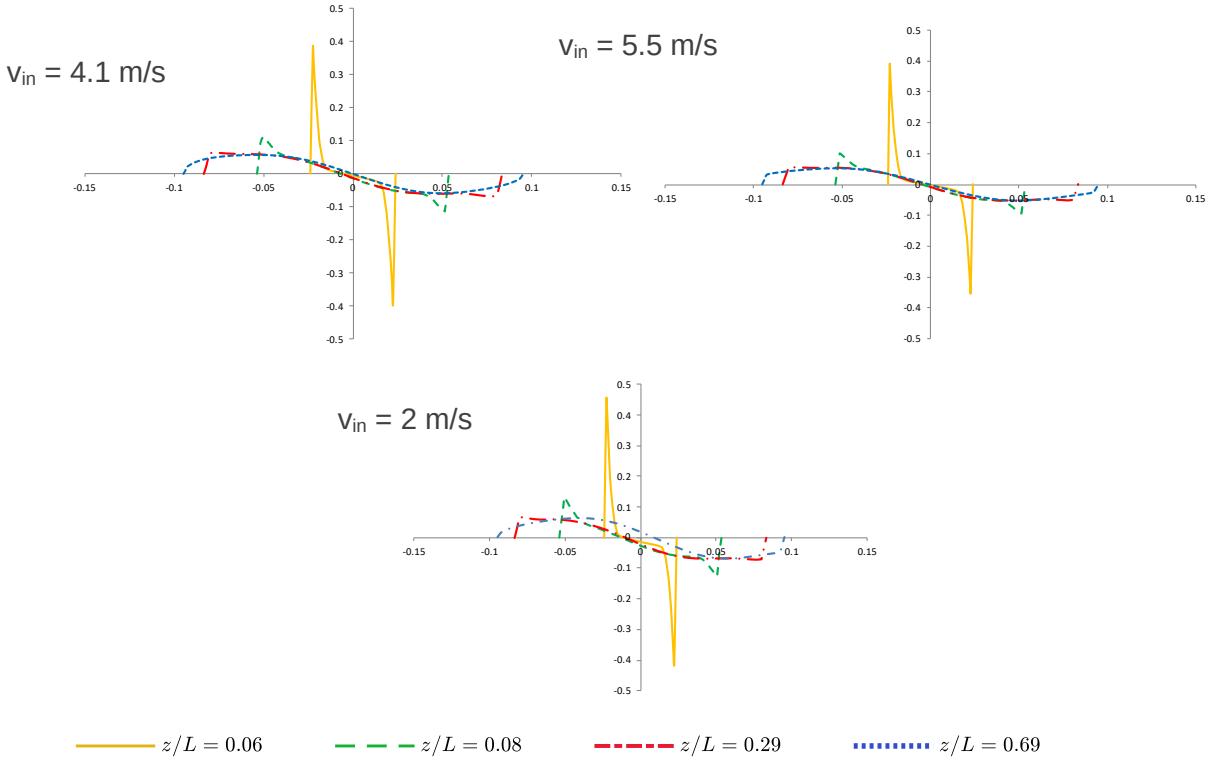

Figure 5: Influence of Reynolds jet number on the tangential profiles within the SEVR.

2.1.1.2.2. Flow through the aperture

Figure 6 presents the measured fluid velocity field in the planes just (≈1mm) below and above the aperture plane for a single SEVR configuration. The results show that in the plane just below the aperture plane, a strong vortex is present within the cylindrical section of the SEVR, as expected. This vortex is the dominant structure within the flow. The maximum flow velocity magnitude is ≈0.39m/s (i.e., $U/u_{in} \approx 0.95$) within this plane. Conversely, in the plane just above the aperture plane, the flow velocities become very low, approximately an order of magnitude lower than in the plane below the aperture. No clear flow structure is present. This implies that the dominant flow structures within the main cylindrical section of the SEVR are affected by the aperture, and that there is only a small proportion of the overall flow that penetrates the aperture plane. This suggests that for the current configuration of the SEVR, the flow through the aperture is small relative to the overall flow within the system.

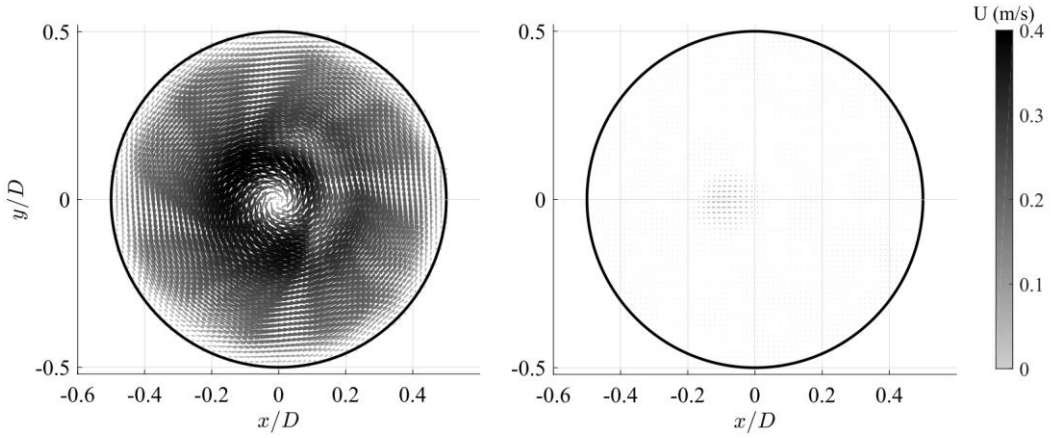

Figure 6: The fluid velocity field ≈1mm below (left) and above (right) the aperture plane measured using PIV. The length and colour of the arrows are proportional to the velocity magnitude. The black solid line refers to the boundary of the cylindrical section of the SEVR.

2.1.1.3. Key outcomes

The single-phase flow field within a laboratory-scale SEVR was characterised under iso-thermal conditions over a range of geometrical and fluid-dynamic input parameters. The key outcomes are as follows:

- For the selected configurations, the flow pattern is characterised by a vortex of strong intensity at the inlet section, which decreases along the receiver length. Also, the flow through the aperture is minimised for these configurations.
- The features of the vortex structure are preserved by varying the inlet jet Reynolds number. This offers enhanced flexibility over previous vortex-based solar devices as it is anticipated that the device will operate dynamically over a wide range of inlet jet Reynolds to accommodate any variation in the solar resource during the day.

2.1.2. Measurement of flow velocity for single-phase flow field

A systematic experimental study to fully characterise the flow-field generated by confined tangential jets within a vortex-based solar cavity receiver, under conditions of relevance to a wide range of industrial Concentrated Solar Thermal (CST) devices, including the Solar Expanding-Vortex Reactor (SEVR), was conducted. In this study, the aperture of a simplified SEVR configuration is configured to be closed or open to represent windowed or windowless CST systems, respectively. A suction system at the SEVR outlet to aerodynamically mitigate the flow egress was also proposed and investigated systematically. Particle image velocimetry was used to investigate the velocity field generated by the SEVR at a fixed inlet Reynolds number of Re_D = 11800.

2.1.2.1. Methodology

The experiment consisted of flow velocity measurements in a laboratory-scale Solar Expanding-Vortex Reactor (SEVR) under isothermal conditions. A schematic diagram of the SEVR investigated in the present study is presented in Figure 7. The geometry of the SEVR is simplified relative to a practical solar reactor

to facilitate understanding and also to increase the relevance to a wide range of solar thermal and vortex devices. The SEVR features a main chamber, consisting of a cylindrical cavity with a conical expansion, two planar-symmetric tangential inlet-pipes and a circular aperture located at the top of the cylindrical cavity. The tangential pipes are distributed around the conical expansion of the main chamber, generating jet flows (total inlet flow rate Q_{in}), to form a large-scale vortex structure within the SEVR configuration. The flow leaves the chamber in the radial direction through an outlet pipe with a diameter of 6 mm. Importantly, the key dimensionless values of the SEVR, such as the chamber length-to-diameter ratios (L_c/D_c = 1.3) and conical expansion angle (α_{cone} = 40°), match that of previous studies to provide complementary velocity data to other measurements that have already been published under similar conditions (Davis et al., 2019, Chinnici et al., 2016). The dimensions of the key geometrical parameters of the SEVR configurations investigated here are summarised in Table 1.

Table 1: Values of the geometric parameters of the SEVR (see Figure 7) in the present study.

Dimensions	Description	
D_c	Chamber Diameter	120 mm
D_{sc}	Diameter of the Secondary Concentrator	120 mm
D_{ap}	Aperture Diameter	45 mm
D_{pipe}	Inlet Pipe Diameter	3 mm
D_{out}	Outlet Pipe Diameter	6 mm
D_{cone}	Conical Diameter	30 mm
L_c	Chamber Length	155 mm
L_{pipe}	Inlet Pipe Length	90 mm
L_{out}	Outlet Pipe Length	30 mm
L_{sc}	Secondary Concentrator Length	30 mm
α_{cone}	Conical Expansion Angle	40°

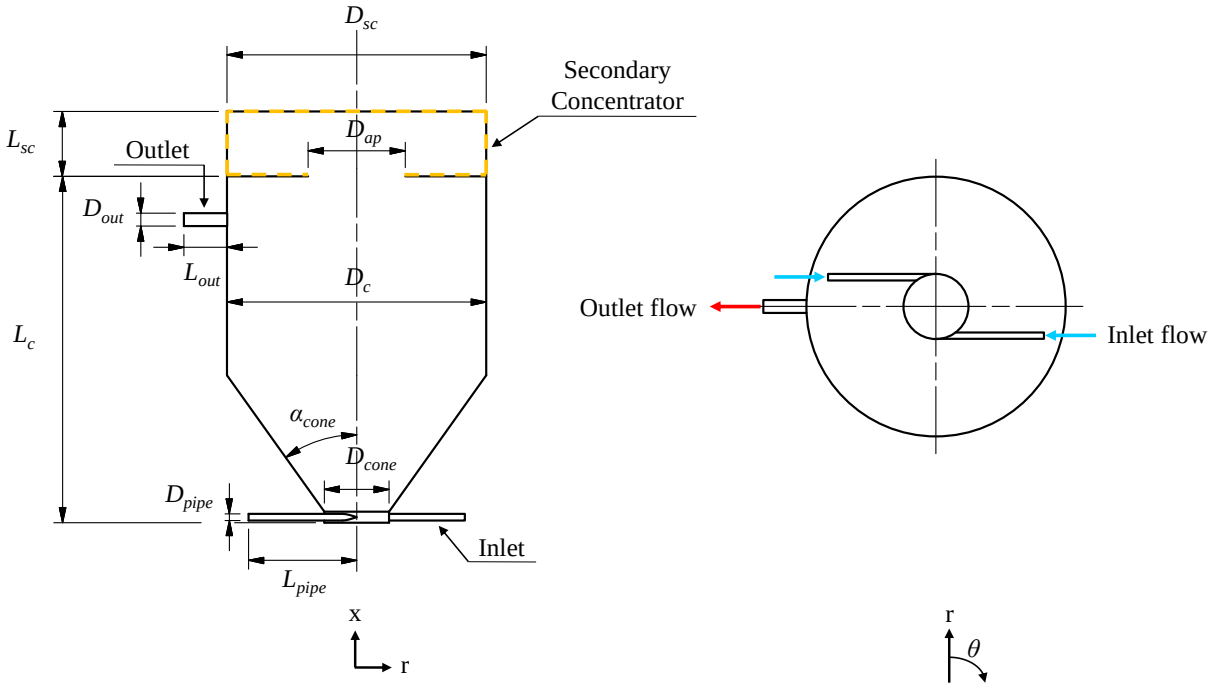

Figure 7: Schematic diagram of the SEVR configuration investigated here, showing the key geometric features from the axial cross section (left) and a radial cross section (right).

For the present study, the SEVR was investigated under both “open” and “closed” configurations to mimic both windowless and windowed systems, respectively. Under the “closed” configuration, a cylindrical body (highlighted as yellow dashed-box in Figure 7) closed at the top-end with a window was used to model the secondary concentrator (SC), such that there is flow between the main cavity and the SC but no flow to the external environment. Under the “open” configuration, the SC is removed, such that the flow can leave the main cavity through both the outlet and the aperture. In this open-aperture configuration, experiments were conducted with (Q_{out} /Q_{in} = 0) and without suction (Q_{out}/Q_{in} > 0) at the outlet.

The experiment consisted of measurements of flow velocity using planar PIV. All measurements were performed under iso-thermal conditions and at ambient temperature (T_{amb} = 25 ˚C). Water was used as the working fluid to avoid deposition of tracer particles onto the cylindrical walls of the device and also to provide a relatively high Reynolds number at low in-flow velocity. The inlet (Q_{in}) and outlet (Q_{out}) flow rates were controlled independently using two pumps equipped with variable speed drives.

The total volume flow rate injected from the two tangential-pipes was fixed at Q_{in} = 3 L/min, leading to a bulk mean velocity at the nozzle exit (U_e) of 3.7 m/s for each inject pipe. The corresponding Reynolds number ($Re_D = \rho_f U_e D_{pipe}/\mu_f Re_D$) for each inject pipe was calculated as 11,800, where ρ_f is the fluid density and μ_f is the fluid dynamic viscosity. This value of Re_D ensured that the inlet flow was in the fully turbulent regime, such that the influence of Re_D is considered to be negligible (Deo et al., 2008). A manifold system, which was generated by a perfectly straight pipe and gently-curved flexible piping, ensured that the overall inlet flow was symmetrical and that a fully developed pipe flow was generated at the exit of the inlet pipe. For the open-suction configuration, the volume flow rate ejected from the outlet was set at either Q_{out} = 2.7, 3.3, 4 and 4.5 L/min, resulting in normalised volume flow rate of Q_{out}/Q_{in} = 0.9, 1.1, 1.3 and 1.5. These four different flow rates were selected to span a sufficient range of suction-rate where Q_{out} is lower and higher than the inflow ($Q_{out} < Q_{in}$ and $Q_{out} > Q_{in}$) and to cover realistic operational conditions for CST applications.

Figure 8 presents the optical arrangement and the measurement planes for the SEVR configurations. Light is sourced from a Quantal Brilliant B Nd:YAG laser which has a wavelength of 532 nm, operating at a fixed pulsing frequency of 10 Hz. Three cylindrical lenses were used to form a laser light sheet to illuminate the measurement regions within the SEVR device. The *x-r* plane (see Figure 8), which provides the instantaneous information of axial (u_x) and radial (u_r) velocity components, was 125 mm × 66 mm in size, while the $r - \theta$ plane, which was used to measure the tangential velocity component (u_θ), was 120 mm × 120 mm in size. Due to the distortion caused by both the SC and the conical expansion of the main cavity, the velocity data of the closed-aperture configuration was collected downstream from the aperture plane to the lower edge of the cylindrical cavity ($0.5 \leq x/L_c \leq 1$), while the data of the open-aperture configuration covers both the regions upstream and downstream from the cylindrical cavity ($0.5 \leq x/L_c \leq 1.2$).

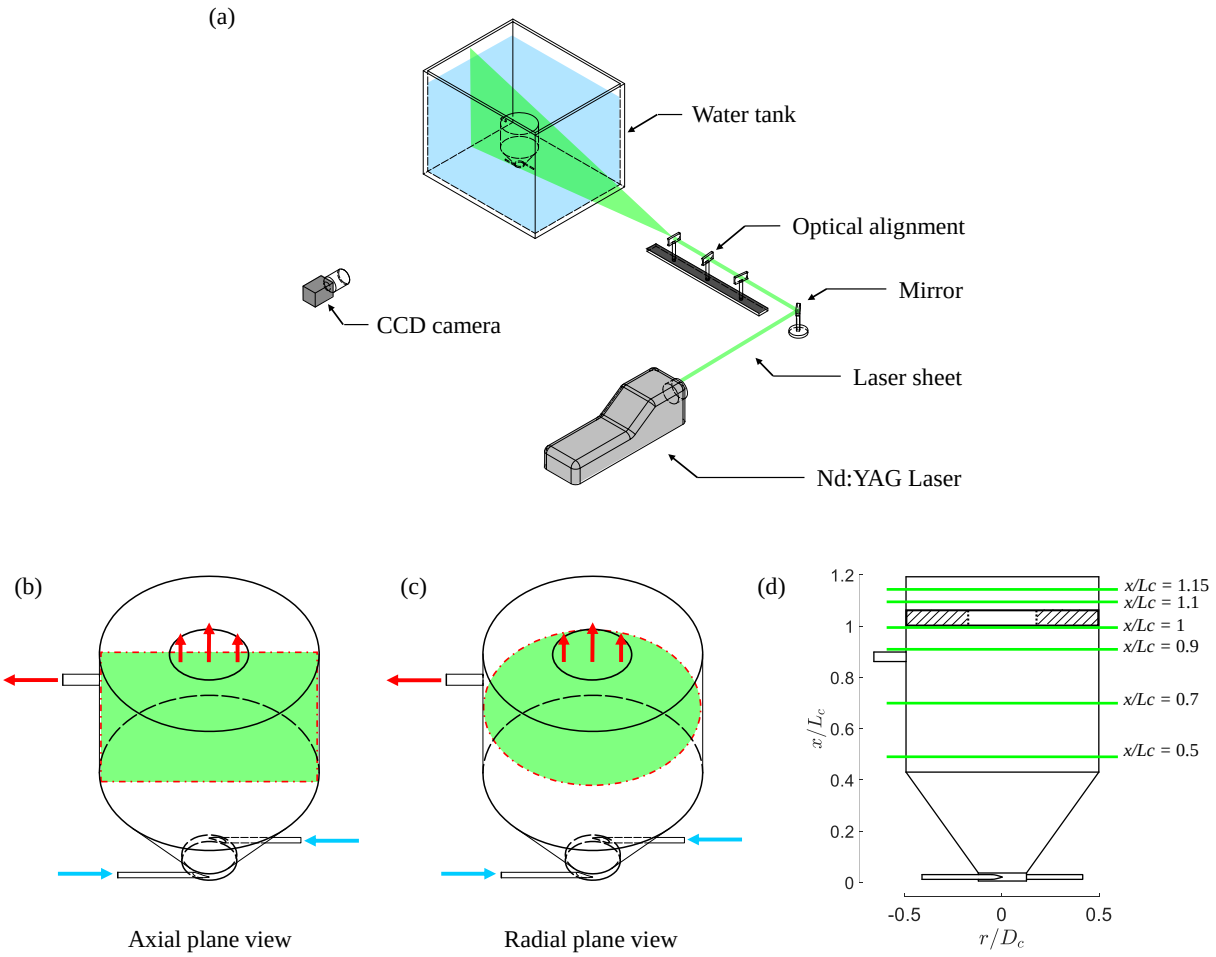

Figure 8:(a) Schematic diagram of the optical arrangement, showing the laser, optics, light sheet and the SEVR configuration, (b) the axial measurement region, (c) the radial measurement region, and (d) the exact measurement locations.

2.1.2.2. Results

Figure 9 presents the contours and streamlines of mean axial velocity (U_x) normalized by the nozzle exit velocity (U_e), labelled with arrows to indicate flow direction (black arrows) and colour to denote magnitude for the configurations of (a) closed-aperture, (b) open-aperture without suction $Q_{out}/Q_{in} = 0$, and (c) open-aperture with suction $Q_{out}/Q_{in} = 1.1$. Here *x* and *r* denote the axial and radial locations of the cavity, respectively. A black arrow at the outlet port is used to indicate the case where the suction system is in operation.

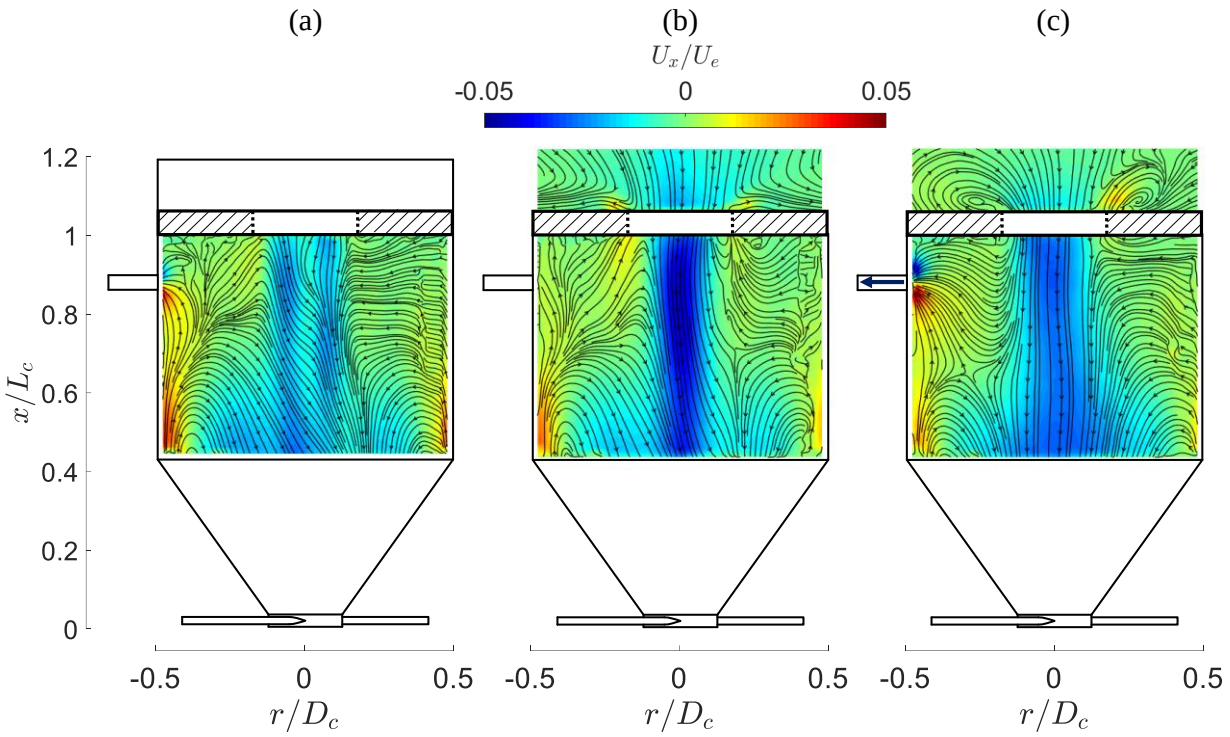

Figure 9: Measured mean axial velocity (U_x) normalized by the nozzle exit velocity (U_e), labelled with arrows to indicate flow direction (black arrows), and magnitude (colour map) at the axial plane for the configuration of (a) closed-aperture, (b) open-aperture without suction $Q_{out}/Q_{in} = 0$, and (c) open-aperture with suction $Q_{out}/Q_{in} = 1.1$.

As can be seen, the flow field of the three cases show significant qualitative differences. For the closed-aperture case (Figure 9a), the main flow within the cylindrical body consists of a central flow downwards from the Secondary Concentrator (SC) towards the conical section, termed the “central reverse flow”, and an upward flow along the edges from the conical section towards the aperture plane, termed the “peripheral flow”. These upward and downward flows generate a large-scale vortex with inward rotation, termed the central recirculation zone (CRZ), within the cylindrical cavity. This CRZ has been identified as a key flow feature in a range of similar vortex-based reactors (Szegö et al., 2009, Syred, 2006). It can also be seen that the flow leaves the cavity through the single outlet port at x/L_c = 0.85, resulting in an overall flow structure that is non-symmetric, consistent with previous investigations (Chinnici et al., 2017).

For the open-aperture case without suction (Figure 9b), it can be seen that external fluid-flow enters the cavity through the aperture to generate a flow ingress (along axial direction), resulting in a strong central reverse flow from the aperture plane towards the conical section. The magnitude of the central reverse flow is significantly higher than that of the closed-aperture case shown in Figure 9a. Almost all of the flow leaves the cavity through the aperture plane rather than the outlet pipe. The lack of flow leaving through the outlet results in a more symmetrical flow within the cavity relative to that of the closed-aperture case. The flow leaves the aperture plane primarily near the edge of the aperture ($|r/D_c|$ = 0.19), where the tangential flow velocity is expected to be high. Therefore, just above the aperture plane, the egressed flow is expected to be “flung” away from the SEVR primary through centrifugal motion, as evidenced by the radial flow near the aperture edge at ($x/L_c \approx 1.10$).

For the case where suction is applied to the flow outlet, such that Q_{out}/Q_{in} = 1.1 (Figure 9c), it can be seen that there is a strong flow from the cavity towards the outlet, as expected. Importantly, the mean flow egress (upwards flow) at the aperture plane on the same side as the outlet port ($r/D_c \approx -0.19$) has been

completely eliminated, while the flow egress on the opposite side of the outlet port ($r/D_c \approx 0.19$), is approximately the same as the case without suction, leaving the aperture tangentially. A secondary recirculation zone is also generated upstream from the aperture plane ($x/L_c \approx 1.1$) due to the suction effect. Interestingly, the velocity contours also show that the magnitude of central reverse flow also decreases with the application of suction, although the radial extent of this reverse flow region increases. These, taken together, show that the application of suction at the outlet port substantially reduces flow egress through the aperture with potentially only a small increase in flow ingress.

Figure 10 presents the contours of normalised mean tangential velocity (U_θ/U_e), together with velocity vectors denoted with black arrows, at four radial planes $x/L_c = 0.50$, 0.70, 0.90, and 1.15 within the SEVR for both windowed and windowless configurations, the latter with and without suction. The black circle denotes the edge of the SEVR cavity and the white dotted-circle denotes the edge of the aperture**.** A black arrow at the outlet port is used to indicate the case where the suction system is in operation.

For the closed-aperture case and for all planes within the cavity ($x/L_c = 0.50$, 0.70 and 0.90), it can be seen that the magnitude of U_θ is almost independent of the axial distance. A high-velocity region occurs within the range of $-0.19 \leq r/D_c \leq 0.19$, corresponding to the size of the circular aperture, while the value of U_θ tends zero towards the cavity axis. This highlights the sensitivity of the swirl strength (characterised by U_θ) within the SEVR cavity to aperture size. However, the magnitude of U_θ was found to be reduced by 30% within the SC ($x/L_c = 1.15$) for this closed-aperture case, as shown in Figure 10, with the value of U_θ approaching zero towards the regions away from the aperture ($|r/D_c| > 0.19$). Hence, the swirl strength generated by windowed SEVR depends strongly on the size of the aperture.

For the open-aperture case with no suction applied (Figure 10e-h), velocity contours show that the distribution of U_θ is qualitatively similar to that of the closed-aperture case except that the tangential velocities typically have a lower magnitude. This indicates that, all else being equal, the swirl strength is greater for windowed than that for windowless configurations. The contours also show that the radial extent of the region of low-swirl (e.g., $U_\theta/U_e < 0.05$) near the cavity axis increases to approximately $-0.1 \leq r/D_c \leq 0.1$, which is three times as large as that in the closed-aperture case. This is consistent with the axial velocity contours shown in Figure 9b, revealing that a large amount of flow is induced from the outside environment into the main cavity. In addition, it can also be seen that for the location upstream from the aperture ($x/L_c = 1.15$), the magnitude of U_θ reduces to almost zero. This also suggests that the swirling flow tends to diffuse rapidly outside of the main cavity.

The results for the open-aperture with $Q_{out}/Q_{in} = 1.1$ (Figure 10i-l) show that while the overall flow structure and distribution of U_θ remains almost identical to that of the case without suction, the magnitude of velocities are significantly decreased for all axial locations within the cavity ($x/L_c = 0.50$, 0.70 and 0.90). That is, the suction of $Q_{out}/Q_{in} = 1.1$ tends to significantly decrease the swirl strength but not change the qualitative flow features within the SEVR cavity.

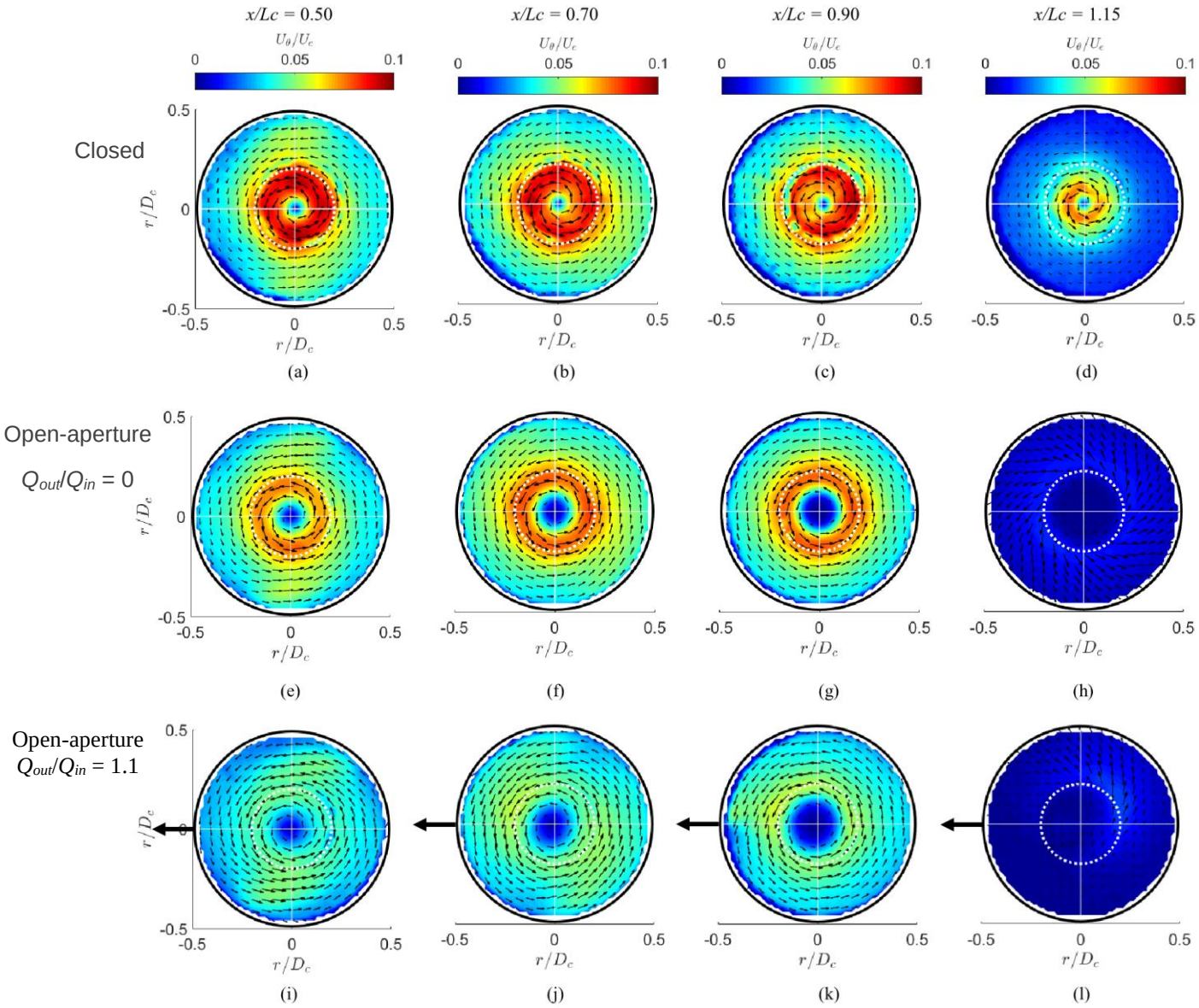

Figure 10: Mean tangential velocity (U_θ) normalized by the nozzle exit velocity (U_e), labelled with arrows to indicate the flow direction (black arrows) and magnitude (color map) at four axial locations x/L_c = 0.50, 0.70, 0.90, and 1.15 within the SEVR for the configuration of (a)-(d) closed-aperture, (e)-(h) open-aperture without suction Q_{out}/Q_{in} = 0, and (i)-(l) open-aperture with suction Q_{out}/Q_{in} = 1.1.

2.1.2.3. Key outcomes

An overview of the resultant flow field within the SEVR for the open-aperture case is shown in Figure 11. Key features of the flow field can be summarised as follows:

- The tangential inlets cause a swirling flow, which propagates upwards within the SEVR body and towards the aperture plane. Just outside of the aperture plane, the swirl dissipates quickly;
- Most of the up-flow (labelled as peripheral flow) within the SEVR occurs at the edges of the cylindrical body (i.e. at the radial extents);
- There is strong downward flow within the core of the primary vortex (central reverse flow), which induces recirculation within the cavity (i.e. the central recirculation zone);

- The strong downward flow extends to outside of the aperture plane, such that most of the flow ingress into the cavity occurs near the centre of the aperture;
- Flow egress out of the aperture occurs right at the edge of the aperture, primarily through tangential motion.

Importantly, the flow field implies that the mechanism of flow ingress (via the centre of the aperture, through axial motion) and flow egress (via the edge of the aperture, through tangential motion), are significantly different such that they may be influenced independently. Additionally, the results presented here also show that suction at the outlet can significantly reduce flow egress, while only causing a small increase in flow ingress. That is, there is a strong potential to reduce or eliminate flow egress with only a small increase in flow ingress through both active (e.g. suction) and passive (e.g. cavity geometry) flow control.

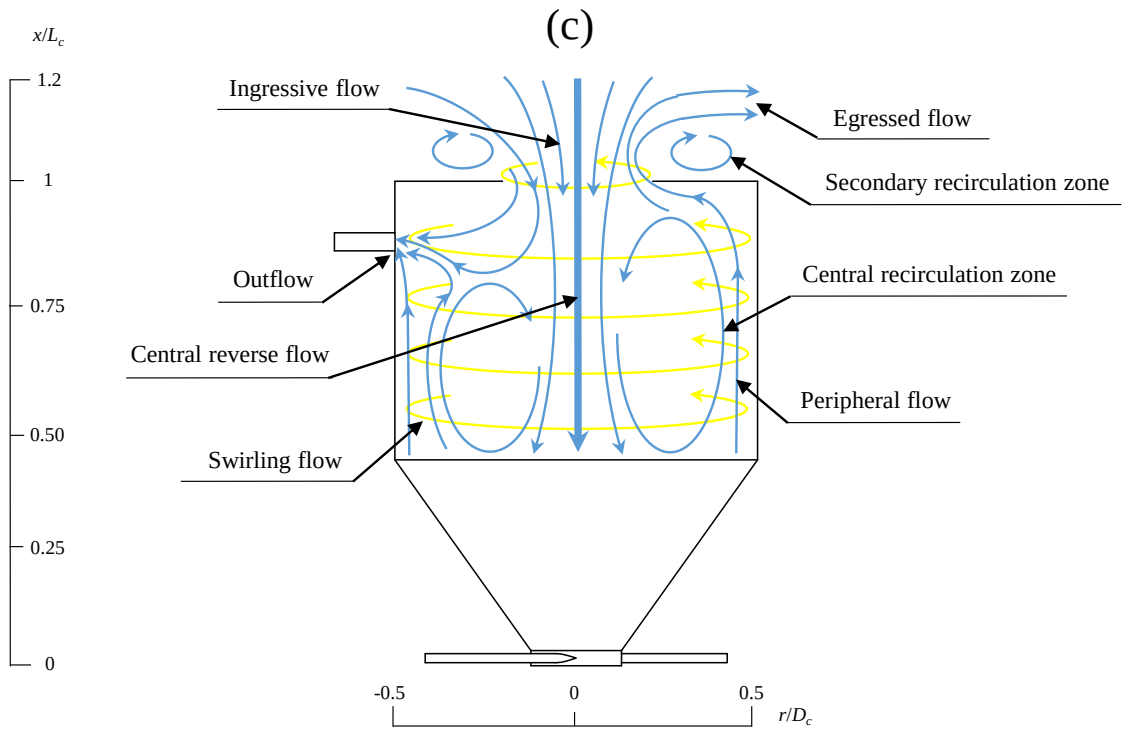

Figure 11: Simplified diagram of the flow field within the open-aperture SEVR.

2.1.3. Fluid concentration measurements of the scalar field of single-phase flow field for the hybrid calciner

A joint experimental and numerical study on the fluid concentration and gas temperatures (i.e., the scalar fields) in a single-phase flow field was developed to understand the fluid exchange between the receiver and the environment together with scalar distributions within a hybrid vortex-receiver under heated conditions. The experimental study employs measurements of gas-phase temperature at the outlet at different inlet air mass flow rates to determine the effects of net air exchange on the thermal performance of the device. While the numerical study assesses the effects on the rate of net fluid exchange to understand planar fluid concentration and temperature distribution within the device.

2.1.3.1. Methodology

Figure 12 presents a schematic diagram of the experimental setup. Ambient air was introduced into the receiver from two tangential inlets, while output radiation from a 1kW$_{th}$ solar simulator was projected into the device to heat up the air. The heated air was measured by a thermocouple located at the outlet. The net mass air exchange was calculated based on the difference of fluid mass flowrate between the outlet ($\dot{m}_{a,o}$) and inlet ($\dot{m}_{a,i}$) section ($\alpha = 100\left[\frac{\dot{m}_{a,o} - \dot{m}_{a,i}}{\dot{m}_{a,i}}\right]$), noting that the difference between the outlet and inlet flow rates is the air flow rate through the aperture. For α>0, there is a net flow ingress into the receiver, while for α<0, there is a net flow egress. For the numerical study, computational fluid dynamics (CFD) was employed under identical conditions to the experiment. Details of the systematic study are shown in Table 2.

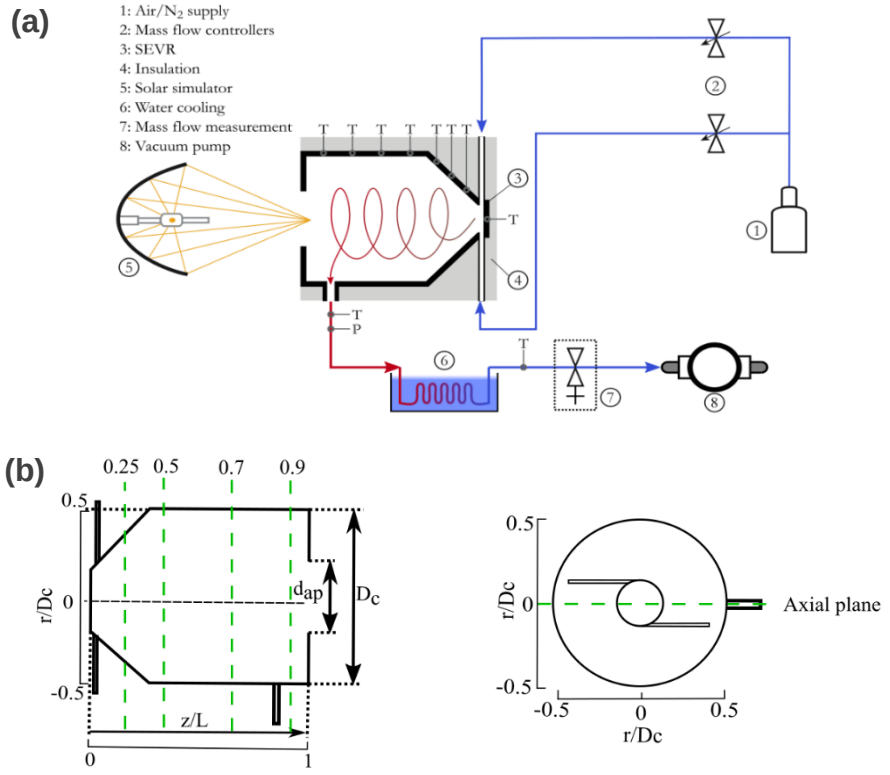

Figure 12: (a) Schematic diagram of the experimental arrangement, a vacuum pump was employed at the outlet region to allow suction for the variation of net mass air exchange (b) Cross-sectional cuts along the radial and axial planes of the SEVR.

Table 2: List of key geometrical and operating parameters specified for the experimental and numerical study.

Key geometrical parameters		
D_c [mm]	190	
d_{ap} [mm]	100	
L [mm]	240	
Key operating parameters	**Experimental**	**Numerical**
Inlet Mass Flowrate [kg/s]	0.0014, 0.0017, 0.0020	0.0014, 0.0027
α [%]	-10, 20, 45	33

2.1.3.2. Results and summary

Figure 13 presents the measured outlet gas temperature of the SEVR as a function of net mass air exchanged through the aperture, α, and the inlet air mass flowrate. An overall trend is observed in Figure 13a, which demonstrates that the outlet temperature decreases as net air exchanged along the aperture is increased, which is as expected as the increase of air exchange introduces more cold air ingress through the aperture. In addition, Figure 13b shows that the increase of inlet mass flowrate leads to a decrease in outlet temperature. This is because the heat flux (i.e., heat input) is constant in the current experiment, and therefore an increase in inlet flow rate results in a decrease in outlet temperature from an energy balance. Overall, it can be seen that the net air exchanged through the device significantly affects the output temperature of the device.

Figure 14 presents both the inlet fluid concentration and temperature distribution within the hybrid vortex receiver. Cross-sectional planar cuts were performed at both radial ($z/L = 0.25,0.5,0.7,0.9$) and axial ($r/Dc = 0$) planes. With comparison to both inlet mass flowrate in Figure 14a, the lower mass flowrate (i.e., 0.0014kg/s) contour plot shows that the fluid concentration is slightly more uniformly distributed across the device, whereas the fluid concentration is slightly less uniform for higher mass flowrate (i.e., 0.0027kg/s). This implies that the lower mass flowrate allows better mixing of the fluid within the SEVR. The reason for this is unclear, however it may be due to the stronger intensity of recirculation dominated by buoyancy effects along the centreline. In contrast, the higher mass flowrate results in the inertial force to be dominant relative to the gravitational force, resulting in a higher fluid concentration at near wall regions. As for the temperature contour shown in Figure 14b, the lower mass flowrate results in a more uniformly distributed temperature within the device due to flow recirculating in the centre, while higher mass flowrate results in a cooler temperature at the centre region as the fluid is more concentrated at the near wall region.

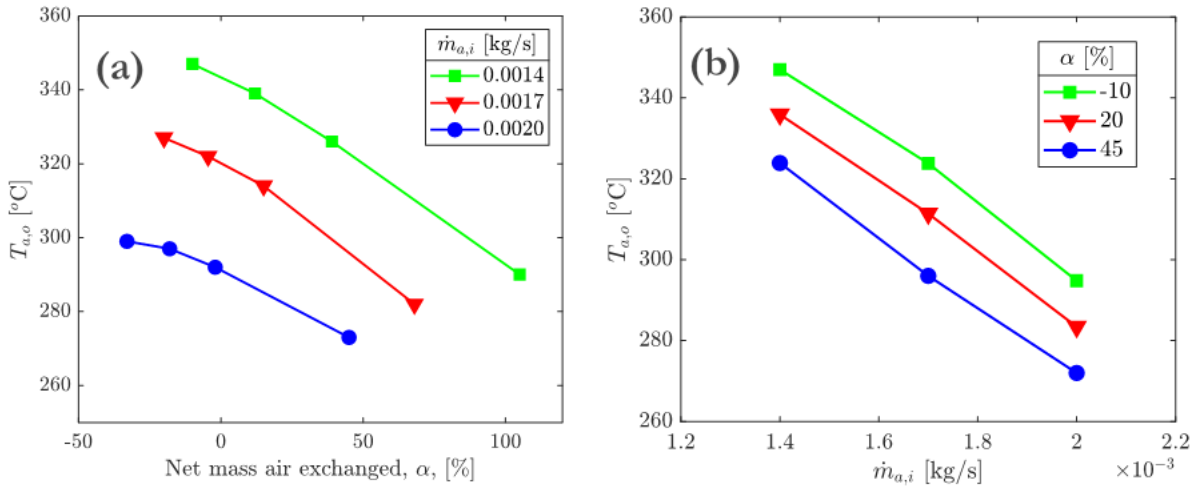

Figure 13: The measured outlet gas temperature of the SEVR as a function of (a) net mass air exchanged through the aperture and, (b) Inlet air mass flowrate.

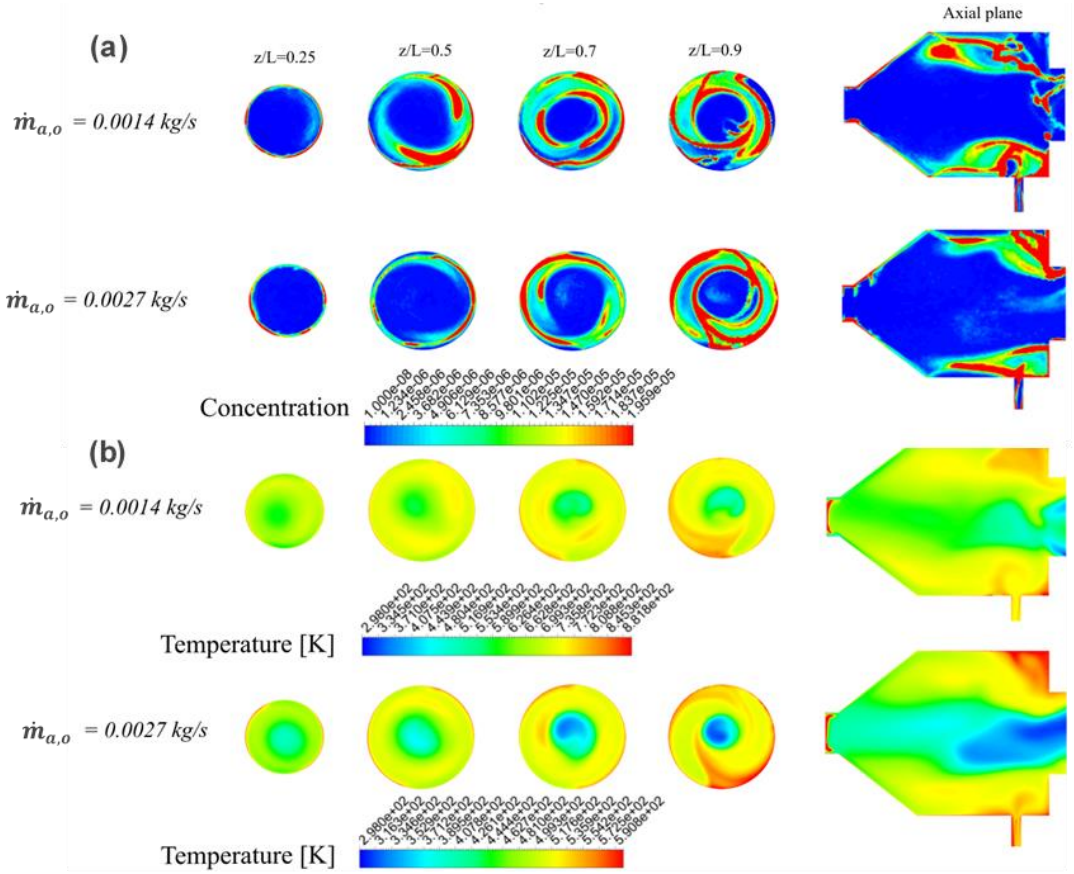

Figure 14: Representative maps estimated for (a) Fluid concentration and, (b) temperature distributions across different radial and axial planes within the SEVR at a fixed net mass air exchange.

2.1.3.3. Key outcomes

- The net flow through the aperture significantly impacts the outlet flow temperature. As the flow ingress increases, the outlet temperature decreases.
- The inlet mass flowrate significantly impacts the concentration and temperature distributions within the SEVR. In particular, lower inlet mass flowrate results in an increased mixing within the flow, and resultantly, a more uniform temperature distribution. For higher inlet mass flowrates, the temperature distributions are less mixed, with the fluid temperatures relatively greater in the near wall region of the SEVR.

2.1.4. Measurements of two-phase flow field under conditions of relevance to a hybrid calciner:

2.1.4.1. Measurements of gas-phase velocity, particle phase velocity and particle number density

A new laser-based diagnosing method for simultaneous, planar measurement of particle and gas velocities was developed to understand the complex interactions between particles and fluid in a range of particle-laden flows relevant to industrial systems, such as those within solar vortex reactors. The technique employs simultaneous laser-induced fluorescence (LIF) and phosphorescence (LIP) to respectively mark the gas- and particle- phases and allow their simultaneous velocity measurement. The technique discriminates the phases by optically separating the fluorescent and phosphorescent signals from each other and also from the scattering signals, thorough the novel use of optical filters and temporal separation.

A proof-of-concept demonstration was conducted using 250 µm PMMA spherical particles and 4 µm BAM:Eu^{2+} phosphorescent tracers, suspended in a water cuvette. Under 355 nm excitation (3rd harmonic of the Nd:YAG laser), both PMMA fluorescent and BAM:Eu^{2+} phosphorescent signals are shown to be sufficiently strong for imaging with CCD cameras, and sufficiently separable using spectral filters and temporal profiles.

2.1.4.1.1. Methodology

Figure 15 presents a schematic diagram of the experimental setup. PMMA and BAM:Eu^{2+} particles, suspended in water within a cuvette, were excited by a laser sheet at 355 nm from a pulsed Nd:YAG laser (~ 6 ns). The laser-induced signals were spectrally selected using optical filters and collected with two dual-frame CCD cameras typically used for particle image velocimetry (PIV) measurement. Details of the optical imaging system can be found in Table 3. The use of water as the fluid, rather than gas, allows the fluid and particle velocities to be reduced, which in turn allows measurements with a single laser head running at 10 Hz.

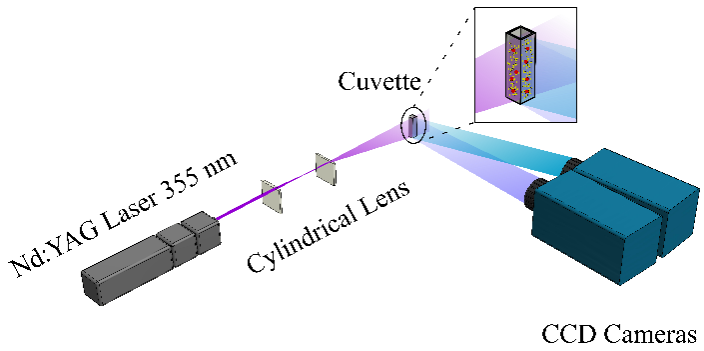

Figure 15: Schematic diagram of the experimental arrangement. The experiment consists of measurements of LIP and LIF from tracers and particles, respectively, within a water cuvette. The source of illumination was a single pulsed Nd:YAG laser operating at 355 nm, while two separate CCD cameras were used to measure LIF and LIP.

Table 3: Imaging arrangement for separately capturing LIP and LIF.

Detection channels	No. 1	No. 2
Objective signals	BAM:Eu^{2+} LIP	PMMA LIF
CCD cameras	PCO. 2000 (1)	PCO. 2000 (2)
Lens	Tamron 70-200 F/2.8	Cerco UV 100 F/2.8
Filters	LP409 Semrock	BP390-18 Semrock
Exposure time (ns)	1000	1000
Delay to laser (ns)	+50	-950

2.1.4.1.2. Results and summary

Figure 16 presents representative images of the flow containing both large PMMA particles and small BAM:Eu^{2+} tracers simultaneously recorded from both cameras. The image on the left represents the temporally delayed (+50ns) LIP signals for BAM:Eu^{2+} tracers, while the image on the right represents the un-delayed LIF signal at a wavelength of around 390 nm for PMMA particles. As can be seen, the signals from both the PMMA particles and BAM:Eu^{2+} tracers can be effectively separated. Since the tracers are sufficiently small such that they can act as fluid tracers, these results demonstrate that the optical

separation technique is capable of allowing separate measurements of particle and fluid velocities through independently applying either particle image velocimetry and/or particle tracking velocimetry to both the tracers and particles.

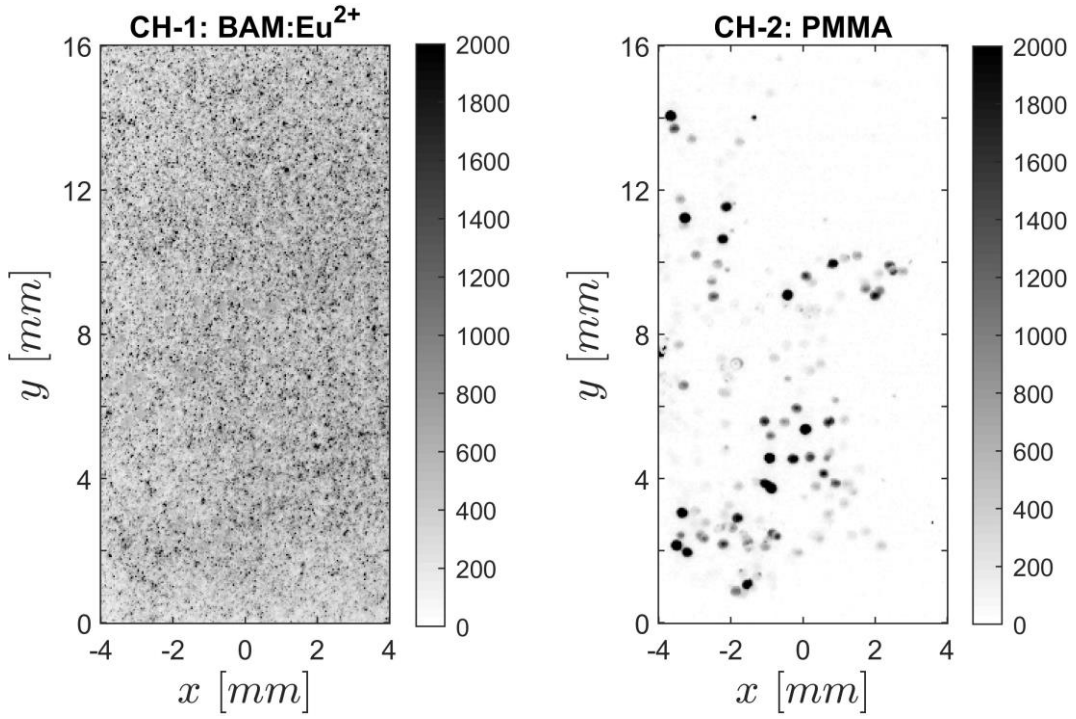

Figure 16: Simultaneous, single-shot images of laser-induced signals of (left) BAM:Eu^{2+} phosphors and (right) PMMA particles. The values of the colour bars present the signal intensities recorded on the CCD cameras.

This technique is directly demonstrated in Figure 17, which presents representative instantaneous images for the velocities of fluid and PMMA particles simultaneously measured in a process of dropping PMMA particles into the cuvette. In particular, the figure demonstrates that the instantaneous velocities of the fluid and particles can be measured separately and reliably, despite both velocity fields appearing to be quite different. This technique is readily applicable to a range of flow conditions and system geometries, including in swirling, turbulent, heavily-seeded particle-laden flows such as those found within solar reactors and industrial systems.

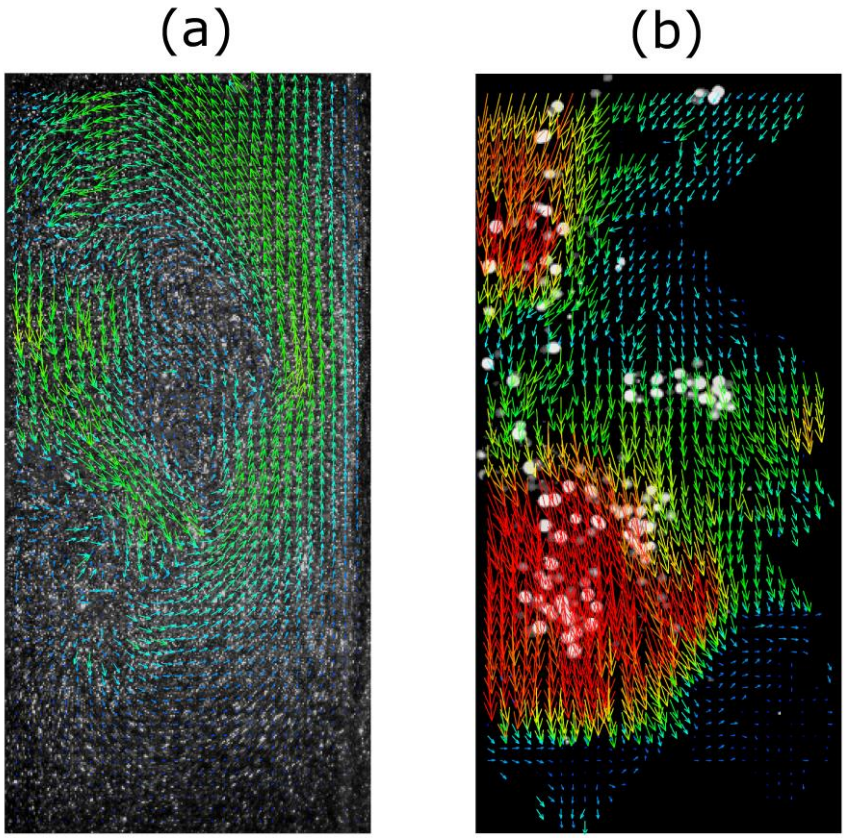

Figure 17: Representative velocity maps simultaneously measured for (a) the fluid and (b) larger PMMA particles in the cuvette. Grey dots in (b): PMMA particles.

2.1.4.2. Measurements of particle temperature and particle number density

Detailed experiments of particle number density and particle temperature have been conducted in a particle-laden flow under the high-flux radiation conditions relevant to solar thermal systems, such as the proposed solar expanding vortex receiver (SEVR). The experiment consisted of measurements in a particle-laden jet flow radiatively heated with a solid state solar thermal simulator (SSSTS) capable of achieving fluxes up to 30.5 MW/m^2 utilising state-of-the-art laser diagnostic techniques. The measurements utilised laser induced phosphor thermometry and direct particle imaging to obtain spatially-resolved, simultaneous measurements of particle temperature and number density under a wide range of radiative heat fluxes. An analytic model of the particle temperature was also developed, taking into account of particle radiation absorption, particle re-radiation, convection between the particle and the gas, together with particle sensible heat gain.

2.1.4.2.1. Methodology

The experiment was conducted on a laminar particle-laden jet issuing from a long, round pipe, as shown in Figure 18. The pipe diameter was D = 12.8mm, while the pipe length-to-diameter ratio was L/D = 39.06. This is sufficiently long to result in a fully-developed laminar pipe flow at the pipe exit for the single-phase case, although the required length for fully-developed two-phase flow is not yet well understood. The pipe was oriented vertically downwards within a vertical wind tunnel with a 300mm × 300mm cross section. The

jet bulk velocity was maintained at U_b =1.7 m/s resulting in a Reynolds number, based on the pipe diameter, of Re_D =1,500.

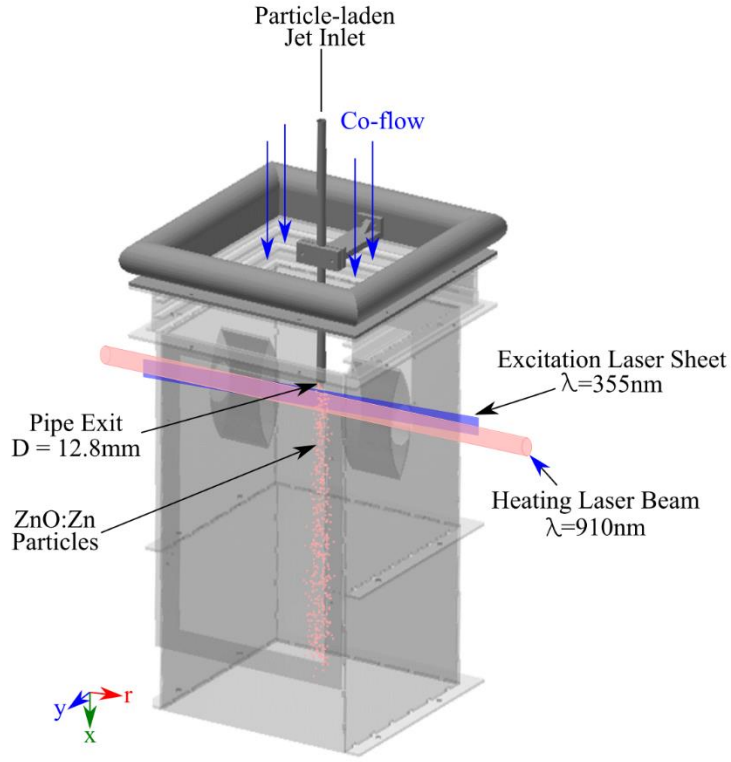

Figure 18: ZnO:Zn particles (red dots) seeded through a 12.8mm diameter round pipe in a 300mm x 300mm wind tunnel. The blue laser path indicates the 355nm Nd:YAG laser excitation, while the red indicates the 910nm SSSTS heating beam.

The particle-laden flow consisted of air and ZnO:Zn thermophosphors (TPs) seeded from a fluidised bed feeder. This TP was chosen due to its high phosphorescence emission signal and temperature sensitivity at operating temperatures below 625°C (Kueh et al., 2017). The particles had a polydisperse size distribution in the ranging from 1µm to 300µm in diameter, with the mass-mean diameter of 240µm.

The third harmonic of a pulsed Nd:YAG laser operated at a wavelength of at λ = 355nm and an energy per pulse of 6.24 ± 0.41mJ (shown in blue in Figure 18) was used to excite the TP particles. The geometry of the laser beam was manipulated with three cylindrical lenses positioned in series to form a 0.3mm (thickness) × 18mm (height) laser sheet. The top of the laser sheet was aligned directly below the pipe exit. The resultant phosphorescent emissions from the excited ZnO:Zn TPs were recorded with an ICCD camera fitted with an image splitter, through a 40mm spacer and an f/2.8 Tamron lens. The image splitter, which has an in-built dichroic mirror that divides the imaging area into two equal 18.2mm × 9.6mm images, was fitted with two high transmission (> 93%) interference filters at 392 ± 9nm and 440 ± 20nm. These filters were chosen for their sensitivity to ZnO:Zn phosphorescent emissions at temperatures below 625°C. A detailed analysis of thermophosphor spectral response, filter selection, and measurement accuracy is provided by Kueh et al. (Kueh et al., 2017). Images of the flow were recorded within the region corresponding to -0.06 ≤ r/D ≤ 0.72 and 0 ≤ x/D ≤ 1.57, where r and x are the radial and axial co-ordinates, respectively.

Particles were heated using a SSSTS operating with a 10.5mm beam diameter (shown in red in Figure 18) and at a wavelength of λ = 910nm. The SSSTS beam was aligned at a 7° angle to the Nd:YAG laser path and placed approximately 6.5mm below the pipe exit, such that the region heated by radiation corresponded to 0.1 ≤ x/D ≤ 0.9. A water-cooled power meter acted as SSSTS beam dump, while also providing in-situ laser power measurements at a sample frequency of 10Hz. Temperatures of the ZnO:Zn particle aggregates and their respective positions were investigated at 13 different heat fluxes in the range 2.1MW/m^2 ≤ $\dot{Q}_{rad}$ ≤ 35.5 MW/m^2. For each flux, 4000 single-shot images were collected over several days to ensure repeatability.

A simple first-order heat transfer model of a single spherical particle subjected to radiative heating at high fluxes was used to estimate particle temperature, T_p, under conditions similar to that of the experimental arrangement. The heat transfer modes taken into account were the radiative heating of the particle, $\dot{Q}_{rad,heat} = \alpha(\pi/4) d_p^{\,2}\, \dot{Q}_{rad}$, convective cooling between the particle and surrounding flow, $\dot{Q}_{conv} = h\pi d_p^{\,2}(T_p - T_a)$, and particle re-radiation to the surroundings, $\dot{Q}_{rad,cool} = \grave{o}\sigma\pi d_p^{\,2}(T_p^{\,4} - T_a^{\,4})$, where α =0.15 is the absorptivity of the particle, h is the convective heat transfer coefficient, T_a is the ambient temperature, ϵ = 0.69 is the particle emissivity and σ =5.67 × 10^{-8} W/(m^{2}K^4) is the Stefan-Boltzmann constant.

2.1.4.2.2. Results

Figure 19 presents the experimentally measured mean particle aggregate temperature, $\bar{T}_{agg}$, averaged over the heating region as a function of the heating flux, $\dot{Q}_{rad}$. Also shown are the results from the analytical for a 240μm diameter particle. It should be noted that the “error-bars” in the figure shows the maximum-minimum range of $\bar{T}_{agg}$ measured over 4000 single-shot measurements and is not indicative of the accuracy of the measurement. From this figure, it can be seen that the measured $\bar{T}_{agg}$ increases approximately linearly with heat flux for $\dot{Q}_{rad}$ < 20.6MW/m^2. Within this range, the measured temperature increases with $\dot{Q}_{rad}$ at a rate that is approximately equal to the rate calculated with the analytical model. However, as $\dot{Q}_{rad}$ is increased above 20.6MW/m^2, the measured value of particle temperature plateaus at approximately 150°C, in contrast to the predictions of the analytical model, which predicts a continuous linear increase within the examined radiative fluxes. This indicates that phenomena other than those accounted for in the analytical model are generated for heat fluxes above approximately 20MW/m^2.

The lower than expected particle temperatures may be due to a combination of increased particle cooling and/or lower particle heating, with the convective heat transfer mode being the most likely for the former because the radiative heat losses from the particles at these temperatures is relatively low. A higher than expected particle cooling rates may be due to the polydisperse size distribution of the particles, which has been theorised to more effectively transfer heat to the surrounding gas compared to monodispersed particles due different sized particles having different preferential concentration at various regions of the flow. This has been deduced to lead to increased heat losses from the particles, a more uniform heating of the gas phase, together with a more uniform gas phase temperature. However, this trend is likely to be independent of heat flux, so does not explain the critical threshold of radiation flux that augments cooling.

In contrast, the role of buoyancy can provide a plausible explanation for the departure. Buoyancy can be expected to augment the convective cooling on a particle by two potential mechanisms. Firstly, any buoyancy-induced lift will increase the local slip velocity, since buoyancy is in the opposite direction of the bulk flow. A second potential mechanism by which buoyancy can increase convective cooling is via the local generation of turbulence around the particle by the high flux radiation, as has been hypothesised from a DNS assessment by Rahmani et al. (Rahmani et al., 2018). Since both of these effects are highly non-linear, we begin by assessing the magnitude of their combined influence on a lumped effective convective heat transfer coefficient, $h_{eff} = h\, k_{corr}$, where k_{corr} is the lumped correction factor. As can be seen, a value of k_{corr} that increases from 1 to approximately 16 as $\dot{Q}_{rad}$ increases from 20MW/m^2 to 35.5MW/m^2 results in calculated values from the analytic model that more closely matches the overall trend of the experimental results. This implies that the combined effects of radiation-induced buoyancy and turbulence generation on particle-fluid heat transfer becomes significant at sufficiently high radiative heat fluxes.

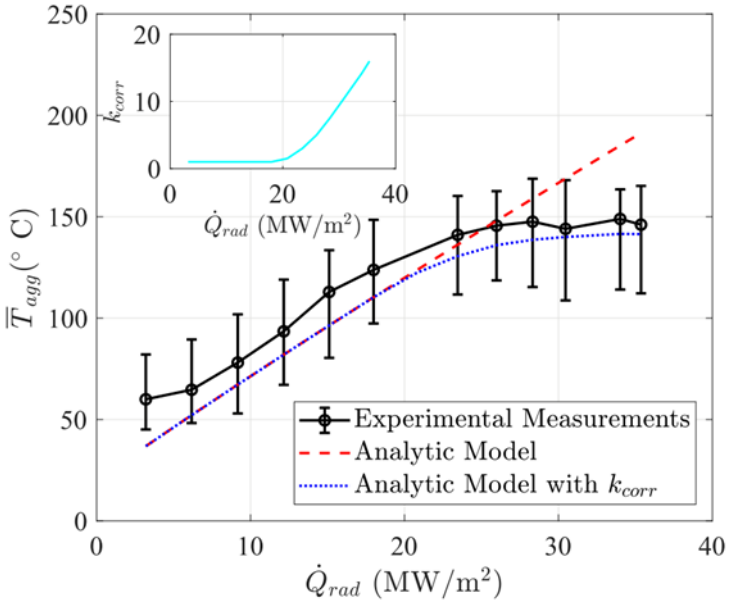

Figure 19: Mean temperature of all particles in all images, T_{agg}, as a function of radiative heat flux. The red dashed line and the blue dotted line shows the theoretical behaviour of particle temperature of a 240µm diameter particle agglomerate calculated from the analytical model without and with the usage of a correction factor, k_{corr}, to modify the effective convective heat transfer coefficient. The inset shows the calculated values of k_{corr}.

Figure 20 presents the radial distributions of (a) particle aggregate temperature, $\overline{T}_{agg}$, and (b) number density relative to the bulk value, Θ/Θ_b, for 4 values of $\dot{Q}_{rad}$. From Figure 20(a), a clear increase in average particle temperature with $\dot{Q}_{rad}$ can be seen for all cases for $\dot{Q}_{rad}$ ≤ 23.5 MW/m^2. However, $\overline{T}_{agg}$ does not increase between 23.5 MW/m^2 ≤ $\dot{Q}_{rad}$ ≤ 30.5 MW/m^2 despite the increasing heat flux. Additionally, a local maximum in $\overline{T}_{agg}$ occurs close to jet edge for all values of $\dot{Q}_{rad}$. This can be partially explained by the radial distribution of particle number density, shown in Figure 20 (b), which also shows a local maxima Θ/Θ_b at r/D ≈ 0.5. A possible explanation for preferential concentration of particles towards the jet edge is the effect of continuity, together with the expectation that the particle velocity profile should approximate a laminar pipe flow velocity profile. That is, particle concentration should increase in regions where the axial velocities are low. In any case, the results show strong correlations between particle number density and

particle temperature. This correlation is attributed to particle-to-particle heat transfer, either direction via inter-particle radiation, or indirectly through convective heating of the local gas. In both mechanisms, heat transfer increases with particle number density.

The results presented in Figure 20(b) also show that the particle number density at r/D ≈ 0.5 decreases as $\dot{Q}_{rad}$ is increased from 6.2MW/m^2 to 23.5MW/m^2, while the particle number density at r/D ≈ 0 increases. This increase in particle number density close to the jet axis also correlated an additional local maximum in $\overline{T}_{agg}$ at r/D ≈ 0 (Figure 20a). The presence of a local maxima of Θ/Θ$_b$ at r/D ≈ 0 indicates a possible particle migration from the jet edge towards the jet axis. This can be partially attributed to thermophoresis, an effect known to cause small particles to migrate towards regions of lower temperatures where large temperature gradients are present (Tsai et al., 2004).

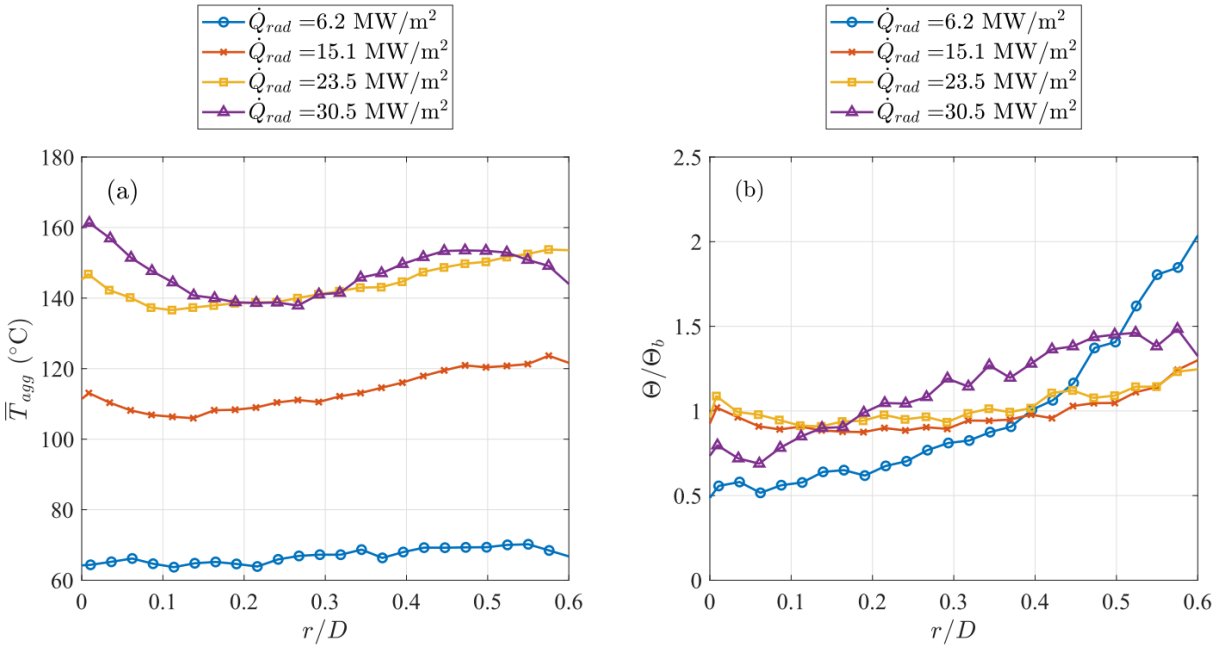

Figure 20: Radial distributions of (a) particle aggregate temperature, T_{agg} and (b) number density relative to the bulk value, Θ/Θ$_b$, at 4 values of radiative heat flux. The radial distributions were obtained from the ensemble encompassing all axial positions within the measurement region.

Figure 21 presents a cartoon of the mechanisms that have been deduced to be induced by the strong radiative heat fluxes within the current particle-laden jet flow. It identifies radiation-induced buoyancy and turbulence generation as the mechanisms deduced to increase large scale recirculation and mixing of the flow and particles. This effect is expected to be particularly significant in regions of low fluid axial velocity, i.e., at r/D → 0.5, where buoyant forces are strong enough to overcome jet velocities and gravitational accelerations to cause upward particle drifts. These particles may be lifted to the zone above and upstream from the heating region, and may eventually return to the original direction of flow when sufficiently cooled, possibly inducing an additional recirculation within the flow. Towards the jet axis, i.e. r/D → 0, the buoyant forces are expected to increase slip velocity, slowing down the particle descent while increasing local turbulence and convective heat transfer. Additionally, regions were observed with high concentration of high particle temperatures. This suggests a possible regional influence of buoyancy-induced lift to a cluster of hot particles, with heat transferred by convection to region of warm gas. This is qualitatively consistent with the DNS results presented by Frankel et al. (Frankel et al., 2016). Taken together, the overall effect

of the increased mixing, turbulence, large-scale recirculation is a more uniform distribution of temperature, and lower peak particle temperatures.

Additionally, the present measurements also provide support for thermophoresis, which in the present case, is expected to result in smaller particles migrating away from the region near the jet edge where the particle temperatures were found to be the highest. These potentially hot particles can be expected to migrate towards the jet axis, or outside of the jet where they may be recirculated back into the jet further upstream. Furthermore, even though the Reynolds number of the particle-laden flow was 1500, making it laminar within the pipe, the jet itself may transition to turbulence downstream. In such case, turbophoretic drifts in the radial direction may occur. Nevertheless, further research is required to confirm these complex mechanisms.

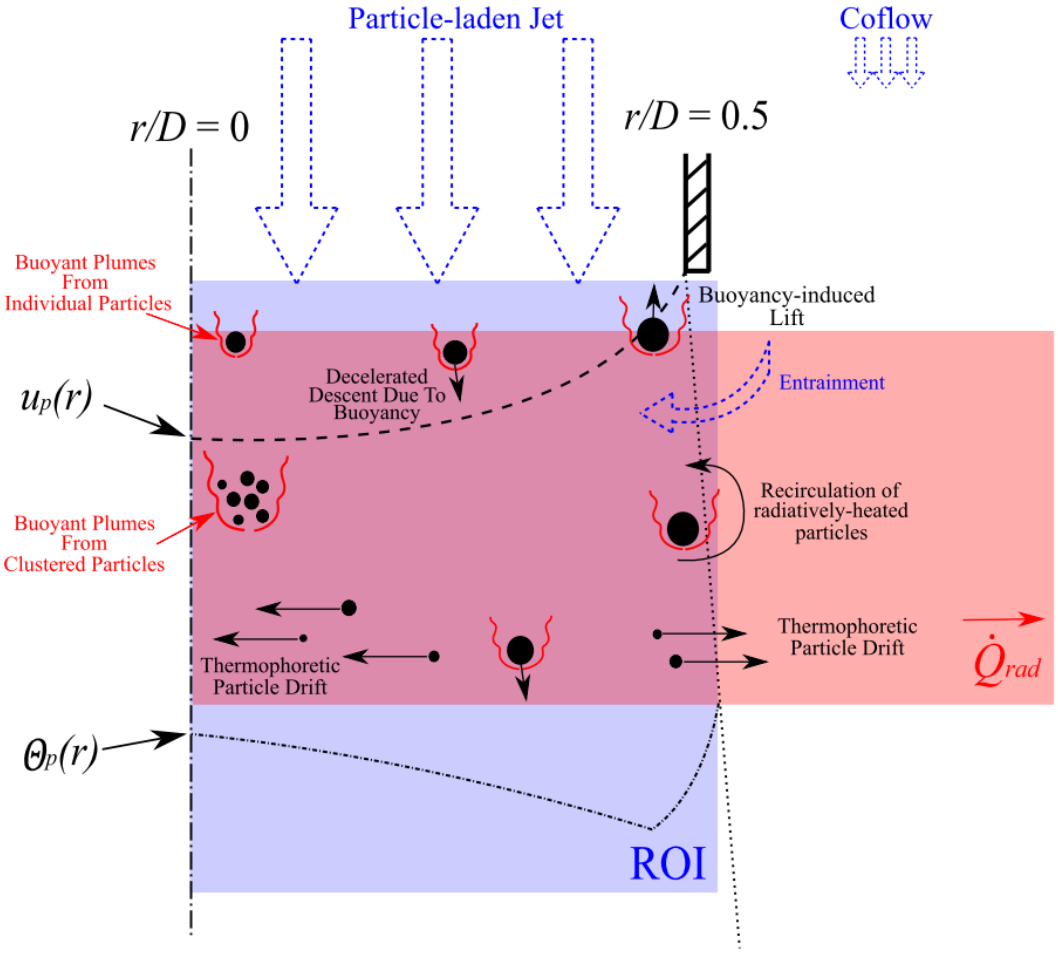

Figure 21: Illustration of the proposed driving mechanisms in a radiatively-heated particle-laden jet flow.

2.1.4.2.3. Key outcomes

Detailed measurements of the particle temperature distribution in a radiatively heated particle-laden jet have revealed that complex mechanisms of radiation-induced buoyancy and turbulence become significant at sufficiently high radiation fluxes. While the measurements show that for radiative heat fluxes below $\dot{Q}_{rad} \leq 20.6 MW/m^2$, particle temperatures, $\overline{T}_{agg}$, increase approximately linearly with heat flux consistent with the trends from an analytical model, for $\dot{Q}_{rad} > 20.6 MW/m^2$, the trends of $\overline{T}_{agg}$ depart

significantly from expectation. It was deduced that for these higher heat fluxes, the convective heat transfer increases, while the particle residence time within the heating region decreases, due to the combined effects of radiation-induced buoyancy and turbulence. Buoyancy was also deduced to result in increased large-scale mixing and recirculation of the flow, such that individual particles or clusters of particles in regions of low average axial velocity can be lifted upstream of the flow, leading to additional complex flow mechanisms. This, in turn, leads to a more uniform temperature distribution within the flow, consistent with the measurement of particles with high $\overline{T}_{agg}$ upstream of the heating region. Additional evidence for the deduced role of buoyancy is the observation that particles attach to the outside of the pipe when, and only when, the fluxes are sufficiently high. These phenomena do not appear to have been observed before, making them worthy of further investigation.

2.2. DNS and RANS tools for two-phase flow field activities

A project has also been undertaken to develop both new understanding of, and improved simplified models for, the flow and the heat transfer processes under conditions of relevance to the vortex particle receiver. Improved models are needed because of the extreme complexity of these heat and mass transport processes, which involve turbulence, radiative heat transfer, two-phase flows and non-linear physics spanning a very wide range of temporal and spatial scales. Also, the volumetric particle loading generates highly non-uniform particle distributions (termed clusters), which are preferentially distributed in regions of high strain and low vorticity. In addition, the mechanisms controlling heating and cooling processes within such devices remain poorly understood. For these reasons, simplified but reliable CFD Reynolds-averaged Navier–Stokes equations (RANS) models are inevitably required for the design and development/optimisation of practical devices, which, in turn, requires detailed and reliable data for the development and refinement of such models. These data are best obtained from a combination of experiments and high-fidelity simulation (DNS)

One of the difficulties identified at the outset is that the existing RANS models are not able to accurately predict particle dispersion in such complex flows, particularly with regard to the effects of particle size and its distribution, together with volumetric particle loading. Understanding each one of these influencing parameters requires detailed knowledge of various physical processes. Each influencing parameter is coupled to the others because these parameters affect the particle behaviour such as preferential distribution, and the particle behaviour affects the local values of these parameters. There is therefore a need to develop more reliable RANS models of particle dispersion under conditions of relevance to the SEVR.

2.2.1. Project Scope

This project has developed an improved particle dispersion model for use in RANS simulations for isothermal, two-phase jet configuration under conditions of relevance to the SEVR. A two-phase jet flow is chosen in the initial stage for its well-controlled conditions and a simplified configuration compared to the actual device. Additionally, data are available of the effect of particle size on particle dispersion for these flows. While some previous work has been undertaken for these flows using DNS and Large eddy simulation (LES) models, no previous numerical works are available that aim to develop improved RANS approaches.

The modified dispersion model was developed, calibrated, and validated against DNS predictions of mean particle statistics in two-phase jets. The new model develops improved prediction of the impact of particle size on average particle dispersion statistics by accounting for Stokes number. These statistics include the rates of spread and decay of both particle velocity and concentration distribution under the influence of various particle sizes. While the limitations imposed by the nature of RANS simulations (Reynolds-average solutions of the flow field) limit the predictions to average particle statistics, rather than instantaneous particle behaviour, this is nevertheless an important advance for industrial prediction.

2.2.2. Project Outcomes

It is found that the new modified particle dispersion model yields improved predictions of mean particle statistics over the existing model for RANS simulations of two-phase jet configurations in comparison with DNS predictions.

- The mean error in the spread and decay of particle velocity in the jet is less than 6%.
- The mean error in the spread and decay of particle number density distribution in the jet is less than 15%.
- The dependence of the controlling coefficients in the modified model on particle size has been identified, enabling reasonable predictions of mean particle statistics under the particle size within a certain application range.
- The model modifications were simplified and easy to implement into the RANS simulations.

In addition, during the development of the new particle dispersion model, other parameters such as the volumetric particle loading, particle polydispersity, etc., were found to affect mean particle statistics significantly. The next step is to verify and assess the validity of the tools in the RANS simulations for vortex particle receivers.

2.2.3. Transferability

Current work is focused on implementing the jet-configuration-based modified particle dispersion model into the RANS simulations for SEVR and assessing the validity of such a modified model for particle predictions in SEVR.

This work provides insights on improving the accuracy of RANS simulations for solid particles in anisotropic flows. It contributes to better modelling engineering processes like combustion, spray, and other types of concentrated solar thermal systems, where such particle-turbulence flows are significant.

The newly developed modifications of the particle dispersion model can be integrated into the commercial CFD tools/existing model for related engineering applications mentioned above.

Further reading

Davis D, Troiano M, Chinnici A, Saw WL, Lau T, Solimene R, Salatino P, Nathan GJ., (2020) Particle residence time distributions in a vortex-based solar particle receiver-reactor: An experimental, numerical and theoretical study, Chemical Engineering Science, 115421.

Davis D, Troiano M, Chinnici A, Saw WL, Lau T, Solimene R, Salatino P, Nathan GJ., (2019) Particle residence time distributions in a vortex-based solar particle receiver-reactor: The influence of receiver tilt angle, Solar Energy, 126-138.

Long, S., Lau, T. C. W., Chinnici, A., & Nathan, G. J. (2021). The flow-field within a vortex-based solar cavity receiver with an open aperture. Experimental Thermal and Fluid Science, 123, 110314.

Tang, Y, Sun, Z, Tian, ZF, Lau, TCW, Chinnici, A, Saw, WL & Nathan, GJ., (2022) Direct measurements and prediction of the particle egress from a vortex-based solar cavity receiver with an open aperture, Solar Energy, 105-117

Zhang, X., Nathan, G. J., Tian, Z. F., & Chin, R. C. (2021). The influence of the coefficient of restitution on flow regimes within horizontal particle-laden pipe flows. Physics of Fluids, 33(12), 123318-1-123318-19.

Zhang, X., Zonta, F., Tian, Z. F., Nathan, G. J., Chin, R. C., & Soldati, A. (2021). Dynamics of semi- and neutrally-buoyant particles in thermally stratified turbulent channel flow. International Journal of Multiphase Flow, 139, 103595-1-103595-12.

Zhang, X., Nathan, G. J., Tian, Z. F., & Chin, R. C. (2021). Flow regimes within horizontal particle-laden pipe flows. International Journal of Multiphase Flow, 143, 1-12.

2.3. References

CHINNICI, A., ARJOMANDI, M., TIAN, Z. & NATHAN, G. 2016. A Novel Solar Expanding-Vortex Particle Reactor: Experimental and Numerical Investigation of the Iso-thermal Flow Field and Particle Deposition. *Solar Energy,* 133**,** 451-464.

CHINNICI, A., XUE, Y., LAU, T. C., ARJOMANDI, M. & NATHAN, G. J. 2017. Experimental and numerical investigation of the flow characteristics within a Solar Expanding-Vortex Particle Receiver-Reactor. *Solar Energy,* 141**,** 25-37.

DAVIS, D., TROIANO, M., CHINNICI, A., SAW, W. L., LAU, T., SOLIMENE, R., SALATINO, P. & NATHAN, G. J. 2019. Particle residence time distributions in a vortex-based solar particle receiver-reactor: The influence of receiver tilt angle. *Solar Energy,* 190**,** 126-138.

DEO, R. C., MI, J. & NATHAN, G. J. 2008. The influence of Reynolds number on a plane jet. *Physics of Fluids (1994-present),* 20**,** 075108.

FRANKEL, A., POURANSARI, H., COLETTI, F. & MANI, A. 2016. Settling of heated particles in homogeneous turbulence. *Journal of fluid mechanics,* 792**,** 869-893.

KUEH, K. C. Y., LAU, T. C. W., NATHAN, G. J. & ALWAHABI, Z. T. 2017. Single-shot planar temperature imaging of radiatively heated fluidized particles. *Optics Express,* 25**,** 28764-28775.

RAHMANI, M., GERACI, G., IACCARINO, G. & MANI, A. 2018. Effects of particle polydispersity on radiative heat transfer in particle-laden turbulent flows. *International Journal of Multiphase Flow,* 104**,** 42-59.

SYRED, N. 2006. A review of oscillation mechanisms and the role of the precessing vortex core (PVC) in swirl combustion systems. *Progress in Energy and Combustion Science,* 32**,** 93-161.

SZEGÖ, G., DALLY, B. & NATHAN, G. 2009. Operational characteristics of a parallel jet MILD combustion burner system. *Combustion and Flame,* 156**,** 429-438.

TSAI, C.-J., LIN, J.-S., AGGARWAL, S. G. & CHEN, D.-R. 2004. Thermophoretic Deposition of Particles in Laminar and Turbulent Tube Flows. *Aerosol science and technology,* 38**,** 131-139.

3. Lab scale demonstration of SEVR

A systematic experimental study of a lab-scale, windowless configuration was performed to characterise the impact of all major variables on its global thermal performance. While previous investigations have identified that the SEVR design greatly reduces the transport of heat and mass through the aperture compared to other suspension-flow particle receivers proposed to date, making it potentially suitable for windowless applications, no data on its performance had previously been available. In addition, the available data on earlier windowed receiver designs was mostly limited to solar thermo-chemical applications, so that there is a lack in understanding on the use of this technology as either air or particle heater. This is also critical because of the complex, non-linear relations between heat transfer and heating requirements (the absorption of radiation scales with the square of the particle size, dp^2, while the mass loading scales with dp^3), and the high centrifugal motion in the device, which generates a variability in particle radial distributions, trajectories, and residence times. Hence, the overall objective of this investigation is to provide an experimental demonstration of the technical feasibility and performance of a laboratory scale, directly irradiated windowless vortex-based particle receiver. Various operational conditions of the SEVR were assessed, this includes looking at the effects of outlet overventilation, inlet flow speed, inlet particle loading and particle size on the wall and outlet temperatures, as well as thermal efficiency of the device. In addition, these experimental campaigns aim to generate useful datasets for the validation of the mathematical and computational fluid dynamics (CFD) model.

3.1. Methodology

3.1.1. Experimental arrangement and operative conditions

The laboratory-scale windowless SEVR and the experimental set-up employed in this study are schematically shown in Figure 22. The device features a stainless-steel (2-mm thick) cylindrical cavity receiver with a conical inlet at the opposite end of the chamber to the aperture, insulated with a 75-mm thick layer of ceramic thermal insulation (60% SiO_2 – 30% Al_2O3 – 10% ZrO_2). It also features two tangential inlets (inlet diameter, d_{in}, of 6mm) to inject particles and compressed air into the device, together with a radial outlet port. Silicon carbide particles (density = 3160 kg/m^3) with a mean particle size, d_p, of 60 μm and a standard deviation ≤ 6% were used in this study. The cavity diameter, D, is 190mm, the length-to-diameter cavity, L/D, ratio is 1.25 and the aperture-to-diameter cavity, d_{ap}/D, ratio is 0.52. For all the experimental tests, the tilt angle was fixed to 0˚ (horizontal position), while the volumetric particle loading, ϕ (defined as the ratio of the particle-to-air volumetric inlet flow rates), and the total inlet mass air flow rate, $\dot{m}_{air,in}$, were varied in the range 0-1.5e^{-4} and 1.3e^{-3}-2.8e^{-3} kg/s (i.e. 70-130 *slpm*), respectively. An electronically controlled screw feeder was used to finely control the particle feeding rate (±1% accuracy).

To allow measurements of the global thermal performance of the device, the air temperature at the inlet and outlet sections ($T_{air,out}$) of the device, together with the inner cavity temperature (T_w) and external wall temperature of the insulation layer were continuously monitored. Both particle and air were injected into the receiver at ambient temperature. An array of 16 K-type thermocouples (acquisition rate = 1 sec, maximum specified error of ±1.5 ºC) was distributed throughout the device and its inlet and outlet sections. The outlet of the device was water-cooled and connected to a suction blower, which allows the use of different levels of suction to control the egress of both particle and air through the aperture. Five levels of suction were tested here, ranging from the minimum up to the maximum suction power of the blower. The

blower also features a bag filter to collect the particles at the outlet section of the device prior to discharge the gas stream. It's worth noting that the use of suction to control particle egress was already successfully implemented in a windowless directly irradiated solar rotary kiln, although it is proposed here for the first time for a two-phase suspension solar receiver-reactor.

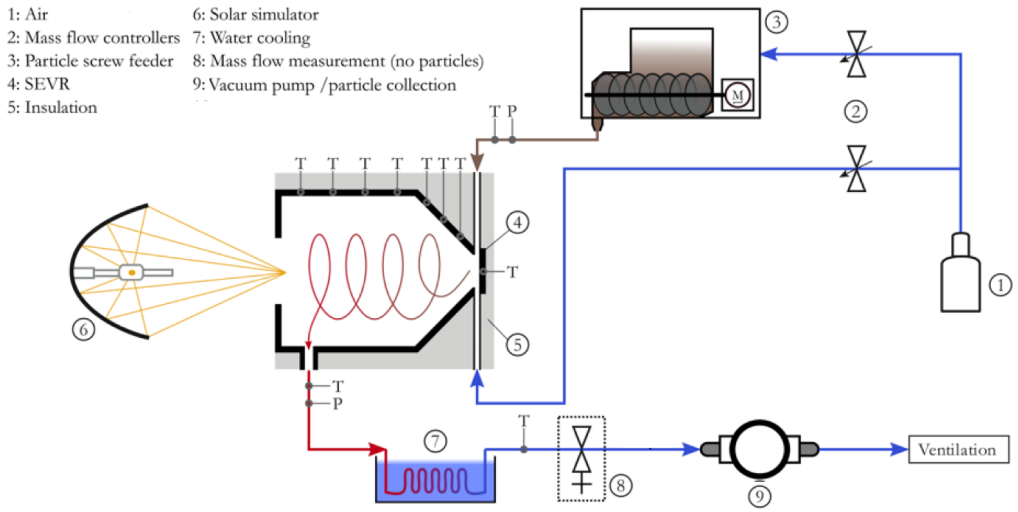

Figure 22: Schematic diagram of experimental set-up of the laboratory-scale windowless SEVR [Chinnici et al. 2022].

Electronic mass flow controllers (ALICAT MCR-series, ±0.2% accuracy) were used to control the inlet flow rate of air while an additional ALICAT mass flow reader was used to measure the total air flow rate at the outlet section of the device, and the net air ingress/egress through the aperture as a function of the suction level. No additional control strategies to mitigate particle egress (e.g. sealing gas systems) were applied here. A 5-kWel short-arc xenon lamp was used as the energy source. The focus from the solar concentrator was aligned with the aperture plane, so the beam diverges into the cavity, following previous studies. With this arrangement, the total simulated solar energy introduced into the receiver, was $\dot{Q}_S$≈1.1 kW. This value is based on the measured heat flux profiles reported previously.

Both single-phase and two-phase flows experiments under cold and hot conditions were carried out in this study. For all tests, quiescent conditions (i.e. no simulated wind) were considered. Single-phase tests were carried out to systematically assess the influence of the suction on the net air ingress/egress through the aperture while iso-thermal two-phase tests were carried out to identify conditions for which particle egress from the device was negligible prior to perform hot tests. For the hot tests, time-averaged temperatures were measured continuously and recorded under steady-state conditions. For two-phase hot tests, particles were injected into the device once steady-state conditions were achieved for the single phase. In the present study, steady-state conditions were assumed when the values of all the measured temperatures were steady to within ±0.5°C/min. The warm-up time of the receiver to reach steady-state operation from a cold state prior to the injection of particles was ≈1.5 h, and each test required additional ≈0.1-0.3 hr. The maximum calculated error in the thermal performance and overall energy balance of the device was estimated to be ±1.2% and ±2%, respectively, based on the uncertainties associated with the mass flow and temperature measurements.

3.1.2. Heat transfer analysis

The influence of the particle/gas flow rates, volumetric particle loading, ϕ, and suction level on the global performance of the device was assessed. The overall thermal efficiency, η_{th}, of the receiver, which accounts for the heat absorbed by both the particle and the air phases, is defined as follows:

$$\eta_{th} = \frac{\dot{Q}_{abs}}{\dot{Q}_s} = \frac{\dot{m}_{air,out}\, c_{p,air}(T_{air,out} - T_{in}) + \dot{m}_{p,out}\, c_{p,p}(T_{p,out} - T_{in})}{\dot{Q}_s + P_{suct}} \qquad \text{Eq. 3}$$

where P_{suct} is the power consumption of the suction blower (which is 3-25% of $\dot{Q}_s$ for the operating conditions considered here, calculated based on $\dot{m}_{air,out}$ and the measured value of the pressure at the outlet section of the device close to the blower, provided by the ALICAT mass flow reader). In Eq. 3, it is assumed that i) the solid and the air phases are in equilibrium when exiting the device (i.e. $T_{air,out} = T_{p,out}$), ii) the mass flow rates of particles at the inlet and outlet sections are equal ($\dot{m}_{p,in} = \dot{m}_{p,out}$), and iii) the measured values of $\dot{m}_{air,out}$ under hot, single-phase conditions (for the different values of suction) do not vary for two-phase conditions. The first assumption is based on previous trends from numerical and experimental studies on vortex-based receivers. The second assumption is justified as only a negligible quantity of particle egress (<1% of the total particle injected) was observed when the device was operated with a net air ingress through the aperture due to suction. The particle egress rate (under iso-thermal conditions) was estimated by collecting and weighing the particles escaping the device through aperture, following a previous work, as well as by weighting the particle collected into the bag filter and/or deposited onto the receiver walls, and comparing these values with $\dot{m}_{p,in}$. The third assumption is justified as the device was operated under relatively small particle loading, so that no or little effects of the solid phase on the fluid behavior is expected (one-way or “early” two-way coupling).

For a given level of suction, the measured value of $\dot{m}_{air,out}$ was found to be constant, regardless of the value of $\dot{m}_{air,in}$ (and regardless if the test was performed under cold or hot conditions), so that the value (in %) of the net air ingress into, or egress from the device ($\alpha = 100 * \frac{\dot{m}_{ex}}{\dot{m}_{air,in}} = 100 * \frac{\dot{m}_{air,out} - \dot{m}_{air,in}}{\dot{m}_{air,in}}$) was characterised for each case, as shown in Figure 23. It is worth noting here that a value of α > and <0 indicate a net air ingress into (over-ventilated conditions), or egress (under-ventilated conditions) from the receiver, respectively.

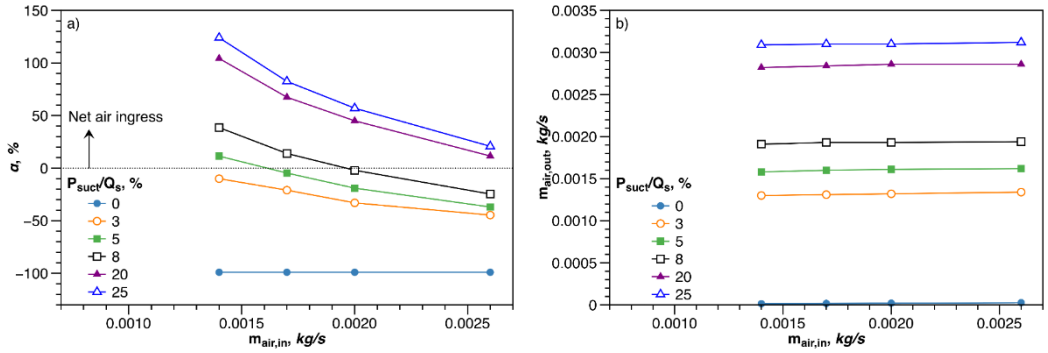

Figure 23: Measured values of a) net air ingress/egress through the aperture, and b) total mass air flow rate at the outlet section of the device as a function of suction level (expressed as % of P_{suct}/Q_s) and different inlet air flow rates, for single-phase (hot conditions) [Chinnici et al. 2022].

3.2. Results

Figure 24a presents the measured axial temperature distributions of the inner receiver wall, T_w, for a fixed value of α and $\dot{m}_{air,in}$, and by varying the volumetric particle loading, ϕ. It can be seen that, for all the cases investigated, the majority of the energy is absorbed near the conical inlet section of the device, at the opposite end to the aperture, so that the maximum T_w occurs at z = 210 mm. This trend is attributed to the particular shape of the beam from the simulator used in this study. It can be also seen that an increase in the particle loading leads to a slight decrease in T_w. This indicates that the total energy transmitted to the cavity walls through radiation and convection are reduced when increasing the particle flow rate. Similar trends were recently observed by others for windowed particle receiver seeded with carbon particles.

Figure 24b presents the measured dependence of the thermal performance, η_{th}, and mean air outlet temperature, $T_{air,out}$, on $\dot{m}_{air,in}$, for a series of values of particle loading, and for a fixed value of α. It can be seen that, either an increase in ϕ for a fixed value of $\dot{m}_{air,in}$, or an increase in $\dot{m}_{air,in}$ for a fixed value of ϕ lead to an increase in η_{th}. This is consistent with expectation because increasing the mass flow rates at a constant energy input will decrease the temperature rise of the two-phase flow by an energy balance. This in turn results in lower thermal losses and, hence, higher efficiency. Similar trends were recently numerically found for windowed vortex-based particle receivers. Overall, values of η_{th} and $T_{air,out}$ of up to 70% and 350°C were measured here.

Figure 24c presents the influence of varying α on both η_{th} and $T_{air,out}$, for different values of ϕ. It can be seen that an increase in the net air ingress into the receiver due to suction has beneficial effects on the performance the device. This js because, similar to the trends reported in Figure 24b, an increase in α (and, hence, $\dot{m}_{air,out}$) leads to a decrease in the temperature rise of the two-phase flow and, hence, lower thermal losses (for a constant energy input and a fixed ϕ).

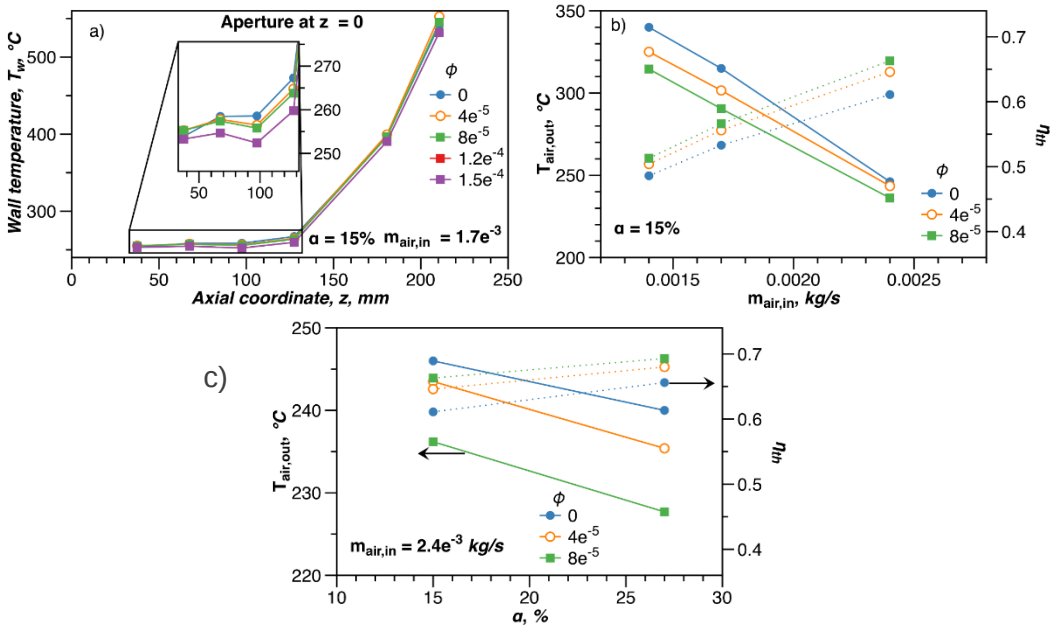

Figure 24: a) Axial distribution of the mean inner surface temperature of the receiver, T_w, for a given inlet air mass flow rate, $m_{air,in}$, and different particle loadings, ϕ, b) thermal efficiency, η_{th}, and mean air outlet temperature, $T_{air,out}$, as a function of $m_{air,in}$ and ϕ, and c) influence of the suction level on η_{th} and $T_{air,out}$ for a given $m_{air,in}$ and different values of ϕ.

Figure 25 presents the measured particle size distribution (PSD) of the particles injected into the SEVR as well as of those deposited onto the receiver walls and collected into the bag filter of the blower, for one particular operating condition ($m_{air,\,in}$ = 1.7e^{-3} kg/s, α =15%, ϕ =8e^{-5}). It can be seen that neither the thermal stress due to the intense simulated solar radiation nor the mechanical stresses (e.g. due to particle-particle and/or particle-wall interactions and suction effects) influence the particle PSD indicating that the particle morphology is not influenced by the different thermo/mechanical phenomena involved here. That is, the particles used in this experimental campaign offers a good mechanical resistance. Scanning electron microscope images (500x magnification) of the particle's samples injected into the SEVR, collected onto the device walls and onto the blower filter confirmed the aforementioned findings (Figure 26).

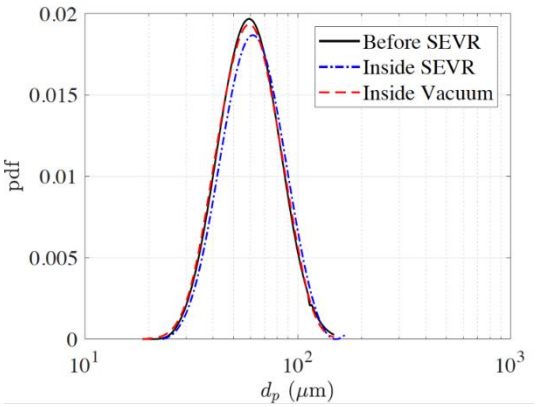

Figure 25: Particle size distribution of the particles injected into the SEVR, collected onto the SEVR inner walls, and onto the blower filter, for one operating conditions [Chinnici et al. 2022].

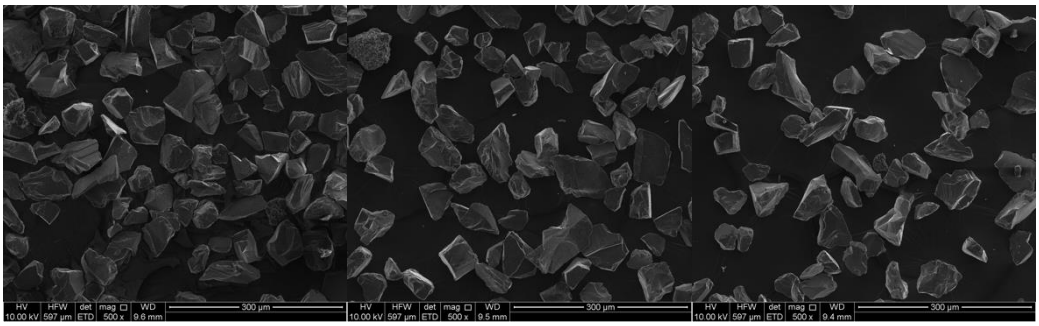

Figure 26: Scanning electron microscope images (500x magnification) of particles injected into the SEVR (left), collected onto the SEVR inner walls (middle), and onto the blower filter (right), for one operating conditions [Chinnici et al. 2022].

3.2.1. Project Outcomes

- A 5-kW SEVR experimental rig was constructed and commissioned with both single-phase (air-only) and two-phase (air with particles) flows under irradiated conditions.
- Successful operation of a directly irradiated windowless suspension-flow solar particle receiver has been reported here, using an outlet-suction strategy to "over-ventilate" by inducing a net inflow through the aperture as means to mitigate particle egress.
- As the inlet flow speed is increased, with other variables fixed, the outlet temperature is reduced. This leads to an increase in the thermal energy captured by the device, while lowering the exergetic efficiency.

- The level overventilation through the aperture has a significant influence on the thermal performance of the SEVR, as expected. From an energy perspective, the amount of air induced through the aperture should be minimised to avoid dilution of fluid temperature at the outlet.
- The mass loading of particles in the SEVR also influences performance. An increase in the particle loading leads to higher thermal efficiencies than that of the single-phase counterpart, owing to the higher adsorption of radiation by particles over air. However, this relationship is highly non-linear and also depends on scale, since adsorption also increases with the radiation path length.

3.2.2. Transferability

The aerodynamic control systems and devices developed here for the SEVR are considered to be transferrable to other solar cavity receivers employing either single or multi-phase flow. Nevertheless, the specific details of the flow-field aerodynamics in other systems will need to be accounted for because it will impact the optimisation and performance of the aerodynamic controls for any specific solar device.

3.3. Further reading

Chinnici, A., Davis, D., Lau, T.C.W., Ang, D., Troiano, M., Saw, W.L., Tian, Z.F., Solimene, R., Salatino, P. and Nathan, G.J., 2022. Measured global thermal performance of a directly irradiated suspension-flow solar particle receiver with an open aperture. Solar Energy, 231, pp.185-193.

Ang, D., Chinnici, A., Tian, Z.F., Saw, W.L. and Nathan, G.J., 2022. Influence of particle loading, Froude and Stokes number on the global thermal performance of a vortex-based solar particle receiver. Renewable Energy, 184, pp.201-214.

4. Use of Computational Fluid Dynamics (CFD)

The project advanced understanding of the impact of various simplifying assumptions and modelling approaches on the accuracy of various Computational Fluid Dynamics (CFD) models, which is a necessary step toward the development and design of optimal devices since it requires reliable prediction of the transport of particles and heat transfer between suspended particles. Extensive validation was performed based on the transporting gas phase, together with assessments of two-phase flows as a function of particle size in the presence of radiative heating and convective cooling. Work was also undertaken to develop simplified models by comparison with results from detailed numerical methods in simplified environments, obtained with Direct Numerical Simulations (DNS). These are complementary because they provide complete data sets for validation, even though the environment is somewhat simpler.

4.1. Development of CFD models of single-phase flow field for the proposed SEVR

Computational Fluid Dynamics (CFD) models for simulating the single-phase flow field within a lab-scale hybrid calciner and 50-MW industrial scale hybrid calciner have been developed. The hybrid calciner is termed as the solar expanding vortex reactor (SEVR). The CFD models have been validated against particle image velocimetry (PIV) measurements of the velocity profiles for a lab-scale SEVR. Sufficient agreement between the experimental results and simulation was addressed. The single-phase flow results of the industrial scale SEVR with an expander are found to have small amount of flow exchange through the buffer and high temperature rise within the main chamber, making the SEVR with an expander a promising design for future commercialization.

4.1.1. Methodology

Figure 27 together with Table 4 present a schematic diagram and the detailed dimensions of the lab-scale SEVR (Figure 26a) and the industrial scale of the SEVR with the expander (Figure 26b). L_c/D_c and θ for both scales are kept the same. The CFD package, ANSYS/CFX 2020 R1 was used and Shear Stress Transport (SST) model was employed in the simulation.

4.1.2. Results and summary

The mesh independence test was performed for the lab-scale SEVR with a coarse mesh of about 4 million nodes, a medium-sized mesh of about 6 million nodes and a fine mesh of about 9 million nodes. Figure 28 shows the comparison performed with these meshes for the normalised axial velocity along 3 lines (1 centreline and 2 axial lines) and the normalised tangential velocity along 2 axial lines. It can be seen that the results predicted by the medium-sized mesh (6 million nodes) and the fine mesh (9 million nodes) are similar to each other. Consequently, the mesh density of 6 million nodes has been selected for further work presented in this study.

A comparison of predicted and measured single-phase axial velocity along the 3 radial transects and the tangential velocity along 2 axial transects is also presented in Figure 28. The input conditions to the model

were set to match the measurements as before. It can be seen that the model gives reasonable qualitative agreement, with broadly similar trends for both the axial and tangential velocity components, although the radial profiles exhibit either much stronger or additional points of inflection. From a quantitative perspective, the axial and the tangential velocity profiles agree to within 10.67% and 21.87%, respectively. On the basis of the validation against experiment measurements, the refined CFD model shows sufficient agreement to be used for the subsequent parametric investigation for the industrial-scale SEVR.

Figure 29 presents the single-phase axial velocity along the 4 radial transects and the tangential velocity along 3 axial transects for the 50-MW industrial SEVR with the expander. It should be noted that the radiation model is employed in the simulation. The air is preheated to 600°C when injected into the receiver, and a total of 50 MW of incident radiation is employed through the aperture. The air velocity at the inlet duct is kept as 36.33 m/s and the air velocity at each circular inlet is kept as 27.6 m/s, resulting in a total of 30 kg/s of preheated air injected into the receiver. The mass flow rate at the main outlet is fixed at 30 kg/s and the one at the secondary outlet is fixed at 5 kg/s. Temperature at the aperture is set to be 25°C to mimic ambient environment. It can be found that a vortex is generated within the main chamber while the vortex intensity decreases significantly within the expander. Due to the presence of the vortex core, the ambient air enters the main chamber through the centre of the buffer. Additionally, the ambient air ingress through the aperture occurs near the lower part of the aperture as the secondary outlet is located at the bottom chamber.

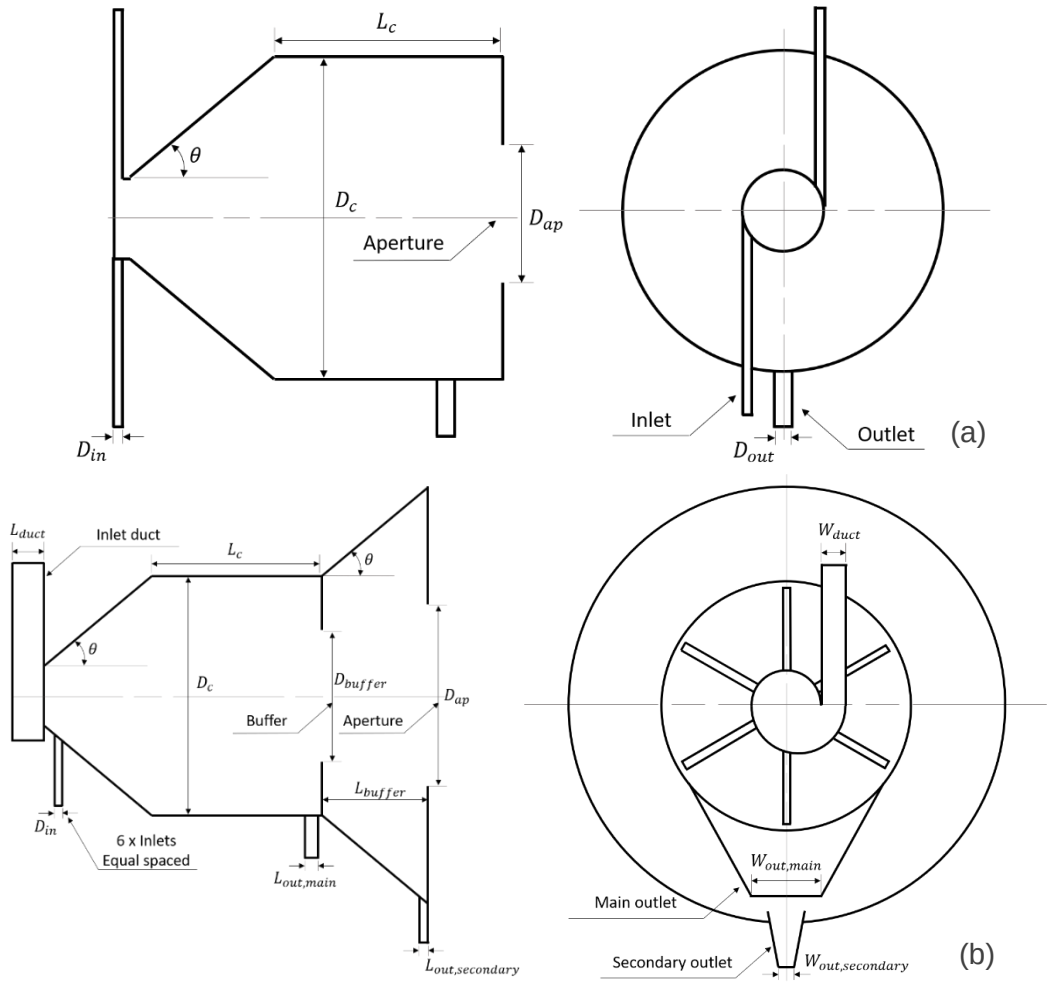

Figure 27: Schematic diagram of the lab-scale SEVR (a) and the 50-MW SEVR with the expander (b). Not to scale.

Table 4: Imaging arrangement for separately capturing LIP and LIF.

Dimensions	Lab-scale SEVR	50MW$_{th}$ SEVR with buffer
L_c	0.09 m	8.54 m
D_c	0.12 m	7.75 m
D_{ap}	0.045 m	5.43 m
D_{in}	0.003 m	0.5 m
D_{out}	0.006 m	
θ	40°	40°
D_{buffer}		3.88 m
L_{buffer}		4.27 m
L_{duct}		1.17 m
W_{duct}		1 m
$L_{out,main}$		0.56 m
$W_{out,main}$		3 m
$L_{out,secondary}$		0.56 m
$W_{out,secondary}$		0.5 m

Table 5 presents the gas exchange through the buffer and the aperture as well as the mean temperature at the main outlet and the secondary outlet. It can be seen that the gas ingress and egress through the buffer is 15.1% and 20.0% relative to the total inlet gas mass flow rate, respectively. In addition, such values for gas ingress and egress through the aperture are 82.6% and 64.3%, respectively. The net gas exchange through the aperture is around 4 times as the one through the buffer, showing that the use of the buffer can significantly prevent ambient air ingress and heated air egress from the main chamber. The temperature at the main outlet is around 500°C higher than at the secondary outlet, while the gas temperature at the secondary outlet is slightly lower than the preheated temperature at the inlets, indicating ambient air enters the buffer cooling down the air in the buffer but not significantly cooling down the air in the main chamber. Figure 30 also shows the temperature contour at the cross-sectional plane and the velocity vector of the air. It can be found that the use of the secondary outlet can effectively prevent the ambient air entering the main chamber and hot air exiting it. For a particle-based receiver, the secondary outlet can also prevent particle egress through the aperture.

Table 5: Simulation results for gas exchange at the buffer plane and the aperture plane, and mean gas temperature at both outlets.

Parameter	Value
$\dot{m}_{ingress,buffer}$	$4.5\ kg/s$
$\dot{m}_{egress,buffer}$	$6.0\ kg/s$
$\dot{m}_{ingress,aperture}$	$24.8\ kg/s$
$\dot{m}_{egress,aperture}$	$19.3\ kg/s$
$T_{out,main}$	860°C
$T_{out,secondary}$	395°C

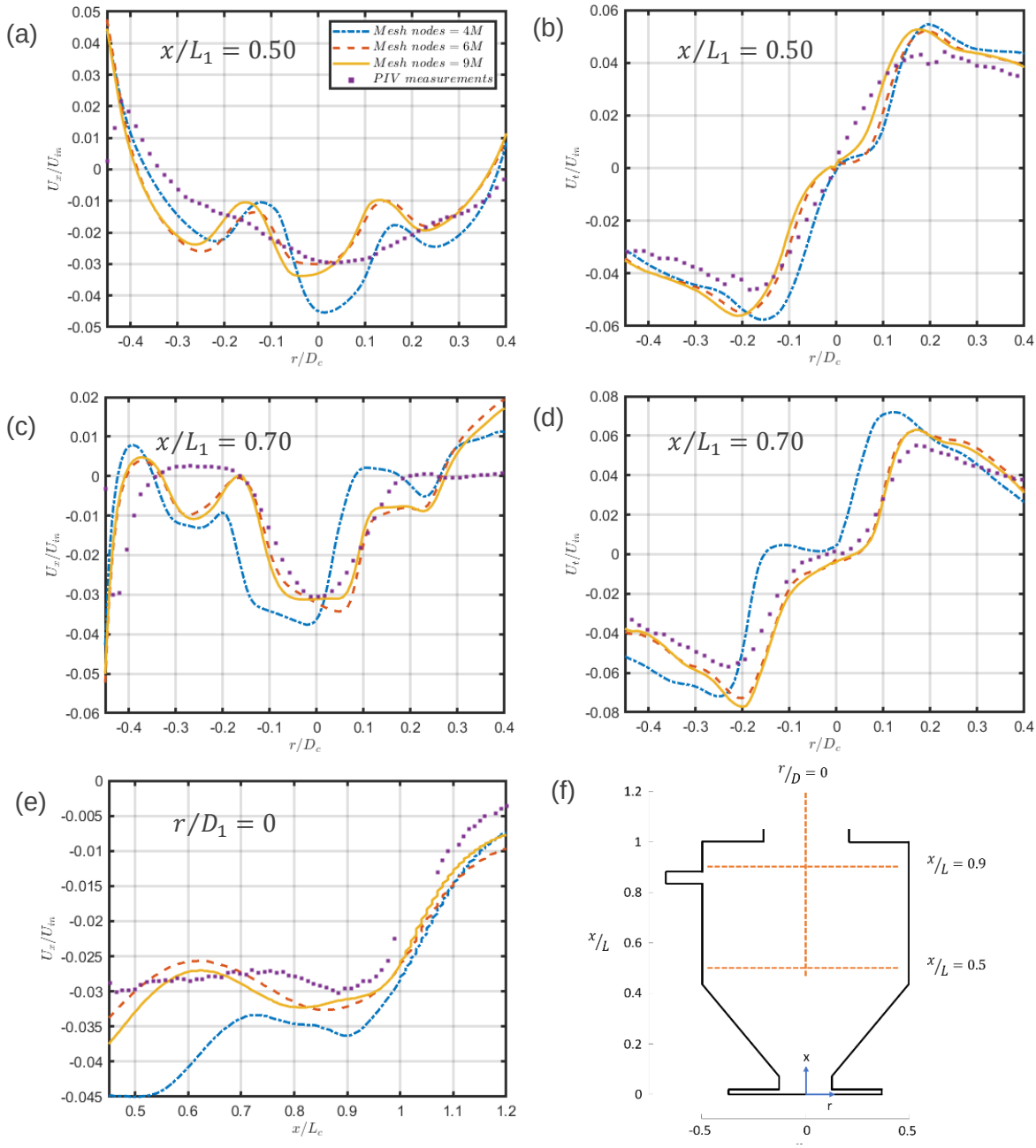

Figure 28: Profiles of the measured (data points) and predicted (lines) of normalised mean axial velocity at three locations (left) and mean tangential velocity at two locations (right) for three different mesh sizes and the PIV measurements for the lab-scale SEVR.

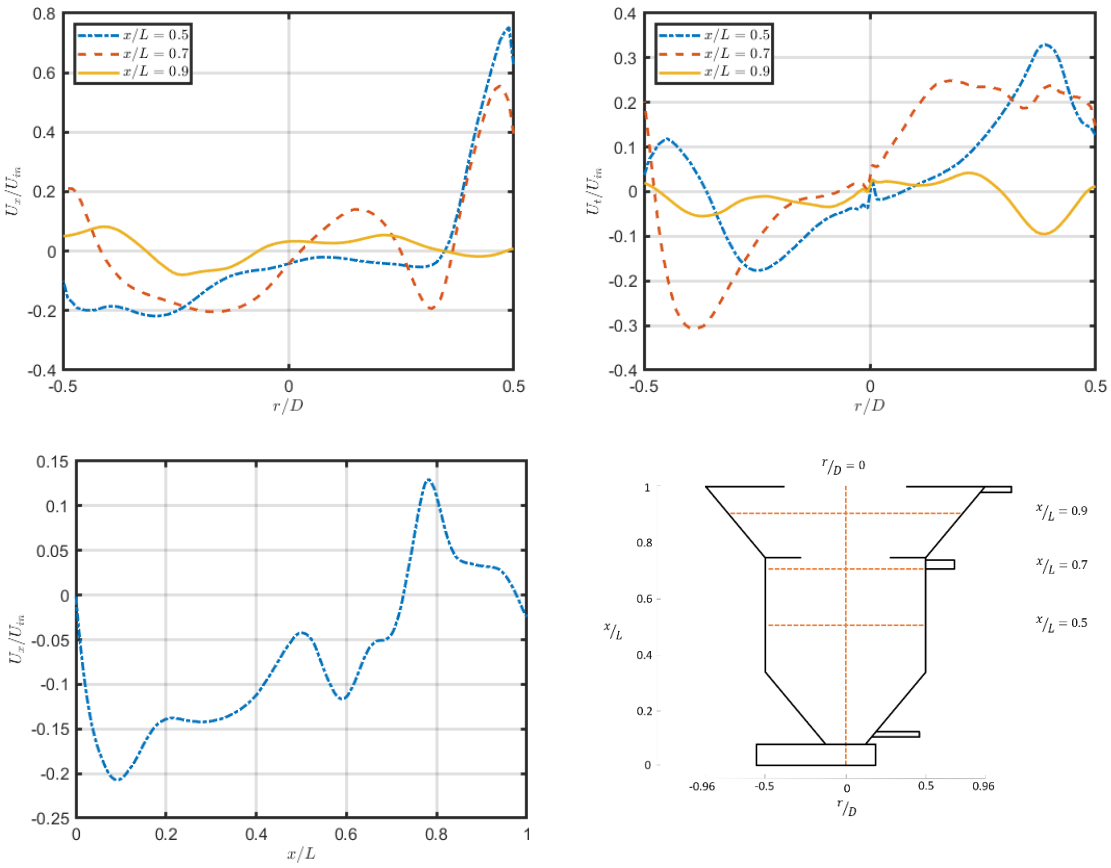

Figure 29: Profiles of simulation results of normalised mean axial velocity at four locations (left) and mean tangential velocity at three locations (right) for the 50-MW industrial SEVR.

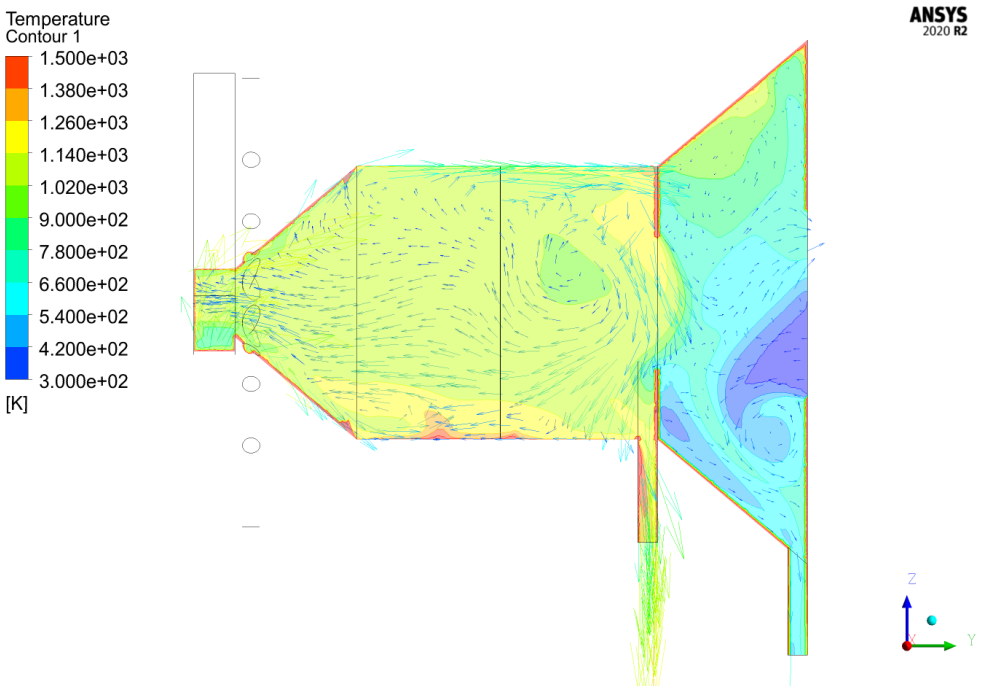

Figure 30: Air temperature contour and velocity vector (arrow shows the moving direction of the gas) for the 50MW$_{th}$ industrial scale SEVR.

4.2. Development and validation of CFD models using experimental results collected from small-scale reactor.

A new CFD model has been developed to provide estimation of gas and particle temperature as well as particle distribution to better understand the thermal performance and heat transfer within a vortex-based solar reactor under both single-phase and two-phase conditions. The developed CFD model needs to be validated against experimental data obtained from the small-scale solar vortex receiver. The numerical study provides prediction of the gas-phase temperature at the outlet with variations of inlet air mass flowrate studied under the single-phase conditions, while systematic parameters, such as, particle volumetric loading and particle size were varied to characterise the thermal performance of the two-phase flow within the SEVR.

4.2.1. Methodology

Figure 31 presents the schematic diagram for the experimental setup. Ambient air and inert particles were injected from the inlets through air flowmeters and particle screw feeder, while a 2.1 kW three lamp solar simulator was projected into the device to heat up the flow. The temperature measurement data were taken by the thermocouple at the outlet. In the numerical study shown in

Figure 32, the incoming radiative heat flux from the aperture was modelled based on the Gaussian shaped solar flux input through a user defined subroutine with the option of Monte-Carlo ray tracing for more accurate and robust computation. For both single and two-phase flow in the device, shear-stress-transport (SST) model was applied as good agreement was found based on previous study of solar vortex gasifiers. Overventilation at the outlet was fixed at a rate of 33% throughout the experimental and numerical study to prevent particle egress. The thermal efficiency for all cases were evaluated based on the energy balance equation, that is, $\eta_{th} = 100\,[\dot{m}_{a,o}\,c_{p,a}(T_{a,o} - T_{a,i}) + \dot{m}_{p,o}\,c_{p,p}(T_{p,o} - T_{p,i})]/\,\dot{Q}_{total}$. Details of the systematic study can be found in Table 6.

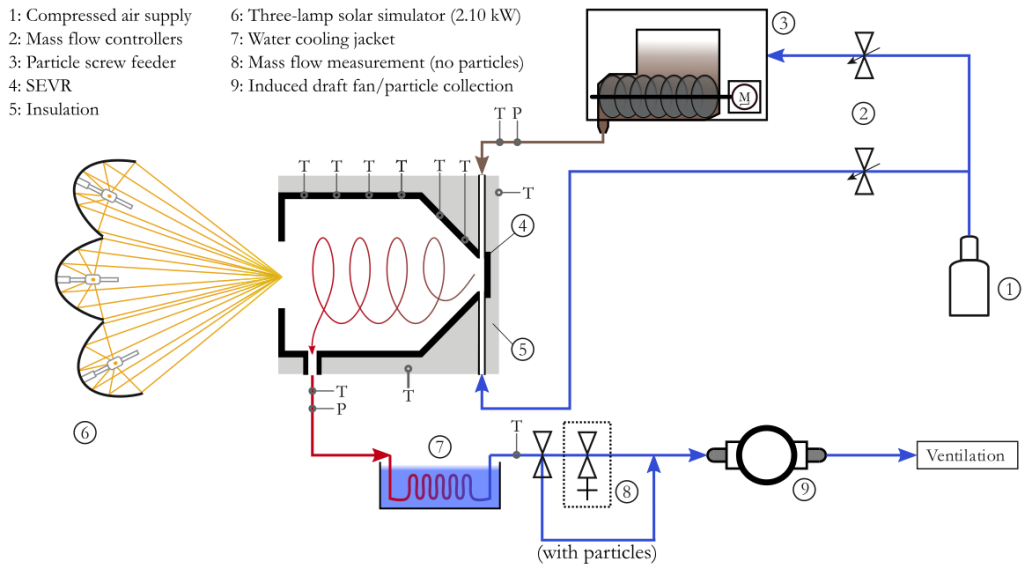

Figure 31: Schematic diagram of the experimental arrangement. The experiment consists of thermocouple measurements at the wall and outlet of the reactor, while a total flux input of 2.10kW was provided by the three-lamp solar simulator.

Table 6: List of key operating parameters specified for the experimental and numerical study.

Outlet Mass Flowrate (Single-phase) [kg/s]	0.0014, 0.0017, 0.0023,0.0027
Outlet Mass Flowrate (Two-phase) [kg/s]	0.0014, 0.0023
Particle size [μm]	85 (CFD),120, 155, 185, 240 (CFD)
Particle volumetric loading (ϕ) [x10^{-5}]	2.96, 4.45, 9.01

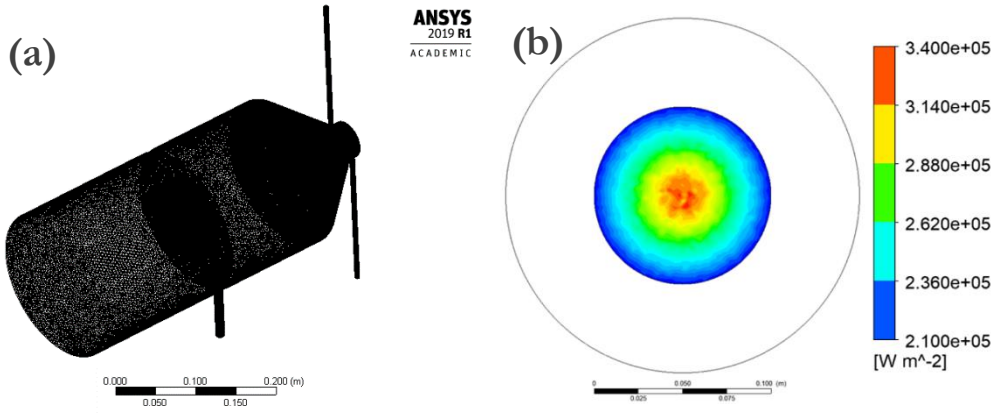

Figure 32: (a) Schematic diagram of the lab-scale SEVR CFD model, (b) The Gaussian distributed input solar flux profile of the CFD model.

4.2.2. Results and summary

Figure 33 presents both the measured and estimated thermal efficiency of the SEVR as a function of inlet air mass flowrate under single-phase flow conditions. An overall trend was spotted, which shows that the thermal efficiency of the reactor improves with the increment of flowrate. This is as expected as the increase in mass of air introduced into the system results in a boost in efficiency, as described in the energy balance equation. Comparison of the thermal efficiency from previous and current experimental study shows that numerical model possesses high confidence in model validation as the average percentage difference between the experiment and numerical thermal efficiency data differs by less than 10%.

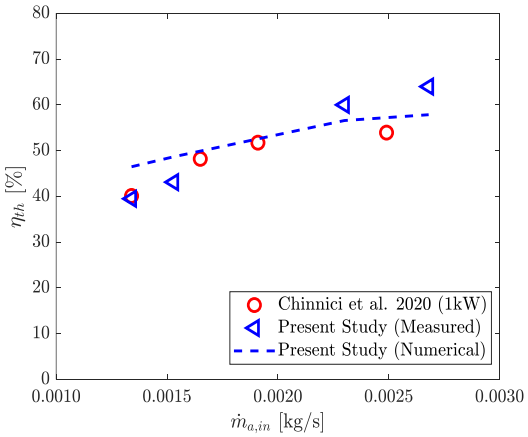

Figure 33: Thermal efficiency of the SEVR as a function of the outlet mass flowrate under single-phase conditions.

For the numerical study under the two-phase flow as shown in Figure 34, the increment of particle size demonstrates little to no changes in thermal efficiency. This implies that the particle size has a secondary influence on the thermal performance of the device. As shown in Figure 34a, the increment of mass flowrate shows a similar trend, that is, similar to that observed in Figure 33. Meanwhile, the increment of particle loading leads to an increase in thermal efficiency as shown in Figure 34b. This is because the increment of particle loading leads to a rise of particle mass in the particle phase, thereby, increasing the energy absorbed by the reactor, which could be referred to the energy balance equation. Nevertheless, the percentage difference between the measured and simulated results are less than 10%. Therefore, the current CFD model establishes a high confidence on the validation of experimental data.

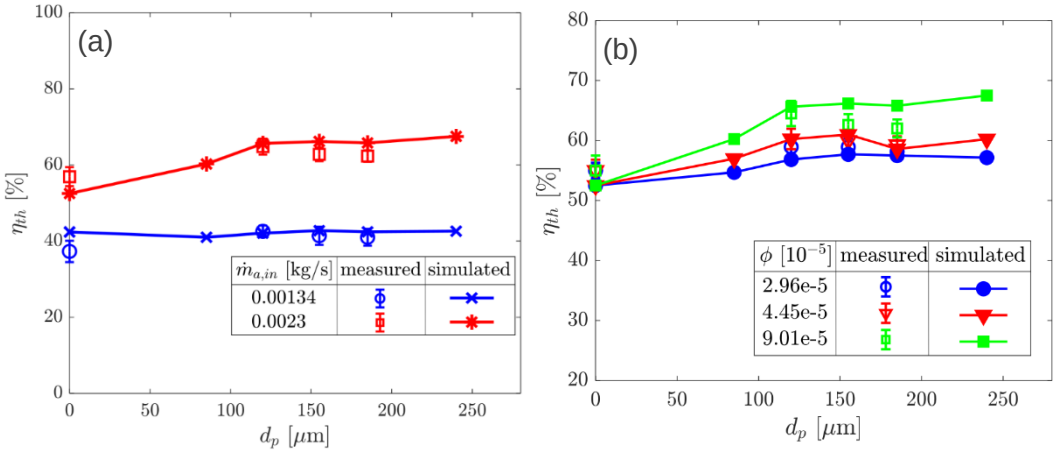

Figure 34: Thermal efficiency of the SEVR as a function of particle size for different (a) inlet mass flow rate, (b) particle volumetric loading under two-phase flow conditions.

4.2.3. Complete development of a scale-up plan for demonstrating the hybrids calciner based on the experimental results collected from the small-scale hybrid calciner

A computational study on the scaled-up vortex-based hybrid calciner was performed to understand its thermal performance, which is a crucial component for calcination requiring high-temperature process heat with a target operating temperature between 950°C and 1300°C. The current study focuses on a preliminary scaled-up device with a 50 MW_{th} capacity given as the solar thermal input from the heliostat field. This section is a precursor to the development of a framework for the design and scale-up process of the reactor. In addition, the numerical study offers a more comprehensive dataset for predicting thermal performance within the scaled-up system. Although numerical modelling has been widely conducted previously on the lab-scale device, there is still a need to test the confidence of the Computational Fluid Dynamics (CFD) tool at scale. Therefore, the present milestone aims to shed light on these objectives by applying CFD simulation on a 50 MW_{th} demonstration-scale reactor.

4.2.3.1. Methodology

4.2.3.1.1. Strategies of Scaling-up

Several scaling up strategies have been proposed prior to designing the solar receiver. This includes the constant velocity (CV) and constant residence time (CRT) approach. The CV approach maintains the inlet velocity to the receiver to be consistent under different scales using the formulas shown in Eq. 4 to construct its dimensions. Meanwhile, the CRT strategy assumes that the gas residence time in the device

is constant, with dimensions determined by the relationship as highlighted in Eq. 5. Here, D represents the jet diameter at the inlet, while P is the total fixed input solar power into the receiver, along with N as the number of circular or rectangular inlet jets.

$$\text{CV: } \frac{D_{jet,scale-up}}{D_{jet,lab-scale}} = \frac{N_{jet,lab-scale}}{N_{jet,scale-up}} \sqrt{\frac{P_{scale-up}}{P_{lab-scale}}}, \qquad \text{Eq. 4}$$

$$\text{CRT: } \frac{D_{jet,scale-up}}{D_{jet,lab-scale}} = \frac{N_{jet,lab-scale}}{N_{jet,scale-up}} \sqrt[3]{\frac{P_{scale-up}}{P_{lab-scale}}}, \qquad \text{Eq. 5}$$

4.2.3.1.2. Procedure for Scaled-up Receiver Design

As shown in Figure 35, a logic diagram has been constructed to scale the 50MW$_{th}$ receiver. The receiver was initially scaled using the 1.25 length-to-cavity diameter (L/D$_c$) ratio, matching the design of the laboratory scale receiver. The process begins by determining the scaling criteria through hand calculations of both equations. Then, the flux map size from the heliostat field and velocity were thoroughly considered by assessing the requirements. The calculation results show that the constant velocity approach is a more suitable method of scaling up, as this prevents particle erosion under high flow speeds in the receiver while keeping an appropriate aperture ratio for the flux map profile to prevent particle egress and radiation spillage. Once this has been determined, the diameter of inlet jets is evaluated by determining the Reynolds (Re) and Stokes (Sk) numbers, which was done to ensure that particle-laden flow is under the fully turbulent regime, capable of generating a swirling flow. Modification of the jet size and numbers are determined at the current stage, where the suitable size, shape and number of jets are chosen. The gas residence time within the geometry is checked to ensure that it lies between 2 – 25 seconds, which is significant for the calcination process. Once these constraints have been met, the scaled-up receiver geometry is created for CFD simulations. Simulation results such as the thermal efficiency and temperature trend are compared to ensure that the development correlates well with the lab-scale device. Finally, a sensitivity study on the thermal performance is performed to ascertain the optimal geometry (i.e., L/D$_C$ ratio and aperture size).

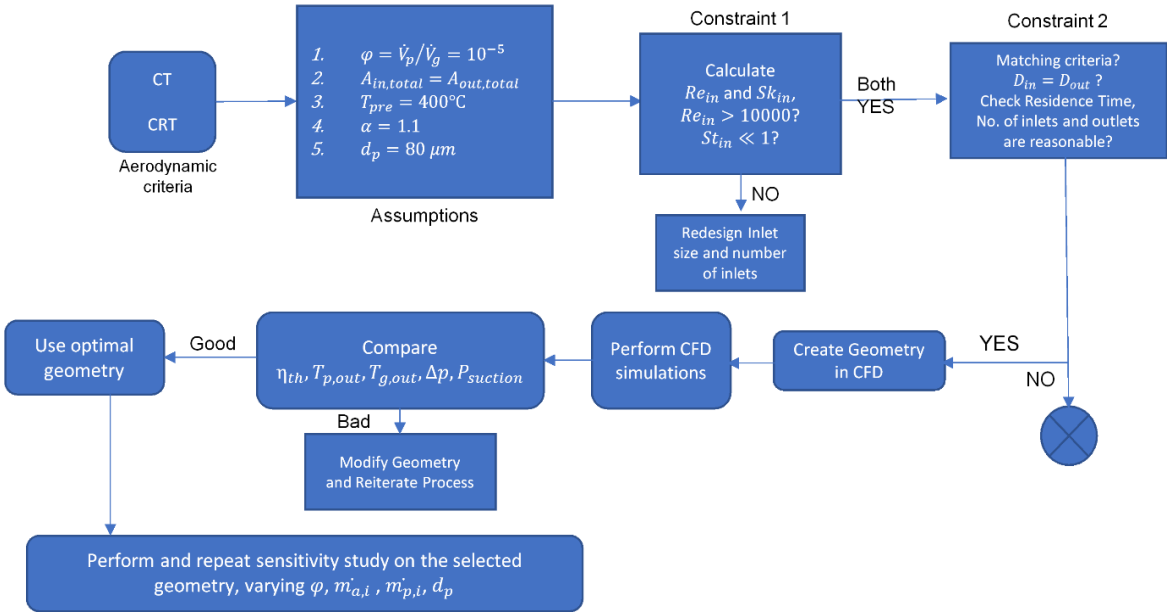

Figure 35: Logic diagram for the scaling-up procedure of the reactor.

4.2.3.1.3. Addition of the Buffer Chamber

A passive control intervention technique (i.e., buffer chamber) was added to optimise the system efficiency by reducing hot air and particle egress and cold air ingress from the secondary aperture, as highlighted in Figure 36a. Compared to one of the original geometries shown in Figure 36b, the buffer region also aims to reduce circumferential velocity, decreasing the particle momentum to propel forward. While the additional features of a primary aperture, as seen in Figure 36a, have also been proven effective in trapping and separating hot particles and air leaving through the cylindrical chamber while preventing backflow of cold ambient air from the secondary aperture. A small amount of overventilation was added at the bypass duct of the chamber region to draw cold air entering through the secondary aperture while collecting the particles egressed from the primary aperture.

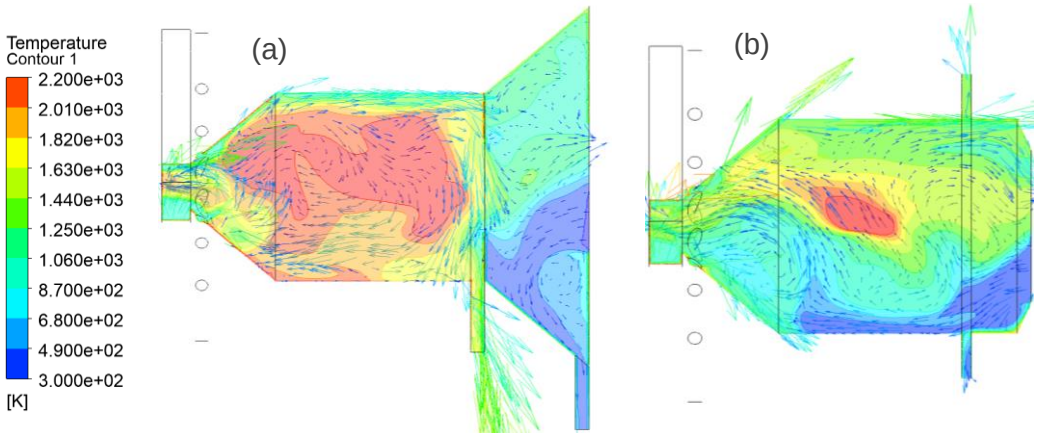

Figure 36: Temperature contour within the SEVR (a) with and (b) without a buffer chamber.

4.2.3.1.4. CFD model development

The scaled-up 50 MW_{th} windowless receiver used for this computational study is shown in Figure 37. For this particular study, the receiver geometrical parameters and operational conditions are presented in Table 7 and Table 8. Both single and two-phase tests were conducted to systematically assess the receiver's thermal performance (i.e., thermal efficiency, outlet temperature, and particle egress). The Monte Carlo ray-tracing approach was employed for the radiation model. In the model, the solar flux distribution input is modelled by radiation flux data provided by CSIRO through the use of in-house software, Heliosim, which estimates the solar flux generated by the heliostat field.

Table 7: Geometrical parameters of the scaled-up 50MW SEVR.

Geometrical Parameters	50MW-SEVR
D_c, Cylinder Diameter [m]	7.75
D_{in}, Inlet Jet Diameter [N x m]	6 x 0.6
L_{duct}, Inlet Duct (Width x Length) [m]	1.3 x 1.4
L_c, Cylinder Length [m]	8.5
D_b, Base Diameter [m]	1.93
θ, Cone Angle [°]	40
$D_{ap,primary}$, Primary Aperture Diameter [m]	3.9
$D_{ap,secondary}$, Secondary Aperture Diameter [m]	5.425
L_{out}, Outlet Duct (Width x Length) [m]	3 x 1.8
L_{bypass}, Bypass Duct (Width x Length) [m]	0.8 x 1.65
L_{buffer}, Buffer Length [m]	1.93
$D_{ap,primary}/D_c$	0.5
$D_{secondary,ap}/D_c$	0.7
L, Total Length [m]	13.95

Table 8: Proposed operating parameters for the scaled-up 50 MW SEVR.

Operational Conditions	50MW-SEVR
$\dot{m}_{a,i}$, Inlet air mass flowrate [kg/s]	30 – 151
$\dot{m}_{a,o}$, Outlet air mass flowrate [kg/s]	30 – 151
$\dot{m}_{b,o}$, Bypass air mass flowrate [kg/s]	6 – 30
$\dot{m}_{a,o}/\dot{m}_{a,i}$	1
$\dot{m}_{b,o}/\dot{m}_{a,i}$	0.2
$\dot{m}_{p,i}/\dot{m}_{a,i}$, Particle mass loading	0 – 0.1
T_{in}, Inlet air and particle temperature [°C]	600
α, Receiver tilt angle [°]	-31

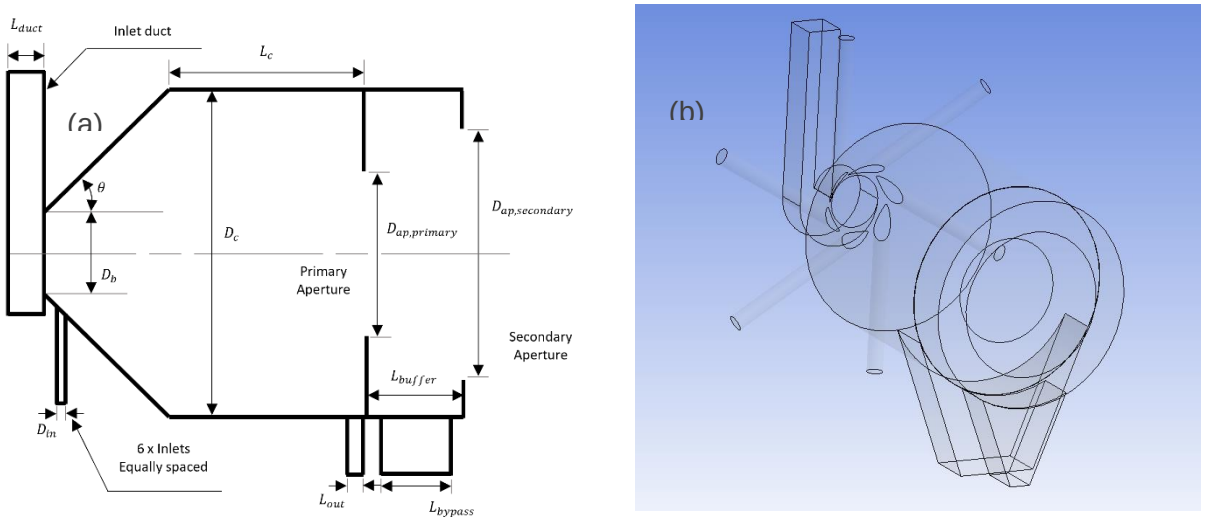

Figure 37: (a) Schematic Diagram of the 50 MW_{th} SEVR, and (b) CFD model geometry.

The geometry of the SEVR was constructed with the DesignModeller along with a Mesh independence study to determine the appropriate mesh size for the simulation. The shear-stress-transport (SST) model was applied as a good agreement was found based on previous studies involving swirling flow. The thermal efficiency of the device is evaluated based on the energy balance equation:

$$\eta_{th} = 100\left[\frac{\dot{m}_{a,o}\, c_{p,a}(T_{a,o}-T_{a,i}) + \dot{m}_{p,o}\, c_{p,p}(T_{p,o}-T_{p,i})}{\dot{Q}_s}\right] \qquad \text{Eq. 6}$$

4.2.3.2. Result and discussion

Figure 38 presents the outlet and wall temperatures, thermal efficiency and particle egress rate of the SEVR as a function of inlet mass flowrate. As highlighted in Figure 38a, similar previous findings have demonstrated that the decrement of outlet temperature results from the energy balance under a fixed thermal input. One novel finding of this study is that the addition of particles can enhance the air temperature, while it is observed that there is no significant temperature difference between air and particles. Thus, it can be concluded that the addition of particles increases the surface area within the reactor, which allows for greater heat absorption within the flow. Furthermore, the wall temperature under particle-laden conditions is much lower than that of the single-phase flow, as particles suspended within the flow has absorbed part of the thermal input. The possible explanation for this is the shadowing of the wall by the particles from absorption of the input radiation.

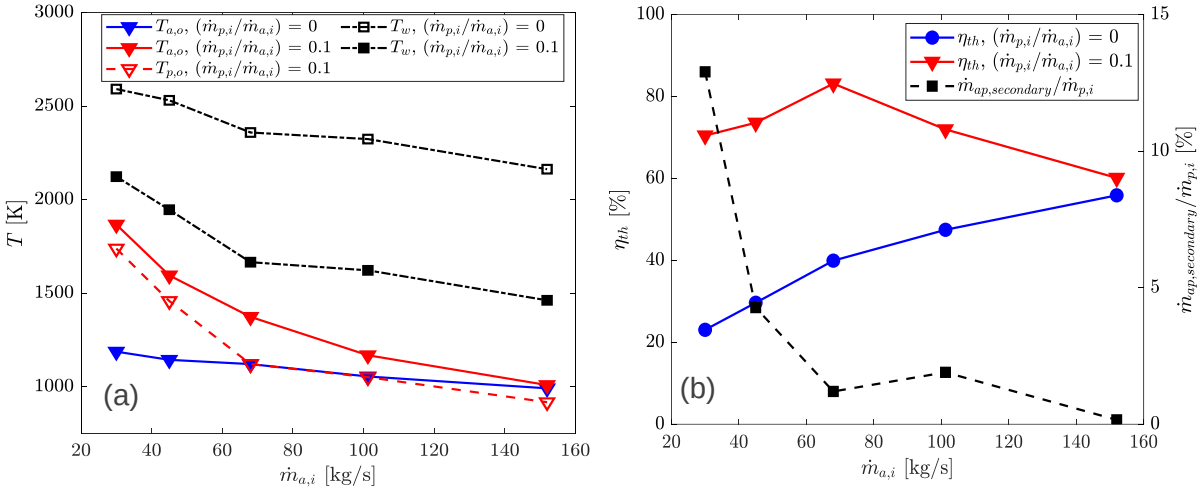

Figure 38: (a) Simulated outlet and wall temperatures of the SEVR and (b) Thermal Efficiency and particle egress rate at different inlet mass flowrates.

Under the single-phase conditions, Figure 38b shows that the thermal efficiency increases consistently as the inlet flowrate increases, while this is only true for flowrates between 30 – 68 kg/s when particles are added into the device. This could be attributed to the particle residence time within the receiver, in which the rate of thermal absorption is strongly reduced. Hence, particles could not fully charge their thermal capacity before exiting the device. However, the particle egress rate shows that the particle egress is strongly reduced upon reaching 40 kg/s. This results from the stronger inertial force as flowrate increases, where particles centrifuge more closely towards the wall, thereby avoiding the aperture region.

4.3. Further readings

Ang, D., Chinnici, A., Tian, Z. F., Saw, W. L., & Nathan, G. J., (2022) Influence of particle loading, Froude and Stokes number on the global thermal performance of a vortex-based solar particle receiver. Renewable Energy, 184, 201-214.

Tang, Y, Sun, Z, Tian, ZF, Lau, TCW, Chinnici, A, Saw, WL & Nathan, GJ., (2022) Direct measurements and prediction of the particle egress from a vortex-based solar cavity receiver with an open aperture, Solar Energy, 105-117

5. Development of sub-model of particle thermo-physical-chemical and optical properties

5.1. Property measurement of calcined alumina resulting from different gas environments:

The alumina calcination process starts with the conversion of gibbsite to boehmite in the pre-calciner at around 250°C. One molecule of water is removed via calcination for each molecule of boehmite product formed. Boehmite is then fed into the main calciner and heated to approximately 900°C for the removal of 2 water molecules per molecule of aluminium oxide formed. The aluminium oxide formed in the main calciner could be in three forms: gamma, theta and alpha alumina as shown in Figure 39. Both gamma and theta alumina are transitional alumina and are not stable whereas alpha alumina has a fixed structure and is stable. The formation of Smelter Grade Alumina (SGA) focuses on the formation of both gamma and theta alumina, with minimal amount of alpha alumina formed while having no gibbsite or boehmite left in the final product. This is to ensure that the final product has the right moisture on ignition (MOI), loss on ignition (LOI) and surface area requirements for the Halt-Heroult process which converts aluminium oxide to molten aluminium.

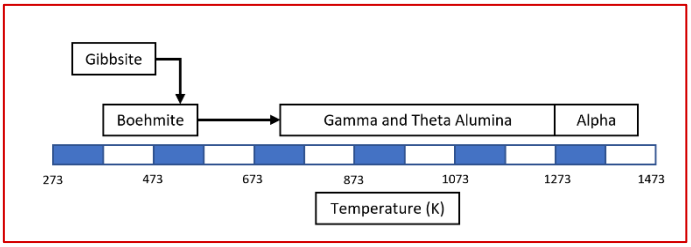

Figure 39: Transformation pathway of gibbsite to alpha alumina under standard industrial conditions.

The presence of steam has been shown to have a positive effect on boehmite calcination (main calciner) and the influence of steam on gibbsite calcination in the pre-calciner is yet to be understood. The steam concentration in the pre-calciner and main furnace depends on fuel input (or input energy) introduce into the calcination process. Solar syngas generated from solar reforming of natural gas (Program 2) can potentially be used to replace conventional natural gas to carry out the calcination of gibbsite in the main furnace. presents the calculated steam concentrations in the pre-calciner and main furnace for various input energy configurations. Interestingly, the calculated steam concentration of the flue gas generated from the combustion of solar syngas is independent from the ratio of hydrogen to carbon monoxide due to the change in the mass ratio being small. However, the calculated steam concentration generated from the combustion syngas is at least 30% higher than that of combustion of natural gas. Therefore, in order to understand the effects of steam concentration on the calcination process, small scale laboratory experiments were carried out in a horizontal tube furnace as shown in Figure 40. The steam concentration is set at 80% by volume and 50% by volume. A completely dry calcination atmosphere (pure nitrogen) was also used as a reference point to study the effects of steam concentration on the calcination process. A quantitative XRD method has been developed to measure the concentration of boehmite, gamma

transitional alumina, theta transitional alumina and alpha alumina. Currently, this project was only focused on the conversion of gibbsite to boehmite and gamma transitional alumina as this is vital information required for the process modelling of the pre-calciner and main furnace. The conversion of gamma transitional alumina to theta and finally alpha alumina is useful when optimizing the setup to ensure the SGA produced are within the industry specifications. The conversion of boehmite can be defined as follows:

$$Conversion = \frac{Weight\ loss\ of\ sample}{Theoretical\ weight\ loss\ for\ complete\ conversion} \times 100\% \qquad \text{Eq.7}$$

Table 9: **Steam concentrations of the flue gas in the calcination process with natural gas or solar syngas as the fuel input**

Input energy	Steam Concentration (vol. basis)	
	Pre-calciner	Main calciner
Conventional natural gas	24%	14%
Direct CST into main furnace and air preheater	19%	9%
Hydrogen into the main furnace and air preheater	31%	21%
Direct solar calcination with steam	>99%	>99%
Solar syngas (steam reforming of natural gas, H_2:CO=1:1, 2:1 & 3:1) into main furnace and air preheater	~31%	~21%

5.1.1. Methodology

5.1.1.1. Experimental setup

of nitrogen was then circulated throughout the furnace to aid the cooling process. It is vital to reduce the temperature of the sample rapidly to room temperature to prevent any further calcination of the sample. The final calcined product was weighed to obtain the weight loss and then analysed using XRD. Table 10 presents the specifications of the gibbsite and boehmites samples used in the present study.

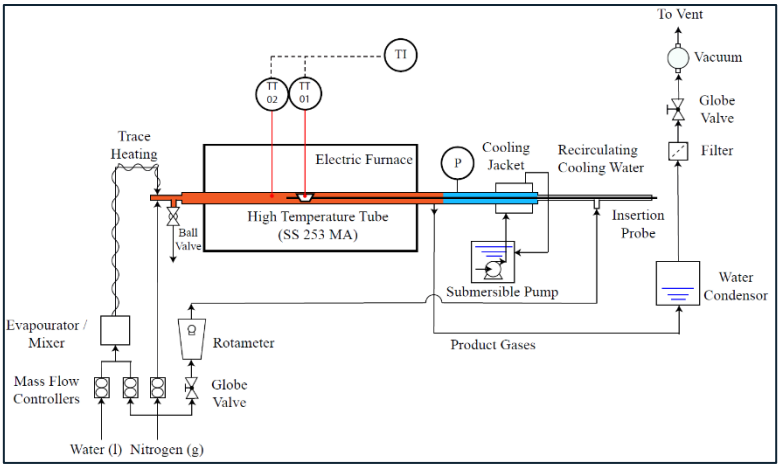

Figure 40: Schematic of fixed bed reactor used to calcine alumina samples.

Table 10: Specifications of the gibbsite and boehmite samples used in the present study.

Specification	Gibbsite	Boehmite
Purity	99.0%	99.4%
Loss of ignition (LOI)	30.8%	18.8%
Surface area (m^2/g)	1.8	230
Particle size distribution (μm)	0.5 to 53	0.7 to 240

Here, the conversion of boehmite is being reported instead of gamma alumina content due to some inconsistency with the obtained XRD data. In our XRD analysis of the calcined boehmite, the amount of gamma alumina detected was a lot smaller than the amount of gamma alumina estimated from the weight loss data. This indicates that there is an intermediate when converting boehmite to gamma transitional alumina. We are currently in the process of investigating if this intermediate alumina can be detected using other methods to account for the difference observed.

5.1.1.2. X-ray Powder Diffraction (XRD)

To calculate the kinetics of the reactions, it is required to determine the amount of converted product in each sample. The fraction of product in the sample could be either boehmite, gamma transitional alumina, theta transitional alumina or alpha alumina. The Australian Standard AS2379.3-2010 (R2013) was used to determine the amount of alpha alumina formed in each sample. The AS2379 quantifies alpha alumina content by calculating the area under the peaks from the XRD data.

From the XRD data of pure alpha alumina obtained from The International Centre for Diffraction Data (ICDD), high intensity peaks that do not interfere with peaks from other components in each sample were selected. The peaks (012) and (116) were selected for alpha alumina as they do not interfere with high intensity peaks from gibbsite, boehmite, gamma transitional alumina and theta transitional alumina. For cobalt radiation in the XRD machine, the peaks should appear at 29.80° (012) and 67.93° (116). A scanning of these two regions would identify the intensity of the high intensity peaks for alpha alumina. The intensity of pure alpha alumina was used as a reference for the other samples to determine their relative intensity. This relative intensity was used to calculate the relative percentage of alpha alumina formed in other samples.

Similarly, reference samples of boehmite, gamma transitional alumina and theta transitional alumina were used to obtain the concentration of each of the alternative phases. A similar American Standard D4926-06 is also found to quantify the amount of gamma alumina content using similar methods. Under cobalt radiation, the two scanning angles would be 43.96° (311) and 53.80° (400). Table 11 summarizes the key scanning angles for various components in the present study.

Table 11: Key XRD scanning angles used to quantify calcined products.

Compound	D value (Å)	Relative intensity (%)	(hkl)	2T angle (Degrees)
Boehmite	6.11	100	020	16.84
	3.164	65	120	32.84
Gamma Alumina	2.39	80	311	49.96
	1.977	100	400	53.80
Theta Alumina	2.837	80	400, 401	36.76
	2.73	65	202,002	38.25
Alpha Alumina	3.479	75	012	29.80
	1.601	80	116	67.94

5.1.1.3. Data from XRD

The method used to study the calcination kinetics involve the utilization of the Kolmogorov-Johnson-Mehl-Avrami (JMA) kinetic equation, which is in the following form (Avrami 1939, Avrami 1940, Avrami 1941):

$$x = 1 - exp(-kt^n) \qquad \text{Eq.8}$$

Where:

x = Fraction of the converted product

k = Rate constant

t = Effective time

n = Avrami constant (constant related to the physical characteristics of the system).

A plot of ln $(1-x)^{-1}$ vs ln (t) can be used to determine the values of n and k respectively (Bagwell and Messing 1999). Alternatively, Macedo et al. (2007) have fitted the Avrami mentioned above to various kinetic curves with the help of the Origin software to obtain the n and k values.

Similarly, the reaction rate constant, k can be calculated with by using the Arrhenius equation below:

$$k = A\, exp(-\frac{E_A}{RT}) \qquad \text{Eq.9}$$

where:

A = Arrhenius constant

E_A = Activation energy

R = Gas constant

T = Absolute temperature.

5.1.1.4. Loss on ignition

Pre-calcination (Gibbsite → Boehmite)

Gibbsite samples were calcined at 250°C, 300°C and 400°C with various residence times of 5, 30 and 120 minutes. Note that 250°C is the lowest temperature for calcination of gibbsite with measurable boehmite content. At 300°C, most of the gibbsite has reacted to form boehmite. At longer hold times, the boehmite produced have calcined into gamma transitional alumina. At 400°C, gibbsite reacts rapidly to form boehmite and then gamma transitional alumina. A conversion of 100% is achieved within 10 minutes at this stage. The samples were then analysed using a thermogravimetric analysis (TGA) technique to determine the moisture on ignition (MOI) and loss on ignition (LOI) values.

Modified Methodology for MOI and LOI

The current standard used to obtain MOI and LOI of aluminium oxide is the ISO806-2004 standard. This standard is extremely useful as it allows determination of MOI and LOI using traditional manual methods as well as more modern automatic TGA methods. For this standard, the sample is required to be heated to 300°C and held for 2 hours to remove all the volatiles/chemical water in the sample. However, as our products are aluminium hydroxides instead of stable aluminium oxides, by holding our samples at 300°C for 2 hours, the samples were further calcined, which altered the chemical composition of the alumina samples. Therefore, further modification to the methodology of MOI and LOI is required to analyse these gibbsite and boehmite samples as there is no common standard available to analyse the MOI and LOI of aluminium hydroxide. In this modified methodology, only surface moisture in the alumina samples will be removed and no further calcination process will occur in the TGA, yielding a more accurate MOI and LOI value.

The following procedures were adapted from ISO 806-2004:

1) A 10mg of sample was loaded onto a crucible.
2) The crucible was then heated in a TGA in the following order:
   (i) Maintain the crucible at 25°C for 1 minute with no air flow.
   (ii) Then, introduce 80ml/minute of air flow for 10 minutes.
   (iii) Increase the TGA temperature from 25°C to 105°C at a heating rate of 40°C/minute with an air flow of 80ml/minute maintained.
   (iv) Hold the TGA temperature at 105°C for 120 minutes with an air flow of 80ml/minute.
   (v) Increase the temperature from 105°C to 300°C at a heating rate of 40°C/minute with an air flow of 80ml/minute.
   (vi) Hold the TGA temperature at 300°C for 120 minutes with an air flow of 80ml/minute.
   (vii) Increase the temperature from 300°C to 1000°C at a heating rate of 40°C/minute with an air flow of 80ml/minute.
   (viii) Maintain the temperature of the crucible at 1000°C for 120 minutes with an air flow of 80ml/minute.

To determine the moisture on ignition (MOI) and loss on ignition (LOI), the following equations were used:

$$\boldsymbol{MOI} = \frac{\boldsymbol{mass\ loss\ at\ 100°C}}{\boldsymbol{mass\ of\ initial\ sample\ (undried)}} \qquad \textbf{Eq.10}$$

$$\boldsymbol{LOI\ (undried\ basis)} = \frac{\boldsymbol{mass\ loss\ at\ 1000°C}}{\boldsymbol{mass\ of\ initial\ sample\ (undried)}} \qquad \textbf{Eq. 11}$$

$$LOI\ (dried\ basis) = \frac{mass\ loss\ at\ 1000°C}{mass\ of\ dried\ sample\ at\ 100°C} \quad \text{Eq. 12}$$

5.1.1.5. Surface area measurement using BET method

The N_2 (UHP grade, 99.999%) adsorption-desorption measurements at 77K were carried out with a 3-flex physisorption analyser (micromeritics). About 50 mg sample was loaded into a glass tube and was degassed at 150°C for 24 h to eliminate water or other volatiles before the test. The specific surface area and pore size distribution were obtained with BET and Barrett-Joyner-Halenda (BJH) methods from the adsorption-desorption measurements, respectively. The morphology of the samples was characterized with a scanning electron microscopy (SEM, Philip XL30). The samples were loaded on carbon tabs and were coated with carbon coating to reduce charging. The backscattering electron mode was employed to analyse the samples.

To carry out the BET analysis to study the surface area of our calcined boehmite samples, the following procedure was adapted from ISO 9277 – 2010:

(a) Day 1
  (i) Weigh the sample tube for 5 times and calculate the average weight.
  (ii) Load approximately 50mg of the boehmite samples into the sample tube.
  (iii) Connect the sample tube to the 3Flex BET machine for degassing.
  (iv) Decrease the pressure of the sample to as close to 0mbar as possible by using a vacuum.
  (v) Heat the sample to 150°C and maintain the temperature overnight to remove all the volatiles from the sample.

(b) Day 2
  (i) Decrease the temperature down to room temperature.
  (ii) After reaching room temperature, further cool the sample to 77.35K. The surface area of the sample is then tested with nitrogen at a relative pressure range from 0 to 0.25.

(c) Day 3
  (i) After completing the tests at the selected pressure ranges, increase the temperature of the samples back to room temperature.
  (ii) After reaching room temperature, increase the pressure inside the samples tube back to 1000mbar.
  (iii) Disconnect the sample tube from the testing port.
  (iv) Weigh sample tube for 5 times and calculate the average weight.
  (v) Input the weight of the empty sample tube and boehmite sample into the computer for it to calculate the surface area and pore size of the boehmite sample.

5.1.2. Results

Calcination of gibbsite at 250°C, 300°C and 400°C

Figure 41a presents the effects of steam concentration on the formation of boehmite (γ -AlO(OH) from Gibbsite [γ -$Al(OH)_3$,] at 250°C. There is a clear trend that boehmite formation is highest when gibbsite is calcined under dry conditions whereas 80% steam concentration is detrimental to the formation of boehmite by limiting the boehmite formation to approximately 6-8%. However, at a steam concentration of 50%, gibbsite only requires only slightly longer for calcination than under dry conditions (pure nitrogen atmosphere). The conversion of gibbsite to boehmite begins from the change in the internal crystal structure of gibbsite according to Rouquerol et al. (Rouquerol et al., 1975). The yield of boehmite can be increased by maintaining a sufficiently high partial pressure of vapour within the particle to enhance

conversion while also not being so high that it may generate cracking of the particle (Courtial et al., 1966, Rouquerol et al., 1975, Wang et al., 2006). However, from our experimental data, there is a contradiction to the transformation mechanism proposed by Rouquerol et al. (Rouquerol et al., 1975) and Courtial et al. (Courtial et al., 1966). The presence of a high concentration of steam will inhibit the release of a water molecule, thus requiring a higher temperature relative to that needed for a lower concentration.

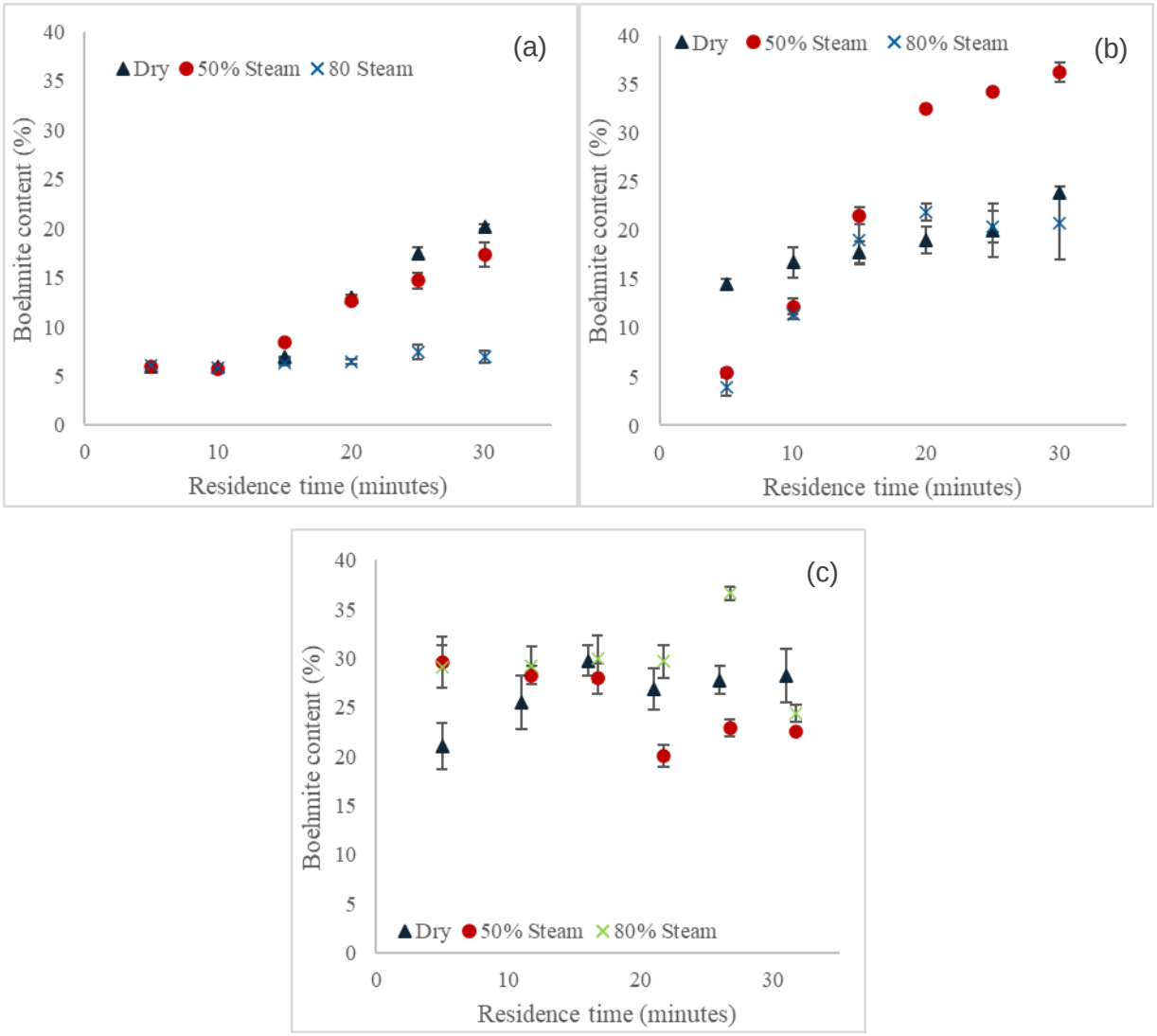

Figure 41: Boehmite content measured by XRD for gibbsite calcination at a) 250°C, b) 300°C, and c) 400°C under pure nitrogen, 50% and 80% steam conditions.

Figure 41b and Figure 41c present the boehmite content for gibbsite calcination at 300°C and 400°C, respectively. It can be seen that the effect of steam is more complex. For the case of 300°C (Figure 41b) the 50% steam shows lower conversion to boehmite at short residence times, but much higher conversion at longer residence times. For the case of 400°C (Figure 41c), this trend is the opposite. The case of 80% steam mirrors that of 50% steam at short residence times, but matches the pure N_2 case at longer residence times for 300°C and even exhibits some enhancement at 400°C. This enhancement was also reported by Inui et al. (Inui et al., 1983 and Bagwell and Messing, 1999). That is, there are some conditions for which the presence of steam has switched from an inhibitor (at 250°C) to being a catalyst, but this response is complex. At 400°C, all of the gibbsite has been converted to boehmite within 10 minutes of calcination and some of the boehmite is started to convert into gamma transitional alumina due to the

reduction of the boehmite content. This is also indicated from the weight loss result, where we have observed a total weight loss exceeding that for the conversion of gibbsite to boehmite.

Figure 42 presents the MOI and LOI of gibbsite calcined at the low temperature of 250°C. It can be seen that the LOI has decreased for the dry case after an isothermal temperature of 120 minutes, but not for the case with steam (Figure 42b). This shows that dry conditions (pure nitrogen) has provided a sufficiently low partial pressure to release some water during the calcination process, in contrast to the steam conditions, consistent with previous work (Rouquerol et al., 1975). This is consistent with the MOI results (Figure 42a), which show that the sample calcined under dry conditions had a significantly higher MOI than those calcined under 50 or 80% steam. That is, crystalline water is evolved more easily in a dry environment than in the steam environment. Our preliminary explanation for this observation is that the incomplete crystallisation process of the conversion from gibbsite to boehmite resulted in high number of voids within the particle. This would allow the re-adsorption of surface moisture onto the pore sizes, which contributed to high MOI value, despite an observed decrease in LOI value.

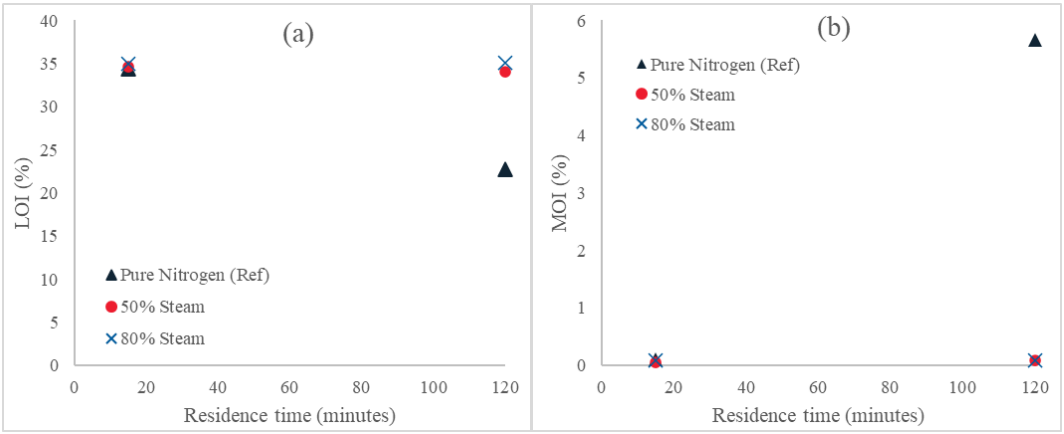

Figure 42: a) Loss on ignition (LOI) and b) Moisture on ignition (MOI) values for gibbsite calcined at 250°C.

Figure 43 presents the MOI and LOI of gibbsite calcined at 400°C. At this temperature, the boehmite formed during the first calcination process has further converted to gamma transitional alumina based on the weight loss measurements. The increase in residence time reduces the MOI and LOI values for all the conditions. According to the previous studies (Krokidis et al., 2001, Wilson, 1979, Xu and Smith, 2012), the conversion of boehmite to gamma begins when there is an initial collapse of the boehmite structure due to the hydrogen transfers and water extraction, followed by a slight shearing into a monoclinic structure with a movement of layers, which is completed by the aluminium migration process filling up the tetrahedral vacant sides. The rate determining step was determined to be the aluminium cation migration rate (Krokidis et al., 2001, Wilson, 1979, Xu and Smith, 2012). At this temperature, gibbsite calcined under dry conditions (nitrogen) has a higher MOI and LOI value as compared to gibbsite calcination under steam conditions. At 400°C, steam has a clear catalytic effect on the calcination process due to the lower MOI and LOI values. Further information of XRD and BET is required in order to better understand the effects of steam on the conversion of boehmite to gamma transitional alumina.

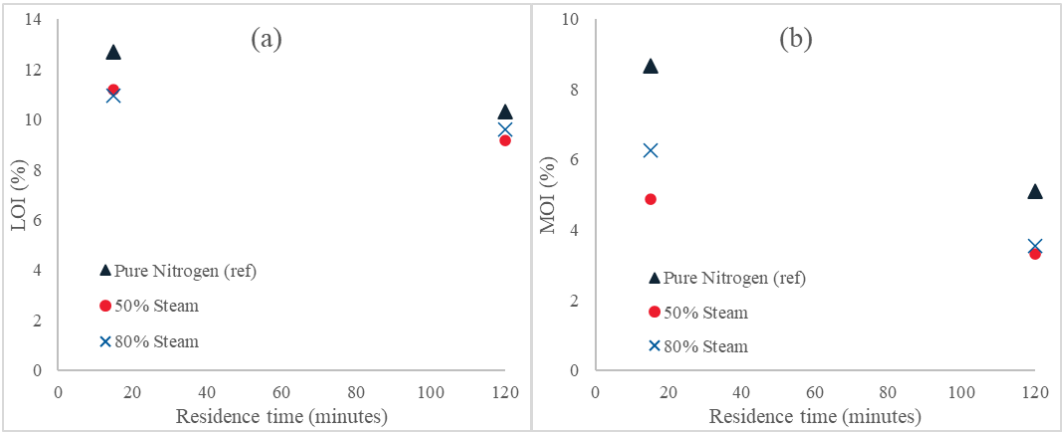

Figure 43: a) Loss on ignition (LOI) and b) Moisture on ignition (MOI)values for gibbsite calcined at 400°C.

Calcination of Boehmite at 400°C, 500°C and 650°C

Figure 44 presents the conversion of boehmite to alumina at 400°C under N_2 and steam conditions as indicated by weight loss measurement. Similar to the gibbsite calcination at 250°C, the presence of steam inhibits the conversion of boehmite to alumina. Under the dry condition, the conversion of boehmite is nearly double as compared to boehmite calcined under 80% steam conditions with the residence time of 120 minutes. The mechanism of boehmite calcination is similar to that of gibbsite calcination where the presence of high concentration of steam inhibits the release of water molecule from the particles. At 500°C and 650°C, the conversion of boehmite is approaching completion, especially with 120 min residence time as shown in Figure 44a and Figure 44b. We are currently exploring boehmite calcination at higher temperatures (>650°C) with shorter calcination times.

Figure 45 presents the MOI and LOI of boehmite calcination at temperatures ranging from 400°C to 650°C with a residence time of 30 minutes. The LOI for boehmite calcined at a low temperature of 400°C increased as steam concentration is increased, indicating an inhibiting effect caused by the presence of steam. This was also reported in the calcination of gibbsite at a low temperature (250°C). However, the MOI for boehmite is less affected by the concentration of steam indicating a more stable evolution of the surface area of the boehmite particle. As surface area is hypothesized to be directly linked to MOI, a constant MOI value would indicate that the surface area is not dependant on the calcination atmosphere. As compared to gibbsite, which requires a cracking in the final particle to complete the transformation, only a small shearing is required for the conversion of boehmite to gamma transitional alumina. For boehmite calcined at a higher temperature of 500°C and 650°C, the higher the steam concentration, the lower the LOI value of the final product. This indicates that the presence of steam has a positive effect on the crystallisation process when converting boehmite to SGA. However, more work needs to be done in order to validate this initial theory.

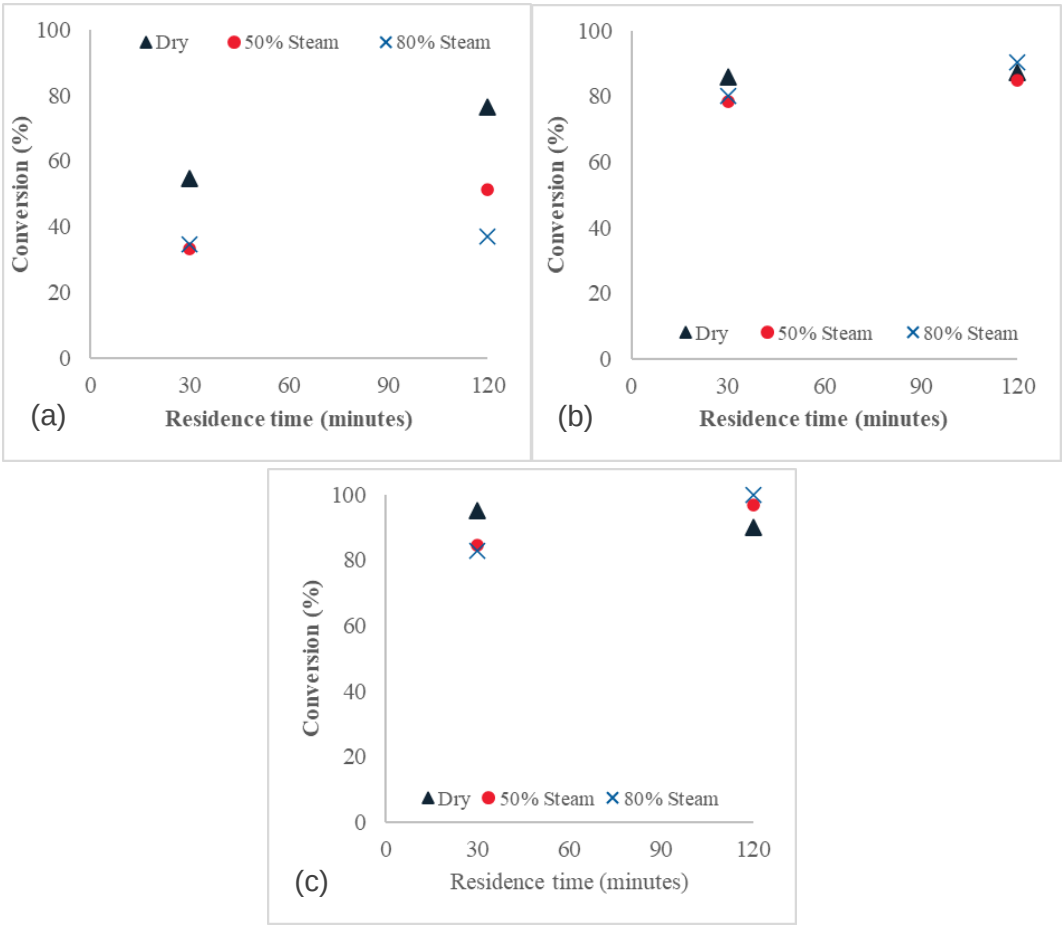

Figure 44: Boehmite conversion measured by weight loss for boehmite calcination at a) 400°C, b) 500°C, and a) 650°C, under pure nitrogen, 50% and 80% steam conditions.

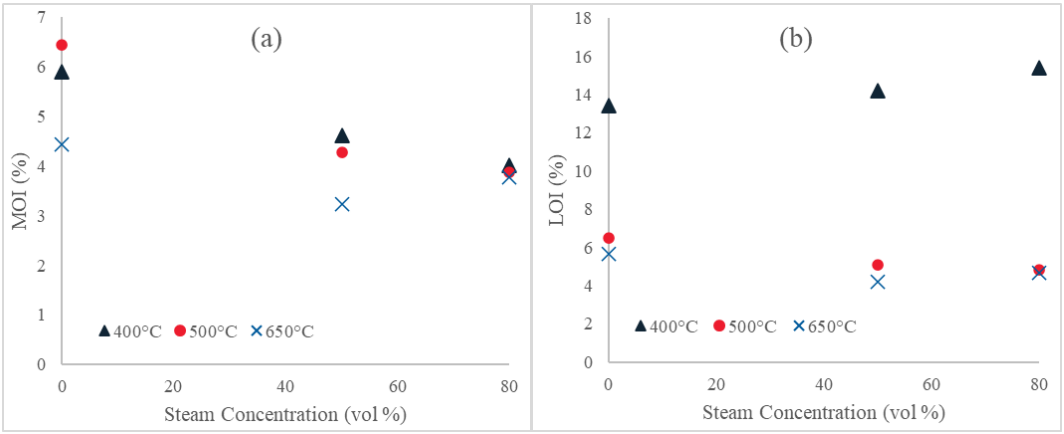

Figure 45: a) Moisture on ignition (MOI) and Loss on ignition (LOI) values for boehmite calcination with residence time of 30 minutes at various reaction temperatures.

Figure 46 presents the surface area of the boehmite samples calcined at 500°C and 650°C with 2 residence times based on the BET analysis. The surface area of the samples gradually decreases with the temperature for the dry and 50% steam while it remains constant for the 80% steam (Figure 46a). The surface area of the samples gradually decreases with the residence time for the case of 80% steam while the opposite trend was found for the dry condition. No change in surface area was noted for the case of 50% steam (Figure 46b). Note that the reference smelted grade alumina (SGA) produced by Alcoa was

measured to be around 70m^2/g. Despite having a positive effect on the surface area of the final product, quantitative data presented above indicated that steam has a negative effect on the yield of the final product by inhibiting the release of the water molecule for calcination experiments carried out under low temperatures. Therefore, there should be an optimum condition in which reaction conditions can ensure yield is not too adversely limited while ensuring the surface area of the product meets SGA requirements. Currently, we are trying to increase the reaction temperature to achieve SGA that meets the specifications.

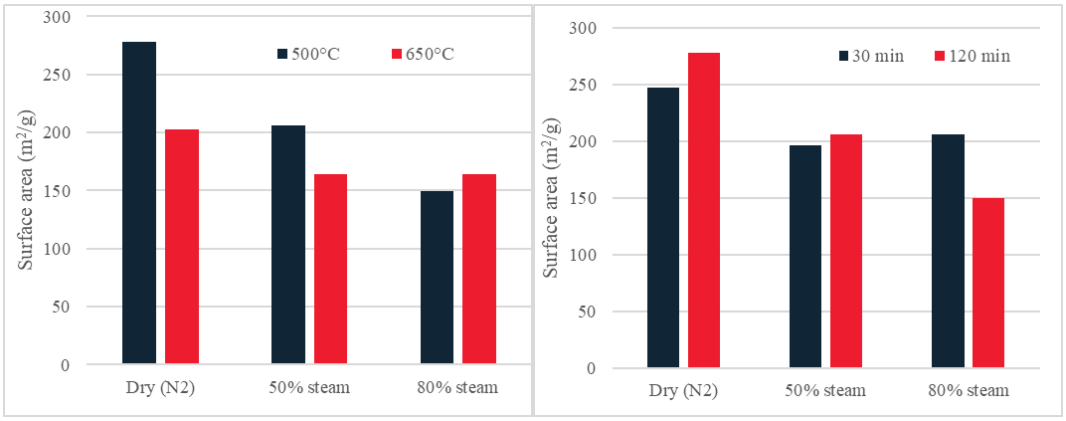

Figure 46: Surface area of boehmite calcined at a) 2 temperatures and b) 2 residence times by BET analysis.

5.1.3. Complete property measurement of calcined alumina resulting from different gas environments:

Figure 47 presents the specific surface area versus loss on ignition (LOI, dried basis) for the boehmite samples calcined under both dry (N_2) and steam (50% or 80% (v/v) steam) conditions at 500°C, 650°C and 850°C with a reaction time of either 30 or 120 min. The LOI was calculated in two ways, the LOI (110) is defined as weight loss from 110°C to 1000°C divided by weight after heating at 110°C, as shown in Figure 47A. For the LOI (300) is defined as weight loss from 300°C to 1000°C divided by weight after heating at 300°C, as shown in Figure 47B. Steam has a significant effect on reducing both the LOI and the specific surface area, except for the boehmite samples calcined at 500 °C. The data from 650°C - 850°C under either dry or steam conditions are almost in a straight line for both LOI (110) and LOI (300), while the effect of steam concentration on either the LOI or the specific surface area is insignificant. This suggests that the 50% (v/v) steam condition is enough to achieve a lower LOI, when compared with the dry condition. In addition, the LOI (110) of samples calcined at 850 °C under steam conditions is lower than that of SGA, while the LOI (300) of these samples is very close to that of SGA. At the same time, the specific surface area of these calcined samples is nearly double that of SGA. This indicates that steam calcination can achieve an equivalent or even lower LOI than that of SGA while maintain a relatively higher specific surface area. The samples calcined at 500°C are different from the samples calcined at higher temperatures. Steam reduces the specific surface area, but steam increases the LOI for some cases, especially for LOI (300). It is reported that steam increases the hydroxyls content on the surface of particles during calcination (Johnson, 1990). These hydroxyls react with each other to increase the growth of grains (Johnson, 1990). Therefore, the specific surface area is decreased by steam. However, the temperature of 500°C is not high enough for the hydroxyls to react effectively. This explains why steam results higher LOI at 500°C, when compared with the dry condition.

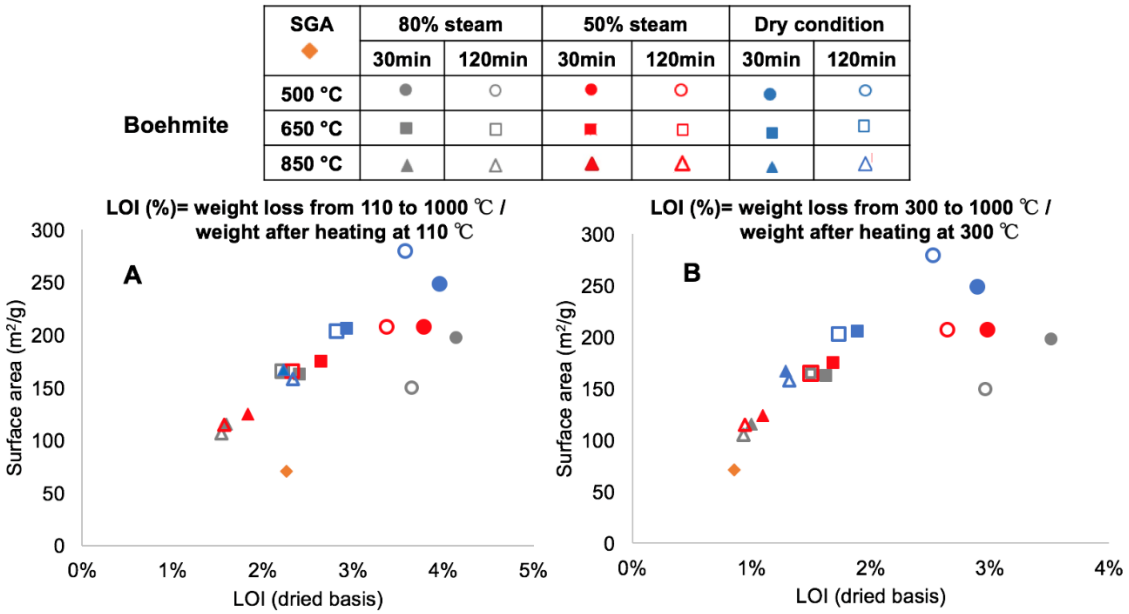

Figure 47: Specific surface area versus loss on ignition (LOI, dried basis) for the boehmite samples calcined under both dry (N_2) and steam (50% or 80% (v/v) steam) conditions at 500, 650 or 850°C with a reaction time of either 30 or 120 min. A) LOI: weight loss from 110 to 1000 °C / weight after heating at 110 °C and B) LOI: weight loss from 300 to1000 °C / weight after heating at 300 °C.

Figure 48 presents specific surface area versus loss on ignition (LOI, dried basis) for the Alcoa Gibbsite samples calcined under both dry (N_2) and steam (50% or 80% (v/v) steam) conditions at 650°C and 850°C with a reaction time of either 10 or 30 min. LOI (110) and LOI (300) are defined in Figure 48. The steam and reaction temperature significantly decrease both the LOI and the specific surface area, while the concentration of steam has a minimal impact on them. The data are almost in a straight line for both LOI (110) and LOI (300). Similar to the boehmite cases, 50% (v/v) steam is enough to achieve a relatively lower LOI, when compared with the dry condition. The LOI (110) of the Alcoa gibbsite samples calcined at 850 °C under steam conditions is lower than that of SGA, while the LOI (300) of these samples is very close to that of SGA. At the same time, the specific surface area of SGA is only about 70% of these samples. Therefore, the samples calcined with steam at 850 °C can reach an equivalent LOI level as SGA while maintain a relatively higher specific surface area. For samples calcined with 80% (v/v) steam at 650°C, the increase of the reaction time from 10 to 30 min significantly reduces both the LOI and the specific surface area. The performance of Alcoa gibbsite is better than that of boehmite, as a 10 min reaction time at 850°C can achieve a similar LOI value as SGA for Alcoa gibbsite, while a 120 min reaction time is required for boehmite.

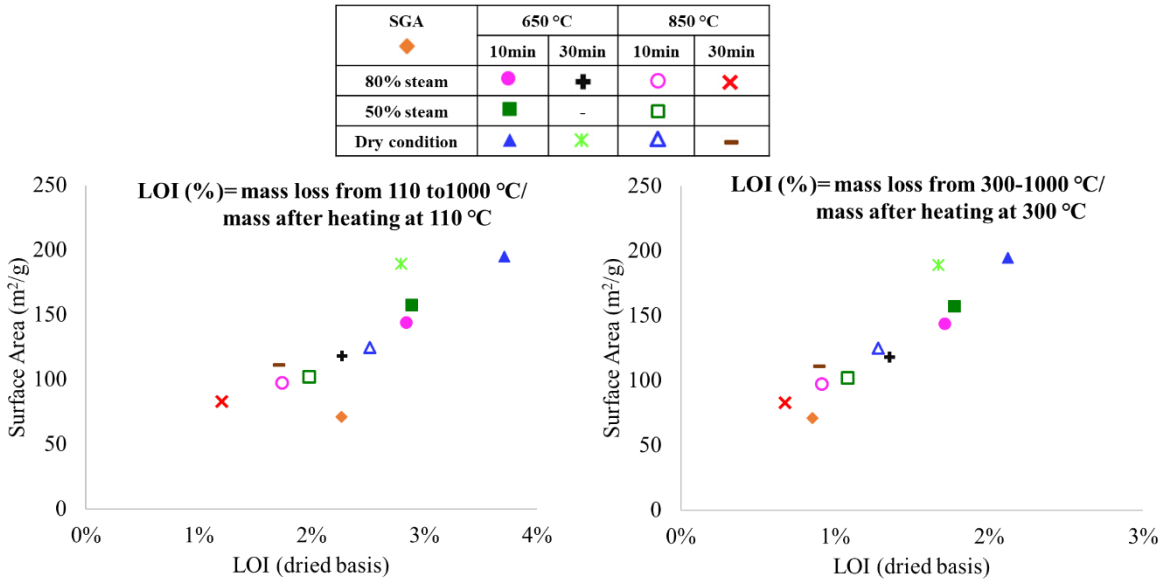

Figure 48: Specific surface area versus loss on ignition (LOI, dried basis) for the Alcoa Gibbsite samples calcined under both dry (N_2) and steam (50% or 80% (v/v) steam) conditions at 650 and 850 °C with a reaction time of either 10 or 30 min. A. LOI: weight loss from 110 to 1000 °C / weight after heating at 110 °C, B. LOI: weight loss from 300 to1000 °C / weight after heating at 300 °C.

Figure 49 presents the nitrogen gas adsorption-desorption isotherms at 77K of SGA, pure boehmite and boehmite or Alcoa gibbsite samples calcined under both dry (N_2) and steam (50% or 80% (v/v) steam) conditions. All of these isotherms are typical type IV-like isotherms with hysteresis loops, which indicates the formation of mesopores in the samples (Bardestani et al., 2019). The pore shape is mostly determined by the loop type (Bardestani et al., 2019). The SGA sample and some boehmite samples calcined at 850°C exhibit type H3 hysteresis, which suggests the existence of slit-shaped pores. Other calcined boehmite samples, the pure boehmite sample and the calcined Alcoa gibbsite samples give a composition of type H2 and H3 hysteresis, which indicates the occurrence of both slit-like pores and “ink-bottle” pores in these samples. The relatively larger loops of the pure boehmite sample, the calcined Alcoa gibbsite samples and some of the boehmite samples calcined at a lower temperature (500°C) reveal a larger total pore volume. In contrast, the relatively smaller loops of the SGA sample and the boehmite samples calcined at a higher temperature (850°C) suggest a smaller total pore volume. For the calcined boehmite samples, both the increase of steam concentration from 0% (dry conditions) to 80% and the increase of temperature reduce the size of the loop and transfer the loop to higher relative pressure, which is associated with a larger pore size. In addition, the effect of steam on the calcined boehmite samples is more significant at a higher temperature (850°C) than at lower temperatures (500°C and 650°C). For the calcined Alcoa gibbsite samples, the effect of steam on the total pore volume is insignificant. The increase of both steam concentration and temperature shift the loop to higher relative pressure, which indicates a larger pore size. For the boehmite samples calcined under dry condition, the increase of reaction time decreases the pore size. In contrast, for those calcined under steam conditions, the increase of reaction time generates larger pores, but this is only obvious at a lower temperature (500 °C).

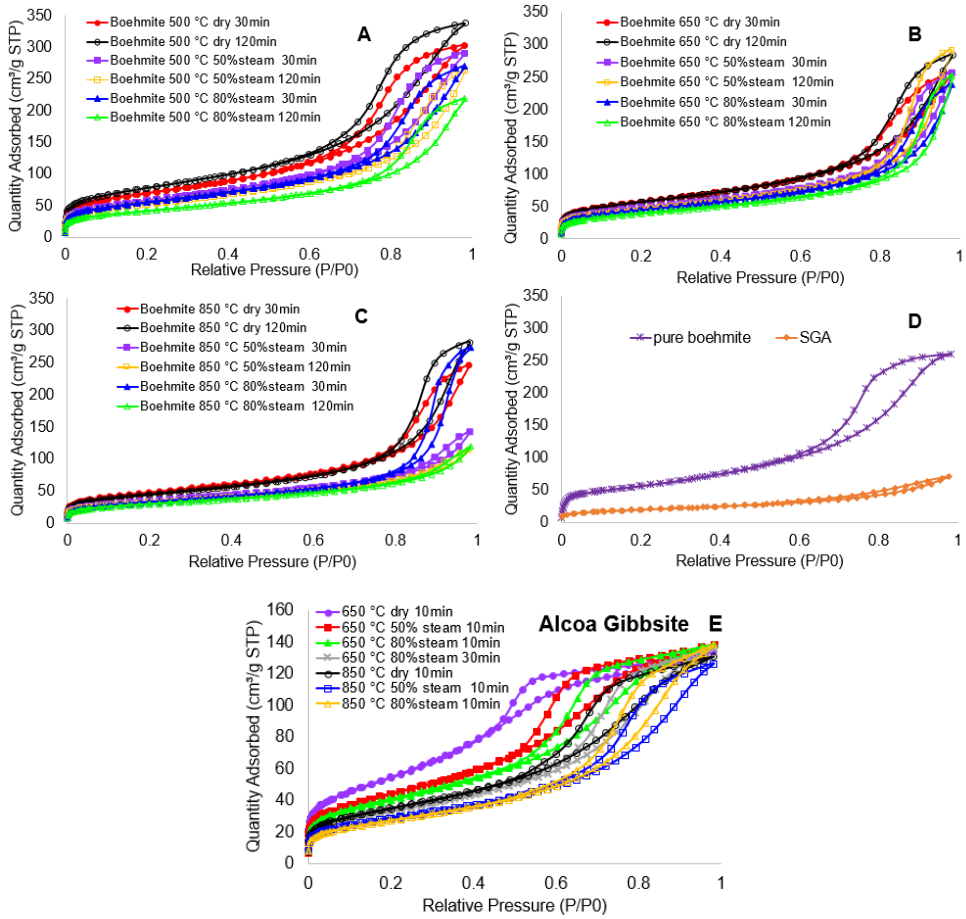

Figure 49: Nitrogen gas adsorption-desorption isotherms at 77K of SGA, pure boehmite and boehmite or Alcoa gibbsite samples calcined under both dry (N_2) and steam (50% or 80% (v/v) steam) conditions. A. Boehmite samples calcined at 500 °C, B. Boehmite samples calcined at 650 °C, C. Boehmite samples calcined at 850 °C, D. SGA and pure boehmite samples, E. Alcoa gibbsite samples calcined at 650 °C and 850 °C.

Figure 50 shows that the pore size distribution calculated with the Barrett-Joyner-Halenda method (BJH) of SGA, pure boehmite and the boehmite or Alcoa gibbsite samples calcined under both dry (N_2) and steam (50% or 80% (v/v) steam) conditions. As shown in Figure 50, the pore size of most calcined boehmite or Alcoa gibbsite samples is larger than that of SGA, which is about 5 nm. Figure 50(A) shows that the pore size distribution of the boehmite samples calcined at 500°C under dry (N_2) condition is similar to that of the pure boehmite sample, with a peak at approximately 9 nm. Steam increases the pore size, with a peak ranging from about 11 to 15 nm. The increase of both the steam concentration and the reaction time increases the peak a bit. At 650°C under dry (N_2) condition (Figure 50(B), the peak of pore size distribution increases to about 11-13 nm, while steam further increases the peak to about 15-18 nm. At 850°C (Figure 50(C)), the peak shifts to approximately 15 nm under dry condition. This suggests that although steam increases the pore size, it also eliminates the pores, especially at higher temperatures for the calcined boehmite samples. The pore size distribution results of the calcined boehmite samples are consistent with the nitrogen gas adsorption-desorption isotherms at 77K, as shown in Figure 49. Other studies indicated that steam increases the pore size significantly, when compared with dry conditions (Hrabě et al., 1992). This is because steam facilitates phase transformation and intensifies diffusion (Hrabě et al., 1992, Angle et al., 2013), which leads to faster nucleation, coarsening and growth (Chinelatto and Tomasi, 2009). The disappeared pores for the boehmite samples calcined with steam at 850°C could be due to the faster growth of particles under steam condition. This generates more rounded particles (as

shown in the SEM images in Figure 51), which eliminates pores between particles. The impact of steam on increasing the pore size is not quite significant at 500°C and 650°C, while steam even has detrimental effect on the pore size distribution at 850°C for the calcined bohemite samples. For the calcined Alcoa gibbsite samples, as shown in Figure 50(D), steam transfers the peak of pore size distribution from about 4-5 nm under dry condition to about 6-9 nm. Therefore, the effect of steam on pore size distribution for the calcined Alcoa gibbsite samples is insignificant.

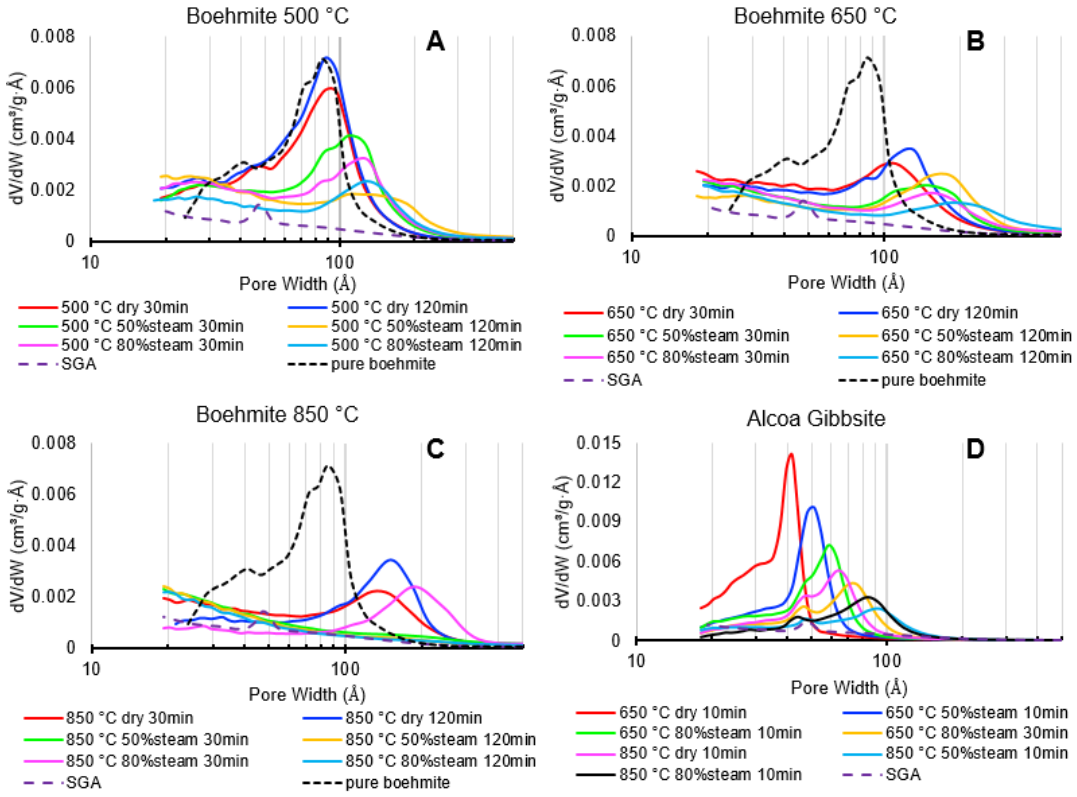

Figure 50: Pore size distribution calculated with the Barrett-Joyner-Halenda method (BJH) of SGA, pure boehmite and the boehmite or Alcoa gibbsite samples calcined under both dry (N_2) and steam (50% or 80% (v/v) steam) conditions. A. Boehmite samples calcined at 500 °C, B. Boehmite samples calcined at 650 °C, C. Boehmite samples calcined at 850 °C, D. Alcoa gibbsite samples calcined at 650 °C or 850 °C.

Figure 51 shows that the SEM images of SGA, boehmite and Alcoa gibbsite and their samples calcined at 850 °C under both dry (N_2) and 80% (v/v) steam conditions. The structure of the SGA sample (Figure 51 (A)) from Alcoa is similar to those of both the uncalcined Alcoa gibbsite sample (Figure 51 (C)) and the Alcoa gibbsite sample calcined at 850°C under dry (N_2) condition for 10min (Figure 51 (F)). However, there are many slit-shaped pores on the surface of the SGA samples and fewer similar pores on the calcined Alcoa gibbsite sample, while almost no pores could be found on the raw Alcoa gibbsite sample. This suggests that calcination generated slit-shaped pores to increase the surface area. In addition, the calcination process does not have an impact on the structure of the particles, except that some parts of the SGA samples were severely fragmented in the industrial reactor. Figure 51 shows that the structures of both the uncalcined and calcined boehmite samples are relatively irregular. Similar to the case of Alcoa gibbsite, calcination does not have an effect on the structure of the boehmite particles. However, there are many fine particles agglomerated on the surface of larger boehmite particles and the shape of most particles became rounded after calcination. The pores of the raw or calcined boehmite particles could not

be easily detected with SEM. Therefore, pores could be formed between the irregular-shaped boehmite particles. The SEM results are yet to be able to provide a conclusive explanation on the influence of steam on either Alcoa gibbsite or boehmite particles. Some studies reported that steam can produce larger crystal aggregates, while dry calcination reduces the size of initial grains (Guzmán-Castillo et al., 2001, Hrabe et al., 2011). This effect of steam was not observed in this study, which could be due to the higher temperature or longer reaction time used in other studies.

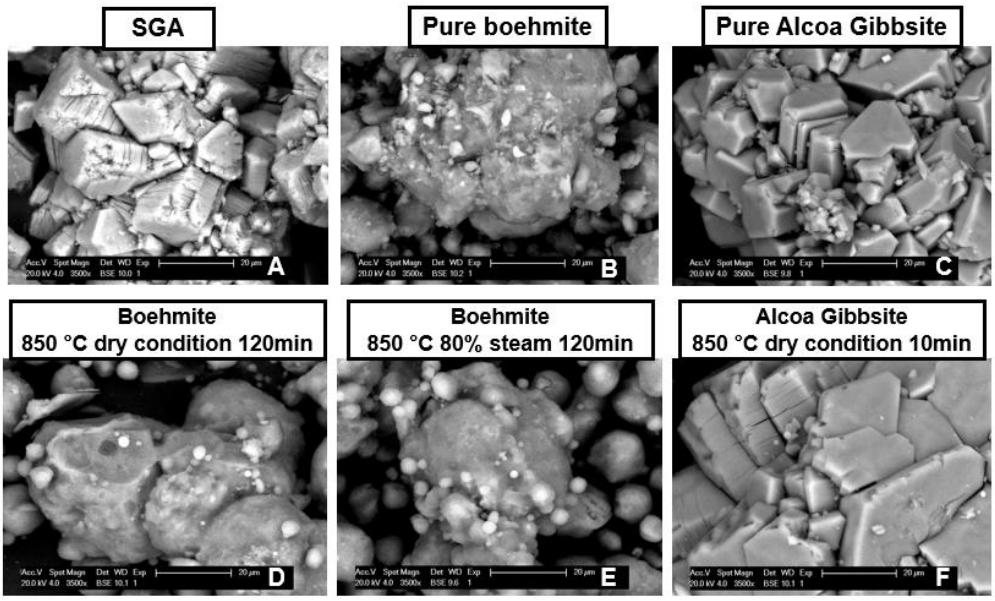

Figure 51: SEM images of uncalcined and calcined samples. A.SGA, B. Pure boehmite, C. Pure Alcoa Gibbsite, D. Boehmite calcined at 850 °C under dry (N_2) condition for 120min, E. Boehmite calcined at 850 °C under 80% (v/v) steam for 120min, F. Alcoa gibbsite calcined at 850°C under dry (N_2) condition for 10min.

5.2. Complete development of new validated alumina calcination models based on effect of gas composition.

5.2.1. Introduction

The alumina calcination process reaction pathway for gibbsite calcination to structurally stable alpha alumina is shown in Eq.13. Each of the different reaction rate constant, k will determine the degree of conversion in each of the calcination stages. The reaction rate constant is also highly dependent on temperature and calcination atmosphere (Fogler, 2016).

$$Gibbsite \xrightarrow{k_1} Boehmite \xrightarrow{k_2} Gamma\ Alumina \xrightarrow{k_3} Theta\ Alumina \xrightarrow{k_4} Alpha\ Alumina \qquad \text{Eq.13}$$

To develop an alumina calcination model, experimental data is fitted using mathematical models developed for crystallisation. Based on literature, the Avrami Equation has been widely used to model alumina calcination processes. The gibbsite calcination process was treated as an overall reaction as seen in Eq.14. Therefore, the reaction rate constants currently available from literature is a combination of k_1, k_2, k_3 and k_4. The Avrami equation is suitable for these calcination reactions as the gibbsite is almost reacted to completion as Smelter Grade Alumina (SGA) is a combination of gamma and theta alumina with trace amounts of alpha alumina.

$$2Al(OH)_3 \xrightarrow{yields} Al_2O_3 + 3H_2O$$ **Eq.14**

5.2.2. Gibbsite to boehmite conversion

5.2.2.1. Methodology

However, to understand the effect of gas composition on the calcination process, each of the individual conversion steps need to be studied separately. For the conversion of gibbsite to boehmite, as shown in Eq.15, a model was developed from the fundamentals of rate law (Fogler, 2016). For the conversion from our starting material, A to our product, B as shown in Eq.16, a mole balance is carried out as shown in Step (i).

$$Al(OH)_3 \xrightarrow{k_G} AlOOH + H_2O$$ **Eq.15**

$$A \xrightarrow{k_1} B$$ **Eq.16**

(i) Mole balance, assuming the volume remains unchanged:

$$\frac{dN_A}{dt} = r_A$$

(ii) Rate law for r, when the reaction rate order, α is approximately set at 1:

$$-r_A = kN_A$$

(iii) Combining rate law and mole balance yields:

$$\frac{-dN_A}{dt} = kN_A$$

(iv) Integrating Equation X with the limit $N_A = N_{A0}$ at t = 0 would give:

$$ln\frac{N_{A0}}{N_A} = kt$$

Where:

N_{A0} = number of moles of A initially.

N_A = number of moles of A remaining (time dependent)

k = reaction rate constant

t = calcination holding time for each sample.

A linear regression of the final equation in Step (iv) would yield a best fit line to estimate the k value for calcination under various temperatures and gas composition. The activation energy, E_A for each condition can be calculated using the Arrhenius Equation as seen in Eq.17. Then by rearranging the Arrhenius equation the activation energy for a given gas composition can be calculated (Eq.18).

$$k = A\exp(-\frac{E_A}{RT})$$ **Eq.17**

$$ln\frac{k_2}{k_1} = \frac{E_a}{R}\left(\frac{1}{T_1} - \frac{1}{T_2}\right) \quad \text{Eq.18}$$

5.2.2.2. Results: Calcination at 300°C – 400°C

Table 12 presents a summary of the key information obtained from small scale gibbsite calcination tests. The reaction temperature is lowered to prevent the further conversion of the boehmite product formed. It was observed that the activation energy calculated for calcination under 50% steam might be lower than expected because the presence of steam has a significant effect on the 300°C cases. For calcination at 300°C, 50% steam concentration by volume was optimum because it yielded the highest amount of conversion. However, the calcination case at 300°C under 80% steam has an opposite effect due to the high steam concentration inhibit the release of water molecules from the gibbsite particle. Similarly, calcination under dry conditions prevented the proper crystallisation of the gibbsite particle to form structurally stable boehmite products. Since Eq.18 is used to estimate the overall activation energy for a given steam concentration, the huge catalytic effect of steam on a 50% volume basis at 300°C has given the overall activation energy estimation a slight bias.

Table 12: Summary of key information for gibbsite to boehmite calcination.

Reaction Temperature (°C)	Steam Concentration (v/v)	Reaction Rate Constant, k_A (min^{-1})	Pre-exponential Constant, A	Activation Energy, E_A (kJ/mol)
300	0	0.010 ± 0.0017	0.16	13.02
	50	0.016 ± 0.00088	0.034	3.47
	80	0.0098 ± 0.0014	0.87	21.34
400	0	0.015 ± 0.0024	0.16	13.02
	50	0.018 ± 0.0040	0.034	3.47
	80	0.019 ± 0.0030	0.87	21.34

For calcination at higher temperatures (400°C), the reaction rate constant is 1.5 – 2 times greater than the reaction rate constant at 300°C clearly indicates that temperature has a significant effect on the rate of reaction.

5.2.2.3. Calcination at 250°C

Table 13 presents the key information obtained from gibbsite calcination at a relatively low temperature of 250°C. At 250°C, some boehmite peaks were detected using XRD but the relative amount detected was not observed in the overall weight loss data. This would suggest that the gibbsite particles were able to crystallise to form a boehmite intermediate before the release of the water molecule then only to form structurally stable boehmite. Eq.19 is a proposed mechanism of the reaction.

The reaction rate constant, k_1 in Table 13 correlates to the crystallisation process whereas the reaction rate constant, k_2 represents the process of losing the water molecule to form boehmite. The values of k_2 are a lot larger than the values of k_1 indicates that the crystallisation process during the conversion of gibbsite to boehmite intermediate is the rate limiting step.

$$Gibbsite \xrightarrow{k_1} Boehmite\ Intermediate \xrightarrow{k_2} Boehmite \quad \text{Eq.19}$$

Table 13: Reaction rate constants for gibbsite to boehmite conversion at 250°C.

Reaction Temperature (°C)	Steam Concentration (v/v)	Reaction Rate Constant, k (min^{-1})	
		k_1	k_2
250	0	0.0069 ± 0.0016	0.059 ± 0.017
	50	0.0076 ± 0.00088	0.047 ± 0.015
	80	0.0030 ± 0.0015	0.074 ± 0.094

5.2.2.4. Model verification

Wang et al. (Wang et al., 2006) had carry out a similar gibbsite calcination reaction under an air atmosphere to simulate gibbsite roasting in a Bayer refinery. At 823K, the reaction rate constant, k was estimated to be approximately 0.234 min^{-1}. The reaction rate constant at a lower temperature of 400°C was then estimated to be approximately 0.0248 min^{-1}. The reaction rate constant, k_{air} at 400°C is slightly greater than the k values from Table 1 indicates that the rate of gibbsite calcination in air is slightly faster than calcination under a pure steam environment.

Wang et al. (Wang et al., 2006) had also estimated the activation energy for boehmite embryo formation to be approximately 44kJ/mol while the activation energy required for the crystallisation process to be approximately 14kJ/mol. The activation energy estimation from Wang et al. (Wang et al., 2006) is higher than the activation energy calculated from our experiments is because Wang et al. (Wang et al., 2006) carried out the calcination experiments at a much higher temperature of 823K. For calcination tests carried out under high temperatures, the conversion of gibbsite to boehmite cannot be isolated and the formation of gamma alumina is expected.

Candela and Perlmutter (Candela and Perlmutter, 1992) have estimated an activation energy value of 142kJ/mol. The activation energy value is much higher than the value obtained from our experiments might be due to the fact that Candela and Perlmutter have not considered the effects of gibbsite particle size on the rate of reaction. The gibbsite used by Candela and Perlmutter (Candela and Perlmutter, 1992) ranged from 38 – 150 microns. Our small-scale calcination tests used gibbsite between 3 - 48 microns. A smaller particle size would allow higher heating rate and would result in lower energy required for complete calcination. A smaller particle size distribution would also reduce the standard deviation of our final result.

Stacey (Stacey, 1987) estimated that the gibbsite composition reaction had an activation energy of 272kJ/mol which is the highest value from literature. This might be because Stacey (Stacey, 1987) used a general activation energy value to fit both gibbsite and boehmite decomposition. This would yield large errors and should not be used for model validation.

5.2.3. Boehmite to SGA (Gamma/Theta Alumina)

The conversion of boehmite to gamma alumina/theta alumina can be seen in Eq.20. The transformation of boehmite to gamma transitional alumina occurs when there is an initial collapse of the boehmite structure due to the hydrogen transfers and water extraction (Krokidis et al., 2001, Wilson, 1979). Generally, a collapse of lattice across the layers with elimination of water between layers (by an internal condensation of protons and hydroxyl groups) was common for the dehydration of layered hydroxides. This is followed by a slight shearing into a monoclinic structure with a movement of layers. The

transformation process is completed by the aluminium migration process filling up the tetrahedral vacant sides.

The experimental data can be used to model the reaction by using fundamental rate laws outlined earlier (Fogler, 2016). The reaction rate constant. k_B can be obtained by carrying out linear regression on Eq.21. Table 14 is a summary of the key information obtained from the analysis of experimental data for the calcination of boehmite to gamma transitional alumina.

$$2Al(OOH) \xrightarrow{k_B} Al_2O_3 + H_2O \quad \text{Eq.20}$$

$$ln\frac{N_{B0}}{N_B} = k_B t \quad \text{Eq.21}$$

Table 14. Summary of key information for boehmite to gamma alumina calcination.

Reaction Temperature (°C)	Steam Concentration (v/v)	Reaction Rate Constant, k_B (min^{-1})	Pre-exponential Constant, A	Activation Energy, E_A (kJ/mol)
450	0	0.0091 ± 0.0078	0.96	28
	50	0.0045 ± 0.0037	0.54	28.33
	80	0.0014 ± 0.0023	0.26	31.56
550	0	0.019 ± 0.020	1.15	28
	50	0.026 ± 0.020	1.61	28.33
	80	0.026 ± 0.022	2.63	31.56
650	0	0.024 ± 0.043	0.91	28
	50	0.031 ± 0.045	1.24	28.33
	80	0.031 ± 0.042	1.89	31.56

Based on the above results, the activation energy required for the conversion of boehmite to gamma transitional alumina is on average at least double the activation energy required during the initial calcination of gibbsite to boehmite. Additionally, the difference of activation energy between the various gas atmospheres is also much lower due to the fact that temperature has a higher effect on the overall reaction. Despite this, the effect of gas composition on the reaction rate constant is similar to what was observed when calcining gibbsite to boehmite.

For the calcination temperature of 450°C, the presence of steam has a negative effect on the overall conversion of boehmite to gamma transitional alumina. The reaction rate constant at 80% steam is almost 6 times smaller than the reaction rate constant at 0% steam conditions. One hypothesis to explain this observation is because the extraction of water molecules between the hydroxide layers is unable to take place due to the saturated amount of water in the gas atmosphere (Krokidis et al., 2001). However, the opposite was observed when the reaction temperature is increased. Steam has a slight catalytic effect on the overall conversion. One hypothesis for this observation is that the higher reaction temperature allows the water extraction process to occur swiftly. Additionally, the higher steam concentration allowed the boehmite particles to fully crystallise before the boehmite structure collapsed.

5.3. Complete measurements of properties of calcined alumina resulting from a high heating rate environment:

5.3.1. Introduction

Section 1.1 reported on the alumina particle properties generated from slow heating rate campaigns. However, heating rate is of critical importance as it determines the phases of alumina that form (either crystalline aluminas or one of many amorphous forms), but also it affects the structure of the particle as it transforms thereby affecting the reaction rate as it progresses.

5.3.2. Methodology

5.3.2.1. Experimental methods

A radiant burner of 5 kW capacity has been used to perform gibbsite calcination under a high heating rate environment. The isometric view of the radiant burner setup is shown in Figure 52a. The dimensions of the radiant burner are 178 mm (L) X 92 mm (W) X 38 mm (H). The active radiant surface area of this burner is 159 mm (L) X 73 mm (W), the 2-D drawing of the radiant burner is shown in Figure 52b. Temperatures of the burner base surface are varied from ambient up to 800°C, based on the vertical distance from the radiant burner surface. The slider joint allows a vertical movement from 40 mm up to 610 mm, measured from the radiant burner surface. The temperature of the burner base surface is continuously monitored using eight K-type thermocouples inserted through the burner base.

Approximately 1.5 g sample was used gibbsite particles are placed on a rectangular crucible and then the crucible is then placed on the burner base directly under the active radiant surface. The crucibles dimensions are 75 mm (L) X 18 mm (W) X 15 mm (H). The sample-bed thickness is approximately twice of the particles, which is in between 75-125 µm. Hence, the particle temperature distribution is assumed to be homogenous. Also, the temperature as a function of the height of the burner has been developed, where the thermocouples were positioned 5 mm above the burner base, and it would be the similar height as the crucibles. During the experiment, gibbsite particles were heated at 650°C, 700°C and 800°C, where the residence time was varied from 30s up to 240s, calcination environment was ambient air. The particles cooled in ambient air for 15 minutes before measuring the weight loss. The ISO 806-2004 methodology was adopted for the LOI measurement, only surface moisture in the alumina samples will be removed and no further calcination process to occur in the TGA, yielding a more accurate LOI value. Details can be found in 5.1.1.4. The characterisation of surface area and pore size distribution can be found in 5.1.3.

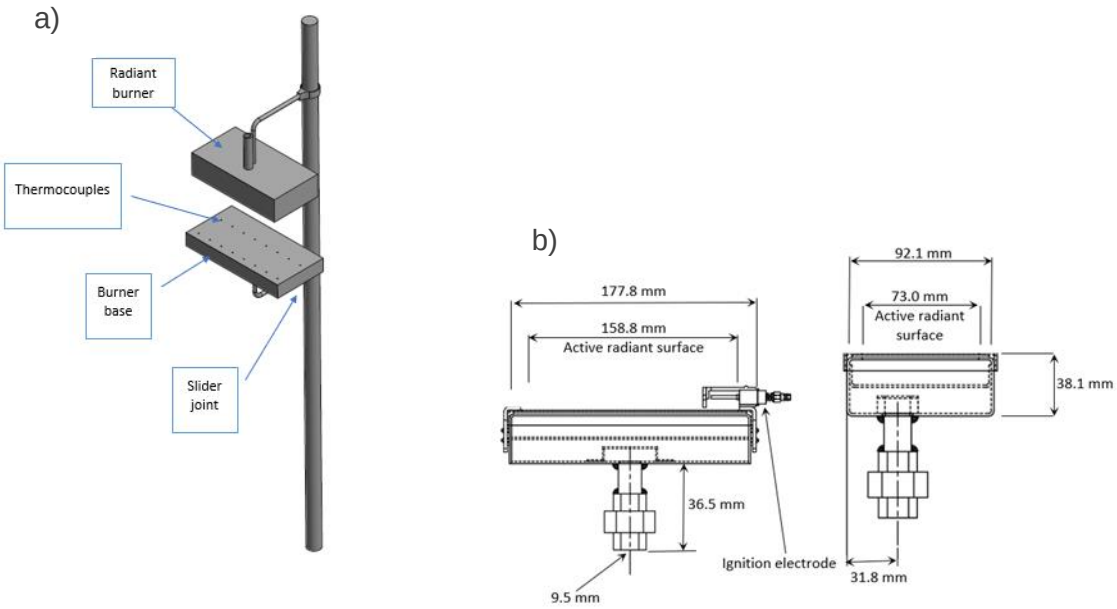

Figure 52: a) Isometric view of the radiant burner and b) 2-D drawing of the radiant burner.

5.3.3. Results and Discussion

Figure 53 presents the profile of loss on ignition (LOI, dried basis) as a function of time (from 30s to 240s) for the gibbsite samples calcined under high heating rate for air atmosphere at temperature ranging from 650°C to 800°C. The reaction temperature and time have a significant influence on the LOI, which has been observed the previous experiments under slow heating rate environment (Sections 5.1 and 1.1). The LOI is expected to reduce further at higher temperature and longer reaction time. The typical calcination temperature in a flash calciner is >950°C with a reaction time 1-2s and then the particles will be conditioned in a holding vessel for several minutes at the particle temperature.

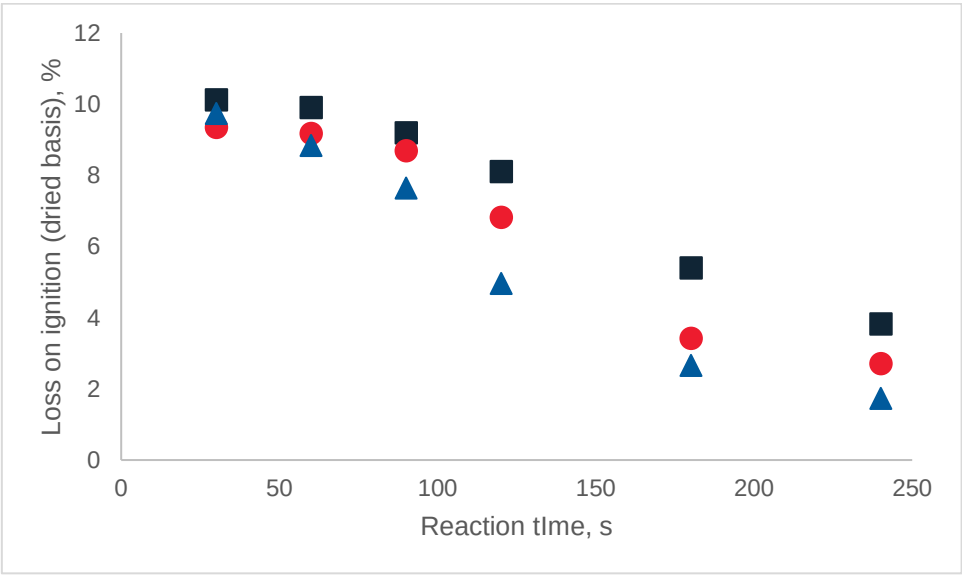

Figure 53: Loss on ignition (LOI, dried basis) vs time for the gibbsite samples calcined under high heating rate in air at temperature ranging from 650°C to 800°C.

Figure 54 presents specific surface area versus loss on ignition (LOI, dried basis) for the gibbsite samples calcined under high heating rate for air atmosphere from 650°C to 800°C with a reaction time of 4 min. In addition, the results from the high heating rate experiments are compared with that of the slow heating rate for both dry (N_2) and steam (50% or 80% (v/v) steam) conditions from 650°C to 850°C with a reaction time of 30 min. The reaction temperature has a significant influence on both the LOI and the specific surface area. However, the temperature of 800°C is not high enough as well as the short reaction time for the hydroxyls to react effectively. Overall, the trend of surface area vs LOI is approaching the SGA. This is similar to the findings from the slow heating rate experiments as shown in Figure 54.

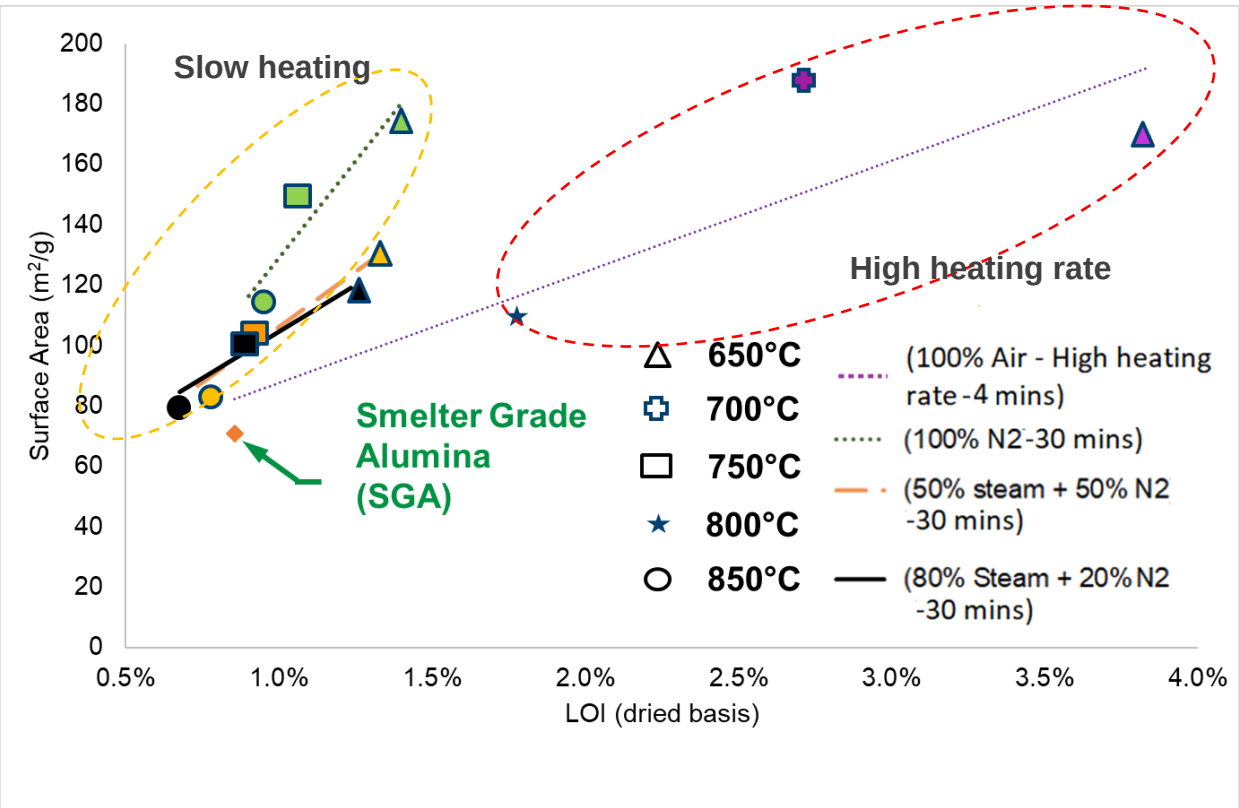

Figure 54: Specific surface area versus loss on ignition (LOI, dried basis) for the gibbsite samples calcined under high heating rate in air from 650°C to 800°C with a reaction time of 4 mins. The results from the previous slow heating rate experiments for both dry (N2) and steam (50% or 80% (v/v) steam) conditions from 650°C to 850 °C with a reaction time of 30 mins are re-analysed and included in this figure. Here, LOI is defined as weight loss from 300°C to1000°C / weight after heating at 300°C.

5.3.4. Crystal Structure

Equation Eq. 22 presents the reaction pathway for gibbsite calcination to structurally stable alpha alumina. Smelter grade alumina (SGA) consists mainly of gamma and theta alumina, with no boehmite left and minimal amounts of alpha alumina. The amounts of theta and gamma alumina formed can be estimated by analysing the crystal structure of the final product formed using XRD (Wefers K. and C., 1987, Wang et al., 2006).

$$Gibbsite \xrightarrow{k_1} Boehmite \xrightarrow{k_2} Gamma\ Alumina \xrightarrow{k_3} Theta\ Alumina \xrightarrow{k_4} Alpha\ Alumina \qquad \text{Eq. 22}$$

Gibbsite begins the dehydration process by the build-up of water vapour pressure within the gibbsite particle and boehmite starts from within the gibbsite reactant (Candela and Perlmutter, 1992) (Whittington and Ilievski, 2004). formation of boehmite from gibbsite can be seen in Eq. 23 and the process stops when

there is a lowering of intracrystalline pressure due to the cracking of the gibbsite reactant (Candela and Perlmutter, 1992).

$$Al(OH)_3 \rightarrow AlOOH + H_2O \quad \textbf{Eq. 23}$$

Boehmite formed is then further dehydrated to form gamma transitional alumina by removing another water molecule as seen in Eq. 24. The conversion mechanism for the dehydration of boehmite to gamma transitional alumina can be described by a collapse of lattice across the layers with the elimination of water between layers by the internal condensation of protons and hydroxyl groups (Krokidis et al., 2001, Wilson, 1979). With the removal of water molecules, there is also an increased in the overall surface area for the gamma transitional alumina. A maximum surface area of 347m^2/g was observed by Vieira Coelho et al. (Vieira Coelho et al., 2007) when dehydrating gibbsite to form SGA.

$$AlOOH \rightarrow \gamma - Al_2O_3 + H_2O \quad \textbf{Eq. 24}$$

The gamma alumina then undergoes crystallisation to form theta transitional alumina as seen in Eq. 25 (Wefers K. and C., 1987). Theta alumina is then finally converted into structurally stable alpha alumina via the crystallisation process shown in Eq. 26 (Wefers K. and C., 1987).

$$\gamma - Al_2O_3 \rightarrow \theta - Al_2O_3 \quad \textbf{Eq. 25}$$

$$\theta - Al_2O_3 \rightarrow \alpha - Al_2O_3 \quad \textbf{Eq. 26}$$

The boehmite, gamma and theta alumina formed are not structurally stable and have the tendency to break down and react further as seen in Eq. 22. Therefore, the levels of boehmite, gamma and theta alumina detected can fluctuate significantly over time as some of the products formed are also converted simultaneously. Figure 55 presents the concentration of crystalline boehmite, gamma and theta formed for gibbsite calcination at 650°C, 700°C and 800°C under air atmosphere and a high heating rate. Since the reaction rate constants, k_2, k_3 and k_4, as shown in Eq. 22, are different, the formation and conversion process can be overlapped one on another. The increased rate of gamma consumption was observed for calcination at 90-120s for all 3 temperatures. The gamma alumina formed initially has been quickly converted into theta alumina. No theta alumina was immediately detected as XRD can only detect theta alumina when it is fully crystalline. The theta alumina formation was then finally detected at 240s. At this reaction time of 240s, more boehmite was converted into gamma alumina, whereas some of the gamma alumina converted to theta alumina. This was also validated when the amount of boehmite detected was the highest between 90 - 120s and gradually decreases as it was being converted into gamma alumina at 240s. Temperature also played a role in maximising the amount of boehmite being formed as boehmite levels peaked at 90s when gibbsite is being calcined at 700°C and 800°C. At a lower temperature of 650°C, it took 120s for boehmite levels formed to reach maximum. No alpha alumina was detected in any of the samples.

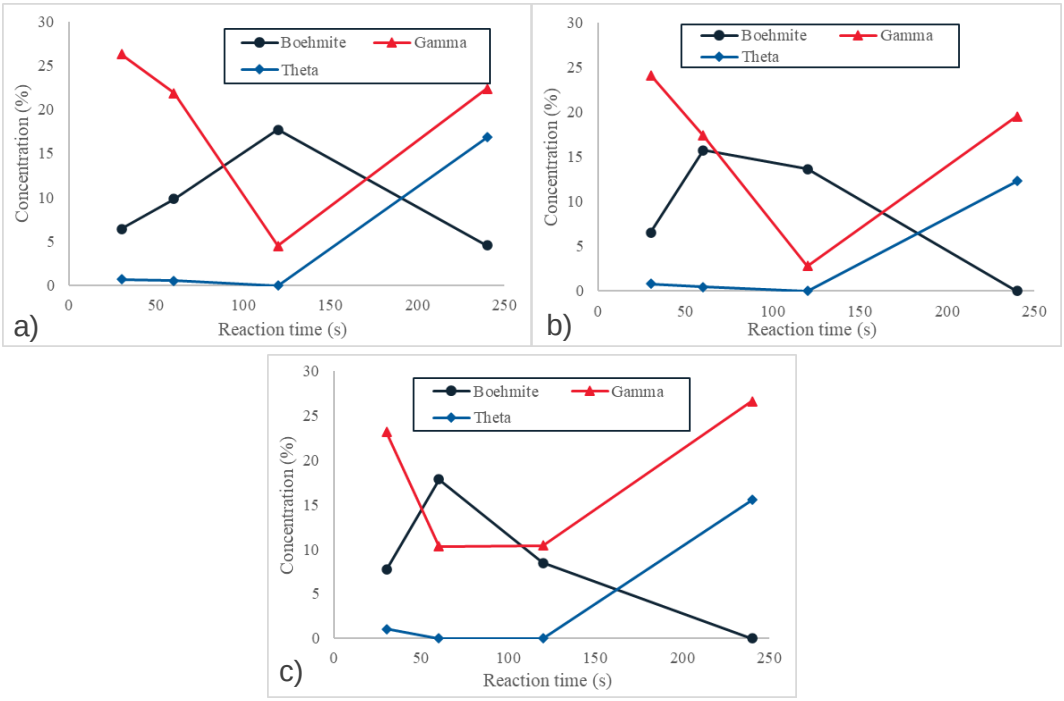

Figure 55: Concentration of boehmite, gamma and theta alumina detected using XRD for gibbsite calcination at a) 650°C, b) 700° and c) 800°C.

5.4. Complete development of new validated alumina calcination models based on the high heating rate experiments.

To develop an alumina calcination model based on the high heating rate experiments presented in Section 5.3, the experimental data is fitted using 2 models developed for crystallisation as shown below:

5.4.1. Methodology

5.4.1.1. Gibbsite to SGA conversion (Rate Laws)

For the conversion of gibbsite to SGA, an overall model was developed from the fundamentals of rate law (Fogler, 2016). For the conversion from the starting gibbsite material, A to the SGA product, B, a mole balance is carried out as discussed in Section 5.2.2.1.

5.4.1.2. Gibbsite to SGA conversion (Numerical Methods)

To verify the accuracy of our model developed earlier using general rate laws, a mathematical model was developed using Numerical Methods. The Numerical method predicts the amount of product formed based on basic guesses for the pre-exponential factor, A and activation energy, E in Eq.18.

The amount of product predicted is then compared to the actual experimental data and the difference is calculated and squared to obtain the residual squared values. These residual squared values are then summed up to minimised to obtain an optimal A, E and reaction rate constant, k values. The optimization process was carried out using Microsoft Excel.

5.4.2. Results

Figure 56 presents the validation of the two calcination models with the experimental data. The initial 1 to 1.5 minute does not fit as well with the experimental data is mainly due to the reactant (gibbsite) temperature was lower the actual set temperature, thus indicating a lower amount of conversion than estimated. Table 15 presents a summary of the key information obtained from the modelling work outlined earlier.

Table 15: Summary of the calculated reaction rate constant, pre-exponential constant and activation energy for gibbsite to SGA calcination under high heating rate environment.

Reaction Temperature (°C)	Reaction Rate Constant from Rate Laws, k (min^{-1})	Reaction Rate Constant from Numerical Methods, k (min^{-1})	Pre-exponential Constant, A	Activation Energy, E_A (kJ/mol)
650	0.51 ± 0.051	0.65	4.92	17.43
700	0.63 ± 0.056	0.75	5.44	17.43
800	0.71 ± 0.074	0.88	5.00	17.43

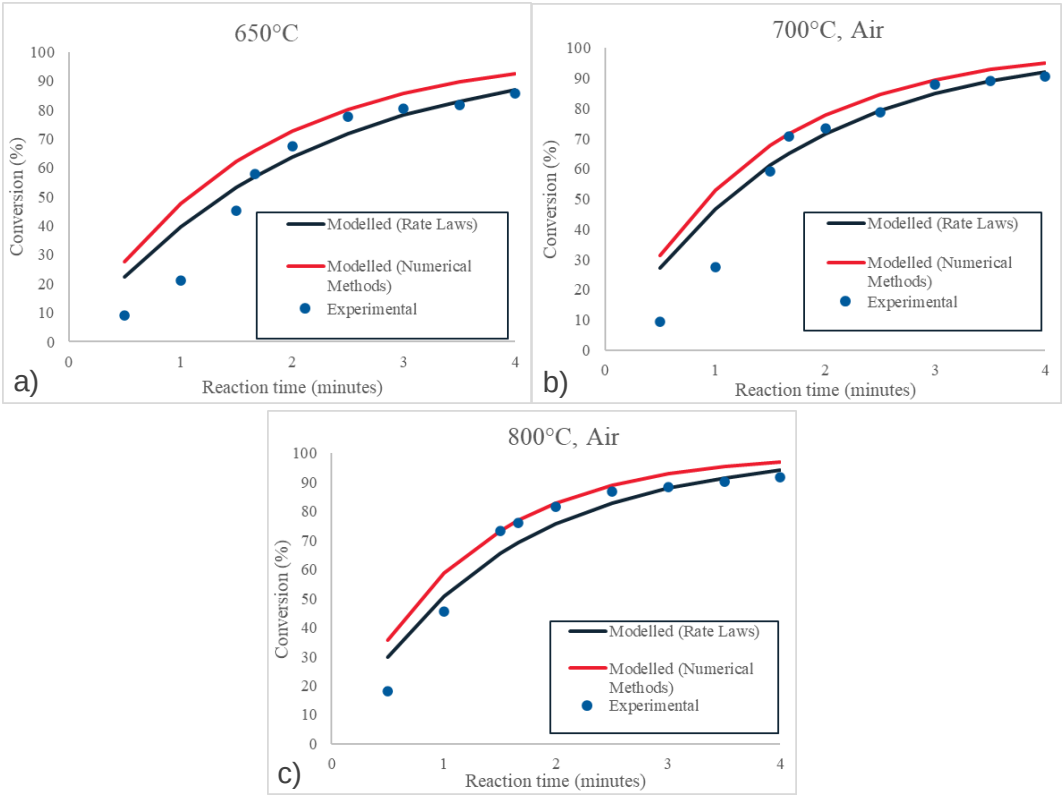

Figure 56: Validation of the rate law and numerical methods calcination models with experimental data at a) 650°C, b) 700°C and c) 800°C.

In our low heating rate experiments, the reaction rate constant, k value obtained for boehmite calcination at 650°C under a pure nitrogen atmosphere was 0.03237 min^{-1} with an activation energy value of approximately 29.67 kJ/mol. Despite having boehmite as the starting material in the low heating rate experiments, results can be cross-compared due to the fact that both gibbsite and boehmite will carry out similar dehydration and crystallisation processes. When gibbsite is exposed to a high heating rate, the reaction rate constant, k was 15 times larger with an activation energy value roughly halved as seen in Table 15. A high k value would indicate an extremely fast reaction, allowing the water molecules to be removed quickly for crystallisation to occur, making the crystallisation process the rate limiting factor. For

our previous experiments under low heating rate, the rate limiting factor could be due to the diffusion of water molecules from the reactant. This is more obvious when the gibbsite or boehmite reactant is reacted under an extremely high steam concentration environment. With a high heating rate setup, the reaction can occur very fast, but the activation energy was also halved compared to a slow heating rate setup. This might be due to the fact that the crystallisation process is still the major determining factor for the activation energy of the entire calcination process. The reactants are required to overcome the activation energy required for the crystallisation process to occur. From the literature, there is little work on high heating rate gibbsite calcination experiments due to the complexity of the experimental setup. In order to verify the model derived from our experimental data, the activation energy values will be compared to similar experiments carried out at low heating rates (less than 25°C per minute).

Wang et al. (Wang et al., 2006) found that the activation energy was 44kJ/mol when calcined at 550-650°C, which is very close to the temperature range our experiments were carried out. Similarly, Jovanovic et al. (Jovanović et al., 1992) found the activation energy was closer to 53kJ/mol when gibbsite is being calcined at 883K. Despite this, (Lopushan et al., 2007) estimated an activation energy value of 150kJ/mol at a wider calcination temperature range of 170 – 510°C. Earlier works by Stacey (Stacey, 1987) and Candela and Perlmutter (Candela and Perlmutter, 1992) estimated the activation energy values to be in the 260 – 272kJ/mol. From Choi et al. (Choi et al., 2009) we know that the activation energy values can be reduced when subjected to a high heating rate. This is due to a lowering of the activation energy for the nucleation and growth phase during crystallisation. Therefore, our estimation of 17kJ/mol is reasonable.

5.5. References

ANGLE, J. P., MORGAN, P. E. D. & MECARTNEY, M. L. 2013. Water Vapor-Enhanced Diffusion in Alumina. *Journal of the American Ceramic Society,* 96**,** 3372-3374.

BAGWELL, R. B. & MESSING, G. L. 1999. Effect of seeding and water vapor on the nucleation and growth of (alpha)-Al2O3 from (gamma)-Al2O3. *Journal of the American Ceramic Society,* 82**,** 825.

BARDESTANI, R., PATIENCE, G. S. & KALIAGUINE, S. 2019. Experimental methods in chemical engineering: specific surface area and pore size distribution measurements—BET, BJH, and DFT. *The Canadian Journal of Chemical Engineering,* 97**,** 2781-2791.

CANDELA, L. & PERLMUTTER, D. D. 1992. Kinetics of boehmite formation by thermal decomposition of gibbsite. *Industrial & Engineering Chemistry Research,* 31**,** 694-700.

CHINELATTO, A. S. A. & TOMASI, R. 2009. Influence of processing atmosphere on the microstructural evolution of submicron alumina powder during sintering. *Ceramics International,* 35**,** 2915-2920.

CHOI, Y., JUNG, M. & LEE, Y.-K. 2009. Effect of Heating Rate on the Activation Energy for Crystallization of Amorphous Ge[sub 2]Sb[sub 2]Te[sub 5] Thin Film. *Electrochemical and solid-state letters,* 12**,** F17.

COURTIAL, R., TRAMBOUZE, Y. & PRETTRE, M. 1966. Influence des Conditions du Traitment Thermique sur la Teneur en Boehmite des Produits de Deshydration Partielle de l'Hydrargillite. *R. C. Acad. Sci., ,* 242**,** 1607-1610.

FOGLER, H. S. 2016. *Elements of Chemical Reaction Engineering, 5th Edition*, Pearson.

GUZMÁN-CASTILLO, M. L., BOKHIMI, X., TOLEDO-ANTONIO, A., SALMONES-BLÁSQUEZ, J. & HERNÁNDEZ-BELTRÁN, F. 2001. Effect of Boehmite Crystallite Size and Steaming on Alumina Properties. *The Journal of Physical Chemistry B,* 105**,** 2099-2106.

HRABE, Z., KOMARNENI, S., PACH, L. & ROY, R. 2011. The influence of water vapor on thermal transformation of boehmite. *Journal of Materials Research,* 7**,** 444-449.

HRABĚ, Z., SPALDON, O. M., PACH, L. & KOZÁNKOVÁ, J. 1992. Thermal transformations of boehmite gel in controlled furnace atmospheres. *Materials Research Bulletin,* 27**,** 397-404.

INUI, T., MIYAKE, T., FUKUDA, K. & TAKEGAMI, Y. 1983. Control of pore structures of γ-alumina by the calcination of boehmite prepared from gibbsite under specific conditions. *Applied catalysis,* 6**,** 165-173.

JOHNSON, M. F. L. 1990. Surface area stability of aluminas. *Journal of Catalysis,* 123**,** 245-259.

JOVANOVIĆ, N., NOVAKOVIĆ, T., JANAĆKOVIĆ, J. & TERLECKI-BARIČEVIĆ, A. 1992. Properties of activated alumina obtained by flash calcination of gibbsite. *Journal of Colloid and Interface Science,* 150**,** 36-41.

KROKIDIS, X., RAYBAUD, P., GOBICHON, A.-E., REBOURS, B., EUZEN, P. & TOULHOAT, H. 2001. Theoretical Study of the Dehydration Process of Boehmite to γ-Alumina. *The journal of physical chemistry. B,* 105**,** 5121-5130.

LOPUSHAN, V. I., KUZNETSOV, G. F., PLETNEV, R. N. & KLESHEV, D. G. 2007. Kinetics of phase transitions of gibbsite during heat treatment in air and in water vapor. *Refractories and Industrial Ceramics,* 48**,** 378-382.

ROUQUEROL, J., ROUQUEROL, F. & GANTEAUME, M. 1975. Thermal decomposition of gibbsite under low pressures: I. Formation of the boehmitic phase. *Journal of catalysis,* 36**,** 99-110.

STACEY, M. H. 1987. Kinetics of decomposition of gibbsite and boehmite and the characterization of the porous products. *Langmuir,* 3**,** 681-686.

VIEIRA COELHO, A. C., SOUZA SANTOS, H. D., KIYOHARA, P. K., MARCOS, K. N. P. & SOUZA SANTOS, P. D. 2007. Surface area, crystal morphology and characterization of transition alumina powders from a new gibbsite precursor. *Materials research (São Carlos, São Paulo, Brazil),* 10**,** 183-189.

WANG, H., XU, B., SMITH, P., DAVIES, M., DESILVA, L. & WINGATE, C. 2006. Kinetic modelling of gibbsite dehydration/amorphization in the temperature range 823–923K. *The Journal of physics and chemistry of solids,* 67**,** 2567-2582.

WEFERS K. & C., M. 1987. *Oxides and hydroxides of aluminum*, Alcoa Research Laboratories.

WHITTINGTON, B. & ILIEVSKI, D. 2004. Determination of the gibbsite dehydration reaction pathway at conditions relevant to Bayer refineries. *Chemical engineering journal (Lausanne, Switzerland : 1996),* 98**,** 89-97.

WILSON, S. J. 1979. The dehydration of boehmite, γ-AlOOH, to γ-Al2O3. *Journal of solid state chemistry,* 30**,** 247-255.

XU, B. & SMITH, P. 2012. Dehydration kinetics of boehmite in the temperature range 723–873K. *Thermochimica acta,* 531**,** 46-53.

6. Integrate the SEVR into the calcination process

6.1. Complete detailed techno-economic evaluation of both beam-up and beam-down configuration for a range of typical conditions.

6.1.1. Beam-up configuration

6.1.1.1. Assess total optical efficiency using modelling tools developed by CSIRO

Optimised heliostat field layouts for the Pinjarra site were calculated for 50MW$_{th}$ direct calcination solar expanding vortex receiver (SEVR) designs using CSIRO's Heliosim (Potter et al., 2018) software. Various heliostat designs, receiver aperture radii, particle optical properties and effective receiver temperatures were considered. It was found that a small heliostat design with accurate facets gave significantly higher efficiencies (by 10 percentage points) when compared to the standard large heliostat design with relatively inaccurate facets. The small heliostat design was also found to allow the high concentration ratios necessary for high operating temperatures to be achieved without a secondary concentrator.

The direct calcination of alumina in a solar receiver, however, suffers from significant intermittency due to limited day light hours, cloud cover, etc. In the present work, therefore, we revisited the 50MW$_{th}$ case study, updated with optical properties and dimensions representative of an SEVR used to provide hot air at 1100°C for the indirect calcination of alumina. This indirect approach has the advantage of allowing particles with more desirable properties, such as sintered bauxite, to be used in the receiver. Sintered bauxite particles such as CARBO HSP are frequently considered for solar particle receiver applications due to their high solar absorptance and durability (Ho, 2016). More detailed optical and thermal models for the SEVR have also been implemented. Previously only the aperture geometry was considered. In the present work, the full receiver geometry is considered for both the optical (i.e. ray tracing) and heat transfer models. This allows solar absorption, thermal emission, convection loss and conduction loss to be calculated more accurately.

Finally, a comparison between the Pinjarra and Learmonth sites has been performed on both efficiency and levelised cost bases. Learmonth, due to its higher solar resource, allows improvements in both measures. The minimisation of levelised cost is used to determine optimum the tower height and aperture radius for both sites.

6.1.1.2. Sites

Two potential sites are considered: Pinjarra and Learmonth in Western Australia. The site location and solar resource parameters are summarised in

Table 16 and

Table 17, respectively. Visualisations of the annual average DNI for both sites are presented in Figure 57. Although both sites have similar DNI at the Equinox design point, Learmonth has a significantly higher annual insolation, making it a more suitable site for a CSP plant. Learmonth also has a more equatorial latitude, which can allow for more compact heliostat fields but can also slightly increase cosine losses due to the angles between the sun and receiver being larger for most of the heliostat field.

Following our previous work, a Buie sun shape with a circumsolar ratio of 0.02 (Buie et al., 2003), and a 20km visibility atmospheric attenuation model (Kistler, 1986) is used for both sites.

Table 16: Site location parameters.

Location	Pinjarra, WA	Learmonth, WA
Latitude (°)	-32.64	-22.23
Longitude (°)	115.95	114.08

Table 17: Site solar resource parameters.

Elevation (m)	3	6
Time zone offset (hours)	UTC +8	UTC +8
Location	Pinjarra, WA	Learmonth, WA
Annual insolation (kWh/m^2)	2280	2740
Equinox design point DNI (W/m^2)	982	984
Insolation source	2015 Pinjarra Bureau of Meteorology data	Learmonth Airport 943020 RMY data

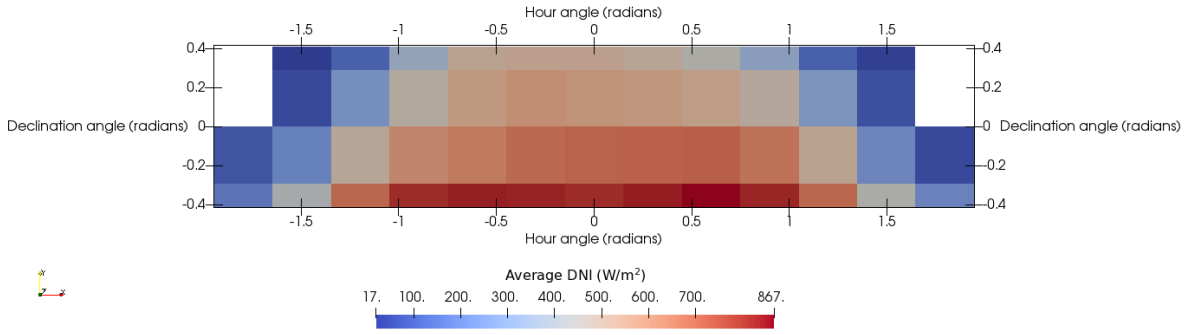

(a) Pinjarra

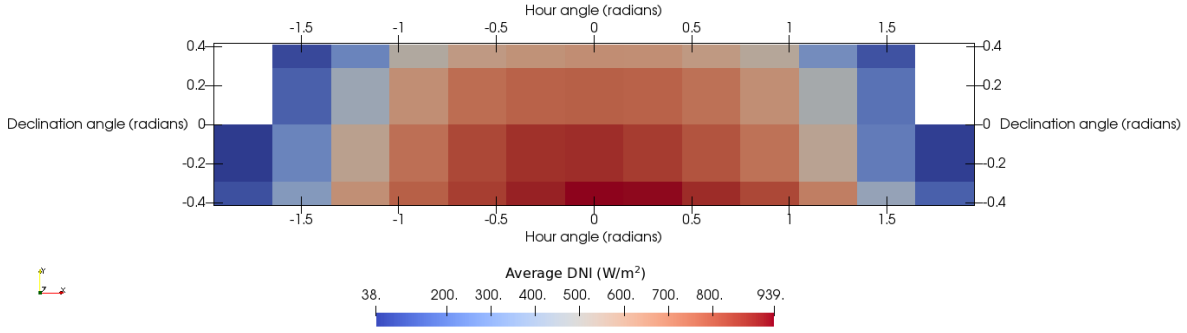

(b) Learmonth

Figure 57: Average DNI histograms for the Pinjarra and Learmonth sites.

6.1.1.3. Heliostat mirror geometry

The small heliostat design with accurate facets from our previous work is used for all cases. The properties of this heliostat are summarised in Table 18. The small facet size and low slope error of this heliostat is required for the present high temperature receiver application, as they allow relatively small receiver apertures without excessive spillage losses.

Table 18: Heliostat parameters.

Shape	Rectangular paraboloid
Width (m)	2.92
Height (m)	2.92
Reflective area fraction	1.0
Width facets	1
Height facets	1
Surface slope error (mrad)	1.0
Tracking error (mrad)	0.3
Actuation	Azimuth-Elevation

6.1.1.4. Receiver geometry

A 50MW$_{th}$ solar expanding vortex receiver (SEVR) of fixed body geometry is considered, however the aperture diameter is left open for optimisation. A dimensioned and labelled cross section view of the cylindrical 50MW$_{th}$ receiver with a 5500mm diameter aperture is presented in Figure 58. The body geometry of 7750mm internal diameter and 12000mm internal length was approximated by residence time scaling of the smaller experimental receiver being tested by the University of Adelaide. The inlet of the particle vortex is at the back of the receiver in the conical region, and the outlet is near the front of the receiver. The particle vortex envelope is expected to closely follow the internal shape of the receiver. When mounted on the tower, the receiver is angled downward towards the field with an elevation angle of -20°. This elevation angle is fixed due to the vortex hydrodynamics. Geometrically, the aperture diameter can extend right up to the internal diameter of 7750mm. Practically, however, the aperture diameter must be smaller than the internal diameter to minimise particle attrition and convective cooling losses.

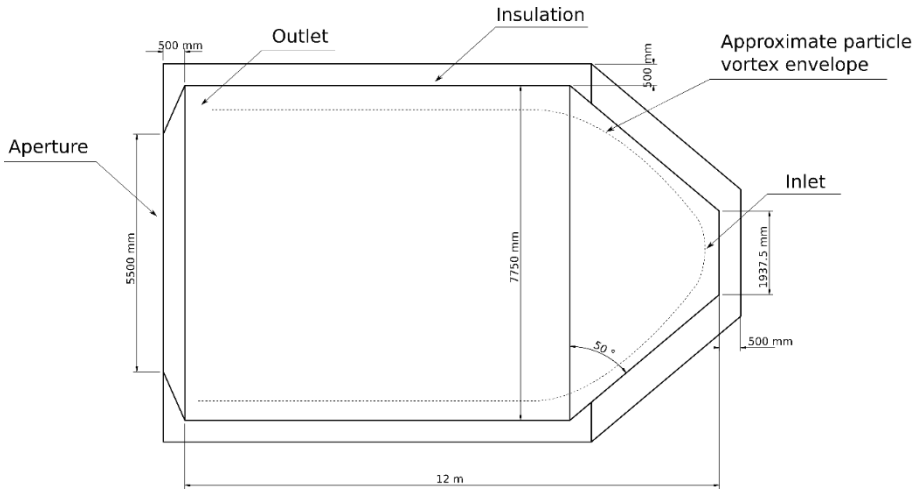

Figure 58: Side cross section view of a 50MW$_{th}$ SEVR receiver with a 5500mm aperture diameter.

6.1.1.5. Physical modelling

Heliostat field optics are simulated using ray tracing, and the receiver heat transfer is simulated using a simple power balance model. Both the optics and heat transfer models are implemented in CSIRO's Heliosim (Potter et al., 2018) software framework. Whilst previously only the aperture geometry was considered, in the present work a surface mesh describing the full receiver geometry is included in the ray tracing scene, Figure 59. By assigning optical properties to the internal surfaces of the SEVR that are representative of that to be expected of the particle vortex envelope, and considering multiple ray reflections inside the cavity, the absorption of solar radiation by the receiver can be more accurately estimated. Furthermore, ray tracing can also be used to numerically calculate view factors of the internal

surfaces, Figure 60, and therefore more accurately estimate the thermal radiation losses from the cavity. The optical properties assumed for the internal surfaces of the receiver when performing the ray tracing simulations are summarised in Table 19. These values were estimated by noting the intrinsic solar reflectance and thermal emittance of Carbo HSP (0.066 and 0.843, respectively (Ho, 2016)), and scaling them by small factors to account for the 3D cloud nature of the particle vortex (i.e. photons will bounce around between particles, therefore slightly increasing radiation absorption). It should be noted that these values are approximations only, and in reality, they will vary as a function of the particle distribution within the receiver. Determining this distribution computationally requires two phase flow Navier-Stokes simulations, which will be assessed outside the scope of this project.

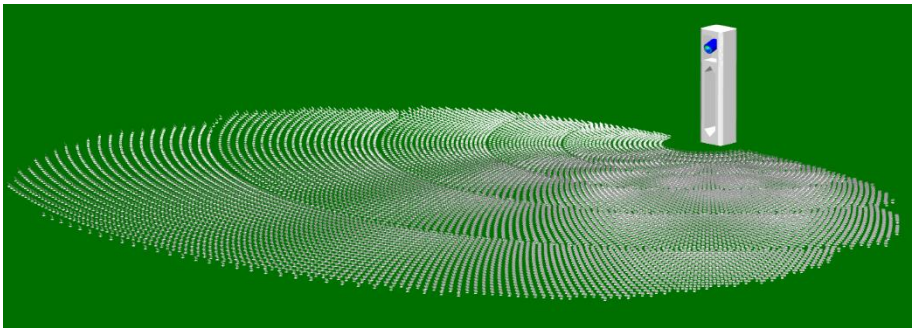

(a) Facility view from south east

(b) Facility view from east, with incident and reflected rays indicated in yellow

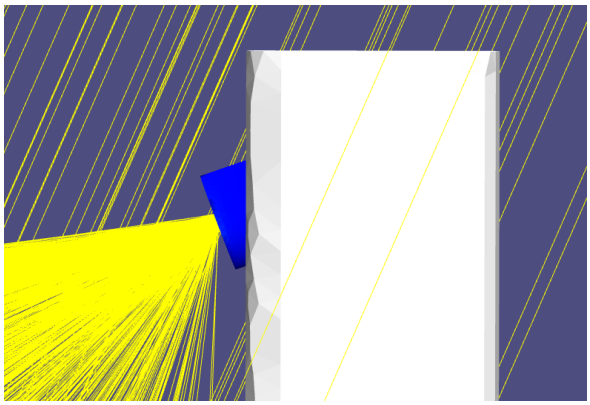

(c) Detailed view of receiver and tower from east

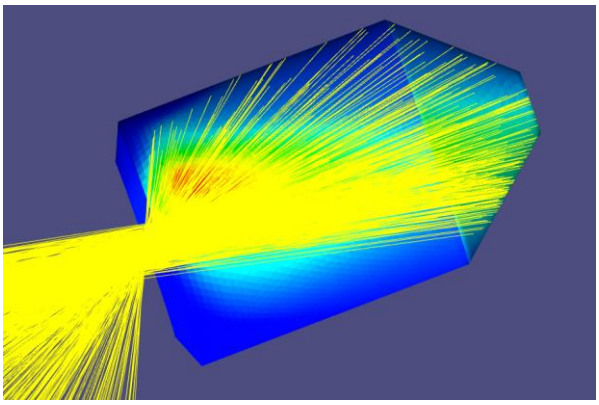

(d) Detailed view of receiver and tower from east, with receiver casing and tower hidden

Figure 59: Visualisation of the SEVR ray tracing model in Heliosim (80m aperture centroid elevation, 2750mm aperture radius, Learmonth site).

Table 19: Assumed optical properties for internal surfaces of the SEVR.

Parameter	Value	Description
$\rho_{s,i}$	0.05	Solar reflectance of the internal surfaces
$\epsilon_{t,i}$	0.85	Thermal emittance of internal surfaces

After the amount of solar radiation absorbed by the internal surfaces of the cavity has been determined via ray tracing, the receiver heat transfer is modelled by assuming fixed ambient (T_a), internal (T_i), and external temperatures (T_e), and performing a simple power balance on the internal surfaces (subscript *i)*:

$$q_{\text{out}} = q_{\text{solar},i} - q_{\text{loss},i} \quad \textbf{Eq.27}$$

where q_{out} is the thermal power captured by the receiver, $q_{solar,i}$ is the solar radiant flux absorbed by the internal surfaces, and $q_{loss,i}$ are the thermal losses from the internal surfaces. The thermal losses are due to thermal radiation loss through the aperture ($q_{rad,i}$), conduction through the receiver wall ($q_{cond,i}$) and convection losses through the aperture ($q_{conv,i}$):

$$q_{\text{loss},i} = q_{\text{rad},i} + q_{\text{cond},i} + q_{\text{conv},i} \quad \textbf{Eq.28}$$

$$q_{\text{rad},i} = f_{\text{view},i} A_i \epsilon_{t,i} \sigma \left(T_i^4 - T_a^4\right) \quad \textbf{Eq.29}$$

$$q_{\text{cond},i} = A_i k \frac{(T_i - T_e)}{\Delta t} \quad \textbf{Eq.30}$$

$$q_{\text{conv},i} = A_{\text{conv},i} h (T_i - T_e) \quad \textbf{Eq.31}$$

The additional parameters used in **Eq.29**, **Eq.30** and **Eq.31** are described in Table 20. It should be noted that due to the absence of experimental results or CFD modelling for this receiver concept, all of these parameters except $f_{view,I}$ and A_i are subject to a high level of uncertainty Table 20.

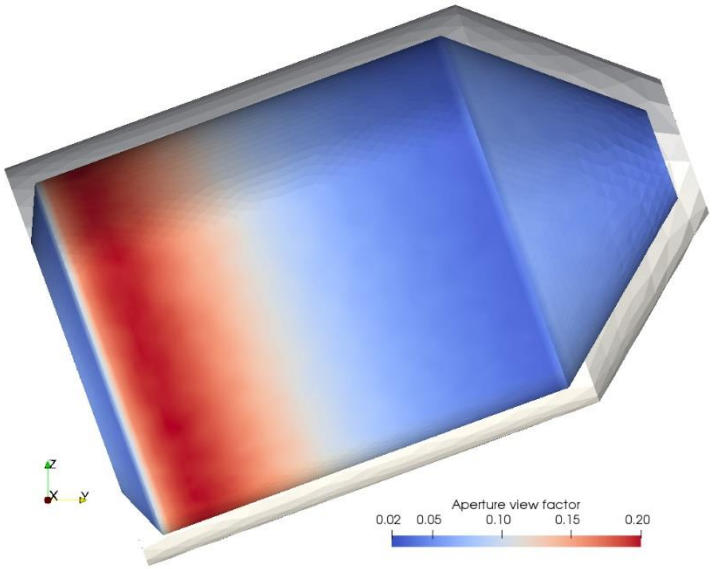

Figure 60: Aperture view factor distribution for the internal surfaces of the SEVR. Multiple ray reflections and an effective thermal emittance of the particle vortex envelope is considered.

Table 20: Assumed heat transfer parameters of the SEVR.

Parameter	Value	Units	Description	Notes
$f_{view,i}$	Variable	-	Area-weighted average view factor of aperture from internal surfaces	Calculated via Monte Carlo ray tracing.
A_i	Variable	m^2	Area of internal surfaces	Assumed to represent the surface area of the particle vortex envelope.
$\epsilon_{t,i}$	0.85	-	Thermal emittance of internal surfaces	Value selected to approximate the expected effective thermal emittance of the particle vortex envelope.
T_i	1373	K	Temperature of internal surfaces	Assumed equal to targeted outlet temperature of 1100°C.
T_e	Variable	K	Temperature of external surfaces	Assumed equal to the ambient temperature, to produce conservative (i.e. higher) convection and conduction losses.
Δt	0.5	m	Insulation thickness	Based on typical thickness of insulation required for high temperature tubular cavity receivers.
k	0.25	W/m/K	Insulation thermal conductivity	Based on value for 128kg/m^3 Superwool blanket at 1000°C .
$A_{conv,i}$	Variable	-	Convective area	Following the Clausing model (Clausing et al., 1987) for cavity receivers implementing tubular-based heat transfer, the receiver is divided into stagnant (upper) and convective (lower) zones separated by a horizontal plane intersecting the upper aperture lip.
h	20	$W/m^2/K$	Convection heat transfer coefficient	Based on doubling the typical value (10 $W/m^2/K$) used for tubular cavity receivers, to account for increased convection losses due to the vortex hydrodynamics.

A final constraint on the receiver thermal output is its ability to operate at off-design conditions. In the present work, the SEVR is assumed to only be able to operate at thermal outputs between 30% and 110% of the 50MW_{th} design capacity. The high turndown ratio of 30% reflects the known difficulty of operating particle receivers at off-design conditions. Again, there is significant uncertainty in these limits and the accuracy will be reassessed as the experimental and CFD investigations progress.

6.1.1.6. Heliostat field layout optimisation

For a fixed receiver design (including its elevation above the ground), an optimised heliostat field layout can be calculated using the Heliosim software. The objective function to be maximised when optimising the heliostat field layout is the annual optical efficiency, subject to the constraint that the design point thermal power of 50MW_{th} is achieved. Algorithms from the NLopt nonlinear optimisation library (Johnson S.G.) are used in Heliosim to perform the optimisation iterations. The variables to be optimised are the 5 parameters defining the customised radially staggered layout pattern implemented in Heliosim (dense to radially staggered transition distance, minimum and maximum azimuthal spacing, zone reset distance, radial spacing between rows and zones).

6.1.1.7. Annual performance modelling

Once an optimised field layout has been calculated, the annual thermal energy captured by the receiver is estimated. The region of the sky occupied by the sun during the year is discretised using Delaunay triangulation, resulting in 52 sample points forming the vertices of a triangular mesh in hour angle and declination angle space. Each triangle has approximately equal area. Ray tracing simulations are performed for each of the sun positions represented by the mesh vertices, and the optical efficiency for each recorded. The optical efficiency (η_{optical}) for any sun position during the year can then be estimated by two-dimensional linear interpolation within each triangle. The solar energy absorbed the internal surfaces of the SEVR ($q_{solar,i}$ in Eq.27) can then be calculated via:

$$q_{\text{solar},i} = \eta_{\text{optical}} A_r I_{\text{DNI}} \qquad \textbf{Eq.32}$$

where A_r is the reflective (i.e. aperture) area of the heliostat field, and I_{DNI} is the direct normal irradiance. Eq.27 through to Eq.31 can then be used to calculate the thermal output from the receiver, and the off-design constraint applied:

$$15\ \text{MW} \leq q_{out} \leq 55\ \text{MW} \qquad \textbf{Eq.33}$$

The annual thermal energy output from the receiver is then calculated by trapezoidal integration over the annual time series:

$$E_{\text{out}} = \sum_{j}^{n=8760} q_{\text{out},j} \Delta t_j \qquad \textbf{Eq.34}$$

The 8760 annual points corresponds to $\Delta t_j = 3600\text{s}$, which is the usual resolution of TMY data. The overall efficiency of the heliostat field and receiver system is calculated as the annual thermal energy output from the receiver divided by the annual solar energy incident on the heliostat field aperture area:

$$\eta = \frac{E_{\text{out}}}{E_{\text{incident}}} = \frac{\sum_{j}^{n=8760} q_{\text{out},j} \Delta t_j}{\sum_{j}^{n=8760} A_r I_{\text{DNI},j} \Delta t_j} \qquad \textbf{Eq. 35}$$

6.1.1.8. Preliminary cost estimation

A simple cost model has been implemented in order to allow a “levelised cost of heat” to be calculated and optimal configurations of the heliostat field, tower and receiver subsystems to be determined. A breakdown of the cost model inputs is presented in Table 21. Notably, balance of plant and storage costs are not included due to lack of data for an indirect calcination plant. The balance of plant and storage costs, however, should be constant for a fixed receiver capacity as considered in this study, and this reduced cost model can still be used to determine the most cost effective heliostat field, tower and receiver designs. The “levelised cost of heat” (LCOH) is calculated by dividing E_{out} from Eq.34 by the lifetime cost. It should be stressed that this LCOH value, due to the omission of balance of plant and storage costs, is merely a metric to compare various heliostat field, tower and receiver subsystem designs, and does not reflect the levelised cost of the complete plant.

Table 21: Cost model breakdown for the SEVR, tower and heliostat field subsystems.

Item	Value	Units	Basis
Site-to-field land area ratio	1.3	-	SolarPILOT value (Wagner and Wendelin, 2018)
Land purchase cost	3.5	AUD/m^2 of land	SolarPILOT value (Wagner and Wendelin, 2018) converted to AUD
Site improvements cost	28	AUD/m^2 of heliostat mirrors	SAM value (Blair N. et al., 2018) converted to AUD
Heliostat field cost	168	AUD/m^2 of heliostat mirrors	SAM value (Blair N. et al., 2018) converted to AUD
Balance of plant cost	-	-	Not included in present work
Storage cost	-	-	Not included in present work
Fixed tower cost	4,363,900	AUD	ASTRI 1.0 (Beath A. et al., 2014) value converted to AUD
Tower cost scaling exponent	0.0113	-	SAM (Blair N. et al., 2018) and SolarPILOT (Wagner and Wendelin, 2018) value
Receiver cost	50	AUD/kW$_t$	Estimated
Contingency	10	%	SAM value (Blair N. et al., 2018)
EPC and owner cost	10	% of direct capital costs	SAM value (Blair N. et al., 2018)
O&M cost	41	AUD/kW$_t$	(Kolb et al., 2010)
Lifetime	30	years	Assumed in this study
Sales tax rate	0	%	Not included in present work
Discount rate	13.1	%	(Bader et al., 2019)

6.1.1.9. Results

A comparison between the Pinjarra and Learmonth sites for a fixed 120m aperture centroid elevation was performed. The annual efficiency versus aperture radius is plotted in Figure 61. A 2750mm aperture radius is seen to be optimal for both sites, with the annual efficiency at the Learmonth site being almost 2 percentage points higher than that for Pinjarra. This improved performance at Learmonth is due to the design point DNI's for the two sites being similar, but the average annual DNI being much higher for Learmonth. As will be shown, this results in improved receiver thermal efficiency in Learmonth due to the receiver being operated, on average, closer to the design point capacity throughout the year.

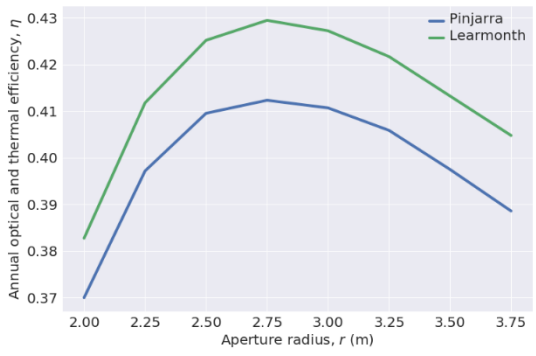

Figure 61: Annual efficiency versus aperture radius for a 50MW$_{th}$ SEVR at 120m elevation from ground level.

Based on this result, the aperture radius was then fixed at 2750mm, and the aperture centroid elevation varied in the range 60 to 140m. Annual efficiencies versus aperture centroid elevation is plotted in Figure

62. Pinjarra is seen to have slightly higher optical efficiency compared to Learmonth. This is due to the more equatorial latitude of the Learmonth site resulting in increased cosine losses. The improvement in annual receiver thermal efficiency for the Learmonth site due to the higher DNI levels, however, outweighs this slightly lower optical efficiency, resulting in Learmonth having better combined efficiency for all aperture centroid elevations considered.

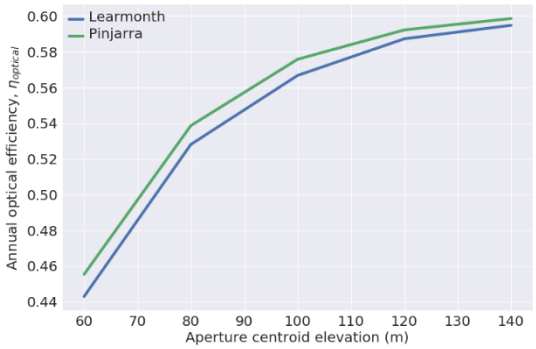

(a) Annual optical efficiency

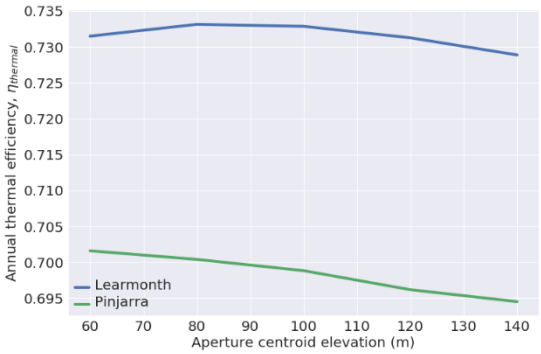

(b) Annual receiver thermal efficiency

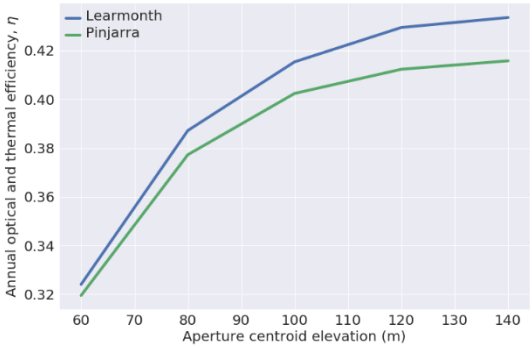

(c) Combined annual efficiency

Figure 62: a) Annual optical efficiency, b) Annual receiver thermal efficiency and c) combined annual efficiency versus aperture centroid elevation for a 50MW$_{th}$ SEVR with 2750mm aperture radius.

Annual thermal energy output, total capital cost and levelised cost of heat versus aperture centroid elevation are plotted in Figure 63. Learmonth is seen to allow a considerably higher annual thermal energy output, again due to the higher DNI levels throughout the year. The total capital cost of the field, tower and receiver subsystems is essentially the same for the two sites, but with strong variation with aperture centroid elevation due to the exponentially increasing cost of the tower as a function of height. The configuration with the lowest LCOH is seen to be Learmonth with an 80m tower. Based on this analysis, Learmonth is clearly the preferred site due to its ability to allow more thermal energy output over the year.

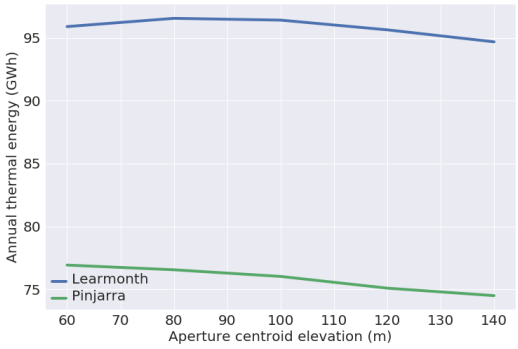

(a) Annual thermal energy output

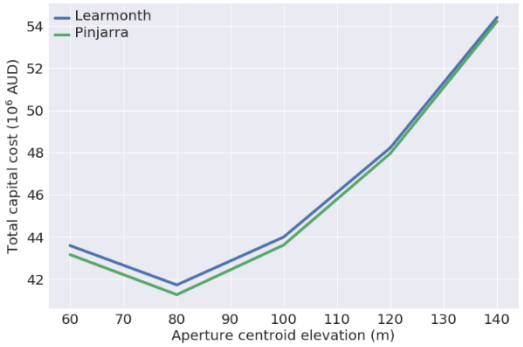

(b) Total capital cost

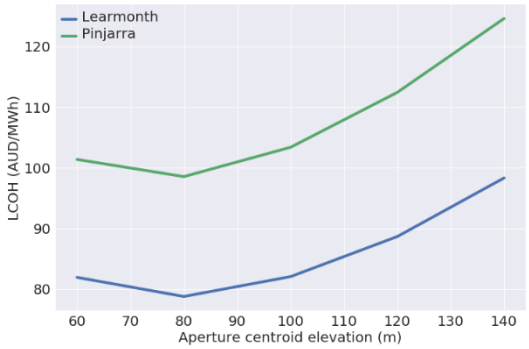

(c) Levelised cost of heat

Figure 63: a) Annual thermal energy output, b) total capital cost, and c) levelised cost of heat versus aperture centroid elevation for a 50MW$_{th}$ SEVR with 2750 aperture radius.

Heliostat field layouts and capital cost break downs for various aperture centroid elevations at the Learmonth site are plotted in Figure 64. As the aperture centroid elevation increases from 60 to 100m, both occupied land area and heliostat count decreases dramatically. The tower cost also increases dramatically, resulting in the tower becoming the dominant cost aperture centroid elevations of 100m and higher.

Finally, a two-dimensional parametric study was performed for the Learmonth site, where both aperture centroid elevation and aperture radius was varied. Efficiency contours are plotted in

Figure 65. As expected, annual optical efficiency increases as both aperture radius and elevation increase, and receiver thermal efficiency decreases with increasing aperture radius. Annual energy, capital cost and levelised cost contours are plotted in Figure 66. An aperture radius of approximately 3m with an aperture centroid elevation is seen to give the minimum LCOH. Such a large aperture (77% of the internal radius), however, may not be possible due to the particle attrition and convective losses previously mentioned.

Based on these results, the Learmonth site with an 80m tower and a 2.75m (or 3.0m if possible) aperture radius is the optimal configuration for the heliostat field, tower and receiver subsystems. Visualisations of this configuration were presented in Figure 59. A contour map of the design point absorbed solar flux on the west internal surfaces of the receiver are presented in Figure 67. A high flux (~1MW/m^2) zone is predicted to occur on both the east and west sides of the cavity just after the aperture. This is also the region where the particle and air outlet are expected to be co-located. Thermodynamically, this could be

advantageous as most of the temperature rise will occur very close to the outlet, resulting in reduced thermal losses. However, the current positioning of the high flux zone may not give enough space for the outlet. The reason for the close proximity of the high flux zone to the aperture is the absence of a secondary concentrator. Although a secondary concentrator would allow high flux to penetrate deeper into the cavity, it severely reduces the optical performance of the heliostat field. The CFD modelling and detailed engineering design of a 50MW$_{th}$ SEVR is required to assess the suitability of flux maps such as that shown in Figure 67.

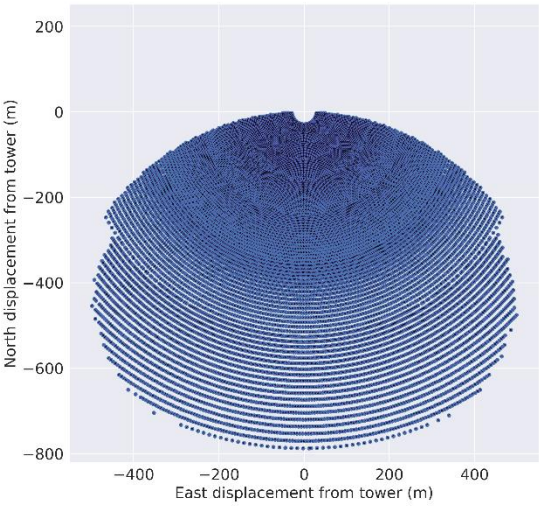

(a) Field layout for 60m aperture centroid elevation (12588 heliostats)

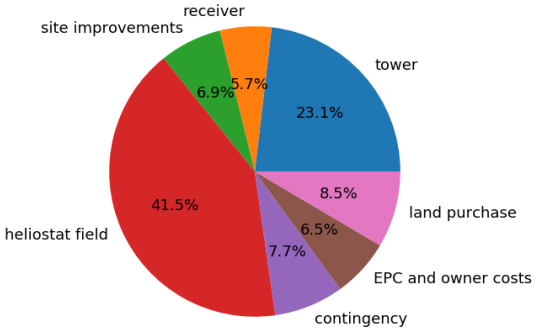

(b) Capital cost break down for 60m aperture centroid elevation (43.6M AUD)

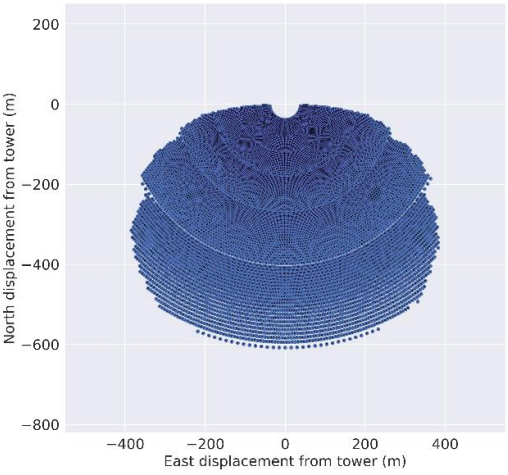

(c) Field layout for 80m aperture centroid elevation (10607 heliostats)

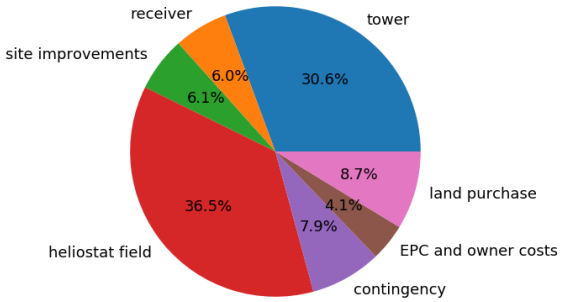

(d) Capital cost break down for 80m aperture centroid elevation (41.7M AUD)

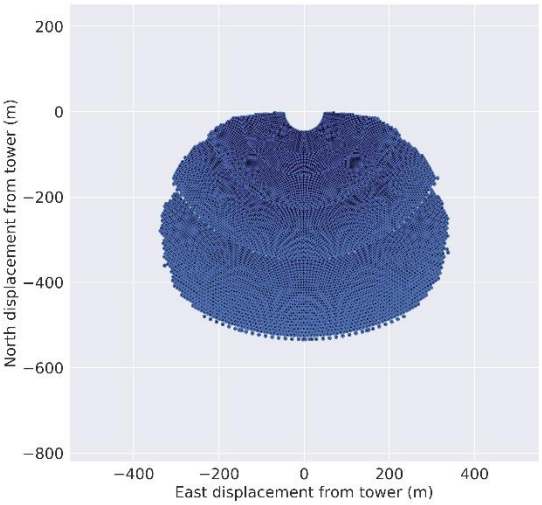

(e) Field layout for 100m aperture centroid elevation (9873 heliostats)

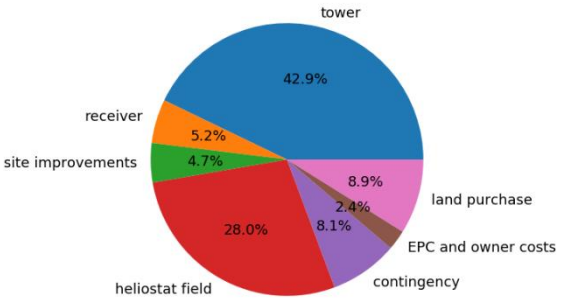

(f) Capital cost break down for 100m aperture centroid elevation (44.0M AUD)

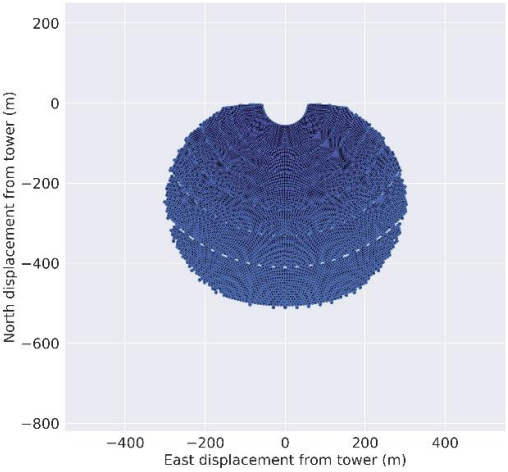

(g) Field layout for 120m aperture centroid elevation (9472 heliostats)

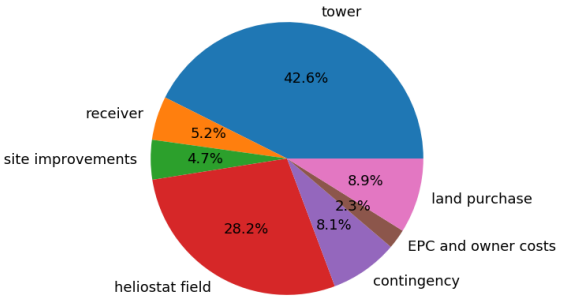

(h) Capital cost break down for 100m aperture centroid elevation (48.23M AUD)

Figure 64: Heliostat field layouts and capital cost break downs for various aperture centroid elevations from 60m to 100m at the Learmonth site.

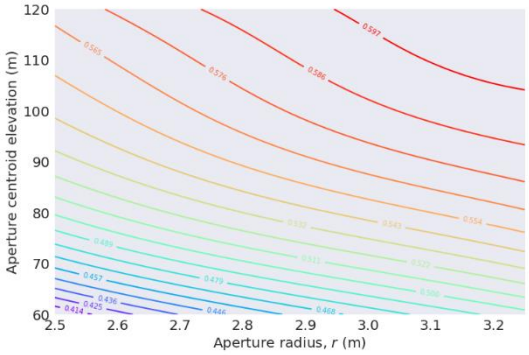

(a) Annual optical efficiency

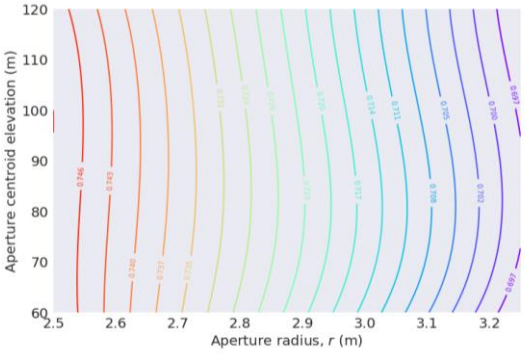

(b) Annual receiver thermal efficiency

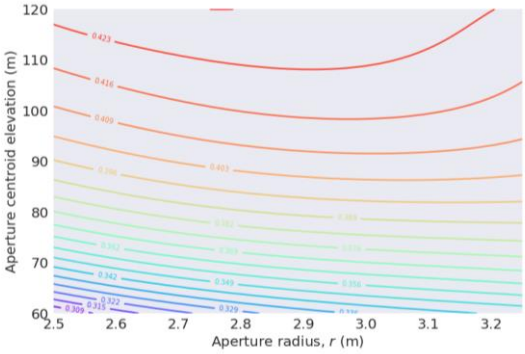

(a) Combined annual efficiency

Figure 65: Annual efficiency contours as a function of aperture centroid elevation and aperture radius for a 50MW$_{th}$ SEVR at the Learmonth site.

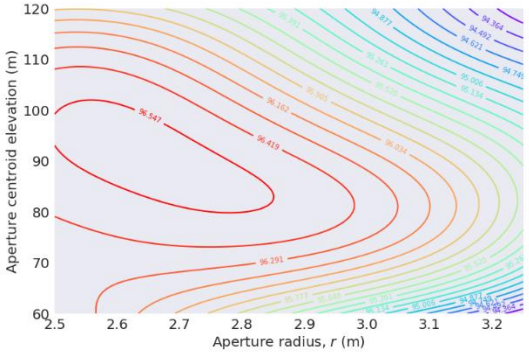

(a) Annual thermal energy output (GWh)

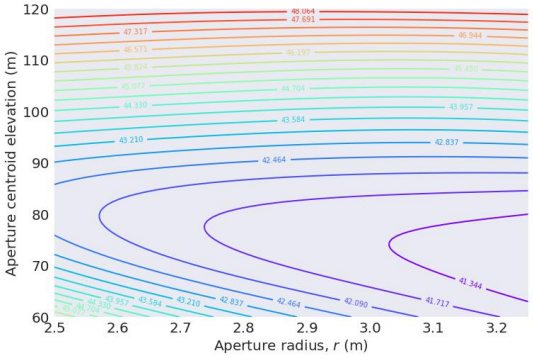

(b) Total capital cost (10^6 AUD)

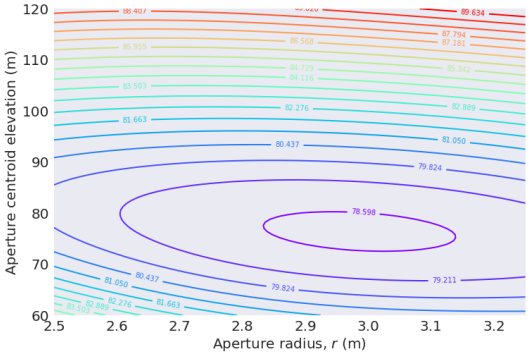

(c) Levelised cost of heat (AUD/MWh)

Figure 66: Annual thermal energy output, total capital cost and levelised cost of heat contours as a function of aperture centroid elevation and aperture radius for a 50MW$_{th}$ SEVR at the Learmonth site.

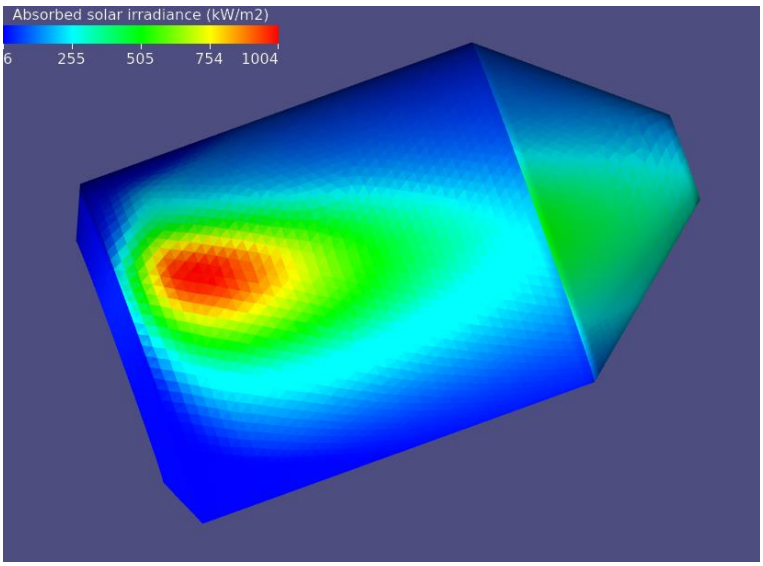

Figure 67: Contour map of the design point absorbed solar flux on the west internal surfaces of an SEVR with 2.75m aperture radius and 80m aperture centroid elevation at the Learmonth site.

6.1.1.10. Summary

Optimised heliostat field layouts, annual performance and levelised cost has been computed for 50MW$_{th}$ SEVR designs with different aperture radii, aperture centroid elevations and site locations. The Learmonth site was found to have considerably higher (~25%) annual DNI, resulting in higher (~20%) annual energy output and lower (~20%) levelised cost of heat compared to Pinjarra. The optimal receiver design for the Learmonth site (on an LCOH basis) was found to be an aperture radius of 3000mm with an aperture centroid elevation of 80m. This aperture radius, however, is likely to be too large and would lead to excessive particle attrition and convective loss. Therefore, a slightly lower aperture radius of 2750mm is recommended. The capital cost of the heliostat field, tower and receiver subsystems for this configuration is estimated to be 41.7M AUD, resulting in an LCOH of 22 AUD/GJ. Note that the cost of pipework for the air or particles from the storage (on ground) to the receiver is not included in the present study.

6.1.2. Heliostat field – Beam down

Beam Down Receivers (BDR) are a promising alterative for small-to-medium tower-based Concentrating Solar Thermal (CST) plants. The BDR design replaces the tower-mounted receiver with a hyperboloid mirror which to redirects the radiation to a receiver on the ground. Several advantages of the BDR design are reduced pumping/particle transportation costs (no fluid flows through the tower), reduced tower structural costs, and the unlocking of co-located receiver-storage. On the other hand, the BDR adds additional optical losses and introduces mirror size and thermal power capacity limitations (Saldivia et al., 2021). Nonetheless, for smaller capacity applications (e.g., industrial processes or modular, high-efficiency power cycles), the advantages may outweigh the disadvantages.

A Monte Carlo ray tracing (MCRT) method was used to assess the optic of beam down configuration. Figure 68 presents the heliostat field (HF) concentrates the radiation toward a focal point, a hyperboloid mirror (HB) intercepts these rays and redirect them to the ground on a second focal point. Due to the magnification involved, a final optic device (typically a compound parabolic collector, CPC) is used to re-concentrate the radiation in the SEVR.

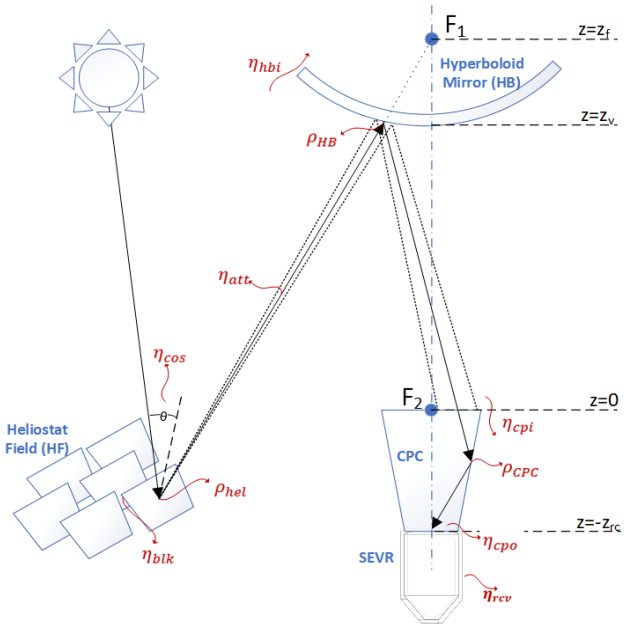

Figure 68: Schematic of the proposed BDR with its three main components: heliostat field, hyperboloid mirror, and CPC concentrator, adapted from (Saldivia et al., 2021).

6.1.2.1. Design conditions and parameters

A set of rays were generated from the sun position, including a degree of randomisation to correctly represent the sun irradiance. Then, the final distribution in the receiver aperture after interacting with different optic devices was simulated. SolarPILOT (Wagner and Wendelin, 2018) was used to assess and optimise CST plants because it can generate a heliostat field layout and run a MCRT simulation (using the well-known SolTrace engine) for a solar field with a focal point at the top of the tower. In this study, the dataset was exported and used to intercept the hyperboloid mirror and the CPC array. Table 22 presents the design consideration for the beam down configuration. The heliostat mirror design and the thermal requirement are similar to the beam-up configuration (reported in Section 6.1.1) for comparison.

Table 22 The datasets were generated using the following assumption and parameters.

Plant latitude	-31.9°	Tower heights (m)	50, 75, 100
Design point	Noon at equinox	BDR mirror type	Hyperboloid
Design DNI	950 (W/m^{2}d)	Final optical device	None
Minimum field radius	1 x height	Receiver aperture diameter	5.5m
Maximum field radius	15 x height	Required power on receiver outlet	50MW$_{th}$
Heliostat size	2.92m x 2.92 m	Receiver height	12m
Heliostat type	1 flat mirror	Mirror reflectivity	0.95
Compound parabolic collector (CPC	With/without	Second focal point (the location of CPC aperture), z_{rc}	25m

First, an oversized heliostat field was generated, and a ray dataset was then developed. With this dataset, the interceptions with hyperboloid mirror and the receiver aperture were calculated, and the optical

efficiency for each heliostat was obtained. Finally, the highest efficiency of a heliostat field was selected until the required power in the receiver aperture is obtained.

The optical efficiencies for the beam down receiver, η_{BDR} and the solar field, η_{SF}, are defined as:

$$\eta_{BDR} = \eta_{hbi}\,\rho_{hb}\,\eta_{rci} \quad \text{Eq. 36}$$

$$\eta_{SF} = \rho_{hel}\,\eta_{cos}\,\eta_{blk}\,\eta_{att}\,\eta_{BDR} \quad \text{Eq. 37}$$

Where η_{hbi} and η_{rci} are the hyperboloid and receiver intercept efficiency; ρ_{hb} and ρ_{hel} are the mirror reflectiveness for hyperboloid and heliostats (assumed both $\rho = 0.95$); and $\eta_{cos}, \eta_{blk}, \eta_{att}$ are the cosine, blocking and attenuation efficiency, respectively.

In each case the hyperboloid geometry is optimized by two variables: the vertex ration ($f_{zv} = z_f / z_v$) and hyperboloid radius (R_{HB}). The function to minimize is the total mirror surface, considering solar field, hyperboloid, and CPC (if correspond) surfaces. Function to minimize:

$$S_{mirr} = N_{hel} A_{hel} + S_{HB} + S_{CPC} \quad \text{Eq. 38}$$

The shadowing from the hyperboloid mirror into the solar field is considered. The shadowing of the sun position through the year is calculated. A simple rule is chosen: all the heliostats covered more than 10% of the time are eliminated. This affects mostly the heliostats located closer to the tower in the southern part of the field as shown in Figure 69. Figure 69 presents the solar field layout and the optical (sun-to-receiver) efficiency of a 50MW$_{th}$ output with a CPC. When the CPC is considered, a 3D-CPC with a fixed concentration ratio of $C_g = \frac{A_a}{A_o} = 2$. The outlet diameter is the same than receiver aperture ($D_O = 5.5m$). This means the aperture diameter is $D_A = 7.78m$ and a height of $H_{CPC} = 7.56m$.

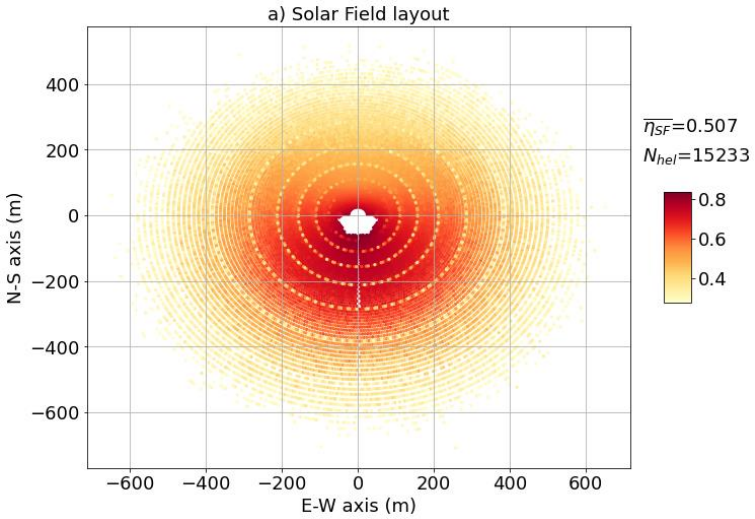

Figure 69: Solar field layout and the optical (sun-to-receiver) efficiency of a beam down configuration for a 50MW$_{th}$ output with a CPC.

6.1.2.2. Results

Figure 70a presents the optimised total mirror surface area with and without a CPC as a function of tower height. The total mirror surface area decreases with the tower height. In addition, the CPC reduces the total mirror surface area, with the largest impact on the shortest tower (50m), by 17% from 0.16 to 0.13

km^2. Figure 70b presents the solar field and BDR optical efficiencies as a function of tower height. The overall solar field efficiency with a CPC increases from 50% to 65% and 42% to 60% without a CPC as the tower height is increased from 50 to 100m. This can be explained by the number of rays intercepted by the aperture area (intercept efficiency) is increased by around 10%, but the extra mirror reflections in the CPC limits this improvement. Also, the efficiencies increase asymptotically with tower height. However, the downside of increasing the tower height is the increment of hyperboloid mirror radius from 20 to 38m for the case with a CPC and from 30 to 52m without a CPC, as shown in Figure 70c. The is mainly due to the cosine efficiency that affects far-away heliostats for shorter towers and hence impacted on the solar field efficiency. In addition, a large hyperboloid mirror is most likely to increase the cost of the tower and more shadowing over the solar field. The impact is even greater without a CPC, which probably will make this option almost unfeasible, regardless the tower height.

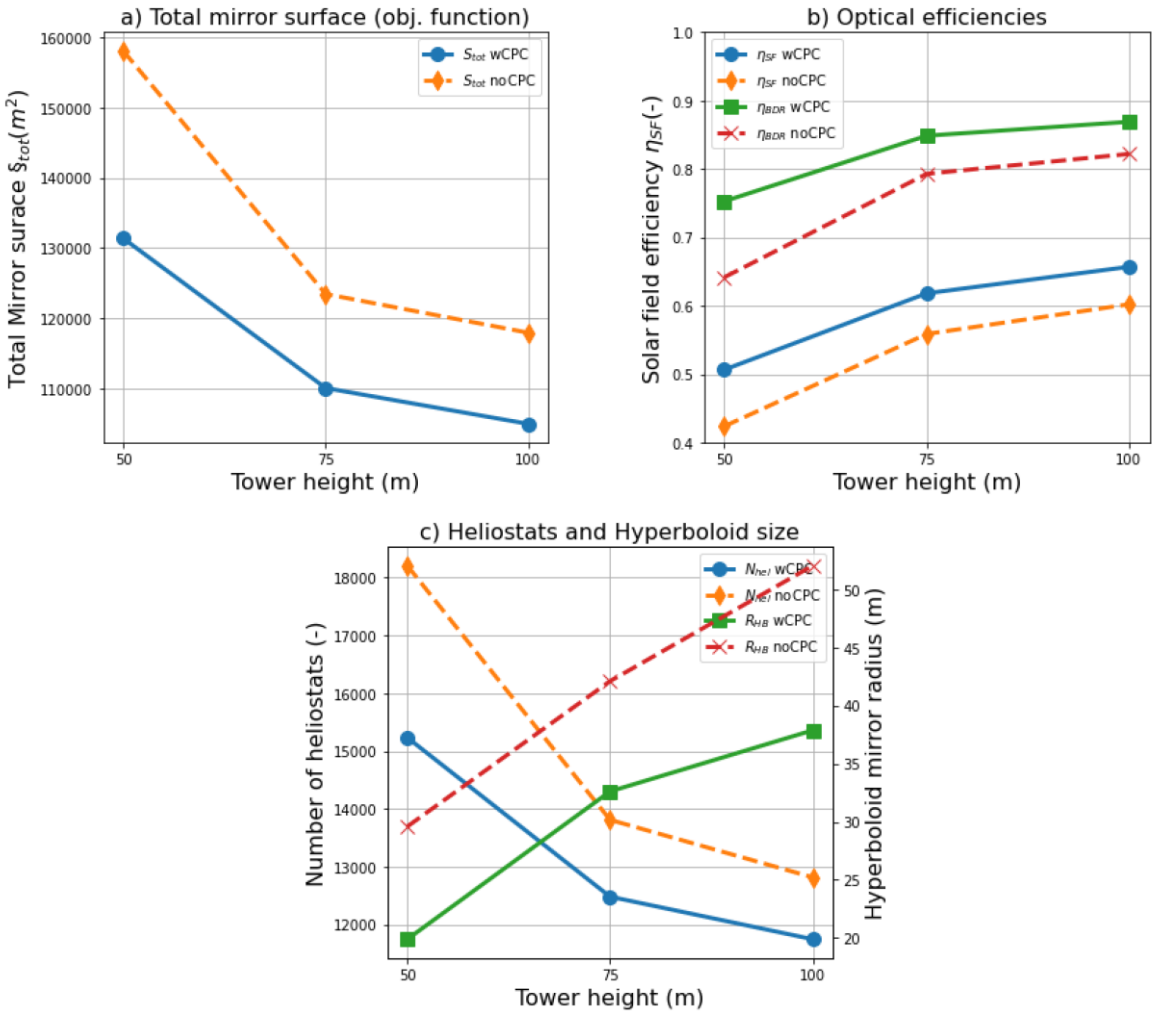

Figure 70: Results of optical optimisation for 3 different tower heights with CPC (blue and green solid lines) and without CPC (orange and red, dashed) for a 50MW$_{th}$ output at the SEVR. a) Total mirror, b) optical efficiencies, c) Heliostats and Hyperboloid

6.1.2.2.1. Cost modeling

A simple cost model has been implemented in order to allow a “levelised cost of heat” to be calculated and optimal configurations of the heliostat field, tower and receiver subsystems to be determined. A breakdown

of the cost model inputs is presented in Table 23 and it adapted from the costing used for the beam up configuration reported in Section 6.1.1.8.

Table 23: Cost model breakdown for the SEVR, tower and heliostat field subsystems.

Item	Value	Units	Basis
Site-to-field land area ratio	1.3	-	SolarPILOT value (Wagner and Wendelin, 2018)
Land purchase cost	3.5	AUD/m^2 of land	SolarPILOT value (Wagner and Wendelin, 2018) converted to AUD
Site improvements cost	28	AUD/m^2 of heliostat mirrors	SAM value (Blair N. et al., 2018) converted to AUD
Heliostat field cost	168	AUD/m^2 of heliostat mirrors	SAM value (Blair N. et al., 2018) converted to AUD
Cost of hyperboloid mirror	500	AUD/m^2 of heliostat mirrors	Estimated
Cost of compound parabolic concentrator (CPC)	500	AUD/m^2	Estimated
Fixed tower cost	5,845,353	AUD	Estimated using Hatch cost analysis
Receiver cost	50	AUD/kW$_t$	Figure 29, Milestone Report 5 (2019)
Contingency	10	%	SAM value (Blair N. et al., 2018)
EPC and owner cost	30	% of direct capital costs	Hatch
O&M cost	41	AUD/kW$_t$	(Kolb et al., 2010)
Lifetime	30	years	Assumed in this study
Sales tax rate	0	%	Not included in present work
Discount rate	13.1	%	(Bader et al., 2019)

The LCOH is computed using:

$$LCOH = \frac{f \cdot C + O}{E} \qquad \textbf{Eq. 39}$$

Where C is the capital cost O is the operational cost and E is the yearly energy yield and f is the annuity factor:

$$f = \frac{d(1+d)^n}{(1+d)^n - 1} \qquad \textbf{Eq. 40}$$

with the discount rate d and the lifetime in years n.

Table 24 presents the cost estimation for the beam down configuration as a function of tower height. An optimal was found at 75 m, with a minimum LCOH of AUD34/GJ. The LCOH of the beam-down configuration is approximately 50% higher than that of the beam-up configuration. Note that there is some uncertainty on the cost of hyperboloid (including cooling system) and tower.

Table 24: Cost estimation for the beam down configuration

Tower height (m)	50	75	100
Land purchase (AUD)	$590,966	$484,163	$455,571
Site improvement (AUD)	$3,636,714	$2,979,465	$2,803,514
Cost of heliostat (AUD)	$21,820,285	$17,876,791	$16,821,087
Cost of hyperboloid mirror (AUD)	$667,122	$1,747,102	$2,338,306
Cost of tower (AUD)	$4,091,747	$4,676,282	$5,845,353
Cost of CPC (AUD)	$80,530	$80,530	$80,530
Cost of receiver (AUD)	$3,125,000	$3,125,000	$3,125,000
Total Cost (AUD)	$47,617,310	$43,357,068	$44,057,105
LCOH AUD/GJ	38.3	34.9	35.5

6.2. Assess parasitic losses associated with proposed particle conveying systems

Pneumatic conveyor is the technology most widely applied to convey solid particles. Pneumatic conveying is suitable for the SEVR system because of the two phase (gas-solid) operating condition in the receiver. Pneumatic conveying offers the advantages of flexibility in pipeline routing, low maintenance, ease of operation and the elimination of moving parts from the conveying process (Chladek et al., 2011, Rizk et al., 2010). On the other hand, their drawbacks include abrasive wear of the conveying pipes, particle degradation and the potential for high electricity consumption (Repole and Jeter, 2016). However, the significance of the parasitic energy losses is system specific and should be assessed systematically in order to identify their preferred configurations and realistic potential (Mehos et al., 2017).

Pneumatic conveying can be categorized into two modes, the dilute and the dense phases. In dilute phase conveying systems, the material is conveyed in a suspension flow regardless of the particle size, shape or density (Mills, 2016). However, a relatively high gas velocity and low solids loading ratio are required to achieve steady suspension flow without any chocking and blockage (Mills, 2016). This can result in a relatively high electricity consumption, together with increased pipe wear and particle degradation (Konrad, 1986, Mills, 2016). On the other hand, in a dense phase conveying system, materials are conveyed in a slug or plug flow, which uses much lower gas velocity. Therefore, this type of conveying system is usually suitable for only Geldart group A particles, which have good air retention characteristics (Mills, 2016). To date, most of the investigations have been carried out on the pneumatic conveying systems applied for the transportation of solids at atmospheric temperature (G.E. Klinzing, 2010, Mills, 2016, 1985, Konrad, 1986, Eduardo J. Díaz et al., 2017, Rinoshika and Suzuki, 2010, Yan and Rinoshika, 2012, Li and Tomita, 1996, Li and Tomita, 1998, Yan et al., 2012, Taylor, 1998, Watson et al., 2012, Kuang et al., 2012). Therefore, in these studies, only the electricity consumed to compress the gas is assessed according to the pressure drop in the pipelines. On the other hand, in a CSP plant, the particle to be conveyed can at high temperatures depending on the configuration of power block. Therefore, other than electricity consumption, any parasitic thermal losses need to be considered as well.

6.2.1. Energy flow of pneumatic conveying process

Figure 71 presents the energy flows of the pneumatic conveying process for solid input temperatures of 25°C and 450 C. It can be seen that the solid input temperatures of 25 C, the only energy input is the

electricity consumed by the compressor. This electricity is converted into enthalpy heat in the gas and mechanical loss in the compressor. After that, in the acceleration zone, most of the enthalpy heat in the gas is transferred into solids via mixing due to the high solids loading ratio while only small proportion of enthalpy is converted into the mechanical energy of both solids and gas. Then, in the following fully developed zone, part of the enthalpy heat in the solids is transferred back to the gas and further converted into mechanical energy of both the solids and gas. Heat loss through the wall occurs on the whole conveying pipe. The rest of the enthalpy heat in the solids could potentially be released to surrounding environment afterwards depending on the application.

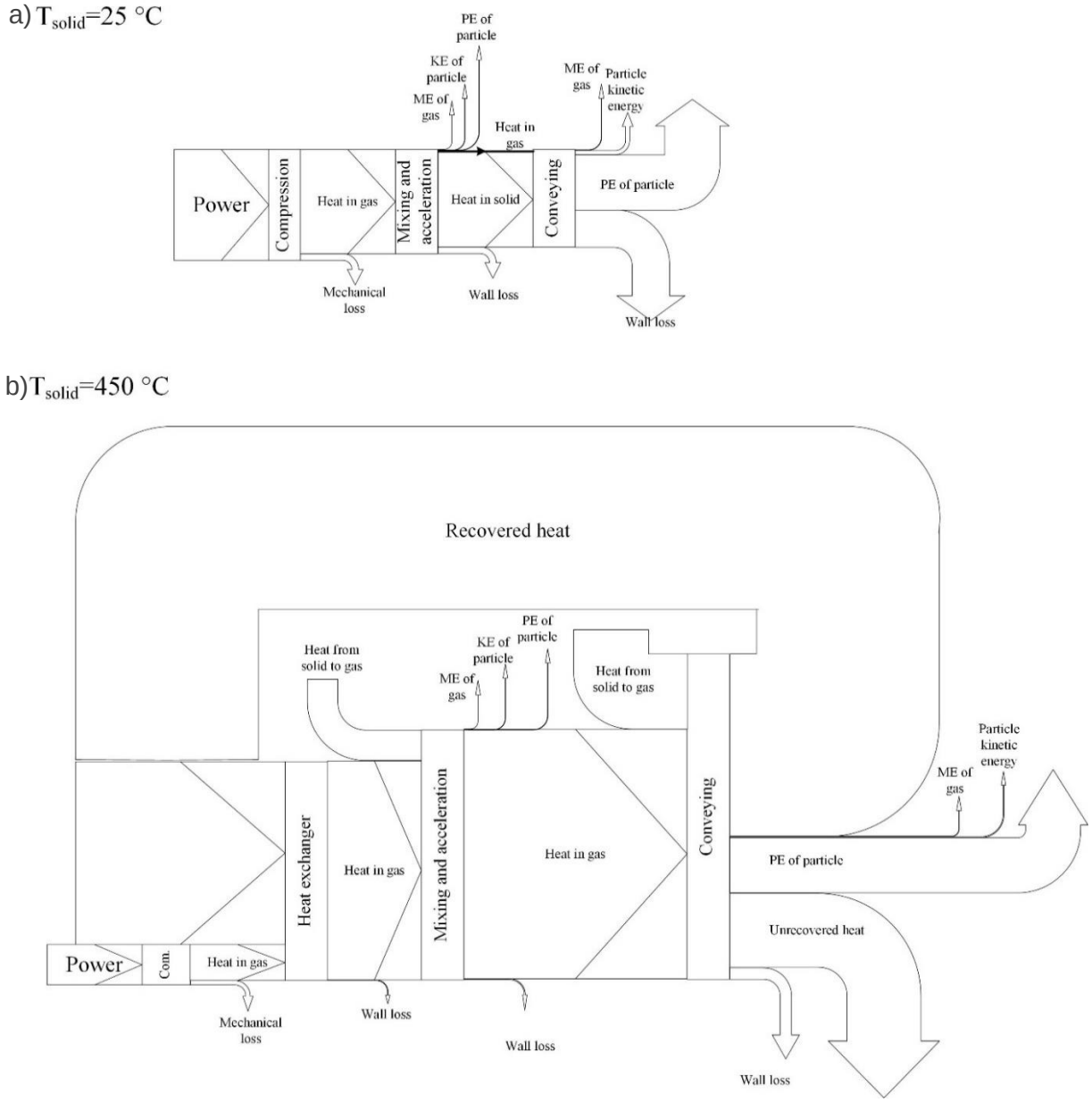

Figure 71: Energy flows of the conveying process for solid input temperatures of 25°C and 450˚C.

However, as shown in Figure 71b, for the solid input temperature of 450 C, electricity consumed by compressor is only part of energy input into the whole conveying process. Another significant energy source is the thermal heat from the solids. Similarly, in the gas compression process, the electricity is converted into enthalpy heat in the gas and mechanical loss in the compressor. Then, the gas is proposed to be preheated by the hot exit gas via a heat exchanger without entering the conveying pipe directly. The

sensible energy can be recovered from the hot exit gas and transferred into the pressurized gas from the compressor. In the acceleration zone, the heat is transferred via mixing with solids with the gas since the temperature of the solids is higher than that of the gas. At the same time, very small amount of the heat in the gas phase is converted into mechanical energy of both the solids and gas. Furthermore, in the fully developed zone above the acceleration zone (Figure 72), more heat is transferred from the solids into gas while part of the enthalpy heat in the gas is converted into mechanical energy of both solids and gas in which the potential energy of solids is the dominant one. In addition, compare with the scenario with a solid input temperature of 25 ˚C, the kinetic energy of the outlet solids is much smaller due to the lower gas velocity at the outlet, which is resulted from the smaller pressure drop as shown in Figure 71.

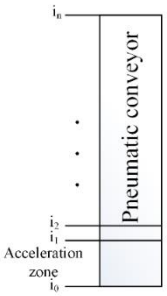

Figure 72: Control volume analysis employed for the vertical conveying pipe used to elevate the particles.

6.2.2. Energy distribution and efficiency

The energy distribution of both the (a) dilute and (b) dense phase pneumatic systems as a function of inlet solid temperature is shown in Figure 73 together with the energy efficiencies of both the presently studied pneumatic conveyor and a typical skip hoist conveyor. The thermal energy from the solids dominates the energy consumption as the solids input temperature is above 250 ˚C, especially for the dilute phase. This is because more gas is required in the dilute phase than that of the dense phase, which leads to higher thermal heat loss in the gas as unrecovered thermal heat as shown in Figure 71. Although the electricity consumption decreases significantly with solids input temperature, the total energy consumed in solids remains relatively constant due the increase of heat loss through the wall with the temperature. On the other hand, significant heat transfer occurs from the solids to the gas phase in the acceleration and conveying zones, converting energy into the mechanical energy of both the gas and solids. Since the logarithmic temperature difference of the heat exchanger used to recover heat from the hot exit gas is assumed to be constant for all scenarios, the sensible energy transferred from solids to gas in mixing zone remains constant as well. In addition, the potential energy is found to be the dominate by the mechanical energy achieved by both solids and gas at the exit of conveying pipe. Therefore, the mechanical energy of both gas and solids remains constant with temperature because the potential energy of solids is independent with temperature.

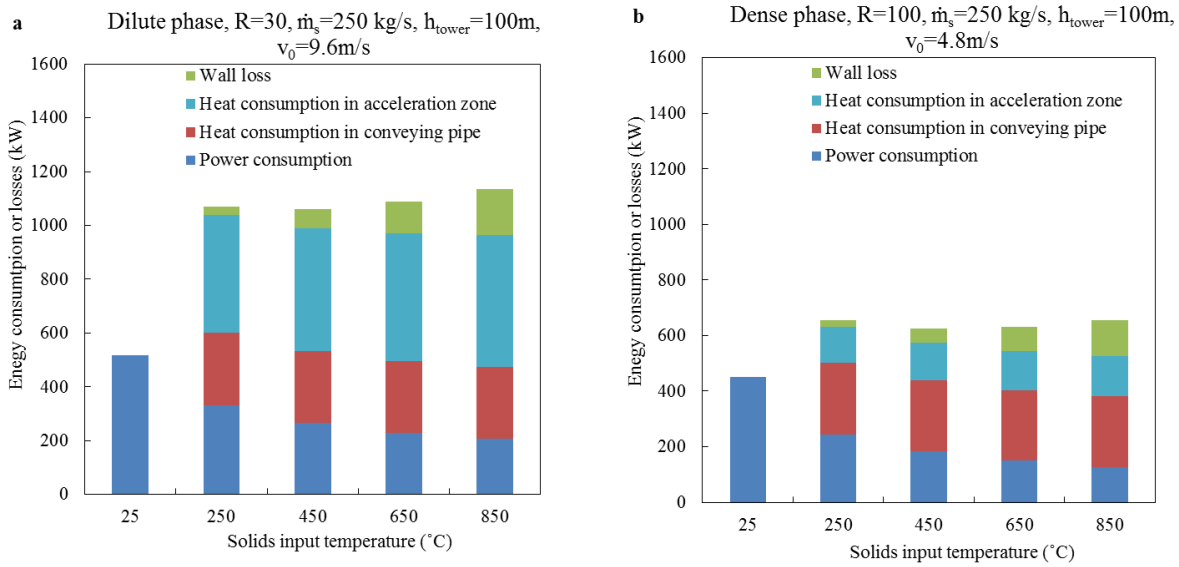

Figure 73: Energy consumption of compressor, enthalpy loss due to the increase in both mechanical energy (ME) and gas enthalpy, and heat loss through the wall of the (a) dilute phase and (b) dense phase conveying systems as a function of inlet solid temperature.

6.2.3. Exergy flow of pneumatic conveying

The energy analysis of the system cannot fully represent the total energy consumption and efficiency of the system since the conveying process is consuming both electricity and thermal energy. Therefore, an exergy analysis is conducted to further assess the consumption and loss of the pneumatic conveying process for various solid input temperatures. Figure 74 presents the exergy flows of the pneumatic conveying process for solid input temperatures of 25°C and 450°C. For the solids input temperatures of 25°C, the only exergy input is the electricity, and it is consumed by the compressor. This exergy is converted into the exergy in the gas while some losses occur via mechanical loss of the compressor and the exergy destruction during the gas compressing process. Most of the thermal heat in the gas is transferred into solids in acceleration zone via mixing and there is a thermal exergy is deducted in the mixing process as well. Only small amount of exergy in the gas is converted into mechanical energy of both solids and gas. In the fully developed zone, most of the exergy in the gas is converted into the mechanical energy of both the solids and gas while some exergy is deducted via friction and heat loss through the wall. Compare with the energy analysis, the main exergy loss in this pneumatic process is in the compressor due to both mechanical loss and exergy deduction in compressing process. The main exergy loss in the acceleration and conveying zones are due to mixing and friction, respectively.

For the solid input temperature of 450°C, the electricity consumed by compressor is only a quarter of the exergy input into the conveying process as shown in Figure 74b. The main exergy source is the thermal heat (or sensible heat) from the solids. In the compression process, this exergy is converted into the exergy in the gas while some losses occur via mechanical loss of the compressor and the exergy deduction in the gas compressing process. The gas is preheated by the exit gas via a heat exchanger without entering the conveying pipe directly. Here, the exergy is recovered from the exit hot gas and is transferred into the pressurized gas from the compressor. Then, in the acceleration zone, the exergy is transferred from solids to the gas since the temperature of the solids is higher than that of the gas and the exergy deduction is due to the temperature difference. There is an insignificant amount of the heat in the gas is converted into mechanical energy of both the solids and gas. Furthermore, in the fully developed zone above the acceleration zone, more exergy is transferred into gas while some of the exergy in the gas is converted into mechanical energy (potential energy) of both solids and gas. Compare with the scenario with a solid

input temperature of 25°C, the exergy deduction caused by friction is less due to the smaller pressure drop which resulted in smaller velocity at the outlet. Also, there is some exergy cannot be recovered from the hot exit gas.

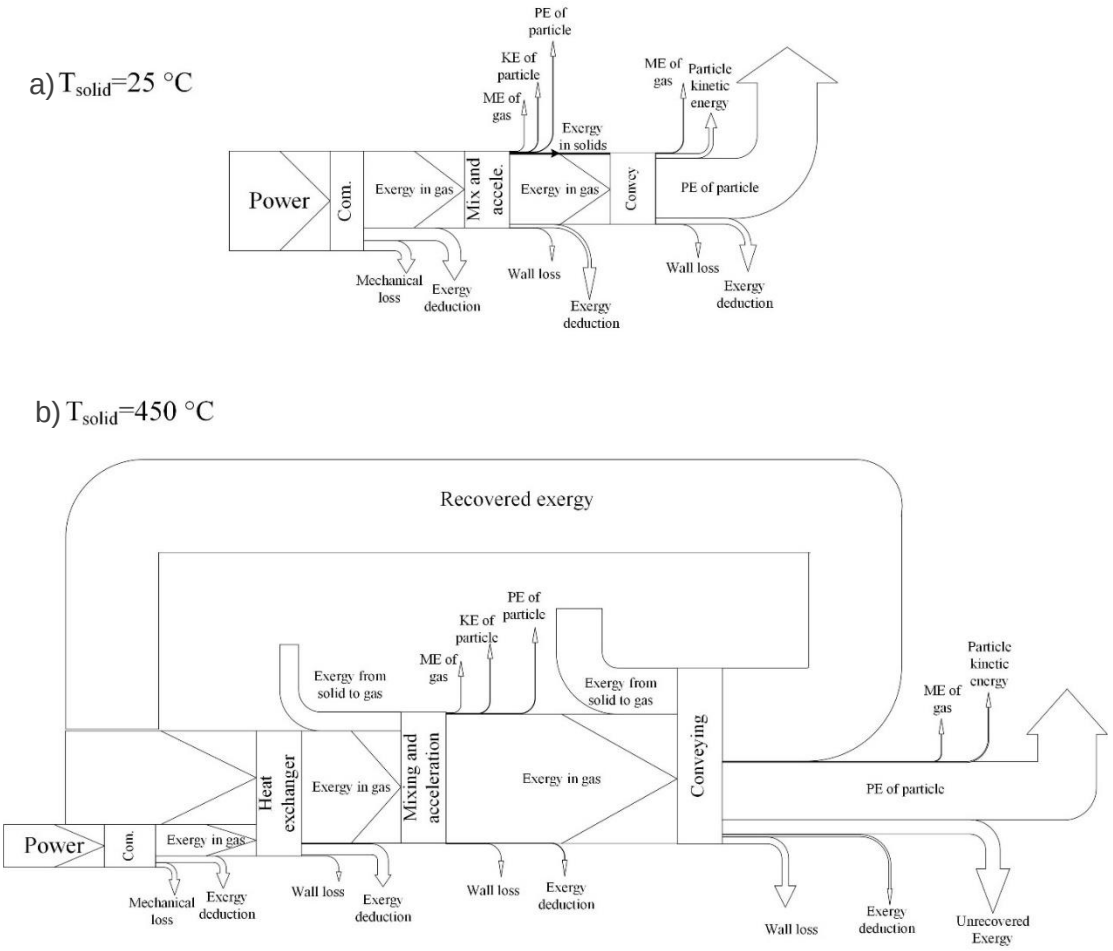

Figure 74: Exergy flows of the conveying process for solid input temperatures of 25°C and 450°C.

6.2.4. Exergy consumptions and losses

The exergy distribution of both the (a) dilute and (b) dense phase pneumatic systems as a function of inlet solid temperature is shown in Figure 75. It can be seen that the exergy of the solids dominates the energy consumption for the solids input temperature above 250°C for both dilute and dense phase. This leads to the increase in the total exergy consumption even with the reduction of the electricity consumption. The trend is different from the relatively constant energy inputs as shown in Figure 73. The high exergy consumption is due to the high exergy deduction of the heat exchanger. As a result, more heat is required to be recovered from the gas phase due to the increase in temperature. The other high exergy loss is the conveying pipe, which is resulted from the high heat loss through the conveying pipe (Figure 73). Moreover, the dilute phase conveying consumes higher exergy than the dense phase because of the greater exergy deduction in the heat exchanger, the conveying pipe and the unrecovered exergy in the hot exit gas. The greater mass flow rate of gas in the dilute phase conveying leads to more recovered gas as well as unrecovered heat.

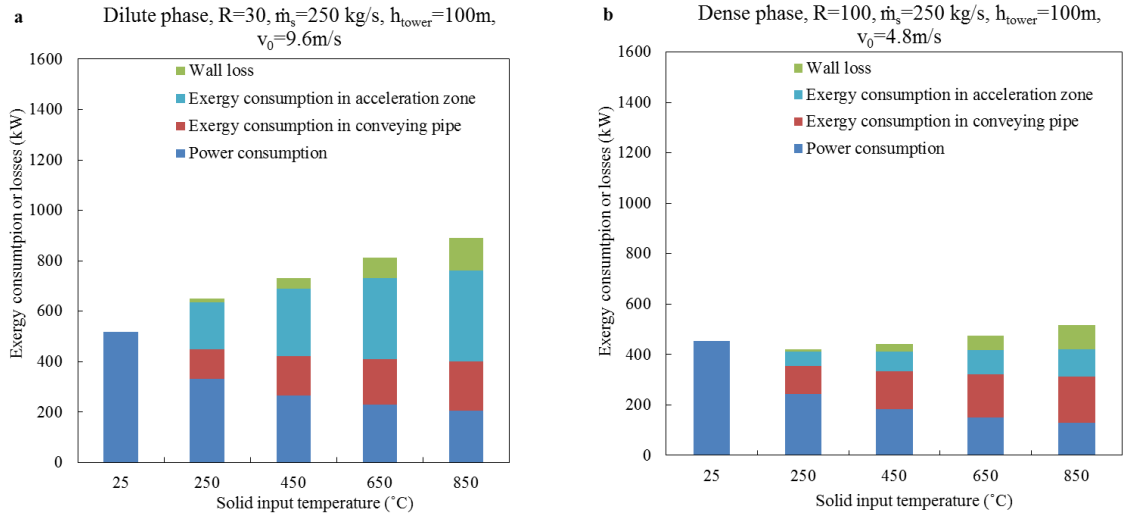

Figure 75: Distribution of input and output exergy of the (a) dilute phase and (b) dense phase conveying systems as a function of inlet solid temperature.

6.3. Assessment of practical constraints from plant integration

We have identified that the size of solar field, including storage, and air transmission lines could be the main physical and operational constraints from potential integration with the calcination plant due to the energy demand of the 6 calciners in the refinery located at Pinjarra is >600MW$_{th}$. The proposed solar fields are located at Site 1, which at the south-west of the refinery, and it is the closest available land to the existing calciners. This will have the shortest air transmission lines from the calciners to the CST plants compared with Sites 2 and 3, as shown in Figure 76. We have assessed the size of CST plants and the overall heat loss through the air transmission lines as a function of insulation thickness as well as the integration of the two into the calciners.

6.3.1. Solar field

We have developed 3 CST plant configurations for the receiver output at 50MW$_{th}$, 200MW$_{th}$ to 500MW$_{th}$, to meet the high energy intensity of the calcination process. An algorithmic optimisation model for optimising heliostat field, receiver and tower for the 3 thermal capacities has been developed using the CSIRO's Heliosim software. The heliostat field optics simulated using Monte-Carlo ray tracing. Note that only solar collection subsystems considered (i.e. heliostat field, tower and receiver). In this study, we use optimisation algorithms (>100 iterations/conditions) instead of parametric variation (limited range of conditions) to improve overall heliostat field optimisation process as well as shorten the overall optimisation time.

Figure 76a presents the layout and the footprint of 8 CST plants of 50MW$_{th}$ (total of 400MW$_{th}$ output) in Site 1. Each CST plant includes a storage system, which consists of 2 thermoclines, is connected to each calciner with 2 air transmission lines (hot and warm air streams). There will be up to 16 air transmission lines for this configuration and the length of each air transmission line is varied from 0.5km to 3km depending on the distance of the CST plant to the calciner. Figure 76b presents the layout out of two CST plants of 200MW$_{th}$ (total of 400MW$_{th}$ output) and each storage system, which consists of 6-8 thermoclines (to support 3 calciners). There will be up to 12 air transmission lines for this configuration and the length of each air transmission line is varied from 0.5km to 2.5km due to the CST plants are closer the calciners. Figure 76c presents the layout out of a large CST plant of 500MW$_{th}$ and each storage system, which

consists of up to 12 thermoclines to support all six calciners. There will be up to 12 air transmission lines for this configuration and the length of each air transmission line is up to 1.5km due to this CST plant configuration is closest to the calciners.

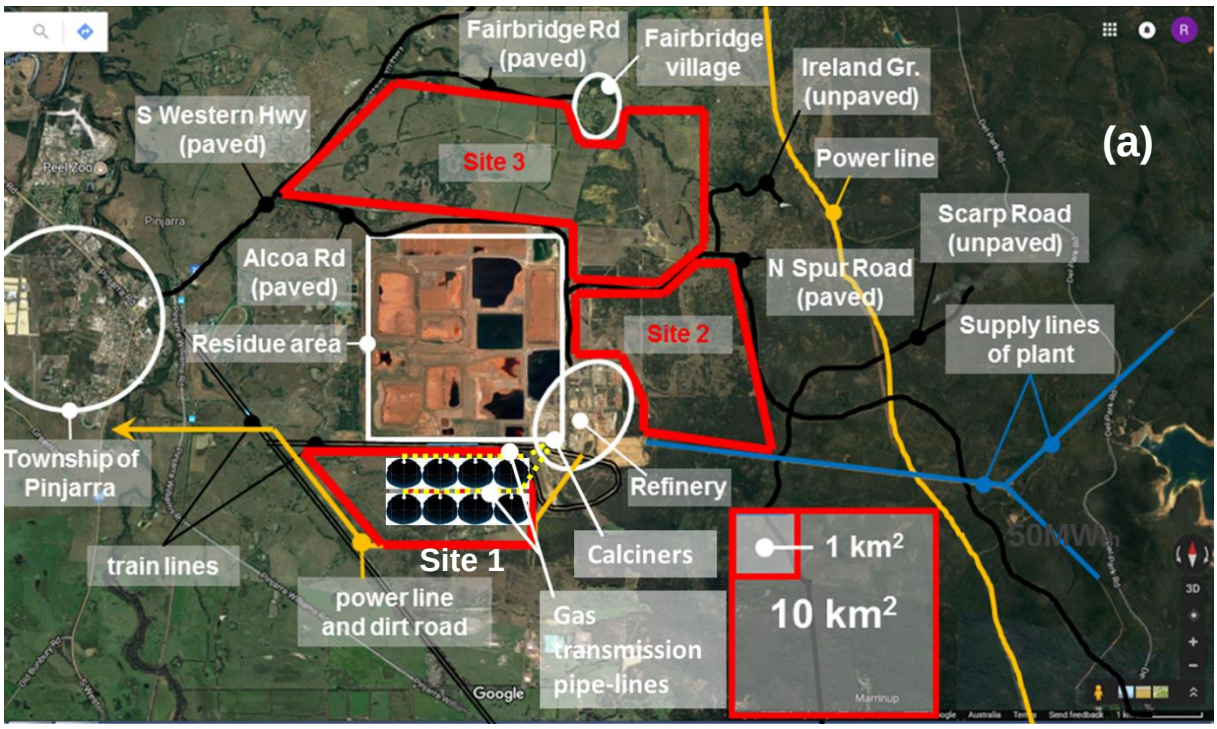

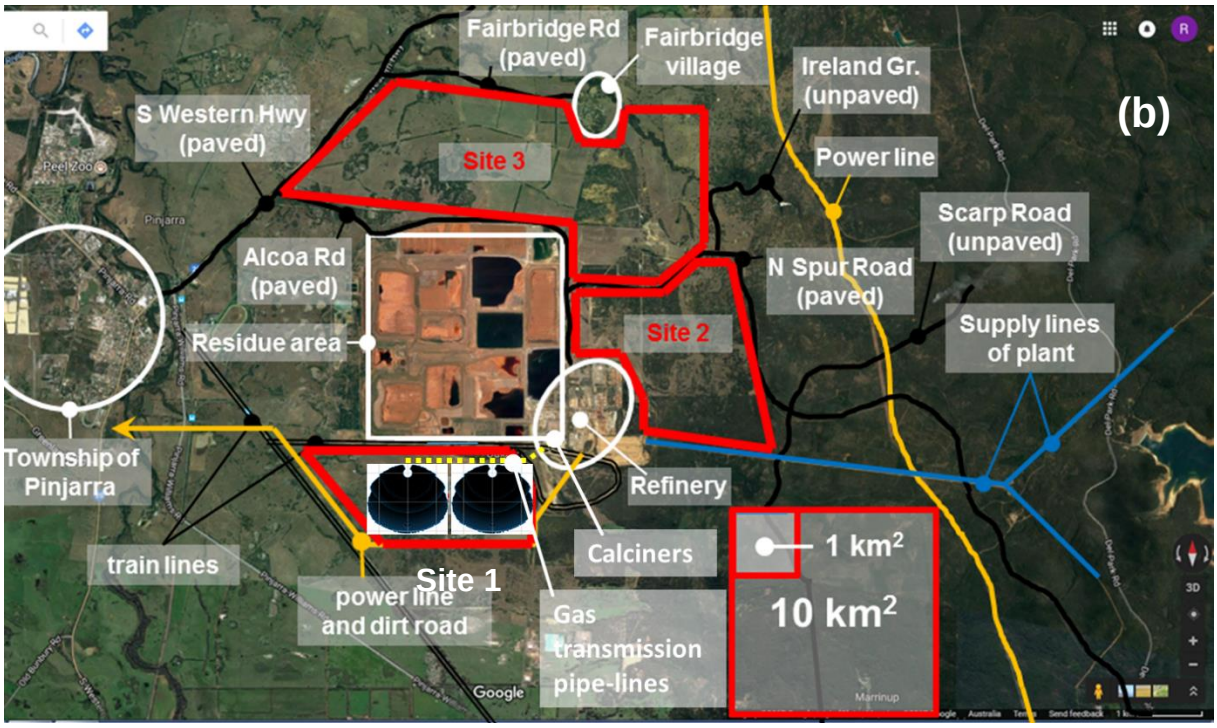

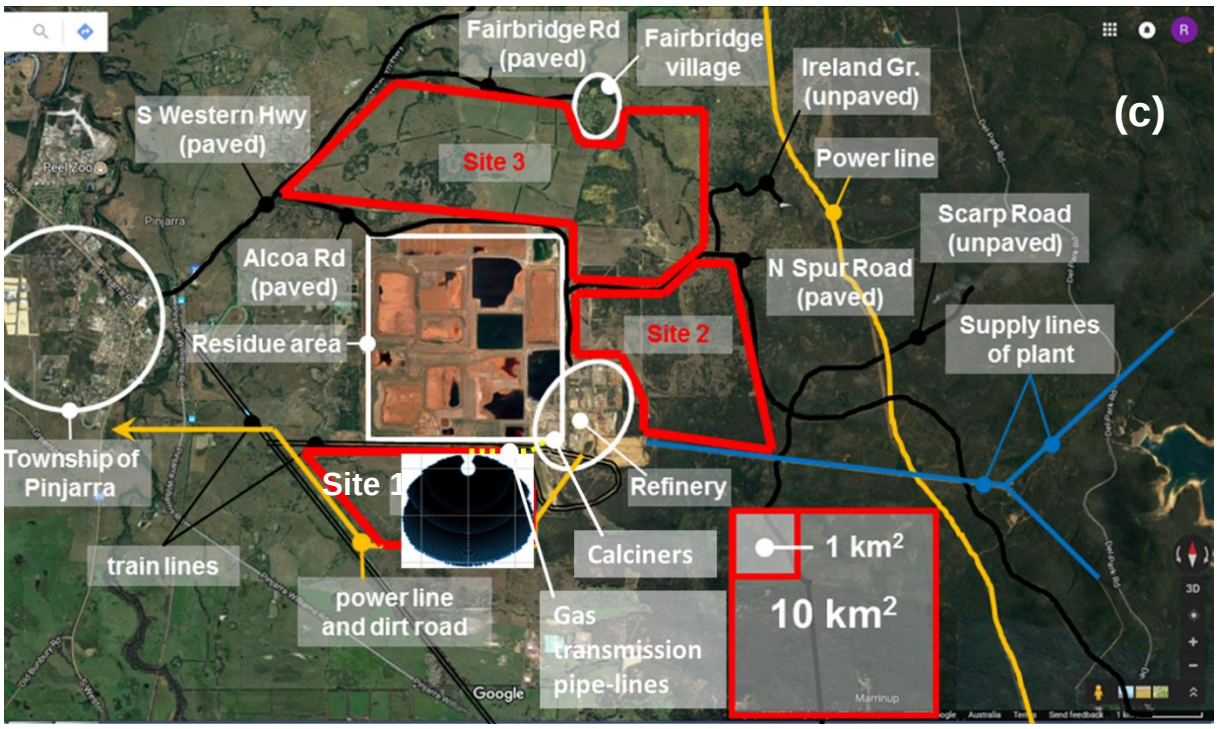

Figure 76: Overview of the Alcoa alumina refinery plant site in Pinjarra, WA (Google, 2017-11-21). Indicated in white are the alumina refinery and calciners, the residue storage area, the township of Pinjarra and the Fairbridge village. Indicated in black are the paved and unpaved roads (single lines) and train lines (double lines) surrounding the plant. Indicated in yellow are over-ground power lines running nearby. Indicated in blue are supply lines to the alumina refinery. Indicated in red are the areas that have been identified as potential sites for a CST plant. Indicated in yellow is the proposed air transportation lines for the air heater(s) (SEVR) at the thermal output of a) 50MW$_{th}$, b) 200MW$_{th}$ and c) 500MW$_{th}$. Also shown in red are areas of 1 and 10 km^2 for comparison. (Adapted from Milestones 3 and 4 reports)

6.3.2. Gas transmission pipelines

Two air transmission lines are required to transport the gas from the calcination plant to the storage system and back to the plant.

The information above will be required to optimise the CAPEX of the hot air transmission lines, a task that will be conducted for the next milestone report. Here, the inner pipe diameter is proposed to be 1.4m and the thickness of the vacuum formed refractory lining is varied from 50 to 400mm, which is enclosed by a 6mm (thick) carbon steel pipe as is shown in Figure 77.

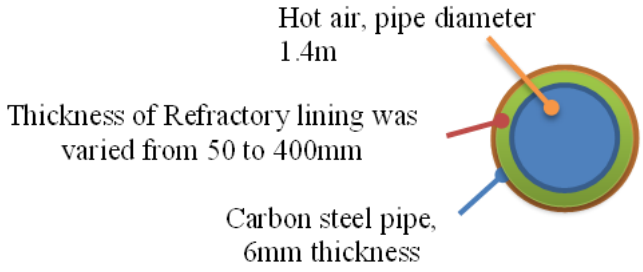

Figure 77: An insulated carbon steel gas pipe proposed for the hot air tranmission line.

The heat loss through each section through the hot air conveying line is calculated based on the conduction across a cylindrical shell as shown in Eq. 41, and the overall heat transfer coefficient, *U*, through area, *A*, can be determined using Eq. 42.

$$\dot{Q} = UA(T_i - T_o) \quad \text{Eq. 41}$$

$$\frac{1}{UA} = \frac{1}{2\pi L}\left(\frac{1}{r_{gas}h_{c,i}} + \frac{In\left(\frac{r_{ins}}{r_{gas}}\right)}{k_{ins}} + \frac{In\left(\frac{r_{cs}}{r_{ins}}\right)}{k_{cs}} + \frac{1}{r_{cs}h_{c,o}}\right) \quad \text{Eq. 42}$$

The inside heat transfer coefficient, $h_{c,i}$, can be determined from Eq. 43:

$$h_{c,i} = Nu_D \times \frac{k_{gas}}{D_{in}} \quad \text{Eq. 43}$$

where Nu_D can be detemined from Eq. 44, assuming it is a fully thermally developed flow in a smooth pipe.

$$Nu_D = 0.023 Re_D^{0.8} Pr^{0.4} \quad \text{Eq. 44}$$

Here Re_D and Ra_D can be calculated using Eq. 45 and Eq. 46:

$$Re_D = \frac{U_{air} D_{out}}{\mu} \quad \text{Eq. 45}$$

$$Ra_D = \frac{\beta(T_{surface} - T_{ambient})D^3}{\nu\alpha} \quad \text{Eq. 46}$$

The outside heat transfer coefficient, $h_{c,o}$, is the heat lost by convection and radiation to the surroundings, here calculated at 20°C.

The convection consists of forced convection and natural convection, which can be calculated using Eq. 47 and Eq. 48, respectively:

$$\overline{Nu}_{D,FC} = 0.3 + \frac{0.62 Re_D^{1/2} Pr^{1/3}}{\left(1 + \left(\frac{0.4}{Pr^{2/3}}\right)^{1/4}\right)}\left[1 + \left(\frac{Re_D}{282,000}\right)^{5/8}\right]^{4/5} \quad \text{Eq. 47}$$

$$\overline{Nu}_{D,NC} = 0.6 + 0.387\left[\left(\frac{Ra_D}{\left[1 + \left(\frac{0.559}{Pr^{9/16}}\right)\right]^{9/16}}\right)^{1/6}\right]^2 \quad \text{Eq. 48}$$

The overall heat transfer coefficient for the convection components can be determined from Eq. 49:

$$h_{c,conv} = \left(\overline{Nu}_{D,combined} \times \frac{k_{air}}{D_{out}}\right) \quad \text{Eq. 49}$$

where,

$$\overline{Nu}_{D,combined} = \left(\left(\overline{Nu}_{D,FC}\right)^4 + \left(\overline{Nu}_{D,NC}\right)^4\right)^{1/4} \quad \text{Eq. 50}$$

The radiation heat coefficient can be determined from Eq. 51:

$$h_r = \varepsilon\sigma(T_{surface}{}^4 - T_{ambient}{}^4)/(T_{surface} - T_{ambient}) \quad \text{Eq. 51}$$

The outside heat transfer coefficient, $h_{c,o}$ can be determined from Eq. 52:

$$h_{c,o} = h_{c,conv} + h_r \quad \text{Eq. 52}$$

The surface temperature of the pipe can be calculated from Eq. 53:

$$T_{surface} = T_{interface} - Qr_{ins} \quad \text{Eq. 53}$$

The heat lost per unit length can be determined with Eq. 54:

$$Heat\ lost = \pi D_{cs} Q \quad \text{Eq. 54}$$

Table 25 presents the iterative calculation process (based on Equations Eq. 41 to Eq. 54 to determine the heat lost per unit length for a hot air conveying line with an insulation thickness of 50mm and an inner gas temperature of 370°C. The heat lost per unit length for various insulation thickness from 50mm to 400mm and inner gas temperatures from 370°C to 1100°C is shown in Figure 78. Also shown is the surface temperature of the pipe for various insulation thickness and inner gas temperature is shown in Figure 79.

Table 25 Calculation of heat lost per unit length for a hot air transmission line with an insulation thickness of 50mm and the inner gas temperature of 370°C.

Radius of Inner pipe	r_{gas}	m	0.7				
Thickness of insulation	r_{ins}	m	0.75				
Outer shell - Carbon steel	r_{cs}	m	0.756				
Length of pipe	L	m	1000				
Gas temperature	T_{in}	°C	370				
Ambient temperature	$T_{ambient}$	°C	20				
Wind speed	U_{air}	m/s	5				
Iteration			1	2	3	4	5
Surface temperature	$T_{surface}$	°C	21.0	46.0	45.9	45.9	45.9
Interface temperature	$T_{interface}$	°C	369.0	370.0	369.6	369.6	369.6
Air properties							
Average film temperature	$T_{average}$	°C	20.5	33.0	33.0	32.9	32.9
		°K	293.7	306.2	306.1	306.1	306.1

Thermal conductivity	k	W/m.K	0.0	0.0	0.0	0.0	0.0
Viscosity	μ	N/s.m²	0.0	0.0	0.0	0.0	0.0
Prandtl number	Pr		0.7	0.7	0.7	0.7	0.7
Expansion coefficient	β	1/K	0.0	0.0	0.0	0.0	0.0
Air density	ρ	Kg/m³	1.2	1.2	1.2	1.2	1.2
Kinematic viscosity	v	m²/s	0.0	0.0	0.0	0.0	0.0
Specific heat capacity	Cp	kJ/Kg.K	1.0	1.0	1.0	1.0	1.0
Alpha	α	m²/s	0.0	0.0	0.0	0.0	0.0
Reynold number (Eq 43)	Re		493693	458417	458578	458584	458584
Rayleigh number (Eq 44)	Ra		3.5E+08	7.5E+09	7.4E+09	7.4E+09	7.4E+09
Insulation resistance							
Average insulation temperature		°K	468.2	481.1	480.9	480.9	480.9
Insulation thermal conductivity	k_{ins}	W/m.K	0.1	0.1	0.1	0.1	0.1
Insulation resistance	r_{ins}	m².K/W	0.8	0.7	0.7	0.7	0.7
Pipe resistance							
Pipe thermal conductivity	k_{cs}	W/m.K	64.0	62.8	62.8	62.8	62.8
Pipe wall resistance	r_{cs}	m².K/W	0.0	0.0	0.0	0.0	0.0
Forced convection (Eq 45)	$Nu_{D,FC}$		691.7	651.2	651.4	651.4	651.4
	H_{FC}	W/m².K	11.8	11.5	11.5	11.5	11.5
Natural convection (Eq 46)	$Nu_{D,NC}$		83.3	219.1	218.8	218.8	218.8
	h_{NC}	W/m².K	1.4	3.9	3.9	3.9	3.9
Combined convection (Eq 47)	$Nu_{D,Combined}$		691.7	653.3	653.5	653.5	653.5
Heat transfer co-efficient convection (Eq 48)	$h_{c,\ conv}$	W/m².K	11.8	11.6	11.6	11.6	11.6
Radiation (Eq 49)	h_r	W/m².K	4.6	5.2	5.2	5.2	5.2
Overall air side HTC (Eq 50)	$h_{c,o}$	W/m².K	16.4	16.8	16.8	16.8	16.8
Overall resistance (Eq. 42)	U	m².K/W	0.8	1.0	1.0	1.0	1.0
Heat flow (Eq. 41)	Q	W/m²	426.1	353.1	351.4	351.4	351.4
Interface temperature	$T_{interface}$	°C	46.1	41.4	41.4	41.4	41.4
Surface temperature (Eq 51)	$T_{surface}$	°C	46.0	41.1	41.1	41.1	41.1
Heat loss per unit length (Eq. 52)		W/m	2024.1	1677.5	1669.1	1669.1	1669.1

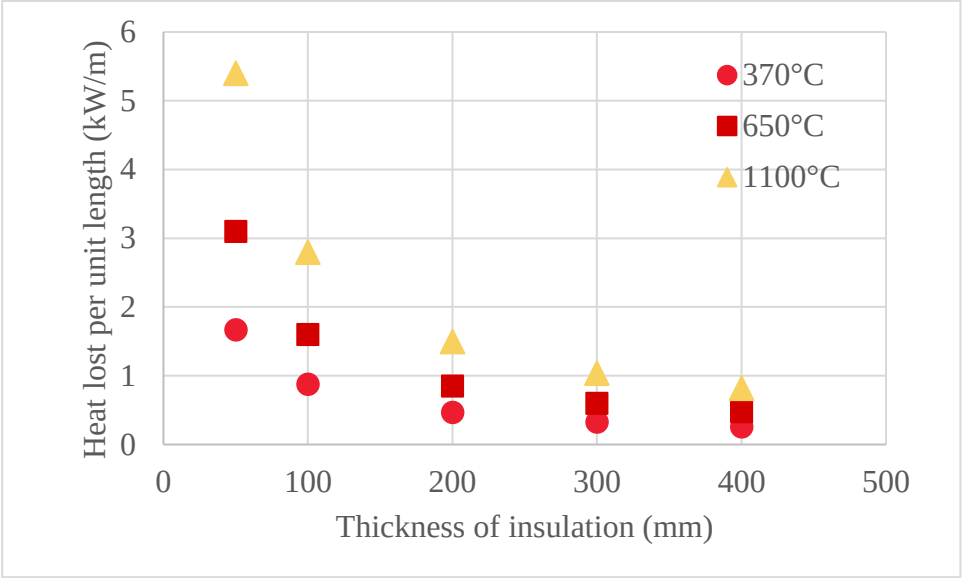

Figure 78: The influence of thickness of insulation layer on the heat lost per unit length for various inner gas temperatures.

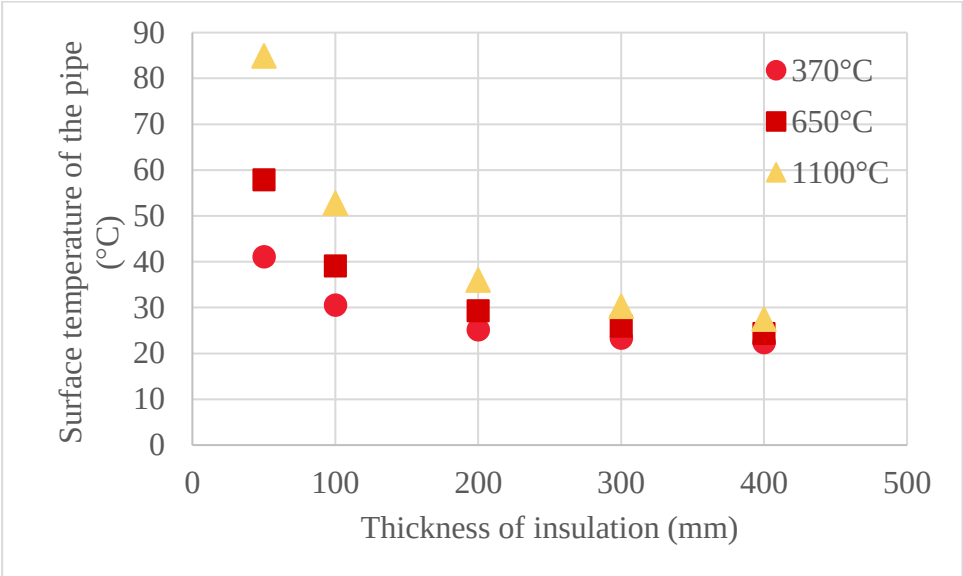

Figure 79: The influence of thickness of insulation layer on the surface temperature for various inner gas temperatures.

The information of the heat loss per unit length in Figure 78 is then used to determine the percentage of heat loss through the pipe. Figure 80 shows the percentage of heat loss for each hot air conveying line with a length of 1000m. A minimum of insulation thickness of 100mm is required if the percentage of heat loss through the pipe to be maintained below 5% for all cases and losses of below 2% can be achieved with sufficient thickness. Further economic evaluation will be performed for the next milestone report.

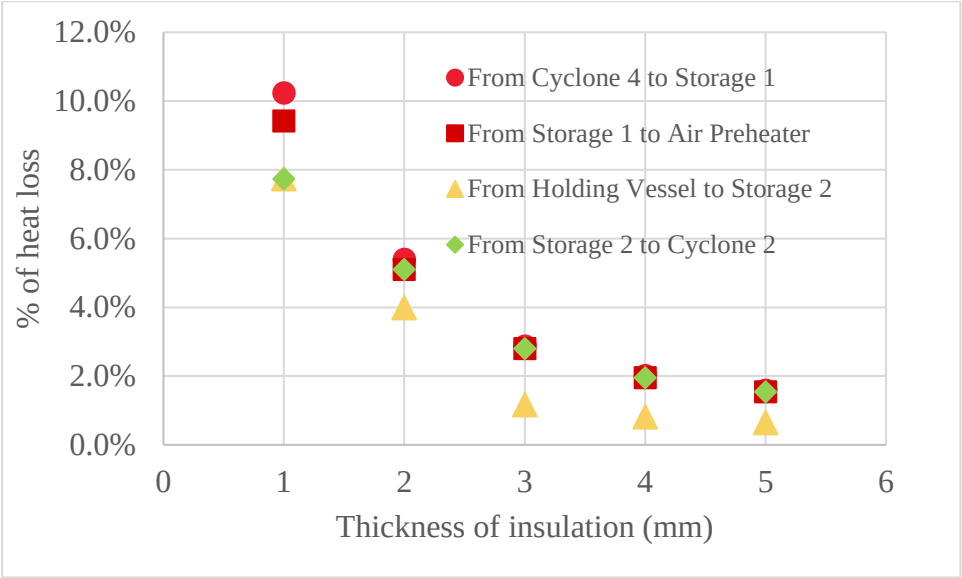

Figure 80: Percentage heat loss of each air transmission line at a length 1000m.

It can be seen in Figure 81 and Figure 82 that a minimum refractory thickness of 300mm is required for 1km and 400mm for 2km. The 3km pipeline requires >400mm thickness for minimise the heat loss. However, this will incur a significant cost of the CAPEX.

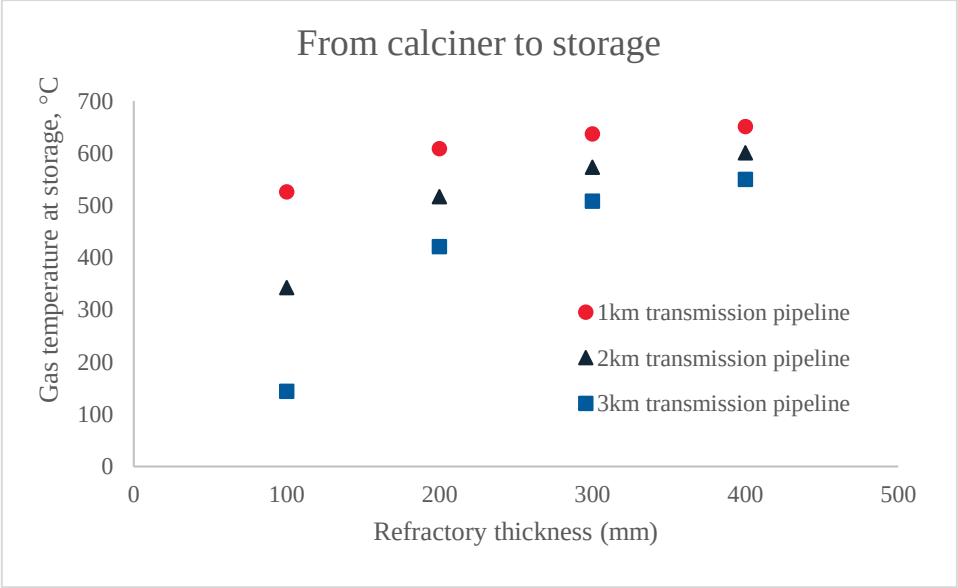

Figure 81: The influence of thickness of insulation layer on the gas temperature arrived at the storage from the calciner at 700°C for various length of transmission pipelines.

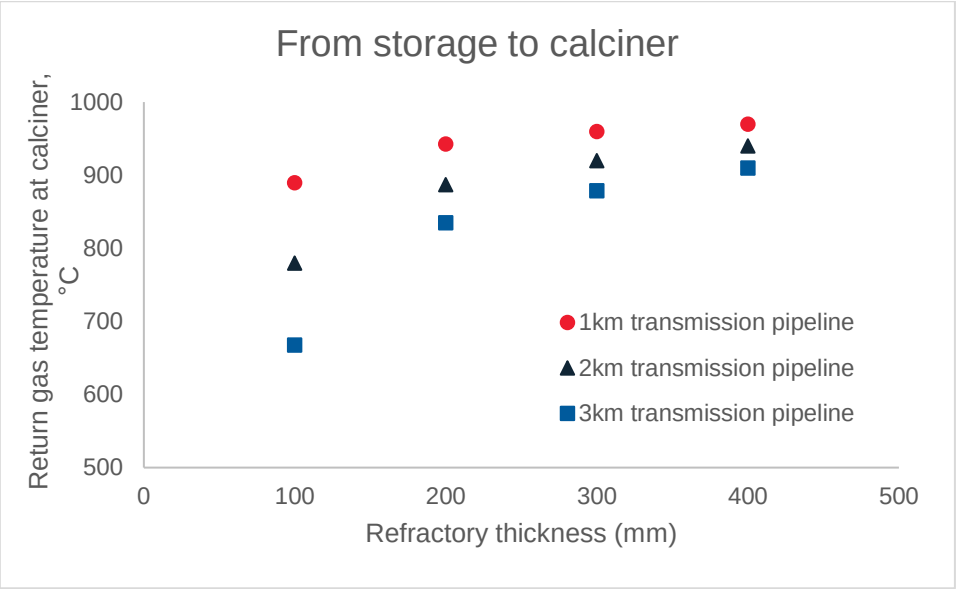

Figure 82: The influence of thickness of insulation layer on the required gas temperature from the storage back to the calciner at 1000°C for various length of transmission pipelines.

6.4. Complete detailed techno-economic assessment of the preferred hybrid calciner configuration

6.4.1. Introduction

Section 6.1 reported a techno-economic assessment (TEA) of both the beam-up and beam down configurations. On that basis, we have selected the beam-up configuration for the detailed TEA reported here due to its greater potential for scaling up above 50MW$_{th}$ compared with the beam-down configuration. We have developed a new CST model, consisting of the SEVR, packed bed storage and air transmission pipelines, using models developed with MATLAB and Simulink tools, to assess the transient behaviour and the annual performance of the proposed CST configurations. Here, we report on the techno-economics of specific configurations, selected to be retrofit able to the existing calcination process without major modification to the existing plant.

6.4.2. Methodology

Plant configuration/layout

Table 26 summarises the three configuration options that have been developed and assessed to. The main difference between these options is whether or not they employ a windowless (opened aperture) or windowed (closed aperture) configuration of the SEVR. In the case of the windowless configurations, we have assessed the two options of an air-only case (Configuration 1a), which does not convey any particles in the heat-transfer media to avoid any potential for particle egress, and an air plus particles case (Configuration 1b) to enhance the overall heat transfer of radiation to the air within the receiver. The third case is a windowed configuration, also employing only air (Configuration 2), because it is not presently possible to avoid particle deposition onto a window, which would lead to window failure. Each of these receiver configurations requires different downstream systems. The storage system can be simultaneously charged and discharged. The advantage of the indirect storage is the decoupling of the usually fine-tuned industrial process from the intermittency of the solar radiation. The charging cycle and the discharging

cycle operate completely independently, which allows the operating pressure and mass flow rates through the SEVR rates to be managed and optimised independently from those of the chemical process.

Table 26 The three configurations of SEVR and the heat transfer media (HTM) used between the receiver and the storage (HTM 1) and between the storage and the process (HTM 2) analysed.

Configuration	Receiver aperture	HTM 1 (CST)	HTM 2(Process)
1a	Open	Air only	Air
1b	Open	Air with particle	Air
2	Closed	Air	Air

Since the SEVR in Configuration 1a (Figure 83) is operated with air only, the dedicated particle management system that is needed in Configuration 1b, can be avoided. However, the disadvantage of using air-only is that the heat exchange from the solar radiation to the air within the receiver is less efficient than occurs with particles, as described below. In both open receiver cases, the pressure in the receiver needs to be managed carefully via a cold air fan that extracts heat from the return air via a heat exchanger. This is needed to balance the pressure at the aperture plane with the atmosphere, to minimise ingress and egress.

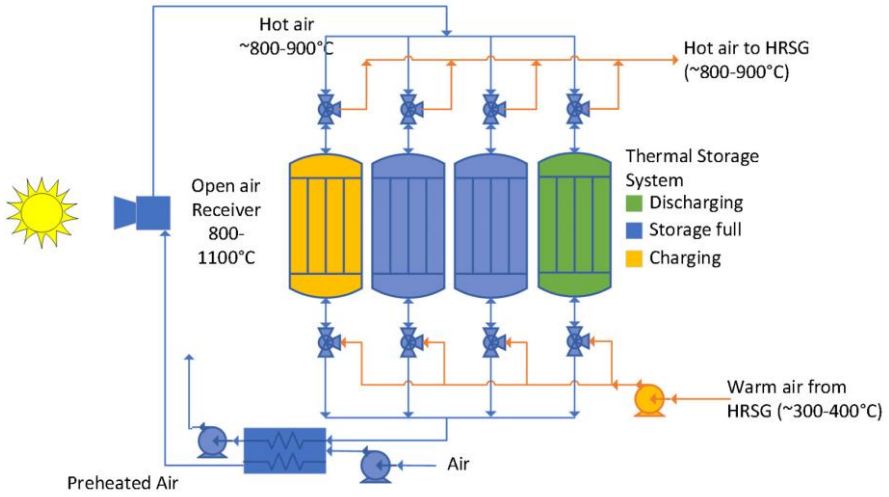

Figure 83: Schematic diagram of Configuration 1a in which the air is heated in a windowless Solar Expanding Vortex Receiver (SEVR), which is directly irradiated, and then stored before transported to the flash calcination plant.

The particles suspended within the HTM in Configuration 1b the SEVR uses adsorb the radiation and transfer heat to the air by convection. This is supplemented by heat transfer from the wall to the HTM. The particles are then separated from the air stream with a dedicated system consisting of an additional cyclone and a particle storage tank before the heated air is fed into the main storage system, as shown in Figure 84.

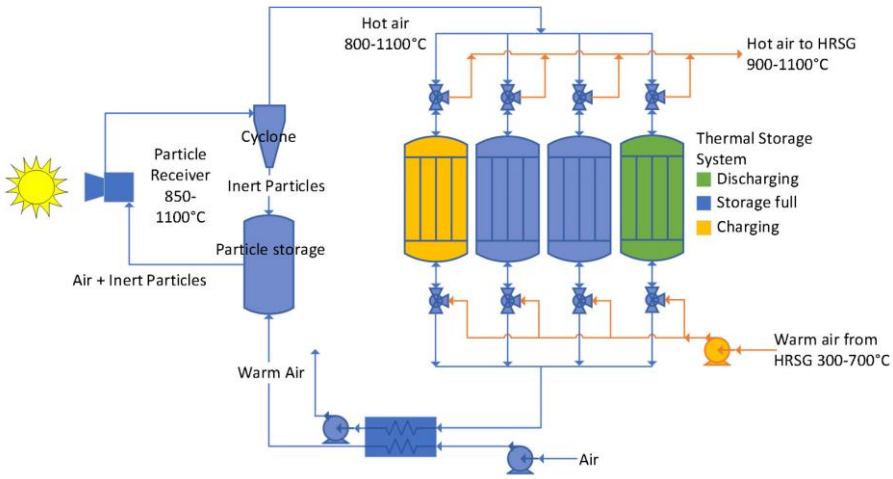

Figure 84: Schematic diagram of Configuration 1b in which the air and particles are heated in a windowless Solar Expanding Vortex Receiver (SEVR), which is directly irradiated. The hot air is then stored before transported to the flash calcination plant while the particles are recycled back to the SEVR.

In Configuration 2, the aperture is sealed with a high temperature quartz window and only air is used. The heat exchanger is avoided because this configuration does not require an exact balance of the pressure with atmosphere, as is needed for the windowless Configurations (1a and 1b) as shown in Figure 85. Hence, air transport is assumed to be provided with a high temperature air blower/pump, based on the availability of a similar technology and materials for the pumping of a high temperature liquid metal pumps and fans as described in (Amy et al., 2017).

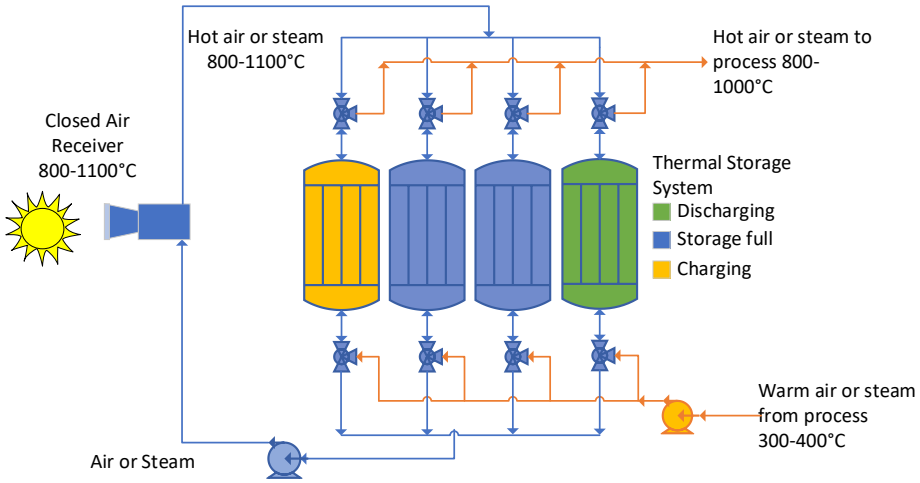

Figure 85: Schematic diagram of Configuration 2 in which the air is heated in a windowed Solar Expanding Vortex Receiver (SEVR), which is directly irradiated. The hot air is then stored before being transported to the flash calcination plant.

6.4.2.1. MATLAB and Simulink

Each configuration was assessed using the in-house codes developed in MATLAB and Simulink with the optical solar input was generated from the Heliosim model as described previously (Potter et al., 2018). The output from the solar field was computed for the reference solar multiple, *SM*, following which the

effect of varying *SM* was estimated by varying the required process power, since the computational effort needed to recompute *SM* for each case was prohibitive. The CST model consists of sub- models that were then connected using the Simulink environment. components that were modelled in detailed are as follows:

- Windowed or windowless Solar Expanding Vortex Receiver (SEVR)
- Packed bed storage
- Particle filtration and feeding systems for the windowless configuration
- Air conveying system, with heat exchanger, for the windowless configurations
- Air transmission pipeline from the storage to the calciner
- Process heat demand

Figure 86 presents the schematic diagram of the complete CST model and the interactions between the sub-models. Here, red boxes indicate the sub-models, whereas the blue arrows indicate the information flow between the sub-models. The advantage of this Simulink model (Figure 87) is that it allows the system to compute the states, such as mass flow rate and temperature, of each sub-model and allows the sub system to exchange this information with each other, so that the effect of all the sub-models on each other and possible feedback effects can be captured within the model.

Firstly, the receiver is heated by the solar radiation until the wall temperature of the receiver is above the threshold temperature of 900 °C before HTM 1 (air or air and particles) is introduced into the receiver. Once the receiver reaches its threshold temperature, the HTM is passed through it and heated by the receiver, then transferred to the packed bed thermal energy storage systems, which have the lowest energy density. The cooled HTM 1 is then used to preheat the incoming air with a heat exchanger. This arrangement allows the operating pressure of the windowless SEVR (Configurations 1a and 1b), to be controlled to balance with the atmosphere using ID and FD fans, to minimise particle egress. Note that the ID and FD fans are assumed to be operated below 100°C.

On the process heat side, the HTM 2 from the calciner is introduced into one of the charged storage systems with the most energy density for heating, following which the heated HTM 2 will be cycled back to the calciner. The process heating cycle only begin, when there is energy in the storage system to heat the HTM 2 from the calciner to deliver a higher temperature back to the calciner. All cases were analysed for one year using 15-minute time-steps.

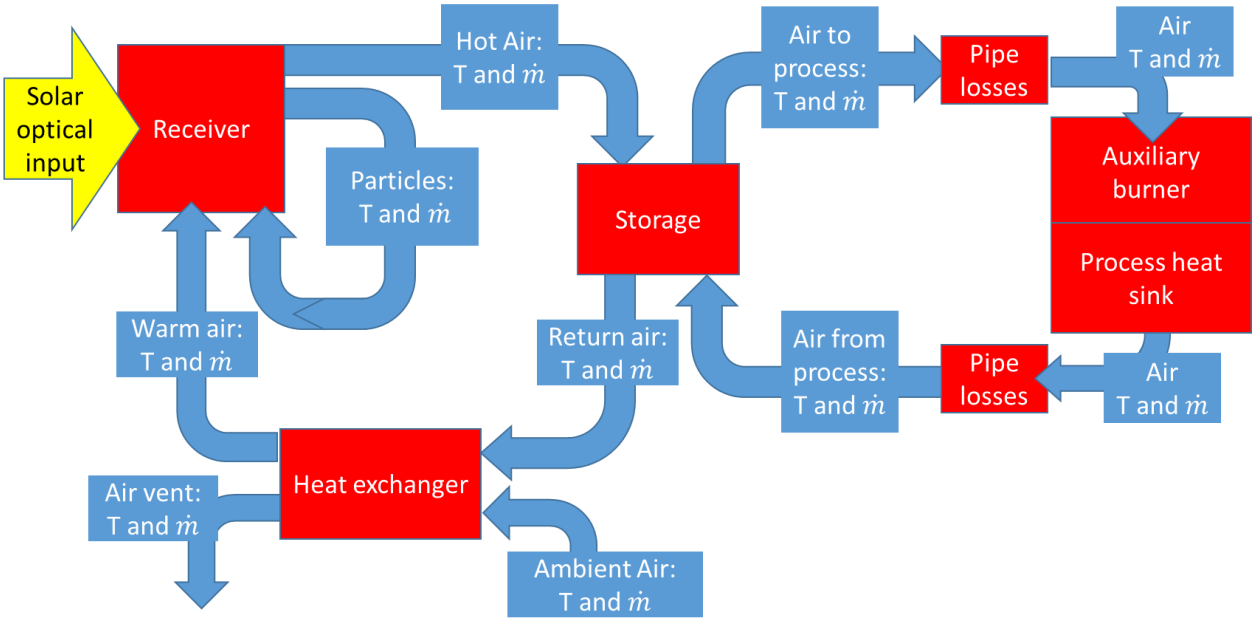

Figure 86: Schematic diagram of the CST model and the interactions between the sub-models. Red boxes indicate the sub-models, blue arrows indicate the operating conditions.

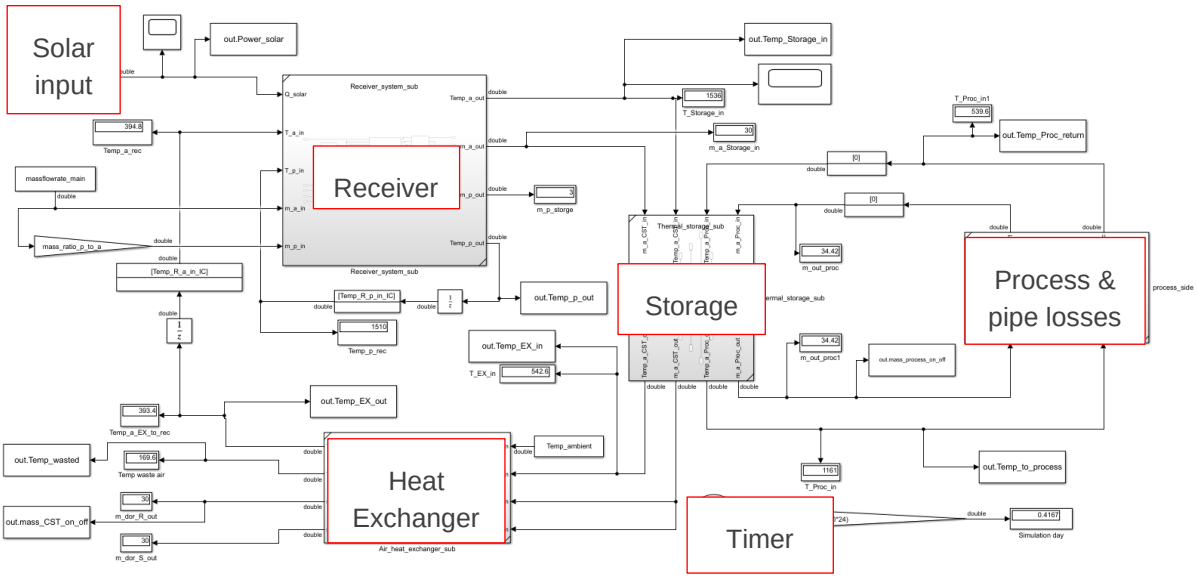

Figure 87: Detailed the Simulink model linking the sub-models.

The separate sub-models are discussed in detail below.

6.4.2.2. Receiver

The receiver was modelled differently for each of the three Configurations (1a, 1b, and 2) as stated above.

1. Windowless SEVR
    a. with air only,
    b. with air and particles,
2. Windowed SEVR with air only,

A zero-dimensional model of the windowless SEVR has been developed by (Rafique et al., 2021) was used for this system modelling. The zero-dimensional model is a multilayered refractory-lined particle-laden solar receiver to allow transient operation (during start-up, turn down, and shut down) over a long time-series of variable solar resource data of 12 months. The transient model employs the governing mathematical equations for mass and energy flows through the receiver cavity, considering the particle and gas phases, thermal losses, and conductive, convective and radiative heat transfer. The windowed SEVR model adapted from the above model to include the window. The solar radiation input of $\dot{Q}_{sol}$ was set at 50 MW_{th} for each case.

For Configuration 1a, the heat transfer coefficient between the receiver wall and the air, together with the effective surface area of the receiver, are the 2 key factors that govern the performance of the receiver. Hence, the effect of the heat transfer coefficient was assessed with a sensitivity study over a range of air mass flow rate from 30 to 67.5 kg/s. The heat transfer coefficient between the receiver wall and air is increased from 50.0 to 95.6 W/m^2K over this range of air mass flow rate. This assessment corresponds to the typical smooth surface. the heat-transfer between the wall of the receiver and the air is poor, so that the temperature difference between the wall and air is high at ~700 °C and the efficiency was found to be about η_{rec}= 62% at the highest tested mass flow rate of air at $\dot{m}_{air}$ =67.5 kg/s.

The next assessment was to artificially increase the heat transfer coefficient between the hot receiver wall and the air (HTM 1) by 50, 100 and 150%, the receiver efficiency increases to η_{rec}= 70, 73 and 75%, respectively. Note that this may be achieved with rough surfaces or fins would lead to higher heat transfer coefficients at the wall, although the direct assessment of performance of specific performance enhancement devices has been made to date.

The energy losses distribution from the receiver is shown in Table 27. It shows that the heat exchange within the air only SEVR is not enough to effectively transfer the energy from the wall of the receiver to the air. It results in a large temperature difference between the wall and air of ~700 °C and achieves an efficiency of only $\boldsymbol{\eta_{rec}}$=62.7% at its highest tested mass flow rate.

For Configuration 1b, the addition of particles into the windowless SEVR employs particles to adsorb energy by radiation (either directly or from the wall) and then transfer the heat to the air by convection. Higher receiver efficiencies are plausible with this configuration because of the increase of effective surface area to the air. Here, the mass flow-rate ratio of particles to air (R_p) is fixed at 10% to ensure the receiver is operating in the 2-way coupling regime, while avoiding the need to recover too much energy from the particles through the particle-clean-up system. It should be noted that the need to achieve sufficiently low convective heat losses through the open aperture is addressed in other sections of the report, below.

For air mass flow rate $\dot{m}_{air}$ = 30 kg/s, a solar thermal input $\dot{Q}_{sol}$ = 50 MW and a particle loading R_p =10%, the calculated thermal efficiency of the receiver is η_{rec}= 69.3%, which is higher than the 67.5kg/s case for Configuration 1a. It further increases to η_{rec}= 74% for $\dot{m}_{air}$ = 67.5 kg/s. Note that these calculations assume a convective loss through 20 % air mixing between the heated air and air from the surrounding, as shown in Table 27.

The increase in thermal efficiency of the particle receiver is achieved at the expense of the need to introduce a particle filtration system, requiring a cyclone and a particle feeder, which induces some additional heat losses, and the need to maintain atmospheric pressure at the aperture, which induces some further heat losses. These losses are accounted for in the system model. The use of high temperature fans is also possible (Amy et al., 2017), since this would reduce heat losses, but would require increased fan power and capital cost.

Configuration 2 employs a window in the receiver to reduce the convective heat loss and also offer potential for increased pressure, which increases heat transfer. While the use of a window in a receiver introduces challenges in terms of reliability and limitations to scale, this approach has recently been advanced commercially by Swiss company, Synhelion, albeit with steam as the HTM. Hence, the project team have recently begun discussions with this company to better understand the commercial status of this approach. These details will be addressed in future reports. Here, the efficiency of the closed air-only receiver was calculated for the same conditions as reported above (air mass flow rate of $\dot{m}_{air}$ = 67.5 kg/s and $\dot{Q}_{sol}$ =50 MW) and estimated be to η_{rec}= 65.2%. This corresponds to as 2.5% improvement comparing with Configuration 1a. However, the value of η_{rec} increases to 74.9% if the mass flow rate is increases to 101.25 kg/s.

The details of the distribution of power losses from this configuration of receiver is shown in Table 28. Note that this assumes that 50 MW_{th} can be accommodated in a single solar receiver with a window, which is not yet confirmed. It is possible that the use of a window may require the use of multiple smaller receivers, which would impact the system configuration. More information of the system performance for case 1a and 1b is reported below (Table 43 and Figure 110).

Table 27: The calculated distribution of power losses from the windowless SEVR configurations.

Configuration	1a (windowless)			1b (windowless)			Unit
$\dot{m}_{air}$	30	45	67.5	30	45	67.5	kg/s
$\dot{Q}$ *solar input*	50	50	50	50	50	50	MW
$\dot{Q}$ *rerad loss, ap*	23.7	17.3	11.2	9.8	7.6	5.7	MW
$\dot{Q}$ *conv loss, ap*	4.0	5.4	7.2	5.3	6.3	7.8	MW
$\dot{Q}$ *other loss*	0.3	0.3	0.2	0.2	0.2	0.2	MW
$\dot{Q}$ *total losses*	27.9	22.9	18.6	15.3	14.2	13.7	MW
$\dot{Q}$ *useful output*	22.1	27.1	31.4	34.7	35.8	36.3	MW
η_{rec}	44.2	54.2	62.7	69.3	71.7	72.5	%

Table 28: The calculated distributions of power losses from the windowed SEVR configuration.

Configuration	2 (windowed)				Unit
$\dot{m}_{air}$	30	45	67.5	101.25	kg/s
$\dot{Q}$ *solar input*	50	50	50	50	MW
$\dot{Q}$ *rerad loss, ap*	23.9	17.2	11.6	7.1	MW
$\dot{Q}$ *reflect loss, ap*	2.5	2.5	2.5	2.5	MW
$\dot{Q}$ *rerad loss, ap*	3.6	3.3	2.9	2.6	MW
$\dot{Q}$ *other loss*	0.8	0.4	0.3	0.3	MW
$\dot{Q}$ *total losses*	30.8	23.3	17.4	12.5	MW
$\dot{Q}$ *useful output*	19.2	26.7	32.6	37.5	MW
η_{rec}	38.4	53.4	65.2	74.9	%

6.4.2.3. High temperature packed-bed storage

Figure 88 present the storage devices consist of large insulated cylinders filled with alumina spheres that act as the thermocline solid storage medium. The inside walls are lined with firebrick, then a layer of insulation material (ceramic fibres) and an outer wall with a layer of concrete. The wall and insulation

design is adapted from (Ma et al., 2020) from the dimensions of the kind of storage device analysed in the following are given in Table 29.

Table 29: Dimension of a single insulated packed-bed storage device.

Material		
r_1	Alumina spheres	2.5m
r_2	Fire brick	2.8m
r_3	Ceramic fibre	4.8m
r_4	Concrete	5.1m

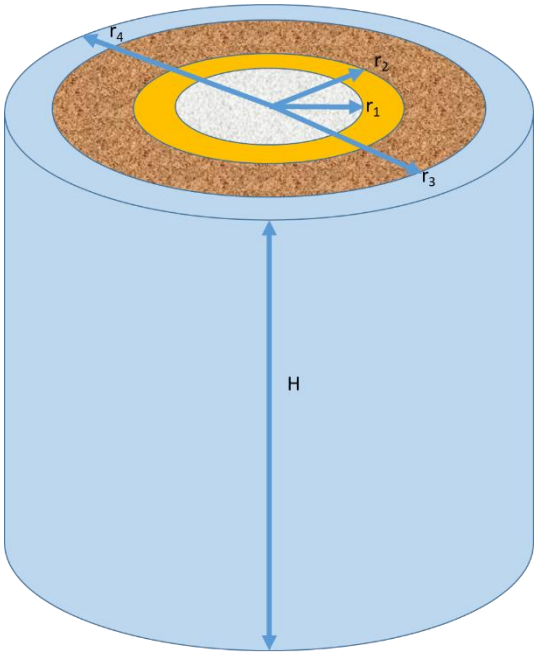

Figure 88: Schematic of the one storage device, the radii are given in Table 29.

Details the model used simulate the storage system are described in the flowing:

The packed bed storage tank has been developed using one dimensional one phase approximation as described in (Hoffmann et al., 2016):

$$(\rho C_p)_{eff}\frac{\partial T}{\partial t} + \varepsilon(\rho C_p)_{HTF} u \frac{\partial T}{\partial x} = k_{eff}\frac{\partial^2 T}{\partial x^2} + U_{tot}\frac{A}{V}(T - T_{ext}) \qquad \text{Eq. 55}$$

where the heat capacities are given as $(\rho C_p)_{eff} = \varepsilon(\rho C_p)_{HTF} + (1-\varepsilon)\left(\rho C_p\right)_{stor}$, with ε=0.4 being the mean void fraction for spherical particles (Benyahia and O'Niell 2005) in a packed bed. The heat conductivity is computed as $k_{eff} = \varepsilon k_{HTF} + (1-\varepsilon)k_{stor}$, and u being the fluid velocity. It is assumed that the temperature T is the same for the storage medium and the heat transfer fluid (HTF), this assumption is discussed and verified in (Hoffmann et al., 2016). The heat loss to the environment is described with the parameter U_{tot}.Which is computed as via the heat losses of the cylinder:

$$\boldsymbol{Q_{tot}^{loss} = Q_{top} + Q_{bot} + Q_{cyl}} \quad \textbf{Eq. 56}$$

where $Q_{top} = Q_{bot}$ is the loss at the two ends of the cylindrical storage device and Q_{cyl} is the loss via the cylindrical surface. The overall heat transfer coefficient U_{tot} or h_{ext} is defined via

$$\boldsymbol{Q_{tot}^{loss} = U_{tot} A_{tot} \Delta T} \quad \textbf{Eq. 57}$$

with $A_{tot} = \pi r_{stor}^2 + 2\,\pi\, r_4 L$.

The heat loss via cylinder surface is computed as follows:

$$\boldsymbol{Q_{tot}^{loss} = \frac{\Delta T}{R_{tot,cyl}} + \frac{\Delta T}{2R_{top}} = \Delta T \left(\frac{1}{R_{tot,cyl}} + \frac{1}{2R_{top}} \right)} \quad \textbf{Eq. 58}$$

with

$$R_{tot,cyl} = \sum_{layers} R_{layer}$$

$$R_{top} = \sum_{layers} R_{layer}$$

The heat resistances of the separate layers are:

$$\boldsymbol{R_{brick,cyl} = \frac{1}{2\,\pi k_{brick} L} \ln\left(\frac{r_2}{r_1}\right)} \quad \textbf{Eq. 59}$$

$$\boldsymbol{R_{ins,cyl} = \frac{1}{2\,\pi k_{ins} L} \ln\left(\frac{r_3}{r_2}\right)} \quad \textbf{Eq. 60}$$

$$\boldsymbol{R_{conc,cyl} = \frac{1}{2\,\pi k_{conc} L} \ln\left(\frac{r_4}{r_3}\right)} \quad \textbf{Eq. 61}$$

$$\boldsymbol{R_{conv,cyl} = \frac{1}{h_{conv} \cdot\ 2\,\pi\, r_4 L}} \quad \textbf{Eq. 62}$$

where R_{conc} is the heat resistance through the concrete, R_{ins} through the insulation, R_{brick} through the fire brick and finally the heat resistance of the outside convection to the air is R_{conv}. Note that is assumed that the inside of the concrete wall is in thermal equilibrium with the storage material. For the bottom and top the heat resistances are simplified as

$$\boldsymbol{R_{brick,top} = \frac{d_{brick}}{\pi\, r_2^2 k_{wall}}} \quad \textbf{Eq. 63}$$

$$\boldsymbol{R_{ins,top} = \frac{d_{ins}}{\pi\, r_3^2 k_{ins}}} \quad \textbf{Eq. 64}$$

$$\boldsymbol{R_{conc,top} = \frac{d_{conc}}{\pi\, r_4^2 k_{ins}}} \quad \textbf{Eq. 65}$$

$$\boldsymbol{R_{conv,top} = \frac{1}{h_{conv} \cdot\ \pi\, r_{st4or}^2}} \quad \textbf{Eq. 66}$$

where the insulation thicknesses are the same as on the side and hence

$$d_{brick} = r_2 - r_1$$
$$d_{ins} = r_3 - r_2$$
$$d_{conc} = r_4 - r_3$$

The overall heat transfer coefficient is:

$$\boldsymbol{U_{tot}} = \frac{\mathbf{1}}{\boldsymbol{A_{tot}}}\left(\frac{\mathbf{1}}{\boldsymbol{R_{tot,cyl}}} + \frac{\mathbf{1}}{\mathbf{2}\boldsymbol{R_{top}}}\right) \qquad \textbf{Eq. 67}$$

The model was implemented using the MATLAB partial differential equation solver. The algorithm computes the state of the storage device at every time-step. The rates of energy fed from the receiver into the storage and from the storage to the process are also computed in order to determine the overall storage efficiency and the solar share. The annual time series of solar power through the SEVR aperture was computed at 15 minutes intervals. The state of each storage device is simulated within the time steps on a shorter time step to have high accuracy of the temperature profile within the device, which is crucial to the understanding of the temperature delivered to the process.

To validate the model for a single storage tank experimental data from literature was used (Meier et al., 1991). The experimental device is a lab scale compared to the sizing considered for our purpose. However, the upscaling should be possible and the results of the model should still be valid. The key dimensions of the experimental setup are:

- Diameter = 0.15 m
- Storage height = 1.2
- Mass flow rate = 0.004 kg/s
- Porosity = 0.36
- T_{low} = 21°C and T_{high} =550°C

The storage temperature was measured at 7 positions along in the centre of the device along the axis of the cylinder. The results of the simulation validation are shown in Figure 89.

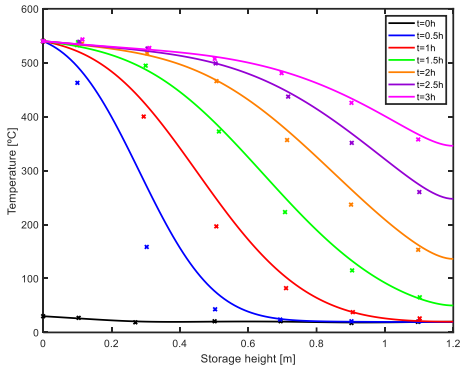

Figure 89: Experimental (x) and simulated (solid lines) results for the thermocline storage device. Experimental data was taken from (Meier et al., 1991).

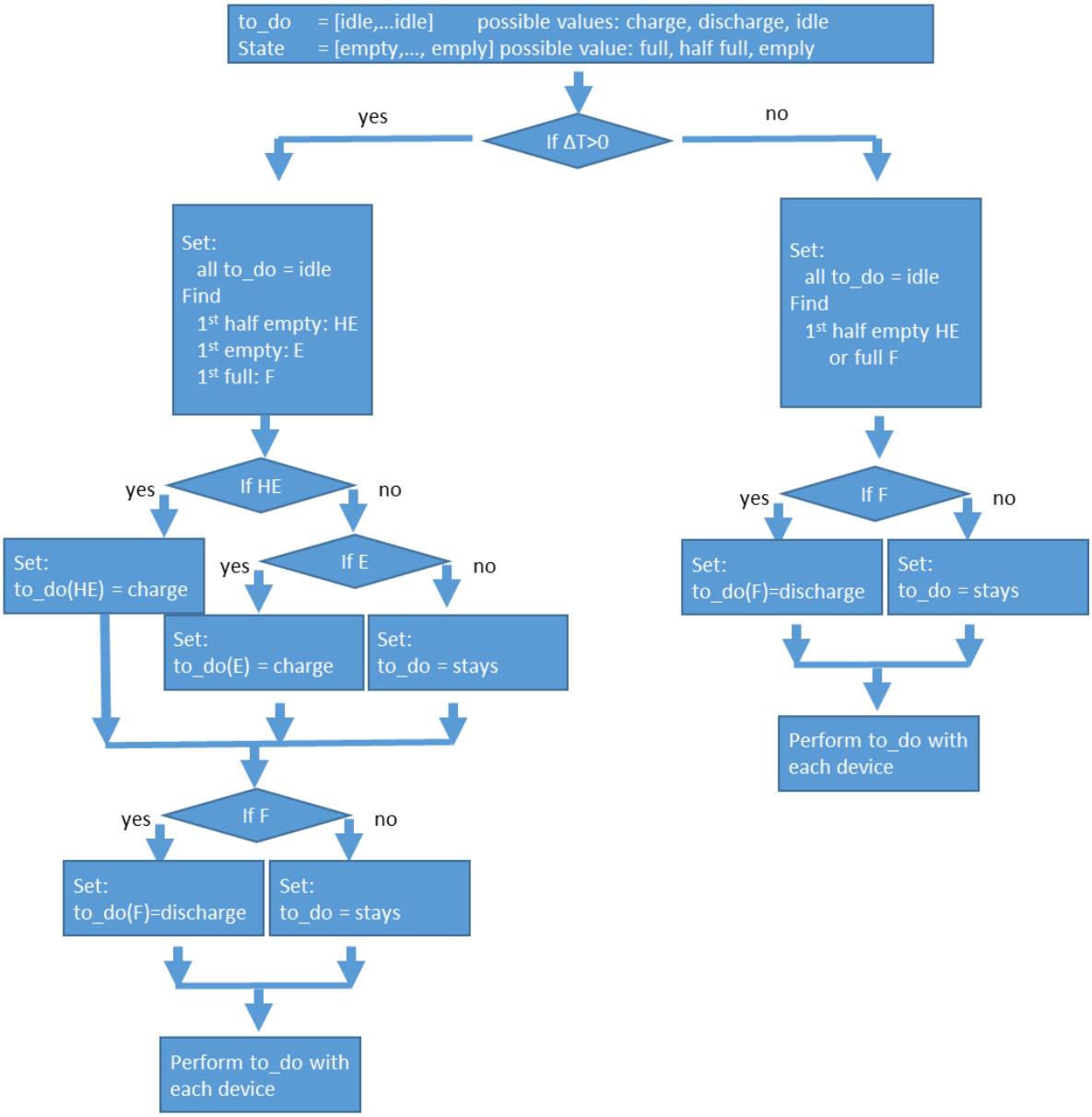

Figure 90: Flow chart to decide which storage device to be charged and discharged.

To control all storage devices the temperatures at the top (inlet during charging / outlet during discharge) and at the bottom (outlet during charging / inlet during discharge) need to be measured. The operating strategy was chosen to be temperature based and will be optimized in future work. An empty or half empty storage device receives hot air from the receiver as soon as the air temperature is above the low storage set point and is charged until the temperature at the bottom of the tank reaches the charging set point. When one device is full it starts to be discharged and the next device will receive power from the solar system. The detailed logic to set the behaviour of the system is shown in Figure 90. With the control strategy, described in Figure 90, two storage devices are sufficient and in all simulations performed a third device was never set to charge. The height and the diameter of the storage were selected and fixed according to the minimum surface to volume ratio of the cylinder in order to minimise the heat losses. Furthermore, the effectiveness of the insulation (ceramic fibre) was analysed to understand the behaviour of the state of charge (SOC) of a full vessel and the impact on the storage temperature of idling for 24h. This was done by maintaining a constant operating temperature of 1100°C. Here, the fully discharged storage temperature was defined to be 600°C, which constitutes the minimum SOC. Table 30 and Table 31 present the calculated storage temperature after 24 hours and the corresponding SOC, respectively.

Table 30: The calculated storage temperatures after lying idle for24 hours as a function of the storage height, H, and the insulation thickness th_{ins}.

Temperature [°C]								
th_{ins} [m]→ H_{stor} [m]↓	5	10	15	20	25	50	75	100
1	140	461	653	765	835	978	1024	1045
2	298	642	800	883	932	1027	1055	1068
5	560	828	929	980	1009	1062	1077	1084
7	656	880	963	1004	1027	1070	1082	1088
10	750	928	993	1024	1043	1076	1086	1090
20	899	999	1036	1054	1065	1085	1091	1094
30	962	1029	1054	1067	1074	1089	1094	1096
40	997	1046	1064	1074	1080	1091	1095	1096
50	1018	1056	1071	1078	1083	1093	1096	1097
60	1033	1064	1075	1082	1086	1094	1096	1097

Table 31: The state of charge (SOC) for a tank after a 24 h idle period as a function of the storage height H_{stor} and the insulation thickness th_{ins}.

SOC [%]								
Th_{ins} [m]→ H_{stor} [m]↓	5	10	15	20	25	50	75	100
1	-92%	-28%	11%	33%	47%	76%	85%	89%
2	-60%	8%	40%	57%	66%	85%	91%	94%
5	-8%	46%	66%	76%	82%	92%	95%	97%
7	11%	56%	73%	81%	85%	94%	96%	98%
10	30%	66%	79%	85%	89%	95%	97%	98%
20	60%	80%	87%	91%	93%	97%	98%	99%
30	72%	86%	91%	93%	95%	98%	99%	99%
40	79%	89%	93%	95%	96%	98%	99%	99%
50	84%	91%	94%	96%	97%	99%	99%	99%
60	87%	93%	95%	96%	97%	99%	99%	99%

From the above data, the minimum insulation thickness to achieve a given state of charge has been identified. We analysed the minimum insulation thickness for target values of SOC over the range 5% to 95% following an idle period of 24h. These values were then fitted with a power law which is given in Eq. 68.

$$th_{ins} = \begin{cases} a \cdot H^b + c & \text{if } (a \cdot H^b + c) > 0 \\ o & \text{if } (a \cdot H^b + c) < 0 \end{cases} \qquad \textbf{Eq. 68}$$

The fitting coefficients are shown in Table 32 and a subset of the computed insulation thicknesses and the resulting fits are as shown in Figure 91. It can be seen that, especially for tanks smaller than 10 m, the

insulation thickness is unreasonably large compared to the size of the device when high heat retainment is required. However, it is possible to achieve SOC=80% with an insulation thickness of 5m for *H* > 40m.

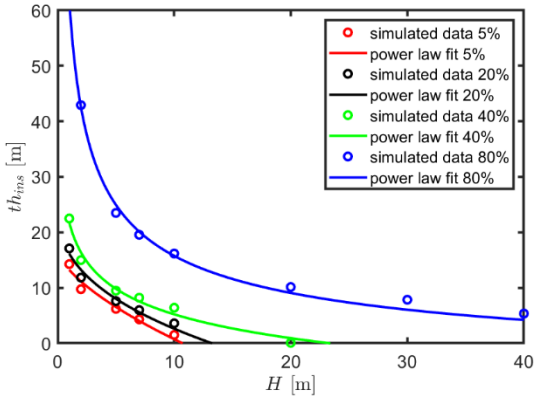

Figure 91: The calculated insulation thickness for the storage device as a function of storage height, to achieve a given state of charge after 24h of idling.

Table 32: The values of the coefficients from Equation Eq. 66 used to find the storage insulation thickness needed to achieve a certain SOC after 24h of idling.

SOC	a	b	c
5%	-81.33	0.0598	95.28
10%	247.7	-0.0215	-233.1
20%	-9.399	0.387	25.54
30%	-27.92	0.1825	46.43
40%	82.74	-0.0969	-60.97
60%	57.89	-0.2712	-23.21
80%	70.58	-0.45	-8.716
85%	81.04	-0.5002	-5.422
90%	112.9	-0.4705	-8.48
95%	185.5	-0.267	-48.06

This procedure was used to define a target 24h storage state of charge SOC_{24} and derive the corresponding insulation thickness. This way, any variation in storage size will not affect the performance and all tested devices have a similar performance. The target 24h storage state of charge SOC_{24} can be varied in the same way for all storage sizes and the insulation thickness chosen in the way described above. Thus, it is possible to derive an insulation thickness for a give storage height, using Eq. 68, which in turn is derived directly from the number of hours the storage can supply the process. The SOC_{24} was introduced to find equivalently performing storage devices for different storage configuration. The SOC_{24} is merely a parameter connecting the different storage parameters in a comparable way. It is important to considered that a $SOC_{24}$of 5% does not mean that the storage device is performing only with a 5% efficiency. The parameter merely states that a full tank will have discharged through losses only to 5% after 24 hours. However, at no time in the simulation did a storage tank need to idle for this long and the energy is recovered at much higher rates after a shorter storage period.

The final change made to the previous model is that the operating strategy for charging and discharging the device was optimised to achieve an overall smoother temperature curve for the air flow sent from the storage device to the alumina process.

6.4.2.4. Heat exchanger

A heat exchanger was used for the windowless Configurations (1a and 1b) to allow the use of a low-temperature fan to circulate the high temperature air through the system. Here, the heat exchanger effectiveness was chosen to be 75% based on a shell and tube heat exchanger. The heat exchanger area was calculated accordingly to meet this requirement; hence the heat exchanger area can be used for the cost estimation, shown in Table 34.

6.4.2.5. Air transmission pipeline

Air transmission pipelines are required for this retrofitting option to connect the CST plants to the calciners. The energy losses through a pipeline have been assessed previously in Section 6.3.2. In the present study, we have assessed the effect of insulation materials (refractory alone or the combination refractory and ceramic fibre) and thickness of insulation material on the energy losses as well as the cost. Similar to the approach used for the storage system, a target efficiency for each pipeline was defined. Also, the pipe diameter and insulation thickness were computed for a normalised transmission pipeline of 1 km length.

6.4.2.6. Process and solar multiple

The energy demand from the calciner was modelled as a heat load with a constant temperature for the incoming air of 600°C being sent to the storage system. The calciner was assumed to be operated at steady-state with a target temperature for the return air from the storage to the calciner being set at 1100°C. This configuration uses the energy from the CST to replace the natural gas consumed in the air preheater only, which is approximately 20MW_{th} or 25% of the total energy consumed in the calciner. In the event that the air temperature from the CST/storage system falls below the target temperature, an auxiliary heater was used in the model to maintain the air temperature.

The influence of solar multiple (SM = 2.5 vs 5) on the LCOH was assessed by varying the process heat output capacity from the storage system from 20 (SM = 2.5) to 10 MW_{th} (SM = 5), while the solar input from the heliostat field was fixed at 50MW_{th}. Note that the SM is ratio of solar field capacity to receiver design output capacity. A high SM allows the plant to maintain output for lower values of solar radiation.

The annual performance (at a time step of 15 minutes) and LCOH simulations were performed using a high-performance computer at the University of Adelaide in order to assess multiple cases (>1000) and to identify the optimistic configurations. The parameters that were varied are listed in Table 33. Most cases were simulated for the location at Pinjarra and only the most optimistic conditions were then also assessed for the location of Learmonth.

Table 33: List of parameters that were varied in the simplified optimization process.

Loc	Solar location	Pinjarra and Learmonth
SM	Solar multiple	2.5 and 5
$\dot{m}_{air}$	Air mass flow rate in the receiver side (kg/s)	30, 45, 67.5
R_p	Particle mass ratio (%)	0, 10
N_s	Number of storage devices	2, 3, 4
H_s	Number of total storage hours	4, 8, 12
SOC_{24}	24 hour target state of charge of the storage (%) to define the insulation thickness	0, 5, 10, 20, 30, 40, 60, 80
L_p	Length of the pipe (m)	1000, 2000, 4000
η_p	Target insulation efficiency of the transmission pipe over 1 km (%)	85, 90, 93, 95, 96, 97

6.4.2.7. Design of a 50MW$_{th}$ CST system

Figure 92 and Figure 93 present a system configuration of a 50MW$_{th}$ SEVR coupled with a packed bed storage and a heat exchanger for Configuration 1b and Configuration 1a or 2, respectively.

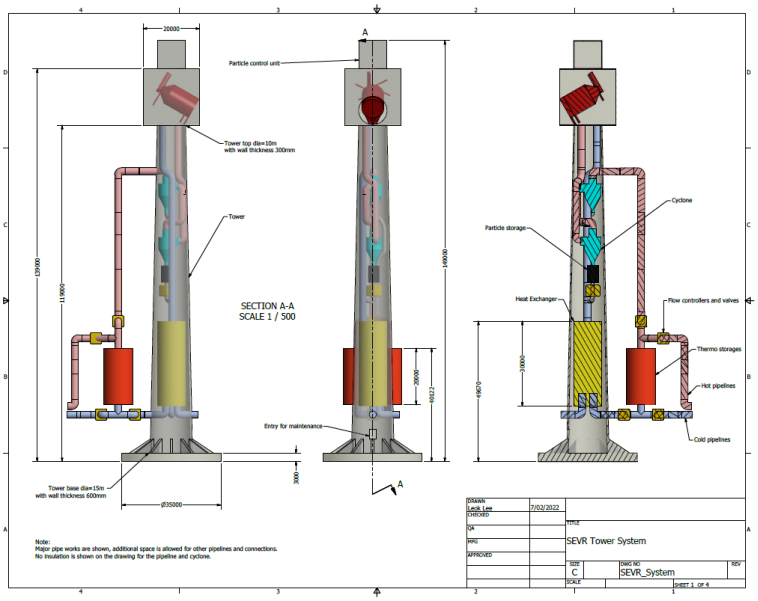

Figure 92: A 50MW$_{th}$ windowless SEVR receiver with air and particles (Configuration 1b) on tower together with a particle conveying system, a packed bed storage (red boxes) and a heat exchanger (yellow box).

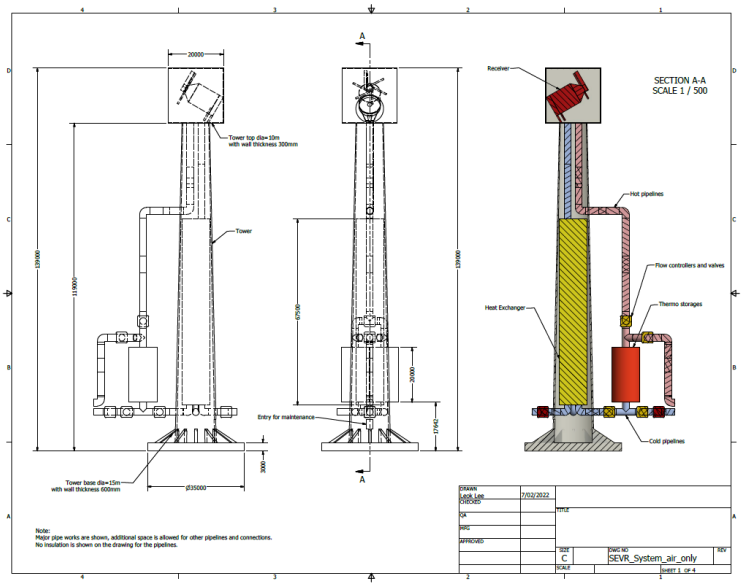

Figure 93: A 50MW$_{th}$ windowless and windowed SEVR receiver with air only (Configuration 1a or 2) on tower together with a packed bed storage and a heat exchanger.

6.4.2.8. Economic analysis

The levelized cost of solar heat (LCOH) is defined as:

$$LCOH = \frac{fC + O}{Q} \quad \text{Eq. 69}$$

where C is the total capital expenditure (CAPEX) of the solar system excluding all materials for the backup system, O is the annual operational expenditure, which includes operation and maintenance of the solar plant only, the cost for fossil backup fuels such as natural gas is explicitly excluded from the calculation and Q is the annual heat from the solar plant delivered to the process. It is assumed that there is no degradation and the power output is assumed to be constant. The annuity factor, f, is computed as follows:

$$f = \frac{r_{disc} \cdot (1 + r_{disc})^n}{(1 + r_{disc})^n - 1} \quad \text{Eq. 70}$$

where r_{disc} is the discount rate (7% and 13%) and n = lifetime in years (30 years). It is important to highlight that all $LCOH$ values in this document represent to the cost for the solar heat only and no backup cost are included in this simulation. The CAPEX was estimated using cost of material as well as engineering procurement, construction and management (EPCM) costs for all the components of the solar plant system and the transmission to the calcination process. The cost for the backup system is not included neither is the cost for fossil back-up fuel. The cost is specified per unit used in this computation as shown in Table 34 so that the cost every sub-system in each of the parametric studies can be calculated.

Table 34: Table of parameters for all components and assumption for the LCOH computations.

Item	Cost	Unit	Source
Field & Tower	$32,500,000	Unit	Milestone 5
Receiver			
Refractory	$8,342	AUD/m^3	Hatch
Insulation	$140	AUD/m^3	market research
Steel	$39,250	AUD/m^3	Hatch
Window	$35,000	AUD/m^2	estimate
Storage tank			
Fire brick	$1,620	AUD/m^3	market research
Ceramic fibres	$140	AUD/m^3	market research
Concrete	$2,426	AUD/m^3	Hatch
Storage material			
Alumina ball	$3,466	AUD/m^3	Milestone 8
Ratcheting	$731	AUD/m^3	Milestone 8
Transmission pipeline			
Refractory	$8,342	AUD/m^3	Hatch
Insulation	$140	AUD/m^3	market research
Duct	$4,846,000	AUD/km	Hatch
Structural support	$400,000	AUD/km	Hatch
Concrete sleepers	$50,000	AUD/km	Hatch
Valves	$200,000	AUD/unit	Hatch
Heat exchanger	28000+54*HX_area^1.2	AUD(m^2)	Garrett 1989 (Garrett, 1989)

Blowers (27°C)	$787,428.17	AUD/unit	Garrett 1989 (Garrett, 1989)
Blowers (600°C)	$1,023,656.62	AUD/unit	Garrett 1989 (Garrett, 1989)
EPCM	30	% of total capex	Hatch
Annual Operational cost	2	% of total capex	(Bader et al., 2019)
Finance			
Lifetime	30	years	Assumed in this study
Discount rate	7 &13	%	(Bader et al., 2019)

6.4.3. Results and summary

6.4.3.1. Reference conditions:

The levelized cost of heat, LCOH, and solar share (SS) are first reported for the reference conditions shown in Table 35. Importantly, these include a length of the air transmission pipeline of 1km, owing to the constraints of operating with a retro-fit condition, which was found to have a big influence on the LCOH, owing to the high cost of this component. Lower costs are reported subsequently for other conditions.

Table 35: The reference conditions used to calculate the LCOH and Solar Share for the alumina process, the detail information and diameters calcination from these parameters are shown in Table 40 to Table 42.

Parameter	Symbol	Reference condition
Solar location	Loc	Pinjarra
Solar multiple	SM	2.5
Air mass flow rate in the receiver side (kg/s)	$\dot{m}_{air}$	45
Particle mass ratio (%)	R_p	10
Number of storage devices	N_s	2
Storage capacity - total storage hours	H_s	4
24 hour target state of charge of the storage (%)	SOC_{24}	5
Length of air transmission pipeline	L_p	1000
Target Effectiveness of air transmission pipeline over 1 km (%)	η_p	95

The choice of reference values for the cost of field and tower were reported in a previous report. Here a sensitivity study of effect on the LCOH of varying the cost of field and tower about the reference values was preformed, the results of which are presented in Figure 94. There is a linear relationship between the cost of field and tower and LCOH for the reference conditions shown in Table 35, with a slope of 60%. That is halving the cost of the field and tower from the reference value of AUD 32.5m (Table 34) reduces the LCOH by 23%.

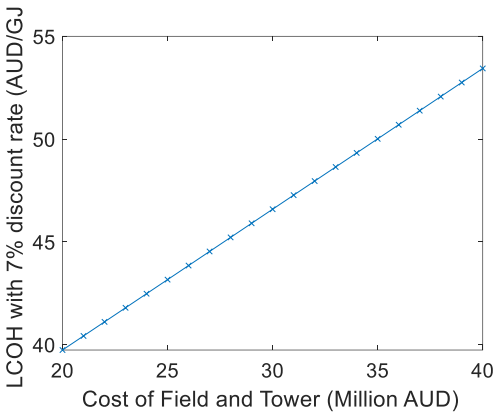

Figure 94: Calculated effect of the cost of field and tower on LCOH (AUD/GJ) for a discount rate, r_{disc} =7%.

6.4.3.2. Effect of 24 hour target state of charge of the storage on annual solar share and levelised cost of heat

Figure 95a and Figure 95b present the effect of 24 hour target state of charge of the storage on annual solar share and LCOH for the reference conditions shown in Table 35. Interestingly, the SOC_{24} = 5% was found to be the most cost effective for these conditions. This is because the insulation is relatively expensive for a small device that need to keep energy for a long time. As the solar multiple does not allow for large amount of energy to be stored, large storage systems do not make sense. As the storage times are much shorter than 24 hours, it is not cost effective to design for long thermal storage with a storage capacity of 4 hours. That is, the annual solar share increases by only 20% as the value of SOC_{24} is increased from 5% to 100%. In particular, the LCOH increases strongly as SOC_{24} is increased beyond 40% due to significant cost associated with the insulation material required for the storage system.

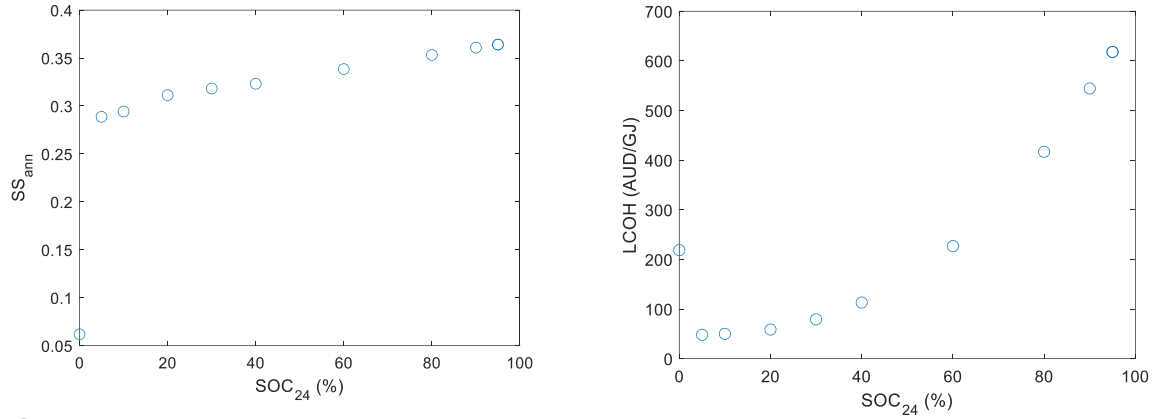

a) b)

Figure 95: Calculated effect of target thermal storage state of charge after 24 hours (SOC_{24}) on a) annual solar share (SS_{ann}) b) LCOH (AUD/GJ) for a discount rate, r_{disc} =7%.

6.4.3.3. Effect of target thermal storage state of charge after 24 hours

Figure 96 and Figure 97 present the influence of the effectiveness of air transmission pipeline E_p on the annual solar share SS_{ann} and the $LCOH$ for the reference conditions (Table 35). These are performed for fixed values of the operating parameters: location = Pinjarra, mass flow rate $\dot{m}_{air}$ = 30 kg/s, particle mass ratio R_p=10%, number of storage vessels N_s=2, total capacity of storage H_s= 4 hours and a 24h target storage efficiency of SOC_{24} 5%. As expected, the SS_{ann} increases with η_p and decreases with an increase

in the length of pipeline both for SM=2.5 and 5 (Figure 96). These trends highlight the challenge of optimisation. For the cases shown here, the lowest value of LCOH occurs for E_p= 93 for the SM= 2.5 and E_p= 95% for SM=5 on $LCOH$ (Figure 97).

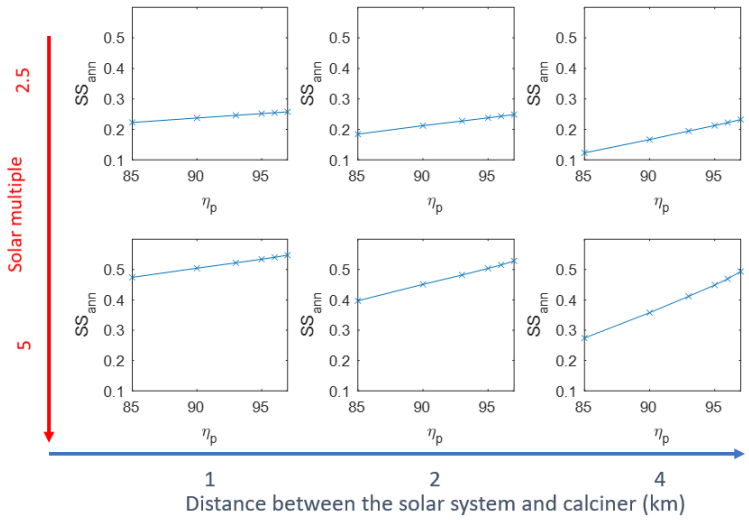

Figure 96: Influence of the effectiveness of the air transmission pipeline on the annual solar share (SS_{ann}) for a series of solar multiples and lengths of the pipeline at Pinjarra. Other conditions are reported in Table 35.

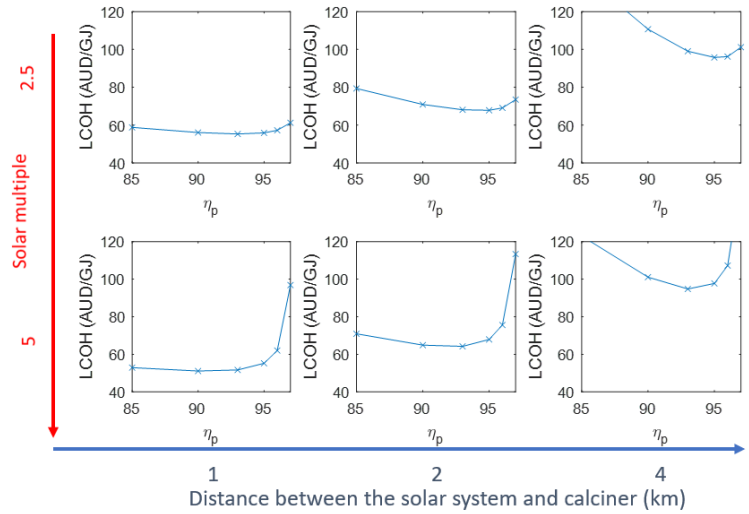

Figure 97: Influence of the effectiveness of the air transmission pipeline on the levelized cost of heat (LCOH) for a series of solar multiples and lengths of the pipeline at Pinjarra.

6.4.3.4. Economic evaluation

Figure 98 presents the effect of number of storage devices (Ns) and number of total storage hours (Hs) on annual solar share for Configuration 1a (windowless SEVR with air only) at Pinjarra for different SM and mass air flow. This is based on 24 hours target storage state of charge $\mathrm{SOC}_{24} = 5\%$ and a pipe length of L_p = 1km with an effectiveness of the air transmission pipeline of E_p= 95%.

The most optimistic configuration for both SM= 2.5 and 5 are shown in Table 36. For SM= 2.5, the annual solar share was estimated to be 23% and with an $LCOH$ of AUD59.5/GJ at a discount rate r_{dsic}=7%, while the $LCOH$= AUD92.3/GJ at a discount rate r_{disc}=13%. These costs are clearly much higher than the current cost of natural gas, which is of order AUD10/GJ.

Similarly, for SM= 5, the annual solar share was found to be 46% with an $LCOH$ of AUD58.2/GJ at a r_{dsic}=7%, and $LCOH$= AUD90.2/GJ at a r_{disc}=13%. Detailed analysis of these two cases is shown in Table 43 and Table 44.

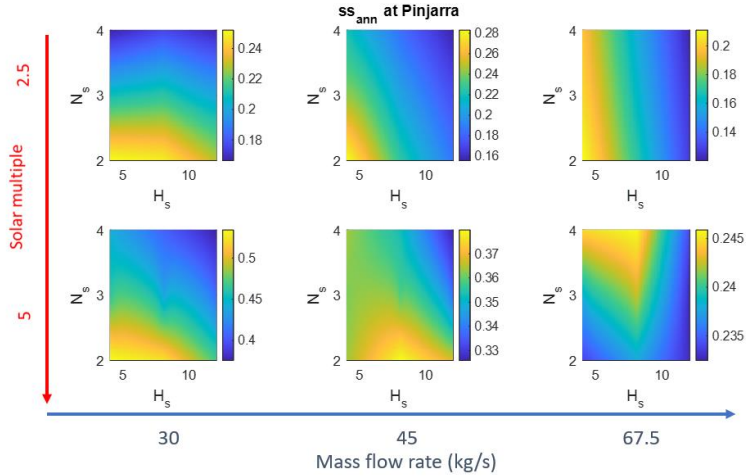

Figure 98: The infleunce of the number of storage devices (N_s) and number of total storage hours (H_s) on the annual solar share (SS_{ann}) for Configuration 1a (windowless SEVR with air only) for the reference conditions (Table 35) at Pinjarra. The top row shows the LCOH for a solar multiple of SM=2.5 whereas the second row for SM =5. The three columns correspond to mass flow rates through the receiver of $\dot{m}_{air}$ =30, 40, to 67.5 kg/s.

Table 36: The most optimistic parameters for Configuration 1a located at Pinjarra and the reference conditions (Table 35).

SM	$\dot{m}_{air}$	R_p	N_s	H_s	SOC_{24}	L_p	η_p
2.5	45	0	2	4	5	1000	95
5	30	0	2	4	5	1000	95

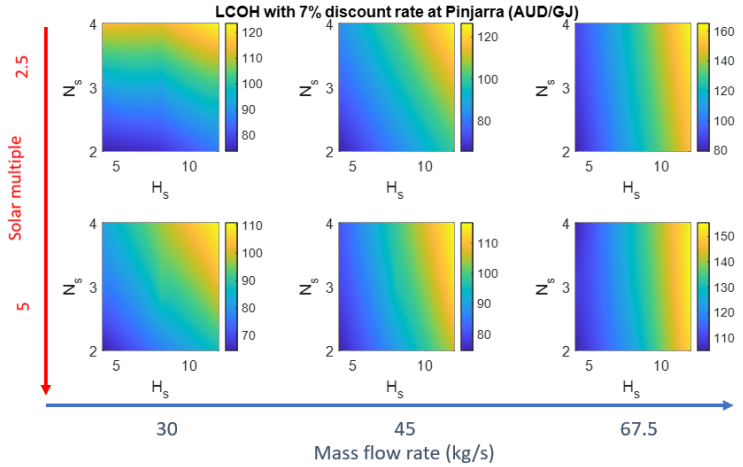

Figure 99: Influence of the number of storage devices (N_s) and of total number of storage hours (H_s) on the LCOH for a discount rate of 7%, the reference conditions (Table 35) and for Configuration 1a (windowless SEVR with air only). The top row is for solar multiple of SM=2.5 whereas the second row is for SM=5. For three columns correspond to mass flow rates through the receiver of $\dot{m}_{air}$ =30, 40, to 67.5 kg/s.

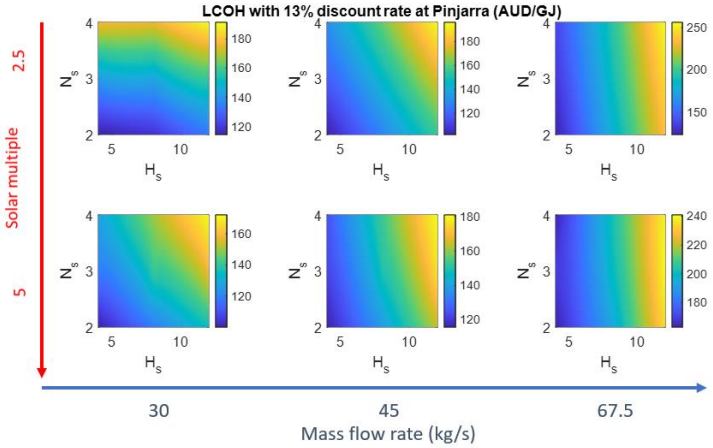

Figure 100: The infleunce of the number of storage devices (N_s) and number of total storage hours (H_s) on levelised cost of heat (LCOH) for a discount rate of 13% for Configuration 1a (windowless SEVR with air only) at Pinjarra and the reference conditions (Table 35). The top row is for a solar multiple of SM=2.5 whereas the second row is for SM=5. The three columns correspond to mass flow rates of air through the receiver of $\dot{m}_{air}$ =30, 40, to 67.5kg/s.

6.4.3.4.1. Configuration 1b (windowless SEVR with air and particles)

Figure 101 presents the influence on the annual solar share of the number of storage devices (Ns) and number of total storage hours (Hs) for Configuration 1b (windowless SEVR with air and particles) for a particle mass loading ratio R_p= 10% at Pinjarra for the reference conditions (Table 35). Data reported for a series of values of SM and mass air flow. The most optimistic configuration for both SM=2.5 and 5 is shown in Table 37. For SM=2.5, the annual solar share was found to be 29%, approximately 20% higher than Configuration 1a. Similar trend was on the $LCOH$ where it was estimated to be AUD48.1/GJ at a discount rate r_{dsic}=7%, and $LCOH$= AUD74.6/GJ at a r_{disc}=13% as shown in Figure 102 and Figure 103, respectively. These are similarly some 20% lower than for configuration 1a.

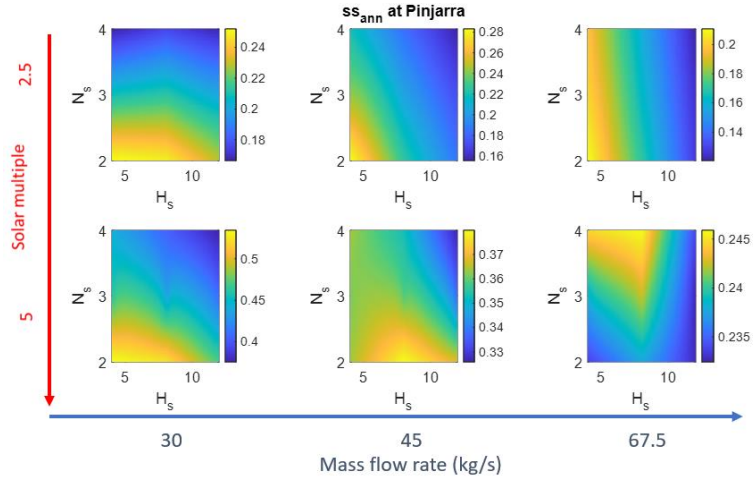

Figure 101: Influence of the number of storage devices (N_s) and number of total storage hours (H_s) on the annual solar share for Configuration 1b (windowless SEVR with air and particles) at Pinjarra for the reference conditions (Table 35). The top row shows a solar multiple of SM=2.5 whereas the second row for SM=5, while the three columns correspond to mass flow rates of air through the receiver of $\dot{m}_{air}$ = 30, 40, to 67.5 kg/s.

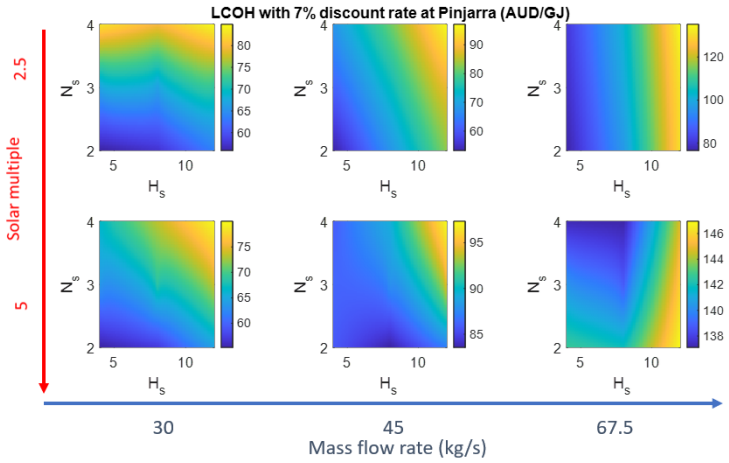

Figure 102: The influence of the number of storage devices (N_s) and number of total storage hours (H_s) on LCOH for a discount rate of 7% for Configuration 1b (windowless SEVR with air and particles) with the reference conditions (Table 35) at Pinjarra. The top row shows a solar multiple of SM = 2.5 whereas the second row for SM=5. The three columns correspond to a mass flow rate of air through the receiver of $\dot{m}_{air}$ =30, 40, to 67.5 kg/s.

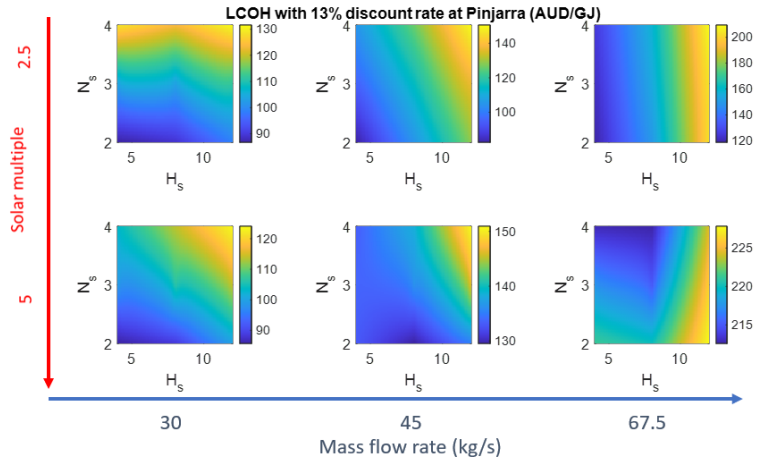

Figure 103: The influence of the number of storage devices (N_s) and number of total storage hours (H_s) on LCOH for a discount rate of 13% and the reference conditions (Table 35) with Configuration 1b (windowless SEVR with air and particles) at Pinjarra. The top row shows a solar multiple of SM=2.5 whereas the second row for SM=5. For three columns correspond to the mass flow rate of air through the receiver of $\dot{m}_{air}$ =30, 40, to 67.5kg/s.

Table 37: The most optimistic parameters for Configuration 1b located at Pinjarra.

SM	$\dot{m}_{air}$	R_p	N_s	H_s	SOC_{24}	L_p	η_p
2.5	45	0.1	2	4	5	1000	95
5	30	0.1	2	4	5	1000	95

We have also assessed the influence of DNI location for the most optimistic configuration of the reference conditions (Table 35) for Configurations 1a and 1b. Figure 104 presents the influence of number of storage devices (N_s) and number of total storage hours (H_s) on the annual solar share for Configuration 1a (windowless SEVR with air only) at Learmonth for a series of SM and $\dot{m}_{air}$. The most optimistic configuration for both SM=2.5 and 5 is shown in Table 38. This can achieve an annual solar share of 36%, which is 20% higher than for Configuration 1b, due the better DNI resources. The lowest $LCOH$ of the optimistic configuration was found to be AUD38.7/GJ at a discount rate r_{dsic}=7%, and $LCOH$= AUD60.1/GJ at a r_{disc}=13% as shown in Figure 106.

Table 38: The most optimistic parameters for Configuration 1b using the reference conditions (Table 35) at the location of Learmonth.

SM	$\dot{m}_{air}$	R_p	N_s	H_s	SOC_{24}	L_p	η_p
2.5	45	0.1	2	4	5	1000	95
5	30	0.1	2	4	5	1000	95

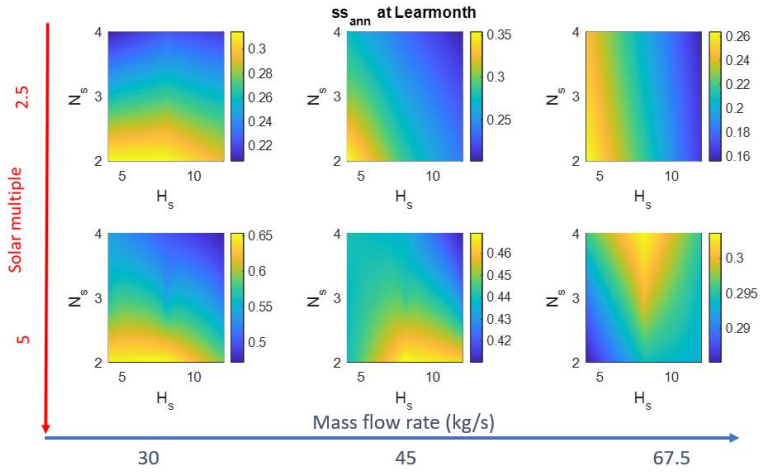

Figure 104: Influence of the number of storage devices (N_s) and number of total storage hours (H_s) on the annual solar share for Configuration 1b (windowless SEVR with air and particles) at Learmonth. The top row shows the solar multiple of SM=2.5 whereas the second row for SM=5. For three columns correspond to $\dot{m}_{air}$ =30, 40, to 67.5kg/s.

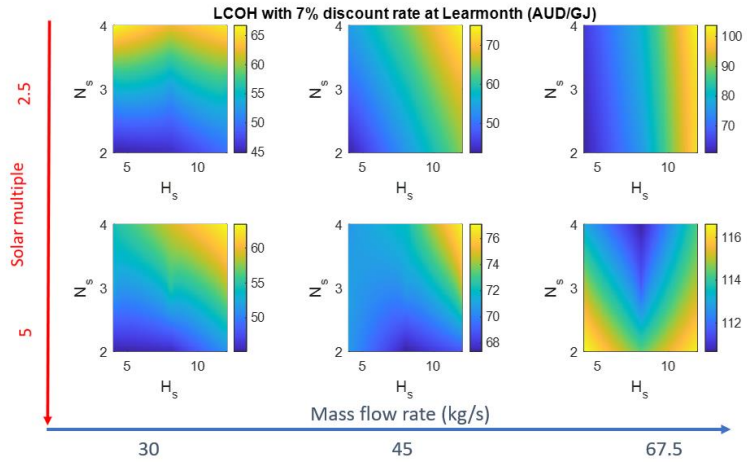

Figure 105: Influence of the number of storage devices (N_s) and number of total storage hours (H_s) on the LCOH for a discount rate of 7% and the reference conditions (Table 35) with Configuration 1a (windowless SEVR with air only) at Learmonth. The top row shows a solar multiple of SM= 2.5 whereas the second row for SM=5. The three columns correspond to $\dot{m}_{air}$ =30, 40, to 67.5 kg/s.

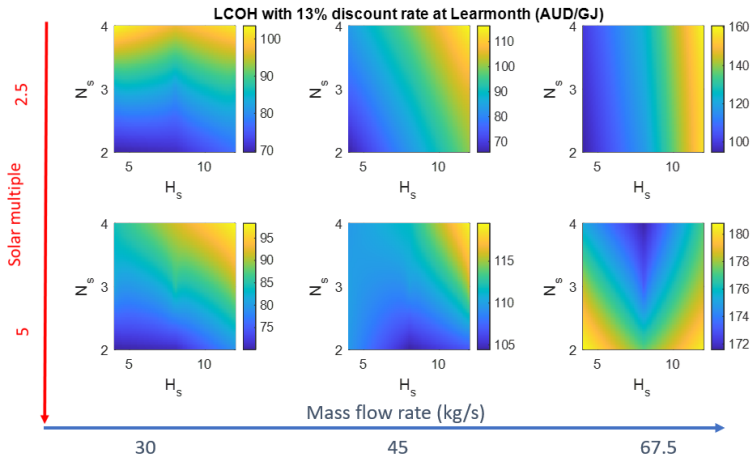

Figure 106: The influence of the number of storage devices (N_s) and number of total storage hours (H_s) on LCOH for a discount rate of 13% and the reference conditions (Table 35) for Configuration 1b (windowless SEVR with air and particles) at Learmonth. Other conditions as per previous figure.

6.4.3.4.2. Configuration 2 (windowed SEVR with air only)

Figure 107 presents the influence on the annual solar share of the number of storage devices (Ns) and number of total storage hours (Hs) for Configuration 2 (windowed SEVR with air only) for a particle mass loading ratio R_p= 10% at Pinjarra for the refertence conditions (Table 35). Data reported for a series of values of SM and mass air flow. The most optimistic condition for both SM=2.5 and 5 is shown in Table 39. For SM=2.5, the annual solar share was found to be 43%, approximately 87% higher than Configuration 1a. Similar trend was on the $LCOH$ where it was estimated to be AUD48.1/GJ at a discount rate r_{dsic}=7%, and $LCOH$= AUD74.6/GJ at a r_{disc}=13% as shown in Figure 108 and Figure 109, respectively. These are similarly some 54% lower than for configuration 1a.

Table 39: The optimistic parameters of a windowed SEVR with air-only at Pinjarra.

SM	$\dot{m}_{air}$	R_p	N_s	H_s	SOC_{24}	L_p	η_p
2.5	67.5	0	2	4	5	1000	95
5	67.5	0	4	4	5	1000	95

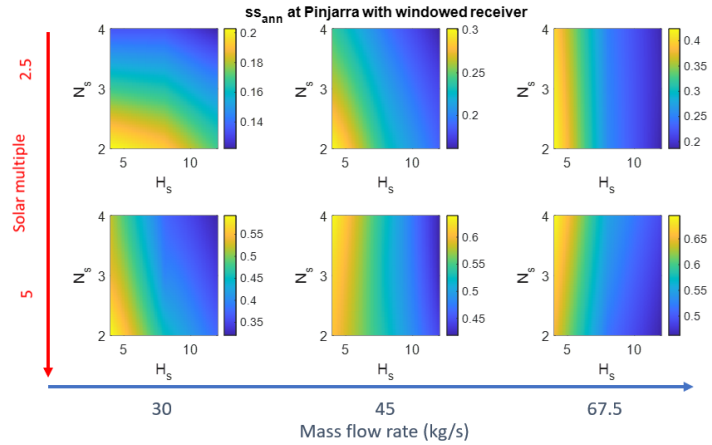

Figure 107: The influence of the number of storage devices (N_s) and number of total storage hours (H_s) on annual solar share for Configuration 2 (windowed SEVR with air only) using the reference conditions (Table 35) at Pinjarra. The top row shows a solar multiple of SM=2.5 whereas the second row for SM=5. The three columns correspond to $\dot{m}_{air}$ =30, 40, to 67.5kg/s.

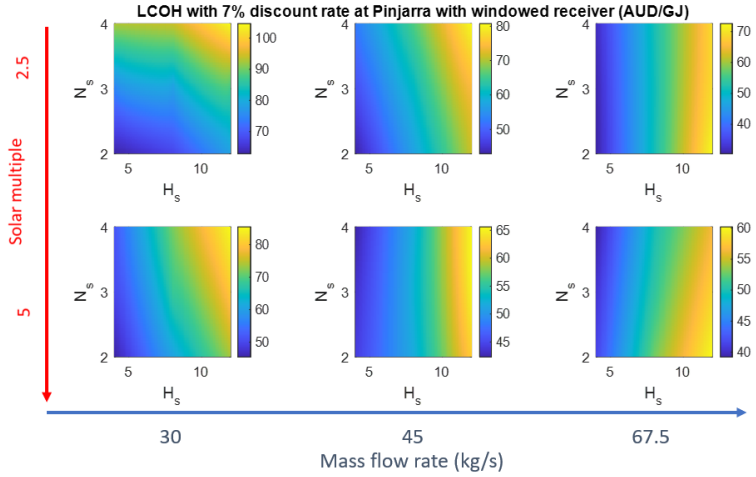

Figure 108: Influence of the number of storage devices (N_s) and number of total storage hours (H_s) on LCOH for a discount rate of 7% and the reference conditions (Table 35) using Configuration 2 (windowed SEVR with air only) at Pinjarra. The top row shows a solar multiple of SM= 2.5 whereas the second row for SM=5. The three columns correspond to $\dot{m}_{air}$ =30, 40, to 67.5 kg/s.

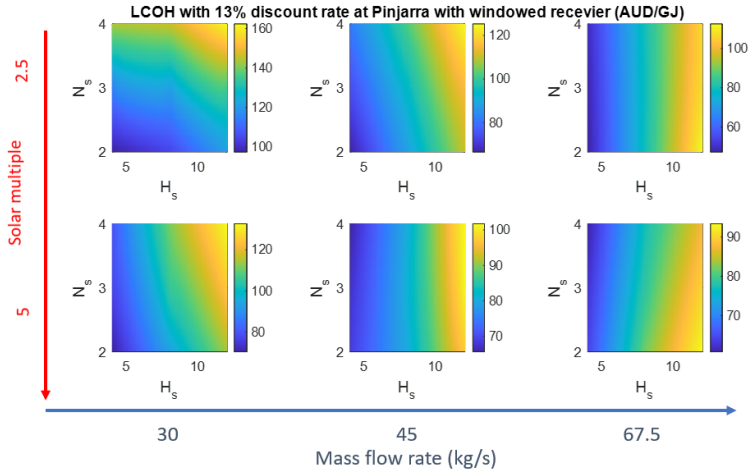

Figure 109: The influence of the number of storage devices (N_s) and number of total storage hours (H_s) on LCOH for a discount rate of 13% and the reference conditions (Table 35) with Configuration 2 (windowed SEVR with air only) at Pinjarra. The top row shows an optical solar multiple of SM=2.5 whereas the second row for SM=5. The three columns correspond to $\dot{m}_{air}$ =30, 40, to 67.5kg/s.

6.4.4. Results summary

Table 40 to Table 42 present the details of the cost breakdown and key dimension for the optimistic LCOH for Configurations 1a, 1b and 2 at Pinjarra with SM=2.5.

Table 40: Breakdown of the costs of the heliostat field and tower for the 3 configurations.

Component	AUD
Tower	$10,300,000
Heliostat field	$19,500,000
Site improvements	$2,500,000
Total	$32,300,000

Table 41: Cost breakdown and key dimension of the SEVR for the 3 configurations.

Component	AUD
Refractory	$315,570
Insulation	$4,938
Steel	$139,960
Particle system (Configuration 1b)	
Cyclone	$515,800
Particles and their storage	$268,960
Window (Configuration 2)	$412,545
Instrumentation (Configuration 1a)	$46,047
Instrumentation (Configuration 1b)	$124,523
Instrumentation (Configuration 2)	$87,301
Heat exchanger (Configurations 1a and 1b)	$7,600,000
Blowers (Configurations 1a and 1b)	$3,100,000
Blowers (Configuration 2)	$6,100,000
Total cost of Configuration1a	$11,206,515
Total cost of Configuration 1b	$12,482,296
Total cost of Configuration 2	$7,060,315
Key information	

Receiver diameter [m]	7.75
Receiver length [m]	8.54
Receiver cone section length [m]	3.46
Aperture diameter [m]	3.875
Thickness of refractory [m]	0.1
Thickness of insulation [m]	0.1
Thickness of steel [m]	0.01
Heat exchanger heat transfer area [m^2]	31489
Flow rate of each blower [m^3/s]	33.3

Table 42: Cost breakdown and key dimension of the storage system.

Storage	**AUD**
Fire brick	$82,840
Ceramic fibres	$450,890
Concrete	$1,844,800
Storage material	$530,000
Valves	$800,000
Instrumentation	$370,853
Total	$4,079,383
Key dimension	
Storage height [m]	5.44
Storage diameter [m]	5.44
Thickness of insulation [m]	5.29
Number of storages	2 units

In the following the results are summarised and discussed. Table 43 and Table 44 present the lowest LCOH for SM = 2.5 and 5, respectively. Figure 110 and Figure 111 present the breakdown cost for the optimal cases for each configuration for SM=2.5 and 5, respectively. For the windowless configurations (1a and 1b), the lowest LCOH were found to be similar for both SM of 2.5 and 5. However, the windowed SEVR (Configuration 2) at SM=2.5 was found to the most cost-effective pathway in this study.

Table 43: Summary of all input parameters together with the energy and economic results for the optimum cases for SM = 2.5.

	1a (Pinjarra)	**1b (Pinjarra)**	**1b (Learmonth)**	**2 (Pinjarra)**
SM	2.5	2.5	2.5	2.5
$\dot{m}_{air}\ [kg/s]$	45	45	45	67.5
R_p	0	0.1	0.1	0
N_s	2	2	2	2
$H_s[h]$	4	4	4	4
$E_s[\%]$	5	5	5	5
L_p[m]	1000	1000	1000	1000
$E_p[\%]$	95	95	95	95
Annual solar input to the receiver [TJ]	428	428	508	428
Annual demand to the process [TJ]	631	631	631	631
Annual solar energy to Process [TJ]	145.6	182.1	227	272

Solar to process efficiency	34%	43%	45%	64%
Annual solar share	23%	29%	36%	43%
CO_2 saving [Tonne]	7281	9106	11352	13598
LCOH (7%) [AUD/GJ]	59.5	48.1	38.7	27.1
LCOH (13%) [AUD/GJ]	92.3	74.6	60.1	42.0
	Unit cost (% of CAPEX)			
Total CAPEX [M AUD]	69.8	70.6	70.8	65.6
Field & Tower	46.2%	45.7%	45.9%	49.2%
Receiver	0.6%	1.7%	1.7%	1.3%
Storage	4.2%	4.1%	4.1%	4.4%
Transmission	31.9%	31.6%	31.5%	34.0%
Heat Exchanger	11.0%	10.8%	10.8%	0.0%
Valves	1.1%	1.1%	1.1%	1.2%
Blowers	4.4%	4.4%	4.4%	9.3%

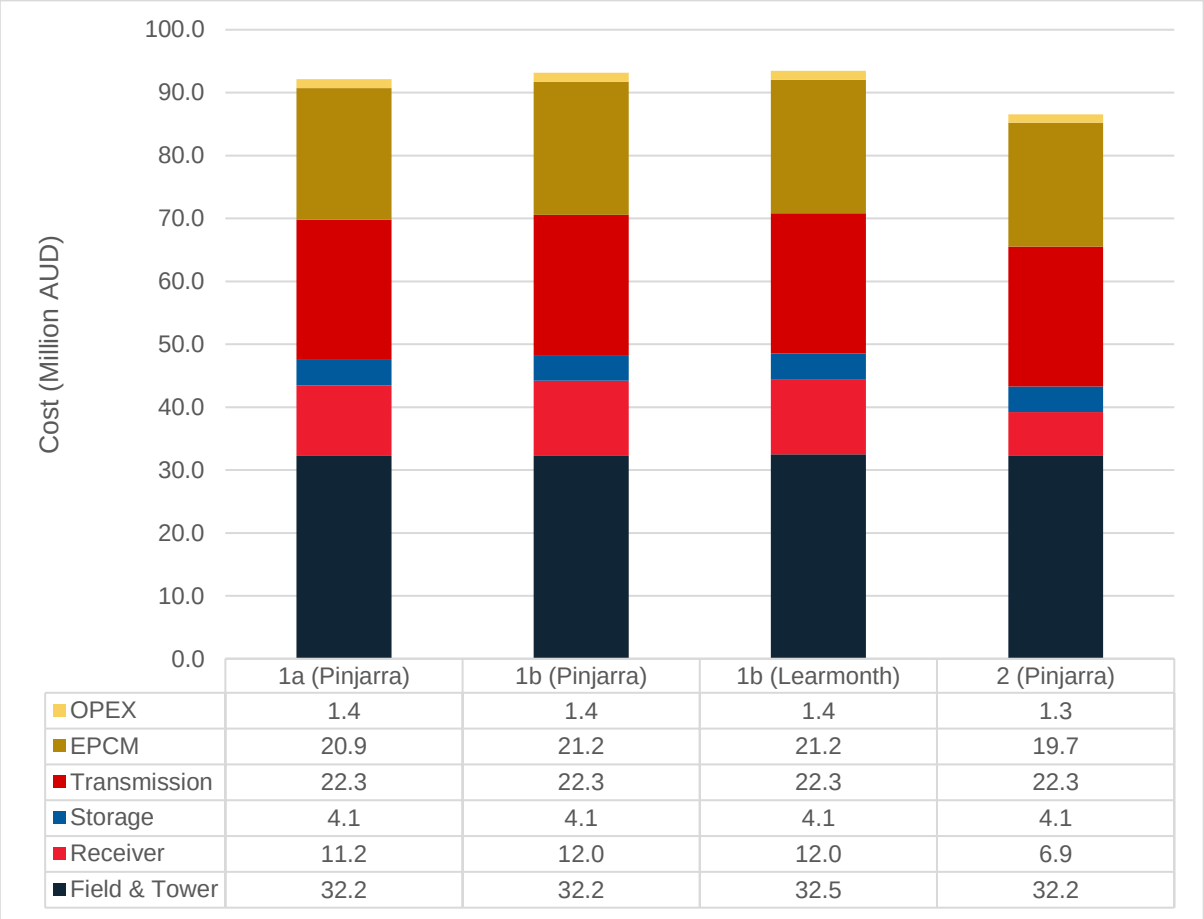

	1a (Pinjarra)	1b (Pinjarra)	1b (Learmonth)	2 (Pinjarra)
OPEX	1.4	1.4	1.4	1.3
EPCM	20.9	21.2	21.2	19.7
Transmission	22.3	22.3	22.3	22.3
Storage	4.1	4.1	4.1	4.1
Receiver	11.2	12.0	12.0	6.9
Field & Tower	32.2	32.2	32.5	32.2

Figure 110: Cost break down for the optimal cases for each configuration for SM=2.5.

Table 44: Summary of all input parameters together with the energy and economic results for the optimum cases for SM =5.

	1a (Pinjarra)	1b (Pinjarra)	1b (Learmonth)	2 (Pinjarra)
SM	5	5	5	5
$\dot{m}_{air}\,[kg/s]$	30	30	30	67.5
R_p	0	0.1	0.1	0
N_s	2	2	2	4
$H_s[h]$	4	4	4	4
E_s[%]	5	5	5	5
L_p[m]	1000	1000	1000	1000
$E_p[\%]$	95	95	95	95
Annual solar input to the receiver [TJ]	428	428	508	428
Annual demand to the process [TJ]	315	315	315	315
Annual solar energy to Process [TJ]	146.0	172.4	209.6	221.0
Solar to process efficiency	34.1%	40.3%	41.2%	51.7%
Annual solar share	46%	55%	66%	70%
CO_2 saving [Tonne]	7301	8618	10479	11051
LCOH (7%) [AUD/GJ]	58.2	49.9	51.1	35.0
LCOH (13%) [AUD/GJ]	90.2	77.3	63.8	54.3
	Unit cost (% of CAPEX)			
Total CAPEX [M AUD]	68.3	69.1	69.4	68.4
Field & Tower	47.2%	46.6%	46.8%	47.1%
Receiver	0.6%	1.8%	1.8%	1.2%
Storage	2.7%	2.7%	2.7%	1.8%
Transmission	38.1%	37.7%	37.6%	38.1%
Heat Exchanger	7.5%	7.4%	7.4%	0.0%
Valves	1.2%	1.2%	1.2%	2.3%
Blowers	2.3%	2.3%	2.3%	9.0%

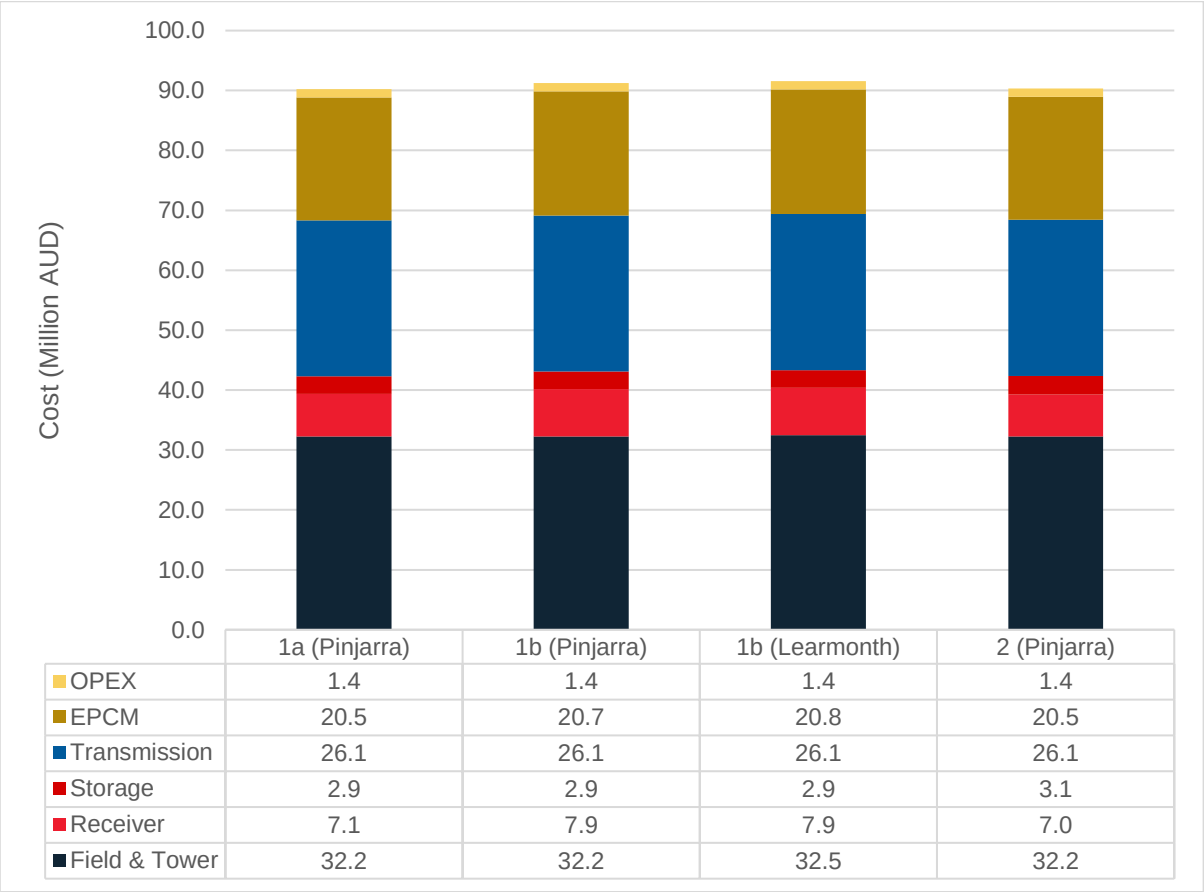

	1a (Pinjarra)	1b (Pinjarra)	1b (Learmonth)	2 (Pinjarra)
OPEX	1.4	1.4	1.4	1.4
EPCM	20.5	20.7	20.8	20.5
Transmission	26.1	26.1	26.1	26.1
Storage	2.9	2.9	2.9	3.1
Receiver	7.1	7.9	7.9	7.0
Field & Tower	32.2	32.2	32.5	32.2

Figure 111: Cost breaks down for the optimal cases for each configuration for SM=5.

Figure 112 presents the sensitivity of financial performance (NPV) to capital cost of Configuration 2 as a percentage of default case by varying the cost of natural gas and the discount rates. The NPV approach has been implemented in Programs 1 and 2 and reported in the previous milestone reports. A minimum capital cost reduction of 40% at 7% discount rate is required to improve the NPV from - AUD25.2M to AUD3.7M if the cost of natural gas at AUD10/GJ. The NPV value can be improved improve for high natural gas price. Note that this NPV is for one calciner at 120 t/hr alumina production rate. The NPV could achieve~AUD18.5M (AUD3.7M x 5 calciners) if to install a large scale of CST plant (250MW_{th}) to provide high temperature air of 1100°C to all the calciners in the refinery.

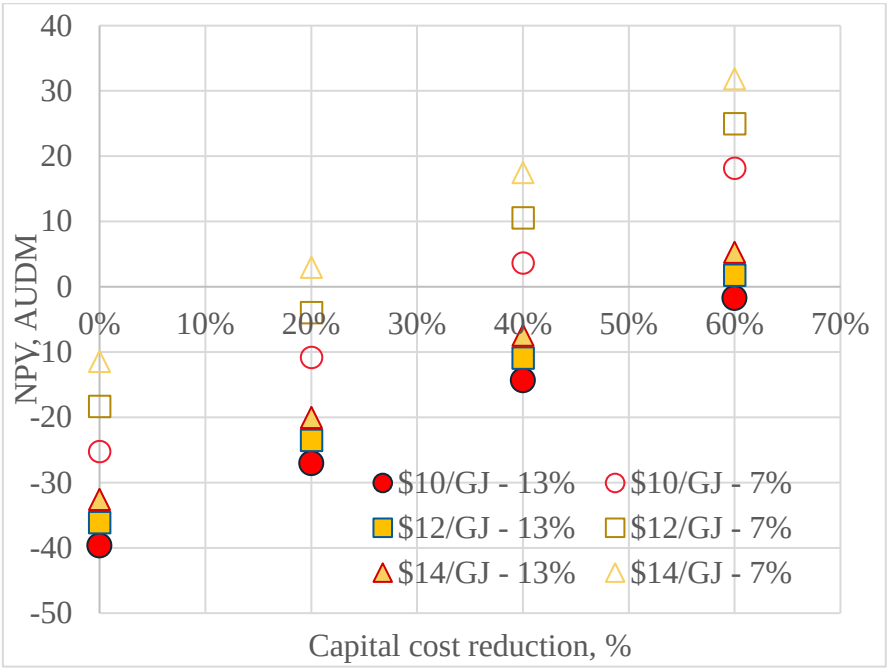

Figure 112: Sensitivity of financial performance (NPV) to capital cost of a windowed 50MW$_{th}$ (Configuration 2) as a percentage of default case by varying the cost of natural gas and the discount rates. Note that this is only for one calciner.

Figure 113 presents the Sankey diagram of the annual averaged energy flow of Configuration 1b. The major energy losses in the system are from the storage system (32.6%) and receiver (20.9%). This suggest that it should be desirable to reduce storage losses.

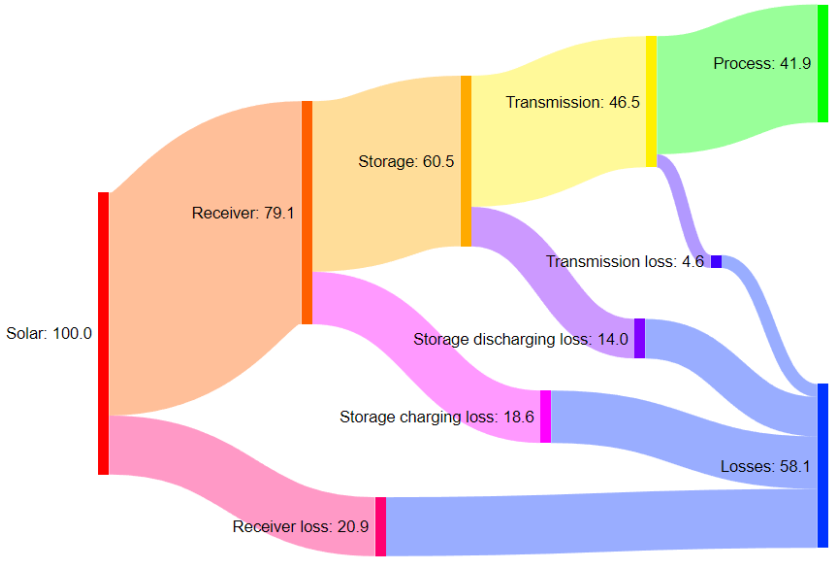

Figure 113: Sankey diagram of the annual averaged energy flow of Configuration 1b in percentage.

Overall, it was found that the cost of transmitting high temperature air through the air transmission pipelines (or cost of integration) is the biggest single, cost followed by the heliostat field cost. This is due to the required length of insulated pipelines >1000m for the Pinjarra context. It should be noted that integration is always more challenging in a retrofit due to the lack of land availability closer the calciners. The cost of

integration is influence significantly by the distance between a CST and a calciner together with the operating temperature.

It is also clear that, although the cost of storage is not dominant, it contributes most to energy losses, which total some 32% of the solar input. This highlights the challenges of the use of sensible energy storage which, while robust, leads to losses during charging and discharging. Nevertheless, there is significant opportunity to reduce these losses by optimisation of the control strategy.

The finding, that the smallest analysed storage size, shows that the solar multiple of 2.5 was not enough to fully utilize the storage system because there is limited surplus energy generated to fill the storage. The solar multiple was defined from the optical input power of 50MW_{th} and the process heat demand of 20MW_{th}. Taking in to account the losses along the way, i.e. receiver, storage, heat exchanger and transmission efficiency, the net solar energy for the process heat is significant less than 50MW_{th} and there is not enough surplus that a need for a large storage system arises. In the case of a solar multiple of 5, there was a surplus energy is generated and the optimal cases that are found for this study include more storage, however this comes with the higher cost of the larger solar field, thus the smaller system without much storage are more economically sensible.

In the case of the open receiver, especially the particle laden flow, it is crucial that direct flow from the receiver into the process is avoided to prevent contamination of the process. This is achieved with the present system.

Following demonstration at this 50MW_{th} scale and assuming that the system can be scaled up 450MW_{th} successfully that a wide range of scatter exists for the value of LCOH achieved for each of these operating conditions, which depend on the selected value for $\dot{Q}_{solar}, SM, H_s, \mathrm{SOC}_{24}$ and η_{tran}, shown as scatter plot in Figure 114. The locus of the lowest LCOH for the cases that were evaluated here shows that the lowest LCOH is achieved for a solar share of about 25%. However, a significant further increase in solar share can be achieved with only a marginal increase in the LCOH over the range 25% < SS < 60%.

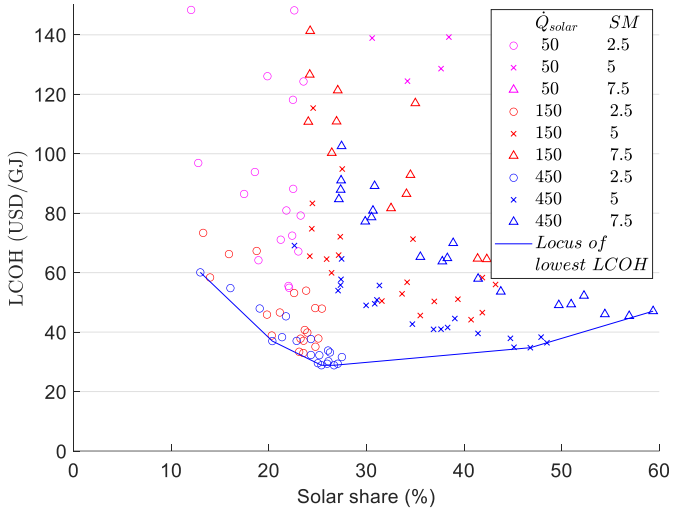

Figure 114: The dependence on solar share of the Levelised Cost of Heat (LCOH) for the system for various H_s, SOC_{24} and η_{tran}. (Nathan et al., 2023).

Figure 115 presents scenarios that illustrate the potential for high temperature solar thermal energy to achieve further reductions up to 40% cost reduction together with the improvement of the efficiency of the receiver and the management of storage charging strategy, together with two scenarios of improved

system performance, namely by factors of 20% and 40%. It is estimated that stored heat could be provided to a plant at costs of around AUD15.6/GJ (USD12/GJ), including the cost of transporting heat from the tower to the plant.

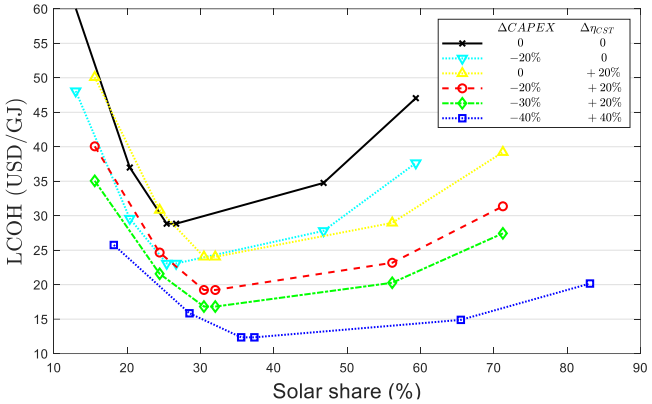

Figure 115: The dependence on solar share of the Levelised cost of heat (LCOH) for the system with the sensitivity to variation in CAPEX and overall efficiency of the CST. The refence case is the Locus of lowest LCOH shown in Figure 114 ('Gus' Nathan et al., 2023).

6.4.5. Summary

A system model has been successfully developed to allow the solar thermal system to be both analysed and optimised techno-economically. A preliminary evaluation has been assessed for the reference configuration of SEVR technology, which is not yet optimised. A preliminary sensitivity study has also been performed to guide further evaluations. These will be used for the final stage of work, which will allow more complete cost comparisons to be performed.

A key finding of the present milestone is that the cost of integration is very important in the supply of solar heat to an industrial process, and can easily become the dominant cost, particularly for a retrofit scenario in which the available land is further from the calciner than would be possible with a green-field layout.

The assessment also highlighted the importance of minimising energy losses from storage, which contribute the greatest energy losses from the reference system, both for the processes of charging and discharging, and from heat losses. We will also do more work to further reduce the energy losses during charging and discharging.

The losses from the solar receiver are the next most significant contributor. There is significant potential to reduce these in the future, particularly if an alternative heat transfer fluid is to be used. A preliminary assessment of the potential to replace the present solar system with a steam-based heat transfer medium (HTM) will also be undertaken in consultation with a solar thermal company, Synhelion, who are developing a windowed, steam receiver system.

6.5. Integration of the solar reforming technology (combined with the preferred storage system) and the low temperature CST technology

6.5.1. Introduction

The project will establish a path to progressively integrate three complementary concentrating solar thermal (CST) energy technologies into the current energy-intensive Bayer Process that produces calcined alumina from bauxite with natural gas. Adding solar energy to this process will offer significant benefits to Australia by decreasing fuel costs (which are anticipated to rise) and by opening up access to new markets for low-carbon, high value products. The project will develop three classes of hybrid technologies for both the low and high temperature processes to enable a 29% – 45% solar share. In doing so, we will ensure that continuous operation can be maintained, and that only minimal changes would need to be made to the refinery process, hence minimising the risk that industry takes on when introducing a new technology like this.

6.5.2. Program 1 - Low temperature CST technology

The assessment of techno-economic viability of integrating low- or medium-temperature process heat generated with concentrated solar thermal energy (CST) into the digestion step of the Bayer alumina production process has completed and reported in the Program 1 report. The most optimistic configuration(s) from Program 1 has been selected to be integrated with the other optimistic configuration from Programs 2 and 3. A brief summary of the techno-economic assessment of Program 1 is summarised here and details can be found in the Program 1 report. Here, the target criteria for a full-scale 392 MW_{th} CST system, capable of providing 500 t/h of steam during peak irradiation. This requires the CST system to operate between around 300 and 500°C. This temperature range is achievable with trough, Fresnel and tower technology.

The resulting component cost models were used with NREL's SAM model to evaluate the annual thermal output and total installed cost (including 25% indirect cost) of a range of large-scale CST system configurations. The CST system configurations considered included the technologies linear Fresnel, parabolic trough and solar tower, with thermal storage sizes of 0, 8 and 14 hours. The solar multiple (solar field size) is optimised in each case to minimise the resulting LCOH. The results of the analysis in Program 1 show that, at present, no CST system configuration could be identified that meets NPV target of >$20M at Pinjarra. However, all large-scale system configurations are found to yield positive IRRs. With average cost estimates, providing a conservative estimate of today's costs, IRR values range from 3.5 to 7%, while with low-cost estimates, representing lowest available cost data, IRR ranges from 6 to 13.5%. The LCOH are estimated to be in the range of AUD14 to 24/GJ_{th} depending on the thermal storage size with low-cost estimates. The solar share is estimated to in the range of 30 to 38%.

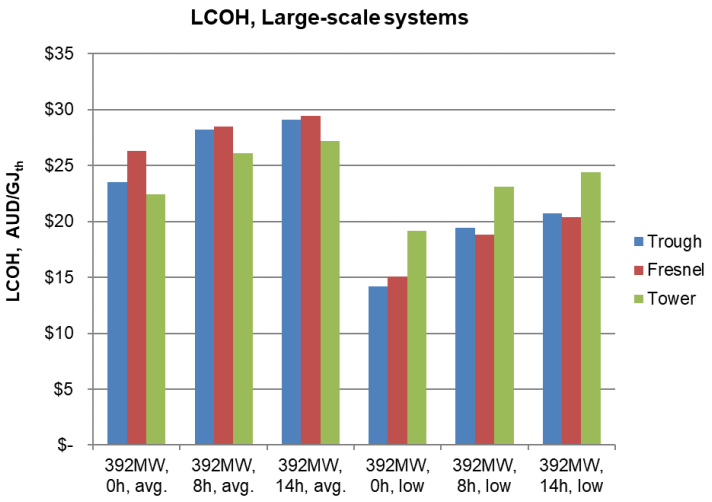

Figure 116: LCOH estimates for large-scale (392 MW_{th}) CST systems for steam generation at Pinjarra with a 20% reduction in CapEx over today's costs for CST for various values of thermal storage and for the average and lowest cost estimates provided by suppliers. (Program 1 report)

Table 45: Summary of best system results for 3 CST technologies for steam generation at Pinjarra. (Program 1 report)

Location	Technology	SM	Storage	Total CapEx	CST	NPV (m)	IRR
Pinjarra	**Trough**	2	6	$452,322,240	30.2%	-$37.5	9.8%
	Tower	2	8	$734,898,488	38.4%	-$96.5	7.9%
	Fresnel	3	4	$496,555,776	32.0%	-$35.1	9.9%

6.5.3. Program 2 - Solar reforming technology

Particle-Reformer system

The configuration of pre-reformer storage of thermal energy has been selected in Program 2 because it allows continuous reformer operation, and it offers the ability to further optimise the reforming process to maximise the capture and utilisation of solar energy in a cost-effective manner. The energy collected into the particles at the receiver was predicted for the optimised field design using CSIRO's Heliosim software package and the typical year of solar data for Pinjarra. A 50MW_{th} solar plant was considered to be an appropriate unit size for demonstration, with a larger system based on a 150MW_{th} and 450MW_{th} solar plant being proposed as a feasible size for a commercial unit that would result in some unit cost savings due to the larger equipment scales. The assessment established that, for Alcoa's Pinjarra refinery location, a system design with 14 hours thermal storage capacity and a reformer operating at 4 bar pressure provided the optimal technoeconomic performance. This data and the predicted heat collection were on an hourly basis for a whole year. For a 50MW_{th} solar plant, the heat losses from the storage and reformer were estimated at 4%, based on a typical 2% loss using similar insulation to the molten salt storages used in conventional solar plants, resulting in approximately 12.5MW_{th} of stored heat being required for 12MW_{th} of reforming duty. Similar assessment was performed on a 150MW_{th} and 450MW_{th} solar plants.

In utilising a reformer to produce a syngas for combustion in a calciner the product required from the reformer is only required to be supplied at approximately atmospheric pressure. This reduces the need for the reformer to operate at high pressures, which has the potential to both produce significant savings in

materials and to improve the conversion efficiency of the natural gas. Using Honeywell's UniSim Process simulation software, a reformer model can be produced that predicts the thermodynamic performance under varying reactor conditions as shown in Table 46. Detailed can be found in the final report of Program 2.

Table 46: Calculated syngas gas composition and mole flow rate generated from the proposed reformers.

Scale – Particle receiver	50MW_{th}	150MW_{th}	450MW_{th}	
Scale – Heat to reformer	12.5MW_{th}	37.5MW_{th}	112.5MW_{th}	
Component	kmol/h	kmol/h	kmol/h	Vol%
CH_4	7.8	23.8	72.0	1.6%
H_2	364.7	1117.7	3388.3	75.6%
CO	76.2	233.5	707.8	15.8%
CO_2	34.0	104.3	316.1	7.0%
	MW_{th}	MW_{th}	MW_{th}	
Natural gas input to reformer	29.2	89.5	271.2	
Syngas output from reformer	36.9	113.0	342.6	

6.5.3.1. Aspen model

The Aspen Plus v12 software is used to perform a mass and energy balance of the calcination process blended with syngas generated from the reformer. This software allows mass and energy balance of each unit operation based on each individual chemical species entering and exiting each individual unit operation in a flash calcination plant to be balanced. Figure 117 presents a schematic diagram of the flash calcination process, where gibbsite particles are calcined into smelter grade alumina (SGA). Fine gibbsite particles (100–200μm) with surface moisture of approximately 5–9%, are preheated and partially calcined with hot flue gas exiting the holding vessel, through a two-stage cyclone (Cyclone 1 and Cyclone 2). Here, the cyclones are assumed to have a solid recovery of 95% and to operate as counter-current heat transfer units, in which the particles and gases enter at different temperatures but reach the same temperature at the outlet. The three-stage cooling cyclone system (Cyclones 3 to 5) is used to cool the alumina particles whilst preheating the fresh air that is required for the combustion in the main furnace. The alumina particles are further cooled down to 60°C using a fluidised bed cooler. The fine particles in the flue gas after Cyclone 1 are removed using an electrostatic precipitator (ESP) before the flue gas, whose temperature is that for water condensation (~160°C), is vented to the atmosphere. Table 47 summarises the key operating parameters calculated from the flash calcination model developed here and compares them with the available data from the literature, which verifies that they are realistic. The input fuel is adjusted to 20% blend of syngas to maintain a constant value of thermal energy input. The 20% blend of syngas to natural gas is expected to have a minimum effect to the calcination process. The operating parameters (Table 47) are then adjusted to keep the process within stable conditions. This includes maintaining the input air mass flow constant to ensure minimal changes to the alumina cooling and preheating systems. This approach requires no changes to be made to the fan setting on the alumina cooling/air preheating side, which ensures that this part of the process is not affected by any variations in fuel mixture. Similar Aspen model is used to assess 3 other cases, where the hot air from the CST reported in Program 3 is integrated into the calciner to replace the natural gas consumption in the preheater as shown in Table 48. We have also included the blend of 20% H_2 in the natural gas as shown in Case 4. Similar Particle-Reformer technology combined with a water-gas shift reactor and a CO_2 removal are proposed to upgrade the syngas into pure 'blue H_2'. The CO_2 are then captured and stored at moderate cost. Detailed of this study will be reported

in the final report. The 'blue H_2' can be blended into the existing natural gas network or the dedicated H_2 network to be constructed in near future. The location of the Particle-Reformer technology would be located where the solar resource is outstanding, and CO_2 capture is also available. Otherwise, the performance for H_2 production is poor, with relatively low carbon and energy benefits.

Table 47: Aspen+ input parameters adopted to represent the gas suspension calcination process in the present study, compared with previous studies. Variations in Present Study relate to the range of hydrogen levels considered.

	Conventional flash calciner (this study)	Kontopoulos et al. (1997) (Kontopoulos et al., 1997)	Williams and Schmidt (2012) (Williams and Schmidt, 2016)	Wind and Raahauge (2013) (Wind and Raahauge, 2013)	Klett and Perander (2015) (Klett and Perander)
Surface moisture of incoming gibbsite particles (%)	8%	5-8%	n/a	6-9%	n/a
Main furnace temperature (°C)	1050	1000	1100-1150	950	950-1000
Set air temperature at air preheat furnace (°C)	1150	1000	1100-1150	950	950-1000
Air and particle temperature prior to the main furnace (Cyclone 2) (°C)	375	320-350	n/a	250-380	300
Energy consumption (GJ /t alumina)	3.0	3.1	3.4	2.80	3.3-2.68

Table 48: Type of energy consumed for each case in the ASPEN model.

	Natural Gas (MW_{th})	Syngas (MW_{th})	H_2 (MW_{th})	CST (MW_{th})
Reference case	101			
Case 1 – 20% Syngas to the Main Furnace and Preheater	83.4	18.6		
Case 2 – CST to Preheater	82			20
Case 3 – 20% Syngas to the Main Furnace and CST to Preheater	67.5	14.6		20
Case 4 – 20% H_2 to the Main Furnace and CST to Preheater	65.6		16.4	20

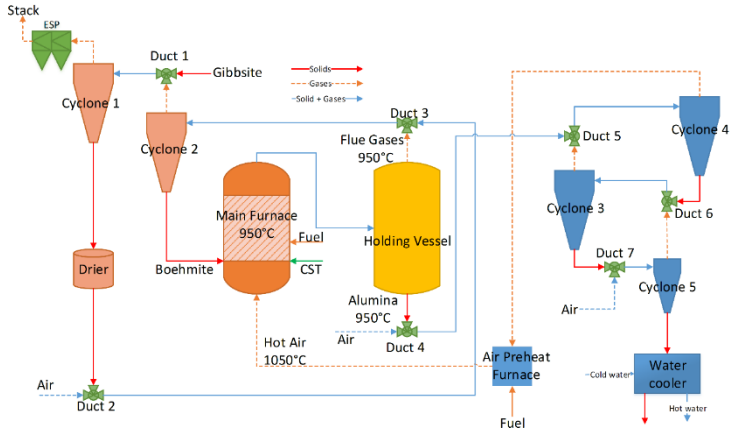

Figure 117: Schematic diagram of the flash calcination process.

Figure 118 presents the influence of the scale of particle-reformer system on the levelized cost of fuel for the syngas (LCOF) at Pinjarra and Learmonth by varying the discount rates. The LCOF was calculated to be in between AUD14-18/GJ at the discount rate of 7% and 13% for a 50MW_{th} system located in Pinjarra. The LCOF can be reduced to AUD12-15/GJ by increasing the system to 450MW_{th} due to economic of scale. Furthermore, the LCOF can be reduced by another 17% if a better solar resource location is selected, such as Learmonth. The levelized cost of H_2 at Learmonth with a carbon capture at AUD30/t_{CO2} is assessed at different scale of the scale of particle-reformer system is also presented in Figure 118. The levelized cost of H_2 was estimated to be in between AUD1.8/kg and AUD2.7/kg depending on the scale and the discount rate.

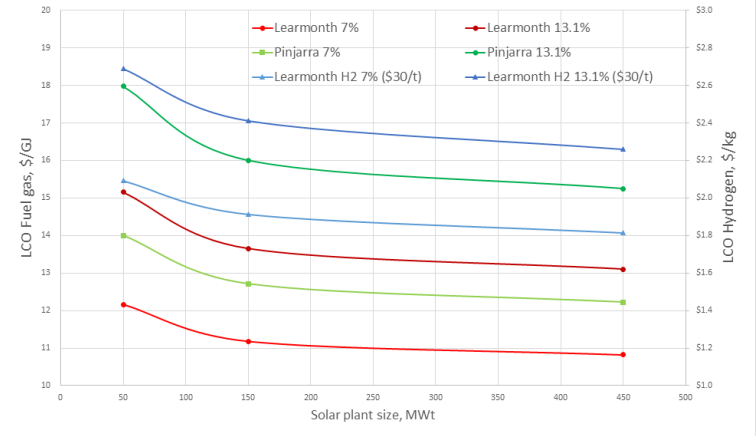

Figure 118: The influence of the scale of particle-reformer system on the levelized cost of fuel for the syngas (LCOF) at Pinjarra and Learmonth by varying the discount rates. The levelized cost H_2 at Learmonth with a carbon capture at \$30/t_{CO2} is assessed at different scale of the scale of particle-reformer system.

6.6. Plans for further development and upscaling of the technology

The further development of the CST technology developed under the present project is now being pursued through the Heavy Industry Low-Carbon Cooperative Research Centre, the planning for which began in 2020 and has included a role for CST from the outset. It can be seen that both Output 2.01 and 2.02 from the HILT Research Strategy (Figure 119) are well aligned with the potential use of CST. Indeed, the outputs from the present program are already being incorporated within HILT's Green Heat for Industry Project to further evaluate the potential of CST for high temperature industrial process heat relative to other alternative options with a view to attracting further funding for these activities.

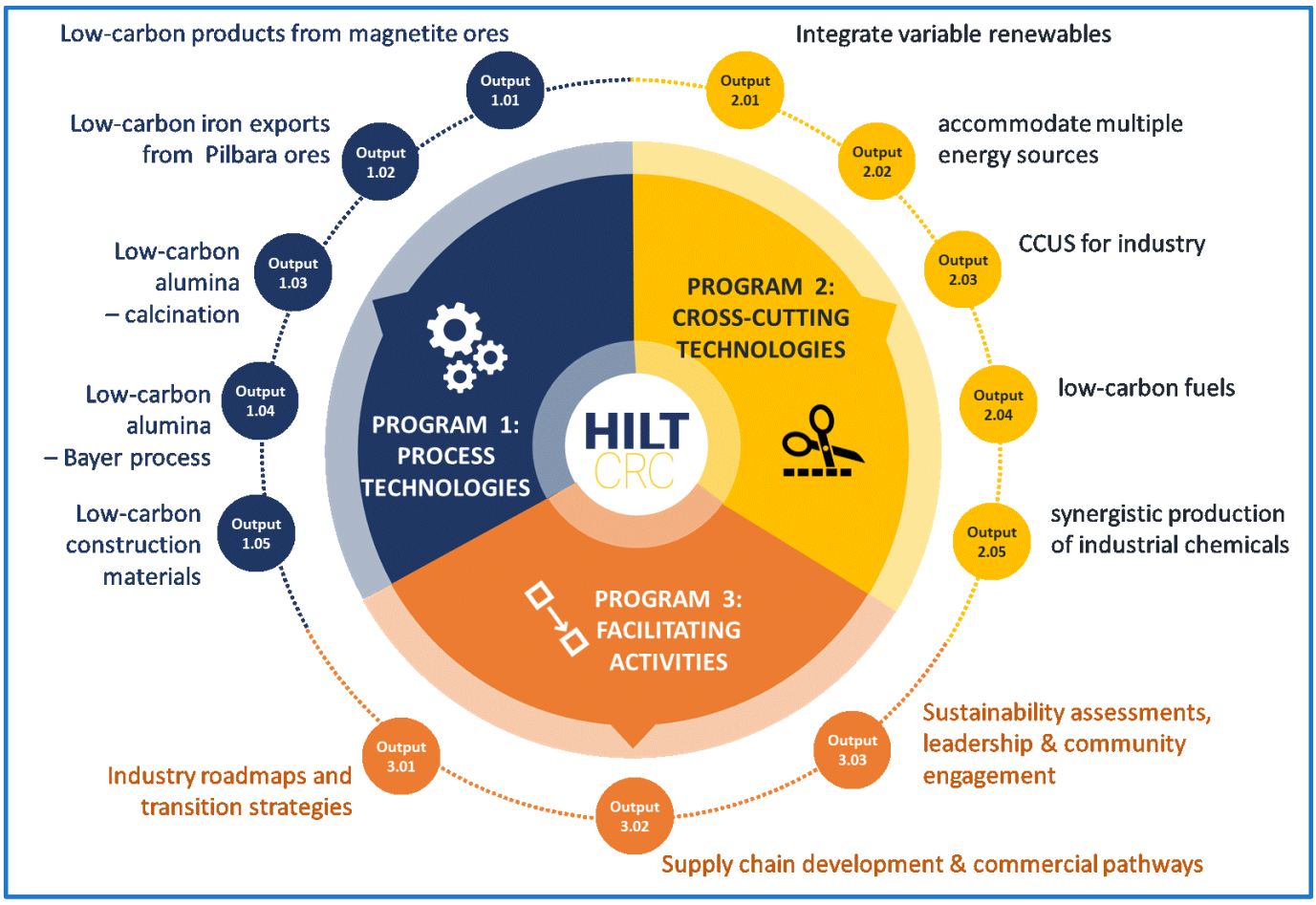

Figure 119: The list of the Program Outputs developed by the Heavy Industry Low-carbon Transition Cooperative Research Centre (HILT-CRC), for which both Output 2.01 (Integrating Varying Renewables) and 2.02 (accommodate multiple energy sources) align with the use of CST.

6.7. References

CARBOHSP High-density sintered bauxite proppant [Online]. Available: https://carboceramics.com/getmedia/dfb6e6a0-46e3-484c-ad77-c43fe362c477/CARBOHSP-Tech-Sheet-2022.pdf?ext=.pdf [Accessed].

Superwool Plus Blanket Product Data Sheet [Online]. Available: https://www.morganthermalceramics.com/media/8946/superwool-plus-blankets_eng.pdf [Accessed].

1985. *Materials Handling Handbook*, John Wiley & Sons, Inc.

2019. 2015/RND054. Integrating Concentrating Solar Thermal Energy into the Bayer Alumina Process. Milestone report number 5.

NATHAN, G. J., LEE, L., INGENHOVEN, P., TIAN, Z., SUN, Z., CHINNICI, A., JAFARIAN, M., ASHMAN, P., POTTER, D. & SAW, W. 2023. Pathways to the use of concentrated solar heat for high temperature industrial processes. *Solar Compass,* 5**,** 100036.

AMY, C., BUDENSTEIN, D., BAGEPALLI, M., ENGLAND, D., DEANGELIS, F., WILK, G., JARRETT, C., KELSALL, C., HIRSCHEY, J., WEN, H., CHAVAN, A., GILLELAND, B., YUAN, C., CHUEH, W. C., SANDHAGE, K. H., KAWAJIRI, Y. & HENRY, A. 2017. Pumping liquid metal at high temperatures up to 1,673 kelvin. *Nature,* 550**,** 199-203.

BADER, R., LOVEGROVE, K., BAYON, A. & BEATH, A. 2019. Feasibility study of CST technologies for the low temperature requirements of the Bayer Alumina Process.

BEATH A. , AGHAEIMEYBODI M. & B., W. 2014. Central receiver reference plant cost breakdown - Internal Report ASTRI.

BLAIR N., DIORIO N., FREEMAN J., GILMAN P., JANZOU S., NEISES T. & M., W. 2018. *System Advisor Model (SAM) General Description (Version 2017.9.5)* [Online]. Available: https://www.nrel.gov/docs/fy18osti/70414.pdf [Accessed].

BUIE, D., MONGER, A. & DEY, C. 2003. Sunshape distributions for terrestrial solar simulations. *Solar Energy,* 74**,** 113-122.
CHLADEK, J., ENSTAD, G. & MELAAEN, M. 2011. Effect of operating conditions and particle properties on performance of vertical air-lift. *Powder Technology,* 207**,** 87-95.
CLAUSING, A. M., WALDVOGEL, J. M. & LISTER, L. D. 1987. Natural Convection From Isothermal Cubical Cavities With a Variety of Side-Facing Apertures. *Journal of Heat Transfer,* 109**,** 407-412.
EDUARDO J. DÍAZ, ENRIQUE T. TAMAYO, DIANA M. VÉLEZ, DIEGO R. SALAZAR, CÉSAR M. DÍAZ & CEDEÑO, M. P. 2017. Energy Consumption and Simulation of Pneumatic Conveying Lateritic Mineral in Dense and Fluid Phase. *International Journal of Mechanics,* 11**,** 6.
G.E. KLINZING, F. R., R. MARCUS AND L.S. LEUNG 2010. *Pneumatic conveying of solids*, Springer.
GARRETT, D. E. 1989. *Chemical Engineering Economics,* Dordrecht, Springer Netherlands.
HO, C. K. 2016. A review of high-temperature particle receivers for concentrating solar power. *Applied Thermal Engineering,* 109**,** 958-969.
HOFFMANN, J. F., FASQUELLE, T., GOETZ, V. & PY, X. 2016. A thermocline thermal energy storage system with filler materials for concentrated solar power plants: Experimental data and numerical model sensitivity to different experimental tank scales. *Applied Thermal Engineering,* 100**,** 753-761.
JOHNSON S.G. *The NLopt nonlinear-optimization package* [Online]. Available: http://ab-initio.mit.edu/nlopt [Accessed].
KISTLER, B. L. 1986. A user's manual for DELSOL3: A computer code for calculating the optical performance and optimal system design for solar thermal central receiver plants. United States.
KLETT, C. & PERANDER, L. Alumina Calcination: A Mature Technology Under Review from Supplier Perspective. Cham: Springer International Publishing.
KOLB, G., HO, C., MANCINI, T. & GARY, J. 2010. Power tower technology roadmap and cost reduction plan.
KONRAD, K. 1986. Dense-phase pneumatic conveying: A review. *Powder Technology,* 49**,** 1-35.
KONTOPOULOS, A., KRALLIS, K., KOUKOURAKIS, E., DENAXAS, N., KOSTIS, N., BROUSSAUD, A. & GUYOT, O. 1997. A hybrid, knowledge-based system as a process control 'tool' for improved energy efficiency in alumina calcining furnaces. *Applied Thermal Engineering,* 17**,** 935-945.
KUANG, S. B., ZOU, R. P., PAN, R. H. & YU, A. B. 2012. Gas–Solid Flow and Energy Dissipation in Inclined Pneumatic Conveying. *Industrial & Engineering Chemistry Research,* 51**,** 14289-14302.
LI, H. & TOMITA, Y. 1996. An Experimental Study of Swirling Flow Pneumatic Conveying System in a Horizontal Pipeline. *Journal of Fluids Engineering,* 118**,** 526-530.
LI, H. & TOMITA, Y. 1998. An Experimental Study of Swirling Flow Pneumatic Conveying System in a Vertical Pipeline. *Journal of Fluids Engineering,* 120**,** 200-203.
MA, Z., DAVENPORT, P. & ZHANG, R. 2020. Design analysis of a particle-based thermal energy storage system for concentrating solar power or grid energy storage. *Journal of Energy Storage,* 29**,** 101382.
MEHOS, M., TURCHI, C., VIDAL, J., WAGNER, M., MA, Z., HO, C., KOLB, W., ANDRAKA, C. & KRUIZENGA, A. 2017. Concentrating Solar Power Gen3 Demonstration Roadmap. United States.
MEIER, A., WINKLER, C. & WUILLEMIN, D. 1991. Experiment for modelling high temperature rock bed storage. *Solar Energy Materials,* 24**,** 255-264.
MILLS, D. 2016. *Pneumatic Conveying Design Guide (Third Edition)*, Butterworth-Heinemann.
POTTER, D. F., KIM, J.-S., KHASSAPOV, A., PASCUAL, R., HETHERTON, L. & ZHANG, Z. 2018. Heliosim: An integrated model for the optimisation and simulation of central receiver CSP facilities. *AIP Conference Proceedings,* 2033**,** 210011.
RAFIQUE, M. M., NATHAN, G. & SAW, W. 2021. A mathematical model to assess the influence of transients on a refractory-lined solar receiver. *Renewable Energy,* 167**,** 217-235.
REPOLE, K. & JETER, S. 2016. *Design and Analysis of a High Temperature Particulate Hoist for Proposed Particle Heating Concentrator Solar Power Systems*.
RINOSHIKA, A. & SUZUKI, M. 2010. An experimental study of energy-saving pneumatic conveying system in a horizontal pipeline with dune model. *Powder Technology,* 198**,** 49-55.
RIZK, F., KLINZING, G. E., LEUNG, L. S. & MARCUS, R. 2010. *Pneumatic Conveying of Solids: A theoretical and practical approach (Particle Technology, Vol 8),* Dordrecht, Springer Science + Business Media.
SALDIVIA, D., BILBAO, J. & TAYLOR, R. 2021. Optical analysis and optimization of a beam-down receiver for advanced cycle concentrating solar thermal plants. *Applied Thermal Engineering,* 197**,** 117405.
TAYLOR, T. 1998. Specific energy consumption and particle attrition in pneumatic conveying. *Powder Technology,* 95**,** 1-6.
WAGNER, M. J. & WENDELIN, T. 2018. SolarPILOT: A power tower solar field layout and characterization tool. *Solar Energy,* 171**,** 185-196.
WATSON, R. J., THORPE, R. B. & DAVIDSON, J. F. 2012. Vertical plug-flow pneumatic conveying from a fluidised bed. *Powder Technology,* 224**,** 155-161.
WILLIAMS, F. & SCHMIDT, H.-W. 2016. Flash- and CFB Calciners, History and Difficulties of Development of Two Calcination Technologies. *In:* SUAREZ, C. E. (ed.) *Light Metals 2012.* Cham: Springer International Publishing.

WIND, S. & RAAHAUGE, B. E. 2013. Experience with Commissioning New Generation Gas Suspension Calciner. Hoboken, NJ, USA: John Wiley & Sons, Inc.
YAN, F. & RINOSHIKA, A. 2012. An Experimental Study of Horizontal Self-Excited Pneumatic Conveying. *Journal of Fluids Engineering,* 134**,** 041302-041302-7.
YAN, F., RINOSHIKA, A. & NONAKA, H. 2012. An experimental study on a horizontal energy-saving pneumatic conveying system with soft fins. *Powder Technology,* 217**,** 516-522.

7. Conclusion

The project has continued to advance the understanding of the potential role for Concentrated Solar Thermal energy technology (CST) in high temperature industrial processing. In so doing, it provides further evidence that CST has realistic potential to contribute cost-effectively to the supply of both high temperature (of order 600 – 1200°C) and medium-grade temperature (of order 200 – 600°C) relative to other net-zero options where the solar resource is sufficient. However, significant uncertainty is inherent in any predictions of future pricing, given that all technologies are under development, and, in addition, further investment is required for CST to realise this potential.

In particular:

- The assessment of commercially-ready steam production via established molten salt storage estimated this technology to be comparably economically viable with the other alternatives that were assessed for net zero, and were also found to yield a positive internal rate of return spanning between 3.5 and 13.5%. The use of between 7 and 14 hours of storage was found to yield a solar share in the range of 29 to 45% and, while the economics generally improve with decreasing storage size, little additional cost is needed to increase the solar share. Furthermore, the LCOH are estimated to be in the range of AUD22 to 30/GJ based on the average costs and in the range of AUD14 to 24 /GJ based on the low-cost estimates.
- The conversion of methane into syngas with concentrated solar thermal energy has good potential to be economically attractive where the sensible energy of the syngas can be harnessed in addition to the chemical energy. This would apply were the hot syngas to be introduced directly to the calciner rather than cooling it down before use. However, it is preferable to run the reactor off-sun and through a storage system, rather than on-sun owing both the challenges of strong syngas and to the challenges of operating a reactor variably.
- There is strong potential for solar thermal energy to provide stored heat to high temperature industrial reactors, such as alumina calciners, at prices that are attractive with other sources of net-zero energy on the proviso that ongoing investment is provided to develop and upscale the technology and that the solar resource is sufficiently good. In particular, we estimate that stored heat could be provided to a plant at costs of around AUD15.6/GJ (USD12/GJ), including the cost of transporting heat from the tower to the plant, where an allowance is made for 40% reduction in CapEx (incorporating benefits of design for manufacture) and 40% for further advances in efficiency that are expected to be achievable by incorporating additional advances in technology already under development and the advantages of processing in steam.

The main specific points are as follows:

- **Flow and scalar fields for single-phase and two-phase flow fields under iso-thermal conditions:** New understanding of the mechanisms that control ingress and egress of flow and particles through an open aperture has been identified**:** New measurements and modelling advanced understanding of the complex flow within a SEVR results in simultaneous ingress and egress through the aperture of a windowless SEVR. This flow is highly three-dimensional, so that that egress occurs through the outer edges of the aperture at the same time as an accompanying inflow to the cavity along the axis of the aperture. This understanding seeded the development of

a series of both primary and secondary control measures, with the primary mechanism being balancing total in-flows and out-flows and the pressure at the neutral plane, while secondary measures include an air curtain and secondary chamber.

- The use of the over-ventilation at the outlet was found to enable fluid phase egress through the open aperture to be mitigated. However, over-ventilation brings both an energetic and an exergetic penalty, by lowering temperature. Egress can also be mitigated by varying the aerodynamics, such as by reducing the swirl intensity at the aperture.
- Aperture size and the magnitude of over-ventilation were found to be the most significant and second important factors on mitigating particle egress for the open SEVR without additional control strategies, respectively.

- **DNS and RANS tools for two-phase flow field activities:** A direct numerical simulations (DNS) has been performed to understand the turbulence modulation and preferential particle response in turbulent jets (in SEVR). The simulation parameters are matched to an experimental case and the results are validated against the experimental data. DNS data is also useful for developing and validating models in the framework of Large eddy simulation (LES) and Reynolds-averaged Navier–Stokes equations (RANS) methodologies. The fluid statistics from an LES configuration showed a good agreement with the DNS data. An initial assessment of physics of heat transfer in particle-laden wall-bounded channel flows was performed with the objective of improving the fundamental understanding of heat transfer in solar particle receivers. It was found that a higher particle concentration is observed in the near-wall region for higher Stokes number particles. Furthermore, the fluid turbulence modulation in the near-wall region is highly anisotropic.

  The baseline **RANS tools** (an improved particle dispersion model) for the assessment of turbulent, multi-phase flows subjected to concentrated solar radiation and for the optimisation/scale-up of the actual device have been completed. In addition to the particle-size-dependent controlling coefficients that have been identified and implemented into the modified particle dispersion model, their dependency on other parameters, like the volumetric particle loading and particle polydispersity. This work provides insights on improving the accuracy of RANS simulations for solid particles in anisotropic flows. It contributes to better modelling engineering processes like combustion, spray, and other types of concentrated solar thermal systems, where such particle-turbulence flows are significant. The newly developed modifications of the particle dispersion model can be integrated into the commercial CFD tools/existing model for related engineering applications mentioned above.

- **Lab scale demonstration of SEVR**: Windowless operations were successfully carried out by applying a suction at the outlet section of the device as primary control strategy to avoid particle egress. Particle and hot air egress from the device through the aperture can be avoided by operating the device with a small net ambient air ingress. The sensitivity of the thermal performance of the SEVR to the particle and air mass flow rates, particle loading, and net ambient air ingress was assessed. It was found that both the ratio of the receiver thermal input to heat capacity of the two-phase flow and the level of suction applied at the outlet section of the receiver have controlling influence on the global performance of the SEVR. Overall, thermal efficiencies of up to 70% were measured for operations with high mass flow rates of both particles and air. For a given value of total inlet air flow rate and particle loading, an increase in the suction power (and, hence, net air ingress into the device) was found to have beneficial effects on performance, for the operating

conditions and geometry considered here. However, an increase in the suction level leads to a reduction in the maximum outlet gas temperature that can be achieved. Also, the exergy rate was found to significantly decrease by increasing the suction level for both single and two-phase experiments. Taken together the above finding, it is recommended to operate the device with the minimum suction level to maximise both the outlet gas temperature and exergy rate.

- The **Computational Fluid Dynamics (CFD) models** of the $5kW_{th}$ lab-scale receiver were found to predict that the temperature difference between the two phases is relatively small at a given location. However, it is expected that the temperature difference between the two phases may be more significant in a scaled-up device. This is because the increased reactor volume allows greater radiant heat absorption and residence time for the particle phase and therefore the temperature of particles at certain locations is likely to be considerably higher than that of the local gas phase. The Froude number (i.e. flow velocity) was found to have significant influence on the convective heat loss through the receiver aperture. This is consistent with previous trends, which have already shown that the flow recirculation in the chamber depends on this parameter. Importantly, new data were obtained that have been used both for model development/validation and for device optimisation. The validated CFD model was used to develop a configuration for an industrial-scale $50MW_{th}$ SEVR. This $50MW_{th}$ SEVR receiver was then developed further by using a control strategy to mitigate particle egress. For all cases assessed, radiative heat loss through the aperture was confirmed to be the dominant loss mechanism, rather than convection. While the trend was expected, the magnitude of the relative losses as a function of conditions is both new and important for technology optimisation and development.

- **Development of sub-model of particle thermo-physical-chemical and optical properties:** New details have been identified about the positive and negative effects of steam on the calcination pathways for gibbsite. Even though the presence of steam increases the content of hydroxyls during the conversion of gibbsite to boehmite and alumina, nevertheless, the calcination in steam can be beneficial in leading to both a higher surface area and a lower loss on ignition (LOI) of the calcined alumina than those of SGA. This cannot be achieved by a dry atmosphere. A LOI value of less than 1% with a specific surface area >75 m^2/g was measured for calcination temperatures above 750°C with a concentration of steam >50%. This is attributed to the role of steam in increasing the presence of hydroxyls on the surface of the samples which, at temperatures of 650 to 850 °C, is sufficient to induce more reactions between the hydroxyls to form water molecules, thereby reducing both the specific surface and the LOI while increasing the pore size. Also, at 400 °C, the presence of steam can significantly increase the LOI value of alumina already calcined at 850 °C, which implies an increase in the hydroxyl content. Similarly, the presence of steam at temperature above 650°C has a positive effect on the overall conversion of boehmite to gamma transitional alumina.

- **Integrate the hybrid reactor into the calcination process:** Recent estimates based on CST systems designed to supply air at temperatures of ~1100 to 1200°C as the heat transfer media (HTM) show that concentrated solar thermal energy has realistic potential to be a part of a lowest-cost energy system for high temperature industrial processes in combination with a back-up source of net-zero emissions energy such as hydrogen and/or green electricity, in those regions with a good solar resource. Importantly too, significant potential remains to further lower cost, both with the use of alternative heat transfer media, such as steam or particles, and with advances in manufacturing methods to lower the cost of solar thermal technology, such as heliostat mirrors. Nevertheless, realising these cost reductions will require the development and demonstration of

new technology based on such an alternative heat transfer media, together with the implementation of improved manufacturing methods, some of which are being developed for applications in power generation. In particular, significant technology development is required, firstly to take the temperature of the receiver and storage technology to sufficiently high values and, secondly, to develop the new systems, both for the reactors to utilise the media, and for the systems to transport the heat.